2018

The Role of Recoverable and Non-Recoverable Defects in DC Electrical Aging of Highly Disordered Insulating Materials

Allen Andersen
Utah State University

THE ROLE OF RECOVERABLE AND NON-RECOVERABLE DEFECTS IN DC ELECTRICAL AGING OF HIGHLY DISORDERED INSULATING MATERIALS

by

Allen Andersen

A dissertation submitted in partial fulfillment
of the requirements for the degree

of

DOCTOR OF PHILOSOPHY

in

Physics

Approved:

_____	_____
JR Dennison, Ph.D. Major Professor	D. Mark Riffe, Ph.D. Committee Member
_____	_____
Lee H. Pearson, Ph.D. Committee Member	Michael J. Taylor, Ph.D. Committee Member
_____	_____
Ryan L. Davidson, Ph.D. Committee Member	Mark R. McLellan, Ph.D. Vice President for Research and Dean of the School of Graduate Studies

UTAH STATE UNIVERSITY
Logan, Utah

2018

ABSTRACT

THE ROLE OF RECOVERABLE AND NON-RECOVERABLE DEFECTS IN DC ELECTRICAL AGING OF HIGHLY DISORDERED INSULATING MATERIALS

by

Allen Andersen, Doctor of Philosophy

Utah State University, 2018

Major Professor: Dr. JR Dennison
Department: Physics

Estimating the likelihood of electrostatic discharge (ESD) in highly discorded insulating materials (HDIM) during application lifetimes is critical in applications including spacecraft and high voltage dc power transmission. The focus of this work is a defect driven model of dielectric breakdown based on a dual-defect assumption. Traditional mean-field theory of breakdown effectively considers the average defect energy and density as the only defect mechanism. The dual-defect model considers high-energy (deep) chemical defects and low-energy (shallow) physical defects. Low-energy defects may have significant thermal recovery rate. Such recoverable defects provide a conceptual physical model for dc partial discharge (DCPD) transient non-shorting events. Dielectric breakdown tests on four common polymers, LDPE, PI, BOPP, and PEEK have been studied in the context of the proposed and existing models of breakdown, together with evaluation using standard empirical Weibull distributions. The resulting fits for voltage step-up to breakdown tests provide reasonable estimations of defect parameters. Static voltage endurance time data show excellent agreement with the dual-defect model. Quantile-quantile analysis demonstrates a strong correlation between DCPD and critical dielectric breakdown. During a typical breakdown test many DCPD are observed prior to the destructive breakdown. The relationship between DCPD and breakdown suggest the possibility for highly accelerated dielectric strength testing of candidate HDIM.

(264 pages)

PUBLIC ABSTRACT

THE ROLE OF RECOVERABLE AND NON-RECOVERABLE DEFECTS IN DC ELECTRICAL AGING OF HIGHLY DISORDERED INSULATING MATERIALS

Allen Andersen, Doctor of Philosophy

Utah State University, 2018

Electrical insulation under high voltage can eventually fail, causing critical damage to electronics. Such electrostatic discharge (ESD) is the primary source of anomalies or failures on spacecraft due to charged particles from the Sun or planetary radiation belts accumulating in spacecraft insulators. High-voltage direct current power distribution is another example of a growing industry that needs to estimate the operational lifetime of electrical insulation. My research compares laboratory tests of ESD events in common insulating materials to a physics-based model of breakdown. This model of breakdown is based on the approximation that there are two primary types of defects in structurally amorphous insulators. One of the two defect modes can switch on and off depending on the material temperature. This dual-defect model can be used to explain both ESD and less-destructive transient partial discharges. I show that the results of ESD tests agree reasonably well with the dual defect model. I also show that transient partial discharges, which are usually ignored during ESD tests, are closely related to the probability of catastrophic ESD occurring. Since many partial discharges are typically seen during one ESD test, this relationship suggests that the measurements of partial discharges could accelerate the testing needed to characterize the likelihood of ESD in insulating materials.

ACKNOWLEDGMENTS

I want to acknowledge the kindness, love, and patience of my wife Lauren who has supported me in this endeavor. Her encouragement and the thought of doing something she and our children could be proud of has been a great inspiration for me. I am thankful for parents Charles and Kerri Andersen, my grandparents, and the educators who have faithfully encouraged and supported me, not only during my graduate training but also throughout my life. One particularly influential moment for me that helped to kindle my interest in science was the time my Grandpa Joe took to show me the moon, planets, and stars through his small telescope.

I feel very lucky to have JR as my graduate advisor. He was kind enough to give me a chance to work in the lab when I first came to Utah State University then has patiently helped me through my graduate work and PhD research. His concern for students and as well as his patience for when they mess up is staggering. I also recognize the help and insights from other members of the Materials Physics Group especially Greg Wilson, Justin Christensen, Charles Sim, Krysta Moser, Tyler Kippen, Justin Dekany, Amberly Evans, Jodie Gillespie, Sam Hansen, and Heather Zollinger. I also want to thank our amazing Physics department staff Karalee Ransom, Sharon Pappas and Vanessa Chambers as well as our librarian, Betty Rozum for their help.

This research was supported by a NASA Space Technology Research Fellowship. I am thankful not only for the generous financial support, but for the summer visiting technologist experience opportunities at NASA labs.

Allen Andersen

CONTENTS

Page

LIST OF TABLES

LIST OF FIGURES

NOMENCLATURE

Symbol

$\mathbf{1}$	= indicator of an event [unitless]
a	= average nearest neighbor trap separation or TAH hopping distance [L]
a_{def}	= mean defect separation [L]
A	= area [L^2] or general constant [various units]
B	= general constant [various units]
C	= general constant [various units]
C_V	= volumetric heat capacity [$EL^{-3}T^{-1}$]
d	= sample thickness or depth [L]
D_{bb}	= bond breaking dose [EM^{-1}]
$\mathcal{E}$	= energy [E]
$\mathcal{E}_B$	= nearest-neighbor coupling energy [E]
$\mathcal{E}_{CB}$	= energy of the conduction band edge [E]
$\mathcal{E}_f$	= Fermi level or chemical potential [E]
$\mathcal{E}_i$	= energy level of a single state [E]
$\mathcal{E}_{ME}$	= mobility edge energy [E]
$\mathcal{E}_{strain}$	= strain energy [E]
$\mathcal{E}_{VB}$	= energy of the top of the valence band, usually set to zero [E]
f	= probability density [unitless]
f_0	= normalization factor [unitless]
$\bar{F}$	= mean electric field [$EQ^{-1}L^{-1}$]
F	= electric field [$EQ^{-1}L^{-1}$]
F_{def}^{s}	= critical electrostatic field [$EQ^{-1}L^{-1}$]
F_{ESD}^{s}	= electrostatic breakdown field [$EQ^{-1}L^{-1}$]
F_{min}	= extreme minimum field with a risk of breakdown [$EQ^{-1}L^{-1}$]

F_{onset} = onset electrostatic field for breakdown $[EQ^{-1}L^{-1}]$

F_0 = Weibull centroid parameter $[EQ^{-1}L^{-1}]$

F_s = Weibull shift parameter $[EQ^{-1}L^{-1}]$

h = Planck constant $[ETL^{-1}]$

$\hbar$ = Reduced Planck constant $[ETL^{-1}]$

$\mathcal{H}$ = Hamiltonian $[E]$

i = index or superscript indicator [unitless] or unitary imaginary number [unitless]

I = current $[QT^{-1}]$

j = index or subscript indicator [unitless]

$K_{def}^{\pm s}$ = rate of defect creation/annihilation (+/-) $[NT^{-1}]$

$\boldsymbol{k}$ = wave vector $[L^{-1}]$

k_b = Boltzmann constant $[EK^{-1}]$

m = mass $[M]$

m_e = electron mass $[M]$

$n(\mathcal{E}_f)$ = defect energy density within a few k_bT of the Fermi level $[EL^{-3}]$

n = normalization constant or counting integer [unitless]

$\langle n \rangle$ = average phonon occupancy $[N]$

n_i = fractional normalization constant [unitless]

$N(\mathcal{E})$ = density of states per unit energy per unit volume $[NE^{-1}L^{-3}]$

N_{bond}^s = density of bonds of species s $[NL^{-3}]$

N_{def0} = undisturbed defect density $[NL^{-3}]$

N_{def}^s = defect density $[NL^{-3}]$

$N_F^s(F)$ = electric field-dependent contribution to the defect density $[NL^{-3}]$

N_{step} = number of voltage steps $[N]$

$N_T^s(T)$ = temperature-dependent contribution to the defect density $[NL^{-3}]$

p = constant for probability conservation [unitless]

P = probability of event [unitless]

P_{def}^{s} = probability of breakdown [unitless]

P_{hop} = hopping probability [unitless]

P_i = fractional probability due the contribution of a single factor [unitless]

P_{mix} = total probability resulting from mixed probabilistic distribution functions [unitless]

P_{step}^{s} = probability of breakdown after N_{step} voltage increments[unitless]

$P_{survive}^{s}$ = probability to survive N_{step} voltage increments [unitless]

P_{SVET}^{s} = probability of breakdown for SVET test after t_{en}^{s} [unitless]

q_e = charge per electron $[Q]$

Q_n = nth quantile [unitless]

R_α = localization length $[L]$

R_{lm} = resistance of current limiting resistors $[\Omega]$

r = voltage ramp rate $[EQ^{-1}T^{-1}]$

$\boldsymbol{r}$ = position vector $[L]$

r_0 = voltage ramp rate of 1 V/s $[EQ^{-1}T^{-1}]$

S = integer constant [unitless]

T = temperature $[K]$

T_{melt} = melting temperature$[K]$

T_0 = initial temperature $[K]$

t = time $[T]$

$t_{elapsed}$ = elapsed time during ESD test $[T]$

t_{en}^{s} = endurance time to breakdown $[T]$

$t_{step-en}^{s}$ = endurance time to breakdown considering the step-up to the waiting voltage $[T]$

u = periodic potential function [unitless]

V = volume $[L^{-3}]$

V_{ESD} = dielectric breakdown voltage $[EQ^{-1}]$

V = electric potential $[EQ^{-1}]$

V_{sample} = voltage applied to the test sample$[EQ^{-1}]$

V_{static} = static applied voltage $[EQ^{-1}]$

w = energy factor $[E]$

W = width of energetic distribution of potential wells; band width, in a density of states $[E]$

x = horizontal Cartesian plotting axis [various units]

x_i = i^{th} datum in a data set [units of the quantity measured]

y = vertical Cartesian plotting axis [various units]

β = Weibull function shape parameter [unitless]

γ = generic constant [various units]

$\Delta\mathcal{E}$ = change in energy $[E]$

ΔF = electric field distribution width$[EQ^{-1}L^{-1}]$

ΔG^{s}_{def} = Gibbs defect activation energy $[E]$

Δt = time interval a field is applied $[T]$

Δt_{step} = elapsed time during voltage increment $[T]$

ΔT = change in temperature $[K]$

$\Delta \mathrm{V}$ = change in volume $[L^{-3}]$

ΔV^{s}_{def} = defect activation volume $[L^{-3}]$

ΔV_{step} = voltage change during voltage increment $[EQ^{-1}]$

ϵ = total permittivity of a material $[Q^2L^{-3}M^{-1}T^2]$

ϵ_r = relative permittivity of material [unitless]

ϵ_0 = permittivity of free space $[Q^2L^{-3}M^{-1}T^2]$

λ = generic variable [various units]

ν = phonon frequency factor [unitless]

ν^{s}_{def} = mean tunneling frequency $[T^{-1}]$

ξ = generic variable [various units]

Ξ = efficiency of radiation to break bonds[unitless]

ρ_m = mass density $[ML^{-3}]$

σ = conductivity $[Q^2L^{-3}T^{-1}E^{-1}]$

σ_{MT} = multiple trapping conductivity $[Q^2L^{-3}T^{-1}E^{-1}]$

σ_{min} = minimum metallic conductivity $[Q^2L^{-3}T^{-1}E^{-1}]$

σ_{TAH} = thermally activated hopping (TAH) conductivity $[Q^2L^{-3}T^{-1}E^{-1}]$

σ_{VRH} = variable range hopping (VRH) conductivity $[Q^2L^{-3}T^{-1}E^{-1}]$

τ_{RC} = RC time constant of the test circuit $[T]$

Ψ = wave function [unitless]

s	Superscripts for defect type
HI	= high energy irreversible defects
LO	= low energy reversible defects
bb	= broken bond defects
K	= Kuhn pair or kink defects
PD	= partial discharge
Tot	= total combined results for all defect types

LIST OF ABBREVIATIONS

ac	Alternating current
ACPD	AC partial discharge
BOPP	Biaxially-oriented polypropylene
CDF	Cumulative distribution function
CEIDP	Conference on Electrical Insulation and Dielectric Phenomena
ECD	Empirical cumulative distribution
ESD	Electrostatic discharge
dc	Direct current
DCPD	Direct current partial discharge
DOS	Density of states
DUT	Device under test
FEC	Field-enhanced conductivity
HDIM	Highly disordered insulating materials
HVDC	High voltage direct current
LDPE	Low-density polyethylene
MAH	Miller-Abrahams hopping
MPG	Materials Physics Group
MT	Multiple trapping
PD	Partial discharge
PDF	Probability density function
PEEK	Polyether ether ketone
PI	Polyimide
PTFE	Polytetrafluoroethylene
RF	Radio frequency
RIC	Radiation induced conductivity
SEU	Single event upset

SVET	Static voltage endurance time
TAH	Thermally activated hopping
USU	Utah State University
VRH	Variable range hopping

CHAPTER 1

INTRODUCTION

1.1. Purpose and Scope of Dissertation

The topic of this dissertation is dielectric breakdown or electrostatic discharge (ESD) and the pre-breakdown electrical aging of highly disordered insulating materials (HDIM). Insulating materials exposed to high electric fields will, over time, degrade and fail, potentially causing catastrophic damage to devices. Although direct current (dc) electrical aging has been studied for decades, it is still poorly understood (Crine, 2005b; Teyssedre and Laurent, 2013). Indeed, the preface of one of the principal textbooks in this field of study begins with the statement "The study of electrical breakdown is not a trivial pursuit" (Dissado and Fothergill, 1992). The extensive structural disorder of HDIM together with underlying quantum mechanical effects, results in fundamentally stochastic behavior. Like other fields of physics dealing with complicated systems, many particles, or inherent uncertainty, there can be no exact solutions. If exact analytical solutions do exist, they are likely too complicated to be practical. Empirical models are most commonly used to describe breakdown in HDIM, but they lack the conceptual economy of physical models and are less useful for extrapolation. Physics-based models of breakdown are necessarily approximations, but they are more suitable for making predictions based on intrinsic material properties and extrinsic material conditions. One of the difficulties in making approximations is striking a balance between capturing the relevant physics while not introducing exceedingly arduous complexity to the theory.

This dissertation proposes a dual-defect driven physical model of breakdown and dc partial discharge (DCPD) in the context of relevant background physics and other models, both empirical and physical, found in the technical literature. This dual-defect model is compared to laboratory data of several typical HDIM to evaluate its merits and limitations as a useful approximate theory of breakdown. Enhanced theoretical understanding of dc aging based on expanded experimental studies is of critical importance not only to understand the physics of HDIM, but also for applications in spacecraft charging, high voltage dc (HVDC) power, thin film dielectrics, and semiconductor devices and sensors.

1.1.1. Spacecraft Charging

Spacecraft charging has been the primary research area of the Utah State University (USU) Materials Physics Group (MPG) research over the last two and a half decades. Streams of charged particles emanate from the sun and interact with planetary magnetospheres creating a variety of plasma and radiation environments in the solar system. As spacecraft in the space plasma environment accumulate charge over time; the lack of electrical ground together with low charge mobility in some materials can cause strong localized electric fields to build up and can eventually lead to catastrophic dielectric breakdown. These ESD events are the primary cause for spacecraft failures and anomalies from interactions with the space environment (Leach and Alexander, 1995; Reed*, et al.*, 2014; Ferguson*, et al.*, 2015). Although they are not covered in detail in this dissertation, material properties such as conductivity, radiation induced conductivity (RIC), and electron yield can influence how charge builds up in a material and therefore influence the likelihood of breakdown (Dennison*, et al.*, 2016b). Other space-environment effects include single event upsets (SEU), total ionizing radiation dose damage, micrometeoroid or orbital debris impact, atomic oxygen erosion, cathodoluminescence, atmospheric drag, etc. (Koons*, et al.*, 1999; Dennison, 2015).

Issues associated with ESD include solar panel power losses and failures, electrical noise, light pollution, and electrical shorts. These issues may trigger spacecraft safe-mode states, loss of data, parametric mission losses, or complete mission failure (Garrett and Whittlesey, 2012). Figure 1.1 is an example of sustained arc damage to a spacecraft solar panel resulting from ESD (Ferguson and Hillard, 2011). It is critical to mitigate the risk of ESD for mission success especially as mission lifetimes increase, components become more compact and sensitive, and spacecraft venture into more extreme space environments. Insights into spacecraft failures follow from comparisons of the field-dependent endurance times with times scales relevant to the space environment and orbital conditions (Dennison, 2015).

1.1.2. Terrestrial Applications

Although the primary impetus for this research is spacecraft charging, it is also readily applicable to earth-bound applications such as the degradation and failure of HDIM insulation for transmission line cables under long-term application of high dc electric fields. There is a push in the United States for HVDC

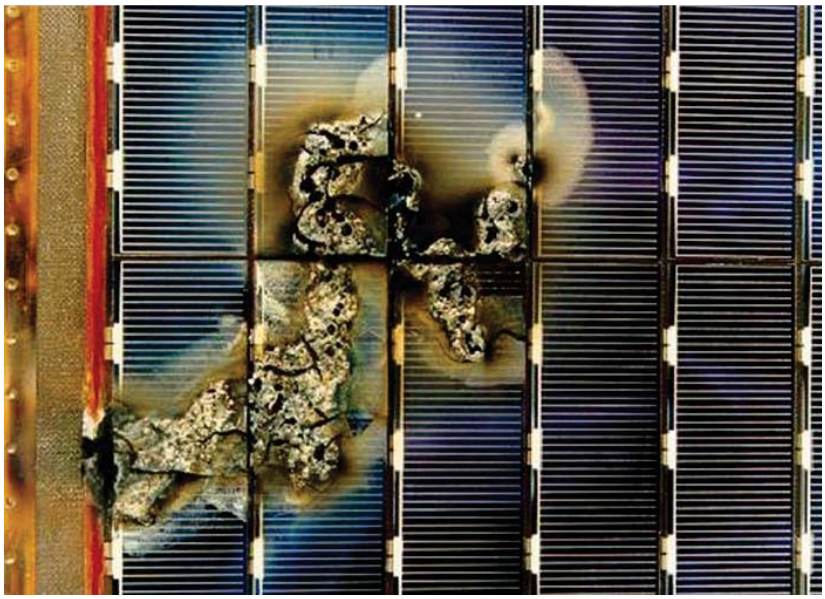

FIG. 1.1. Sustained arcing damage on a spacecraft solar panel resulting from ESD (Ferguson and Hillard, 2011).

power transmission similar to those used in Europe and Asia, due to its increased efficiency and decreased environmental impact (Rongsheng, 2013; Trnka*, et al.*, 2013). The United States ac power grid could dramatically increase efficiency by implementing higher voltage dc lines. To gauge the magnitude of the benefit of switching to higher voltage dc lines across the grid, decreasing transmission loss by ~5% would be equivalent to adding the output of ~30 additional large coal burning power plants to the power grid (Grant*, et al.*, 2006). HVDC suffers less from joule heating, radiation losses, and coronal discharge than HVAC thereby minimizing transmission losses. Over distances of about 100 miles, HVDC lines are more efficient than HVAC transmission, even including ac/dc converter station losses. The present growth of HVDC technologies has resulted in increased interest in the improved characterization and diagnostic of HVDC insulation components (Cavallini*, et al.*, 2016; Corr*, et al.*, 2016). Indeed, despite decades of research, characterization methods and theoretical descriptions of the aging of insulators for HVDC applications lack the sophistication and utility of ac partial discharge diagnostic tools (Crine, 2005b; Vu*, et al.*, 2013; Czaszejko, 2014; Trnka*, et al.*, 2014; Corr*, et al.*, 2016). This dissertation discusses the relationship between DCPD and dielectric breakdown from both a theoretical and practical perspective.

Small-scale semiconductor electronics are also an important application of electrical aging physics. Since the electric field—rather than voltage itself—is what causes material breakdown, the risk of ESD occurs at very low voltages as nanoscale dimensions in devices and composite materials are further reduced. Since breakdown field strengths of dielectric materials are typically in the range of 10^7-10^8 V/m., breakdown can occur in such cases at only a few volts potential for 10-100 nm dimensions. See Table 1.1. This is of concern for all nanoscale electronics. Similar ESD effects have been observed for nanometer thick optical dielectric coatings subjected to electron beam fluxes (Dennison*, et al.*, 2013; Wilson*, et al.*, 2013a).

Table 1.1. Breakdown voltages assuming a nominal breakdown filed of ~10^8 V/m.

Application	**Thickness (m)**	**Breakdown Voltage (V)**
Transmission cables	~10^{-2}	~10^6
Spacecraft	~10^{-5}	~10^3
Circuits	~10^{-4}	~10^4
MOFSET	~10^{-8}	~1

1.2. Outline of Dissertation

This dissertation gives a brief review of the relevant background physics in Chapter 2. This review begins with a short tie-in to standard graduate-level solid state physics, then reviews charge transport in highly disordered insulating materials, followed by a derivation of the standard physics-based ageing dielectric model, the Crine model (Crine*, et al.*, 1989; Crine, 1999).

Chapter 3 outlines the new theory developed in this dissertation. This theory is essentially an extension of the Crine model discussed in Chapter 2. The limiting behavior of these models together with the consequences of considering variable defect densities—primarily due to recoverable defect modes—is discussed.

Chapter 4 transitions into a description of the laboratory test equipment and test methods used to evaluate the predictions made by theories in Chapters 2 and 3. This chapter focuses on the details of each individual test type.

Chapter 5 presents the data processing and statistical analyses of the laboratory test data. These methods allow for the comparison of groups of tests and extracting physical meaning (*e.g.*, estimations of defect energies and densities) from ensembles of tests.

Chapter 6 is a discussion of the results of the studies discussed in Chapters 4 and. This chapter also considers the results in contexts of both empirical and physics based models.

Finally, Chapter 7 examines the conclusions, relevant applications of results, and future.

The Appendices contain detailed procedures regarding the experimental methods, data analysis, and materials properties.

CHAPTER 2

THEORETICAL BACKGROUND

2.1. Physics of Highly Disordered Materials

The topic of highly disordered materials is not part of the standard physics curriculum, even at the graduate level. Indeed, the standard advanced graduate text in solid state physics only briefly addresses amorphous materials to bemoan the pitiful state of the field of the physics of amorphous solids compared to the advanced science of periodic materials and casts doubt on the many conceptual parallels drawn between the two (Ashcroft and Mermin, 2005). Even though this topic is not covered in standard coursework, excellent material on the topic in general does exist, particularly Zallen's and Mott's texts and Rose's article on photoconduction (Rose, 1951; Zallen, 1983; Mott and Davis, 2012).

The discussion of the theoretical background of this dissertation begins with a brief commentary on the physics of the ideal infinite lattice before transitioning into the topic of dielectric breakdown in highly disordered materials. There are two primary reasons for this: first, that the reader with a general physics background may start in somewhat familiar territory, and second, despite the lack of exact analytical solutions for disordered materials, there is strong evidence for the validity of borrowing some concepts from the physics of crystalline solids.

2.1.1. Solid State Physics in an Ideal Lattice

The physics of charge transport in a perfect lattice can be derived from the first principles of quantum mechanics and is covered in standard solid state physics texts (Kittel, 1966; Ashcroft and Mermin, 2005). In a crystalline lattice, we can obtain solutions to Schrödinger's equation, namely the familiar Bloch wave functions,

$$\Psi(\boldsymbol{r}) = u(\boldsymbol{r})\mathrm{e}^{i\boldsymbol{k}\cdot\boldsymbol{r}}\,, \tag{2.1}$$

where $u(\boldsymbol{r})$ has the same periodicity as the lattice. The periodicity restricts the allowable energies, giving rise to band structures (Ashcroft and Mermin, 2005).

The concept of band structures, and most especially forbidden energy bands, is fundamental to the understanding of the electrical properties of condensed matter, and gives a description of why certain

materials are conductors (effectively no band gap due to partially filled bands or overlapping bands) while others are semiconductors (band gap $\sim k_b T$) or insulators (band gap $\gg k_b T$).

In the case of amorphous materials, the lack of long-range order undermines the mathematical underpinnings of Eq. 2.1 and consequently, all the resulting theory describing crystalline solids using Bloch's theorem. Nevertheless, the transparency of common glass makes it quite clear that amorphous materials can have an energetic band gap despite the lack of periodicity that allows for a straightforward analytic description (Mott, 1978). Despite the difficulties involved in exact quantum mechanical calculations, perturbation methods and statistical techniques have led to useful physical models. In Sections 2.1.2 and 2.1.3, we will review a few of the most important concepts in the physics of amorphous solids.

2.1.2. Localization through Disorder

In crystalline materials, energetic band structures dominate conduction; however, in amorphous materials it has been shown that conduction is dominated by the density of spatially localized trap states. The 1977 Nobel Prize in Physics was awarded to Philip Warren Anderson, Sir Nevill Francis Mott, and John Hasbrouck van Vleck "for their fundamental theoretical investigations of the electronic structure of magnetic and disordered systems" (Nobel Media AB, 2014). Anderson and Mott's great contribution was the concept of localization, that is, a transition from spatially extended quantum states to states confined to a localized region (Anderson, 1958; Anderson and Mott, 1978; Mott, 1978; Mott and Davis, 2012). Such transitions in the spectrum of allowed quantum states in a material are effectively metal-insulator transitions (Zallen, 1983). In crystalline semiconductors, the conductivity can be similarly altered extrinsically by means of doping. Although disordered materials can surely be doped, localized states are intrinsic to amorphous materials. Mott demonstrated that by not neglecting electron-electron interactions, localization must occur in materials at low enough atomic densities (Zallen, 1983; Mott and Davis, 2012).

Anderson demonstrated localization by explicitly adding disorder to a periodic lattice. The starting point for Anderson localization is the tight-binding Hamiltonian (Anderson, 1958; Anderson and Mott, 1978; Elliott and Elliott, 1990).

$$\mathcal{H} = \sum_i \mathcal{E}_i |i\rangle \langle i| + \mathcal{E}_B \sum_{i,j} |i\rangle \langle j| \qquad 2.2$$

The diagonal basis states $|i\rangle$ are the sites of a periodic lattice. These basis states are given a random distribution of energies $\mathcal{E}_i$ characterized by a width W. The nearest-neighbor couplings are given by $\mathcal{E}_B$ (or rather $\mathcal{E}_{B_{i,j}}$ inside the second sum for potentials due to a random distribution of nearest-neighbor distances). The perturbation methods applied by Anderson on this model are quite arduous, but they lead to an important result. What Anderson showed is that instead of a band gap of forbidden energies between the valence and conduction states, "one may have a continuum (of allowed states) in energy but not in *space*" (Anderson and Mott, 1978). The criteria for disorder-induced localization is $W > \mathcal{E}_B$. Numerical calculations of the spatial extent of electron wave functions show increasing localization with increasing $W/\mathcal{E}_B$ (Yoshino and Okazaki, 1977).

In Fig. 2.1 we observe the effect of disorder on the familiar crystalline band diagram. In the case of disorder, instead of an empty band gap of forbidden states, we observe a region of localized states. This region is termed the mobility gap and is bounded by mobility edges (Zallen, 1983; Mott and Davis, 2012). The lack of sharp features in the band diagram for the amorphous case is a result of such features requiring long-range order to be present (Zallen, 1983). The density of states in the mobility gap can be negligibly small for a broad range of energies away from the mobility edges, hence the transparency of glass.

Material-specific specific structures such as dangling bonds can cause peaks in the density of localized states in the mobility gap (Mott, 1978; Zallen, 1983; Elliott and Elliott, 1990; Mott and Davis, 2012). Examples of these will be discussed in 3.1.1.

2.1.3. Effects of Disorder on Electrical Conductivity

Localized states in the mobility gap can strongly influence a material's electrical properties. The dielectric breakdown models outlined in Section 2.2 and Chapter 3 are based on runaway hopping conduction. This section briefly reviews conduction models in amorphous solids. Consider the case of a single dominant charge carrier: an electron in a Fermi glass, that is, an amorphous material with the Fermi energy below the mobility edge and therefore among the localized states (Mott, 1978; Mott and Davis, 2012). The dominant conduction mechanism will depend on the thermal energy compared to the mobility gap energy.

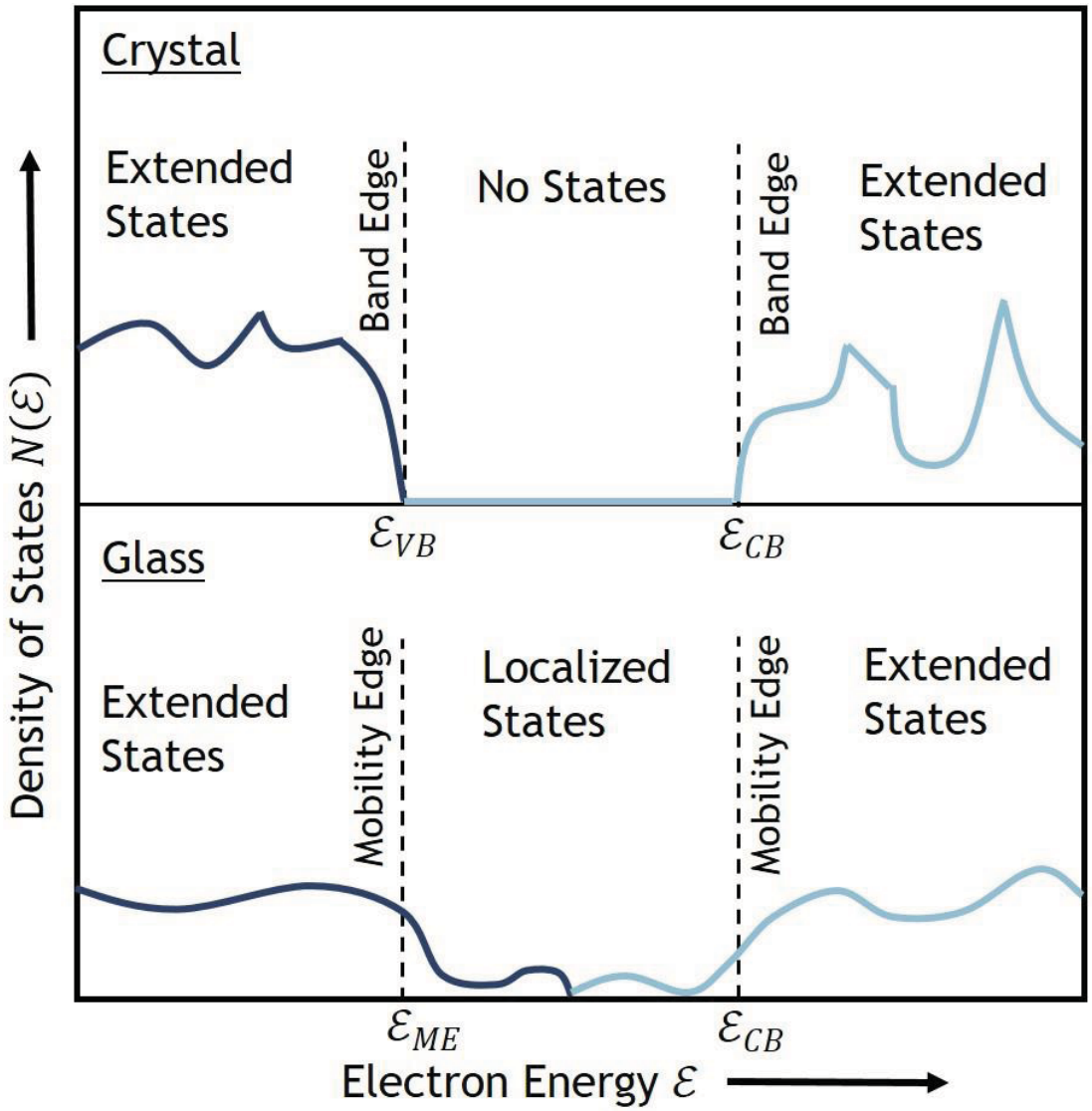

FIG. 2.1. Idealized band diagrams for periodic (top) and amorphous non-metals (bottom). Adapted from (Zallen, 1983)

2.1.3.1. Multiple Trapping

At high enough temperatures, electrons can be excited into the extended states above the mobility edge. Electrons in the extended states have motion limited by scattering, as in metallic conduction, as well as trapping in the energetically shallow localized states below the mobility edge (see paths C and D in Fig. 2.2.) (Zallen, 1983). This transport is known as multiple trapping (MT) because any single carrier may undergo many trapping and de-trapping events (Zallen, 1983). The number of carriers in extended states,

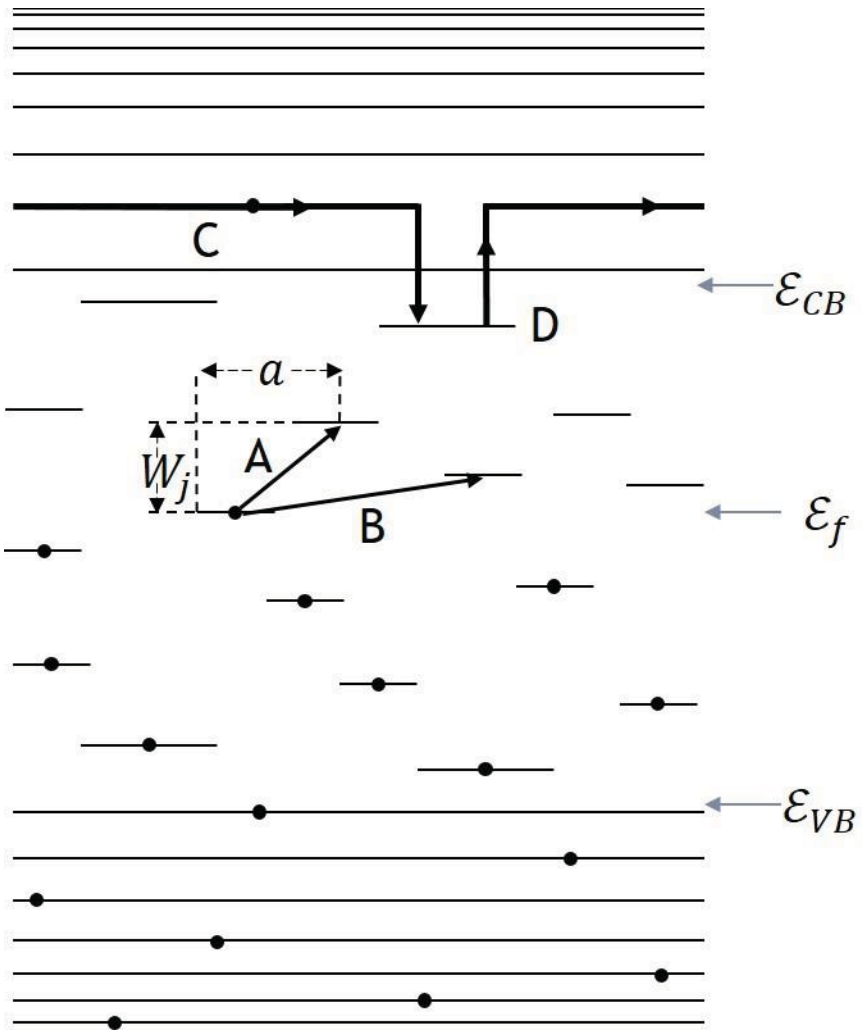

FIG. 2.2. Simplified diagram of the energetic states in a Fermi glass. Short lines between the conduction band $\mathcal{E}_{CB}$ and the valence band $\mathcal{E}_{VB}$ represent localized states. Dots represent filled states below the fermi level $\mathcal{E}_f$. Electrons undergoing multiple trapping conduction follow paths C and D. Hopping a distance a is shown by either path A or B. W is the energy difference from the initial to the final state in the mobility gap to another. Adapted from (Zallen, 1983)

and therefore the resulting conductivity, depends on a Boltzmann factor of the energy gap from the Fermi level to the mobility edge over the thermal energy (Rose, 1951). This conductivity is

$$\sigma_{\mathrm{MT}} = \sigma_{\min}\exp\{-(\mathcal{E}_{CB} - \mathcal{E}_f)/k_b T\}, \tag{2.3}$$

where $\sigma_{\min}$ is the minimum metallic conductivity, related to the degree of localization in the material (Mott, 1978; Mott and Davis, 2012).

2.1.3.2. Hopping and Percolation

Excitations into extended states are not the only charge transport mechanisms available because of localized states in amorphous materials. Charges may, assisted by phonons, quantum mechanically tunnel from one (occupied) localized state to another (vacant). Such transport is known as hopping.

Hopping conductivity is a product of a Boltzmann factor $\exp(-W_j/k_bT)$ where W_j is the energy gap between two states, a factor ν that depends on the phonon spectrum, and a factor $\exp(-2R_\alpha a)$ for the overlap of the wave functions (Mott and Davis, 2012). With sufficient thermal energy, nearest neighbor hops are preferred (see path A in Fig. 2.2). Such hopping is termed thermally activated hopping (TAH) and has temperature dependence similar to Eq. 2.3:

$$\sigma_{\mathrm{TAH}} \propto \exp(-W_j/k_bT). \tag{2.4}$$

As temperature decreases the probability for an electron to hop a larger distance a to reach a smaller energy difference W_j becomes significant (see path B in Fig. 2.2). This hopping mechanism is called variable range hopping (VRH) because the hopping range can vary with temperature and the defect density of states. By considering more than only nearest-neighbor hops in this way, the conductivity dependence on temperature changes to (Mott, 1978; Zallen, 1983; Mott and Davis, 2012)

$$\sigma_{\mathrm{VRH}} \propto \exp(-B/k_bT^{\frac{1}{4}}). \tag{2.5}$$

The factor B in the numerator depends on the density of states and the localization length R_α (Zallen, 1983; Mott and Davis, 2012).

This same $\sigma \propto \exp(-C/T^{\frac{1}{4}})$ form can also be found by statistical methods considering defects randomly distributed in energy and space (Ambegaokar*, et al.*, 1971). In either case, the spatial distribution of traps in the material can be approximated as a large network of resistors. In such percolation models, more favorable transitions have an equivalent lower resistance, effectively shorting out the larger resistors corresponding to unfavorable transitions (Ambegaokar*, et al.*, 1971). The distribution of resistance values maps onto the distribution of trap state energies. Completion of a conduction path follows a path favoring lower resistances (energies). This can lead to enhanced conduction as circuitous low resistance paths can add additional favorable paths for charge flow to the statistically unlikely lowest resistance path comprised

of a direct chain of lowest resistance (energy) states. This construct makes the notions of percolation path and percolation thresholds—both spatial and energetic distortions—relevant to conduction in HDIM.

To summarize, we have reviewed some of the relevant conduction mechanisms by which charge can propagate in amorphous materials. We see that the relationship between the defect density of states (DOS) spatial and energetic distributions and the thermal energy not only changes conductivity but also the physical mechanism of charge transport in disordered materials. A more in-depth discussion of the effects of temperature and radiation on conductivity is beyond the scope of this introduction. For further insights on this topic, I recommend (Gillespie, 2013; Sim and Dennison, 2013).

2.2. Crine Mean Field Theory

We now transition to a discussion of breakdown in amorphous solids. When an electron hops from one trap to another it can gain energy as it travels through an electric field. If it gains sufficient energy to liberate additional charges upon impact, a cascade of charge can propagate into an avalanche breakdown. Therefore, the likelihood of breakdown depends on the relationship between the temperature-dependent probabilities of charge escaping defects, the distribution of defect energies, the non-uniform spacings between defect sites, and the external electric field.

The simplest model of breakdown due to charge motion between defect states is the mean field theory, or canonical Crine model (Crine*, et al.*, 1989). This model assumes a single mean defect energy ΔG_{def} with the defects spaced periodically with a mean separation of a_{def}. Although this is obviously the incorrect picture for HDIM, it is the starting point for creating an approximate physical model of breakdown.

2.2.1. Runaway Miller-Abrahams Hopping as Dielectric Breakdown

Given the assumptions of the mean field theory we can derive breakdown in one dimension by describing the TAH motion of charges (for simplicity we will assume only electrons) in a periodic 1D array of localized defects or traps. This is commonly known as Miller-Abrahams hopping (MAH) (Miller and Abrahams, 1960). In the absence of an applied electric field, there is no net current because there is an isotropic hopping probability. However, as shown in Fig. 2.3, an applied electric field distorts the potential

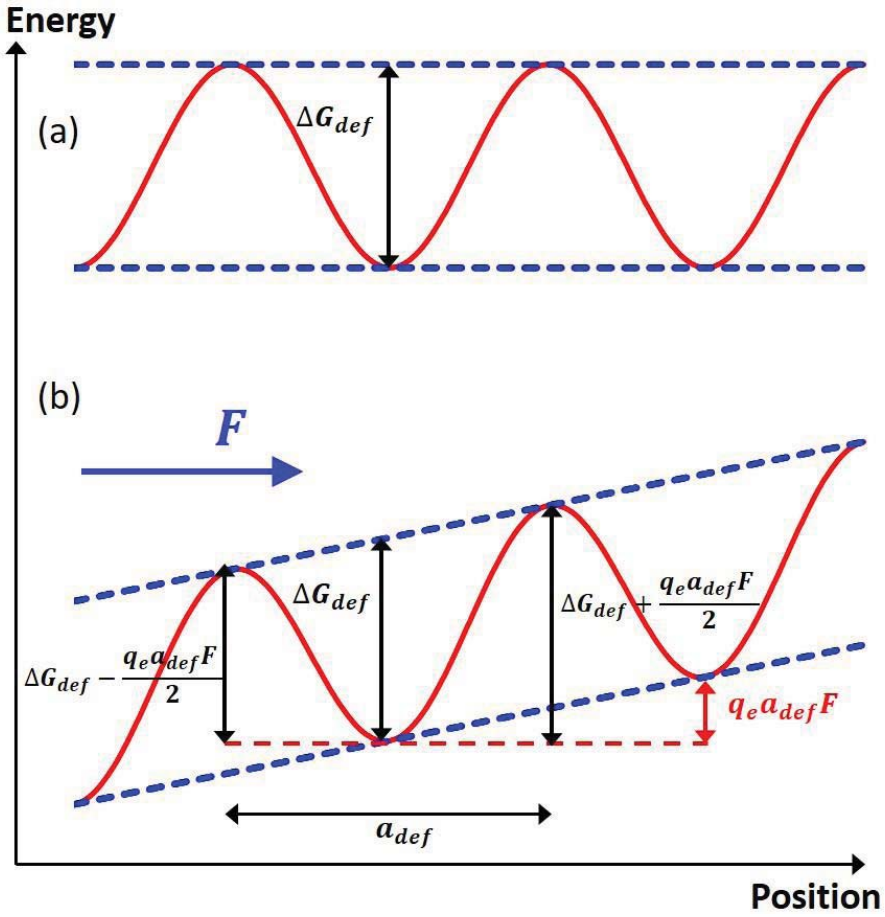

FIG. 2.3. Potential energy versus position diagram. (a) No electric field and (b) with applied electric field. The fields acts to reduce the energy necessary to initiate the degradation process through thermally assisted tunneling from the defect Gibbs energy of activation, ΔG_{def} by an amount $\frac{1}{2} q_e a_{def} F$, where a_{def} is the mean defect separation. The red curves are the carrier potential and the blue dashed curves are the electric field contributions to the potential energy, as functions of position.

wells and creates a preferential hopping direction (Miller and Abrahams, 1960; Wintle, 1983). The net probability of hops per second P_{hop} in the direction opposite the field F is

$$P_{hop} = \nu e^{-\left(\frac{\Delta G_{def} - \frac{1}{2} q_e a_{def} F}{k_b T}\right)} - \nu e^{-\left(\frac{\Delta G_{def} + \frac{1}{2} q_e a_{def} F}{k_b T}\right)} \quad 2.6$$

with a unitless transition frequency factor ν, Gibbs activation energy—essentially well depth—(ΔG_{def}), charge (q_e), mean defect spacing (a_{def}), electric field (F), Boltzmann's constant (k_b), and temperature (T). Although Eq. 2.6 is illustrative for the present derivation, it can be written more conveniently as

$$P_{hop} = 2\nu \exp\left[\frac{-\Delta G_{def}}{k_b T}\right] \sinh\left(\frac{q_e a_{def} F}{2k_b T}\right). \quad 2.7$$

In 1999 Crine transitioned from considering the energy gained and lost by individual hops to the Maxwell stress energy (Crine, 1999). To explain this shift, and include it in the present derivation, we depart from our strictly 1-D model for a moment to understand how the bonds within a polymeric material are affected by an applied stress due to internal or external electrostatic fields. Consider an electric field F across two faces of a cubic unit volume acting as a parallel plate capacitor. The strain energy required to compress this unit volume by an amount ΔV is (Crine, 1999; Anderson*, et al.*, 2004)

$$\mathcal{E}_{strain} = \tfrac{1}{2}\epsilon_0 \epsilon_r F^2 \Delta \mathrm{V}. \quad 2.8$$

More detailed vector or tensor calculations of the strain energy for more realistic, anisotropic shapes yield similar results that differ only by a constant of order unity. The energy strain on the defect sites is defined by the density of defects—*e.g.,* ionization sites or broken bonds—associated with electrostatic discharge N_{def}. This is the inverse of the cubic mean activation volume $\Delta \mathrm{V}_{def} = \left(a_{def}\right)^3 \equiv 1/N_{def}$, corresponding to one such defect. This point is generally ambiguous in the literature although it is occasionally suggested as in (Crine, 2007).

If we set the strain energy of Eq. 2.8 in a volume $\Delta \mathrm{V}_{def}$ equal to the Gibbs defect activation energy ΔG_{def}, we can solve for the critical electric field F_{def} just strong enough to produce one defect per activation volume

$$F_{def} = \left[(2/\epsilon_0 \epsilon_r)\, N_{def} \Delta G_{def}\right]^{1/2}. \quad 2.9$$

The critical field is usually interpreted as the field at defect distortion begins to be significant (Crine, 2002b). Although electrical aging can happen at lower fields due to existing defects, the likelihood of runaway hopping and the creation of new defects is low below F_{def} (Crine, 1999; 2002b). At fields somewhat below the critical field, one can envisage interconnected regions of defective activation volumes—that have essentially undergone an insulator-to-conductor transition—that allow current to propagate through the material via a percolation-like network. Such a percolation-like model lends itself to a decreased but still finite probability of breakdown with decreasing field. As the probability of completing a percolation path across the sample at a given defect density decreases, this also predicts an onset field

F_{onset} at the percolation threshold for defect densities below which breakdown will not occur. Above the critical field one must consider the creation of new defects. For processes that permit repair of the defect, dynamic percolation models need to incorporate defect activation volumes with a finite lifetime. The Crine model does not explicitly consider changes in N_{def} but this is discussed in 3.2.1.

Alternate theories (Wintle, 1983; Dissado and Fothergill, 1992; Lewis, 2002; Crine, 2005b; Montanari, *et al.*, 2005), which produce equivalent results, consider the energy $q_e a_{def} F$ acquired by a charge carrier with charge as it moves through a mean field over the mean separation distance between defects. One can also note the similarities to rate theories in chemistry (Eyring, *et al.*, 1935; Crine, 2016a) and the Onsager capture length theory (Onsager, 1938; Belmont, 1975).

2.2.2. Static Voltage Endurance Time

Given a model for the critical field, a thermodynamic model for the electric field aging process has been developed to predict the mean time to failure or static voltage endurance time (SVET) t_{en} as a function of high electric field and temperature (Crine, *et al.*, 1989; Dissado and Fothergill, 1992; Dang, *et al.*, 1996; Parpal, *et al.*, 1997; Crine, 2005b). There are direct equivalences between the thermodynamic model for ESD and Mott's model for thermally activated hopping conductivity (Mott and Davis, 2012). As with this conductivity model, ΔV_{def} and ΔG_{def} represent a mean defect activation volume (or barrier width) and a mean defect activation energy (or barrier height of the energy well), respectively (see Fig. 2.3 (a)) (Wintle, 1983; Dennison, *et al.*, 2009).

On average, the forward and backward movements of charge carriers from one trap state to an adjacent site can be thought of as a rate process, where motion with (against) the field decreases (increases) the barrier height of the Gibbs free energy, as shown in Fig. 2.3 (b). At breakdown, the critical energy gained from electron motion through the electric field across a defect volume of width a_{def} from Eq. 2.8, is just sufficient to overcome the barrier height ΔG_{def} leading to a cascade of charge. Thus Eq. 2.7 can lead to a similar model of the probability of breakdown as a function of applied field F, temperature T, and time the field is applied Δt (Parpal, *et al.*, 1997):

$$P_{def}(\Delta t, F, T) = \left(\frac{2k_b T}{h/\Delta t}\right) \exp\left[\frac{-\Delta G_{def}}{k_b T}\right] \sinh\left[\frac{\epsilon_0 \epsilon_r F^2}{2k_b T N_{def}}\right]. \quad 2.10$$

Considering the probability of breakdown to be equal to unity at the endurance time, $P_{def}(\Delta t = t_{en}) = 1$. The ratio $\left(P_{def}/t_{en}\right)$ corresponds to the defect to defect tunneling frequency ν_{def}; therefore, $h\upsilon_{def} = h/t_{en}$ can be thought of as the quantum energy uncertainty for a broken bond or P_{def} as the probability of tunneling through the barrier in Fig. 2.3. Solving Eq. 2.10 with $P_{def} = 1$ for the endurance time to breakdown under an applied field, we find

$$t_{en}(F,T) = \left(\frac{h}{2k_bT}\right)\exp\left[\frac{\Delta G_{def}}{k_bT}\right]\operatorname{csch}\left[\frac{\epsilon_0\epsilon_r F^2}{2k_bTN_{def}}\right]. \quad 2.11$$

Eq. 2.11 is the canonical mean field theory aging equation. Eq. 2.10 is a natural step in the derivation of 2.11; although, it is not typically used in the literature. In Chapters 5 and 6, it will be shown that this form of the mean field theory can also be useful in estimating the likelihood of breakdown.

CHAPTER 3

THEORETICAL DEVELOPMENT

3.1. Dual-defect Model

Although the Crine model can be a useful approximation and is a significant improvement over rudimentary empirical models of electrostatic breakdown such as the inverse power law and others (Chinh, *et al.*, 1996), the Crine model often fails to adequately described observed aging phenomena (Andersen and Dennison, 2015a; Andersen, *et al.*, 2015; Crine, 2016b). This will be discussed in detail in Chapters 6 and 7.

One of the primary theoretical developments of this work is to propose a simple extension to the Crine model by considering two representative defect types rather than one. Similar notions have been proposed by other authors (Cho, *et al.*, 2000; Kao, 2004). This is represented in Fig. 3.1. These defect species are: (i) high-energy (HI) chemical defects, such as dangling bonds and (ii) low-energy (LO) physical defects, such as a kink in a polymer chain (Andersen, *et al.*, 2015). High-energy defects have a negligible repair rate, even at high temperatures. However, low-energy defects can have a significant repair rate that increases with increasing temperature. A more detailed discussion of these defects is given in section 3.1.1.

The dual defect mechanism multiple-trapping model equates the total probability of failure from either type of defect to the sum of failures for both HI and LO type processes:

$$P_{def}^{Tot}(\Delta t, F, T) = \sum_{i=HI,LO} P_{def}^{i} = \left(\frac{2k_bT}{h/\Delta t}\right) \sum_{i=HI,LO} \exp\left[\frac{-\Delta G_{def}^{i}}{k_bT}\right] \sinh\left[\frac{\epsilon_0 \epsilon_r F^2}{2N_{def}^{i} k_bT}\right] \quad 3.1$$

This extension to Eq. 2.10 assumes the probabilities P_{def}^{HI} and P_{def}^{LO} are independent of the other defect type.

Once again, to find t_{en}, we set P_{def}^{Tot}=1 in Eq. 3.1 and solve for $t_{en} = \Delta t$. Thus,

$$t_{en}^{Tot}(F, T) = \left(\frac{h}{2k_bT}\right) \left\{ \sum_{i=HI,LO} \exp\left[\frac{-\Delta G_{def}^{i}}{k_bT}\right] \sinh\left[\frac{\epsilon_0 \epsilon_r F^2}{2N_{def}^{i} k_bT}\right] \right\}^{-1}. \quad 3.2$$

In both Eq. 3.1 and Eq. 3.2 it is apparent that the temperature will affect dielectric breakdown since k_bT is found competing in the leading, exponential, and hyperbolic trigonometric terms for each defect contribution. The dominant term will depend on the both the specific intrinsic material properties and the

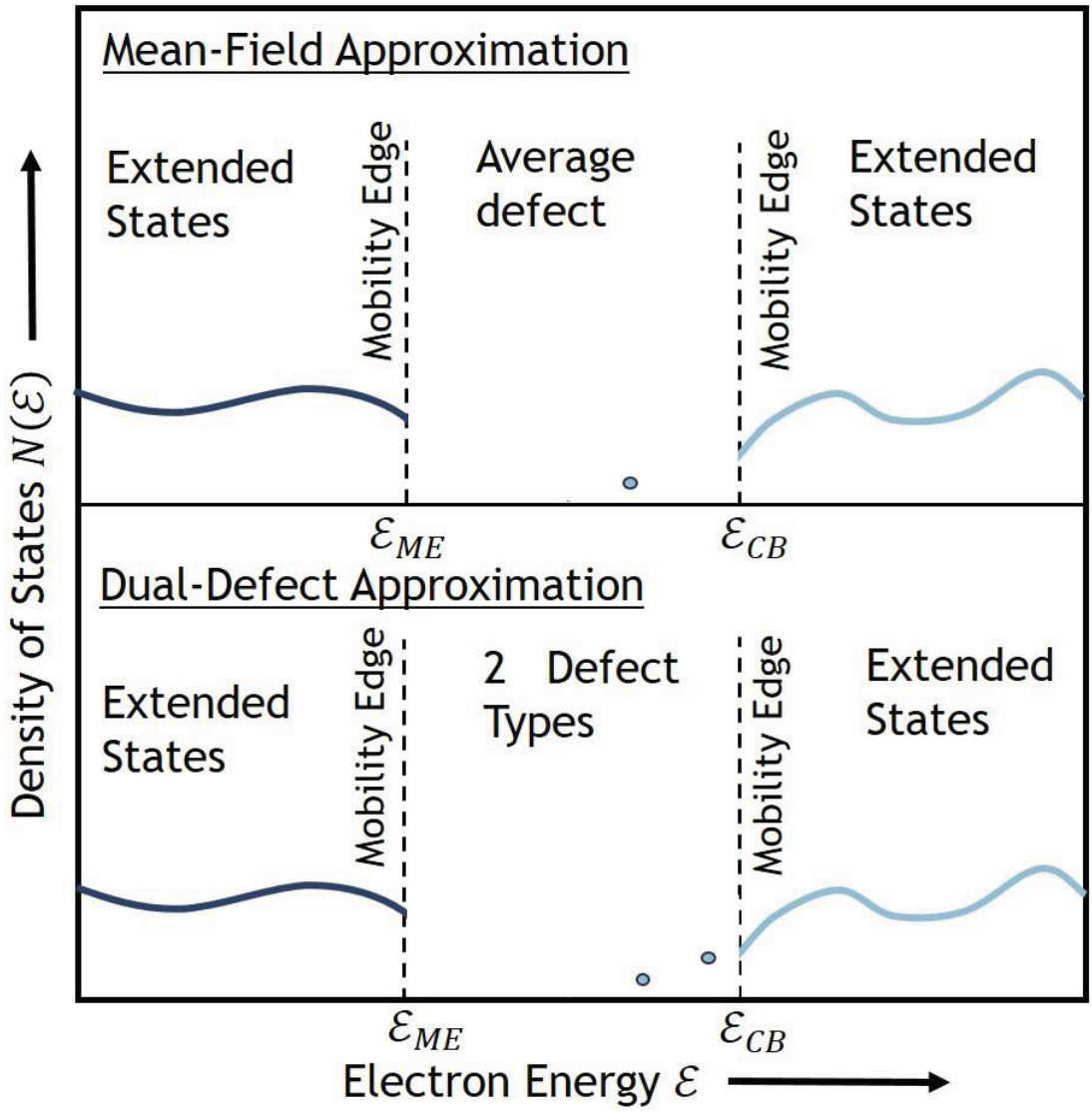

FIG. 3.1. Band diagram representing the Crine model (top) and dual-defect model (bottom). Compare to Fig. 2.1. Note that higher energy defects correspond to lower electron energy states.

extrinsic conditions. So while it is easy to see that temperature should have an important effect on breakdown, what that effect is may vary from material to material and environment to environment. It is reasonable to assume that Eq. 3.1 and Eq. 3.2 are only valid for $\Delta G_{def} > k_b T$ (the well depth must be deep compared to the thermal energy; otherwise, we would have excitations into the conduction band with its much higher density of states rather than hopping between localized states). For now, we have also assumed that the field stress energy is less than the defect energy (*i.e.*, $\Delta G^i_{def} > \frac{\epsilon_0 \epsilon_r F^2}{2N^i_{def}}$) lest the concept of

hopping between potential wells would fall apart (see Fig. 2.3). Neither of these assumptions are made explicit in the model. If care is not taken, one may inadvertently extrapolate into regimes where this model may no longer be a valid approximation.

3.1.1. Defect Mechanisms

We turn our attention now to specific processes involved in ESD to establish relevant values for N_{def} and ΔG_{def}. Consider two types of breakdown process types which we will refer to as LO and HI. Type LO processes are lower energy *reversible* process, which may have a significant rate of defect repair. Type HI processes are higher energy largely *irreversible* processes, with a negligible defect repair rate at temperatures that would not otherwise alter the material.

In type HI viscous or inelastic deformation processes, breakdown of the material is due to direct stress on molecular segments causing irreparable damage with no bond repair possible (Crine, 2005b), where the ends of broken bonds with unpaired sites can act as electron traps (Crine*, et al.*, 1989; Griffiths*, et al.*, 1998; Kao, 2004). In these processes, there is little ionization or segmental motion. Such defects can be generated by the breaking of carbon-carbon bonds of the C_2H_4 monomer alkane single bonds along polymer chains with dissociation energy ΔG_{def}^{bb}=3.65 eV per bond (Frederickson and Dennison, 2003). We can expect similar values of ΔG_{def}^{bb} for many polymers, due to the similarity in carbon-carbon bonds in their polymer chains. The energy distribution for the deep level defects should be fairly narrow since the bonds are relatively homogeneous. ΔG_{def}^{bb} will be largely independent of the environment surrounding the bond and should not depend on the orientation of the bond with respect to the field since it is an impact ionization process creating a point defect. The bond breaking process will not have a significant temperature dependence at accessible temperatures below the melting temperature T_{melt} or decomposition temperature, because $k_b T < k_b T_{melt} \ll \Delta G_{def}^{bb}$.

The total density of such bonds can be estimated from the mass density of LDPE and the mass of the mer to be $N_{bond} \lesssim 4 \cdot 10^{22}$ bonds/cm^3 (assuming one bond per mer). The density of broken bonds N_{def}^{bb} due to a bond-breaking dose D_{bb} at complete breakdown can be estimated from radiation damage studies as $N_{def}^{bb} \lesssim \left[\frac{1}{2}\frac{1}{3} D_{bb}\, \rho_m\, \Xi\, / \Delta G_{def}^{bb}\right] \approx 1.5 \cdot 10^{18}$ broken bonds/cm^3 with the following considerations.

(i) The dose (deposited energy—from the field or from incident electron radiation—per unit mass) at breakdown is ~$2\cdot10^5$ Gy, since irrecoverable electron radiation damage (*e.g.,* electron transport and emission properties) typically occurs for doses $\gtrsim10^5$ Gy (Torrisi*, et al.*, 2004; Hoffman*, et al.*, 2009) and mechanical failure occurs at $\gtrsim10^6$ Gy (Shinyama and Fujita, 2006).

(ii) Results from radiation damage experiments show the mean energy required to break such a bond is $\left[\Delta G_{def}^{bb}/\,\Xi\right]$ ≈130 eV (Zallen, 1983).

(iii) The efficiency of radiation to break bonds is Ξ≈36 (Zallen, 1983). This independent estimate of broken bonds in the amorphous region $\lesssim\left[D_{bb}\,\rho_m\,\Xi\,/\Delta G_{def}^{bb}\right]$≈$7.5\cdot10^{18}$ broken bonds/cm^3 is consistent with the estimated density of chains, ~$1.5\cdot10^{18}$ broken bonds/cm^3 (see 5.2), since there is one broken bond per chain. Note, both N_{bond} and N_{def}^{bb} should be reduced by ~½, since ESD is limited to transport across amorphous regions and N_{def}^{bb} is further reduced by a factor of ⅓ when a percolation threshold in the amorphous region which are typically 50% of the material is taken into account (Dennison and Brunson, 2008). The value obtained, N_{def}^{bb}≈$1.5\cdot10^{18}$ cm^{-3}, is consistent with a range of published values for LDPE near $1\cdot10^{18}$-$3\cdot10^{18}$ cm^{-3} (Cho*, et al.*, 2000; Brunson, 2010).

Taken together, these estimates, in conjunction with Eq. 2.9, lead to a critical field for broken bond defects of F_{def}^{bb}~295 MV/m, with N_{def}^{bb}≈$1.5\cdot10^{18}$ broken bonds/cm^3 and ΔG_{def}^{bb}=3.65 eV/bond.

Type LO processes are reversible; that is, they require a low enough activation energy that such defects can be spontaneously repaired due to thermal activation. These can include weak van der Waals bonds and main chain reconfiguration energies such as chain rotations and kinks. Creation of such defects in molecular or crystalline segments of the polymer chains result either from charge injection and impact ionization or from conformational defect (kink) generation (Kao, 2004). As the injected charge becomes trapped at these defect sites in the ionized molecular segments and on chain segments, a high-localized field develops leading to breakdown.

We will consider one potential type of reversible defects further, kink defects. *Trans-gauche* rotational barriers for typical isolated longer alkane chains are 0.36 eV/kink. In polymers, close proximity of other chains leads to chain-chain interactions and steric hindrance that limits kink formation. It is often found that formation of two kinks in close proximity (which minimize displacement of the overall chain) are energetically more favorable than formation of a single kink and the concomitant large displacement of the rest of the chain. This is referred to as formation of a Kuhn pair with a minimum kink separation (Kuhn length) of ~3.5 C-C bond lengths (~1.3 nm) for low-density polyethylene (LDPE) (Anderson*, et al.*, 2004). A very crude estimate of the magnitude of this effect is based on the ~25% increase in maximum working temperatures of cross-linked polyethylene versus LDPE. We can therefore estimate the defect energy as approximately twice the kink formation energy plus ~25% additional energy to account for chain-chain interactions and steric hindrance; ΔG_{def}^{K}=(1.25·2·0.36 eV/kink)=0.90 eV. An upper bound on N_{def}^{K} can be estimated as ~14% of the mer density (sees sections 6.2.1 and 6.2.2), N_{def}^{K}<3·10^{21} Kuhn pairs/cm^3. This assumes a minimum separation of Kuhn pairs equal to the minimum kink separation of 3.5 mers and only ~50% of the total chains can contribute, since only chains in the amorphous region are free to develop kinks unhindered. These same approximations for polyimide using a working temperature ~75% above LDPE (DuPont Document K-15345-1, 2011), minimal crystallinity, and a Kuhn length of ~8 nm (Chauvet and Laurent, 1993), predict ΔG_{def}^{K}=1.3 eV and N_{def}^{K}<5·10^{20} Kuhn pairs/cm^3.

We can expect that ΔG_{def}^{K} will be substantially different for different polymers due to strong variations in the chain structure, rigidity, and crosslinking. The energy distribution for these defects should be broader, since the local chain environments are not homogeneous. ΔG_{def}^{K} should depend on the orientation of the bond with respect to the field, since this provides the torque to reorient the chains. The applied field has a well-defined direction; however, the field due to internal charge accumulation will be largely isotropic and will not provide net torque. There may even be a saturation effect, as more kinks develop to align the chain segments in the disordered regions with F, or as bond breaking becomes prevalent, producing shorter chains which align more easily with the field. The kink formation process will also have a significant temperature dependence at accessible temperatures below the melting temperature or

decomposition temperature. Thermal annealing may reduce the equilibrium defect density for these lower energy defects.

3.1.2. Voltage Ramp Rate Effects

Having proposed a new theory of breakdown, we now begin to investigate what predictions it makes in practical conditions or laboratory experiments. The service lifetime of a dielectric material in application may range from years to decades. Nevertheless, design engineers must rely on accelerated measurements orders of magnitude shorter in time to estimate long-term behavior, highlighting the importance of estimating the effects of accelerating voltage ramp rates. Consider that a dielectric, whether in service or in a breakdown test, is not instantly brought to some potential V, but rather undergoes a ramp up processes by either a continuous ramp or a voltage step up process to reach either the breakdown voltage or the waiting voltage for an endurance time scenario. This section briefly reviews other published work on ramp rate dependence then considers predictions of the dual-defect models outlined above.

The simplest assumption is that a material's breakdown electric field strength, F_{ESD}, does not vary significantly with voltage ramp rate (Dissado and Fothergill, 1992). Indeed, this is the ideal case because, if valid, it follows that the results of reasonably accelerated tests will be appropriate for any application. Explicitly this is

$$F_{ESD} = C, \tag{3.3}$$

where C is a constant. Dissado and Fothergill discuss a model for the ramp rate dependence of breakdown derived from probabilistic rather than physical considerations (Dissado and Fothergill, 1992):

$$F_{ESD} \approx \left(\frac{\partial F}{\partial t}\right)^{A/A+B} \text{ or } \quad F_{ESD} = C\left(\frac{\partial F}{\partial t}\right)^{A/A+B} \tag{3.4}$$

They mention that in some cases $A + B$ may be at least an order of magnitude larger than A, which is often close to unity, essentially reducing Eq. 3.4 to Eq. 3.3. If the two empirical parameters A and B are constrained to be positive, this model predicts that slower ramp rates tend to have lower breakdown fields. The example they give shows a change of ~20% in breakdown voltage by increasing the ramp rate by about a factor of five. However, they note at very low ramp rates that Eq. 3.4 fails and there can be a significant shift to higher breakdown fields (Dissado and Fothergill, 1992).

Turning to physical theories, we start again with the mean field theory model from Eq. 2.10. A first order approximation for how the estimated breakdown field F_{ESD} depends on the uniform ramp rate $r \equiv dV/dt$ comes by assuming that the ratio of breakdown fields at two different ramp rates is the same as the ratio of the probability of breakdowns at those same ramp rates. This is done by setting the ratio of Eq. 2.10, evaluated at $\Delta t = \Delta t_{step}$ and $\Delta t = 1\ s$, equal to the ratio of the mean experimental ramp rate $\frac{r}{r_0}$ where $r_0 \equiv 1\ Hz$. Recalling that $\sinh^{-1}\lambda = \ln\left(\lambda + \sqrt{1+\lambda^2}\right)$ we can estimate that

$$F_{ESD}(r) \approx F_{ESD}(r_0)\sqrt{\gamma \ln\left(r + \sqrt{1+r^2}\right)} \tag{3.5}$$

Where $\gamma \equiv \left[\ln\left(1+\sqrt{2}\right)\right]^{-1} \approx 1.1346$ and r has units of Hz. This simplified physics model is convenient in that it only depends on the ramp rate and one material constant $F_{ESD}(r_0)$. Like the empirical model, this model predicts that at lower ramp rates the breakdown field decreases. For example, a ramp rate of $100r_0$ is greater than $F_{ESD}(r_0)$ by a factor of ~2.45. Also, at some slow ramp rate Eq. 3.5 must break down, as does Eq. 3.4, since it does not make sense for $F_{ESD}(r_0) \to 0$ as $r \to 0$.

We now develop a more complete correction for ramping time from probability considerations. The probability to break down a sample of thickness d when exposed to a field F for a time Δt is given by Eq. 2.10 or Eq. 3.1; the probability of survival is $1 - P_{def}^{Tot}(\Delta t, F, T)$. The probability to survive N_{step} incremental voltage steps of ΔV_{step} volts, each for a time Δt_{step} up to a some voltage $V = N_{step}\Delta V_{step}$, is the product of the survival probabilities of each increment:

$$P_{survive}^{Tot}\left(\Delta t_{step}, N_{step}, \Delta V_{step}, T\right) = \prod_{j=1}^{N_{step}}\left[1 - P_{def}^{Tot}\left(\Delta t_{step}, \frac{j\Delta V_{step}}{d}, T\right)\right] \tag{3.6}$$

The complementary probability of breakdown $P_{step}^{Tot} = 1 - P_{survive}^{Tot}$ is

$$P_{step}^{Tot}\left(\Delta t_{step}, N_{step}, \Delta V_{step}, T\right) = 1 - \prod_{j=1}^{N_{step}}\left[1 - P_{def}^{Tot}\left(\Delta t_{step}, \frac{j\Delta V_{step}}{d}, T\right)\right] \tag{3.7}$$

This assumes that breakdown during each voltage step in the ramp to breakdown is independent of the other steps. Unlike the models discussed above, ΔV_{step} and Δt_{step} appear in Eq. 3.1 in such a form that one cannot isolate the breakdown voltage (or field) as a function of ramp rate. However, a simple numerical scheme could iteratively calculate either the ΔV_{step} or Δt_{step} (holding the other constant) needed to achieve a specified probability of breakdown. This model predicts significantly lower breakdown fields for

materials with slower ramp rates (Andersen, et al., 2015), in agreement with the empirical model (assuming the two empirical parameters A and B are constrained to be positive) and the simplified physical model. For example, given material constants from LDPE, assuming a 50% likelihood of breakdown ($P = 0.5$), the characteristic breakdown voltage increases by a factor of ~1.75 when increasing the ramp rate from 1 V/s to 100 V/s.

Figure 3.2 shows P_{step}^{Tot} for step-up tests as a function of applied field up to 400 MV/m for four different ramp rates, including the 20 V steps at 3.5 sec intervals used most often in the tests reported here and for a maximum ramp rate of 500 V/s intervals as recommended in the ASTM standard (ASTM D 3755-14, 2014). As expected, the probability of breakdown decreases for faster ramp rates. The analysis in Fig. 3.2 uses Eq. 3.7 with ΔG_{def}^{LO}= 0.95 eV and N_{def}^{LO}=2.8·10^{21} cm^{-3}, and ΔG_{def}^{HI}= 1.07 eV and N_{def}^{HI}=3.15·10^{19} cm^{-3} (Andersen, *et al.*, 2015).

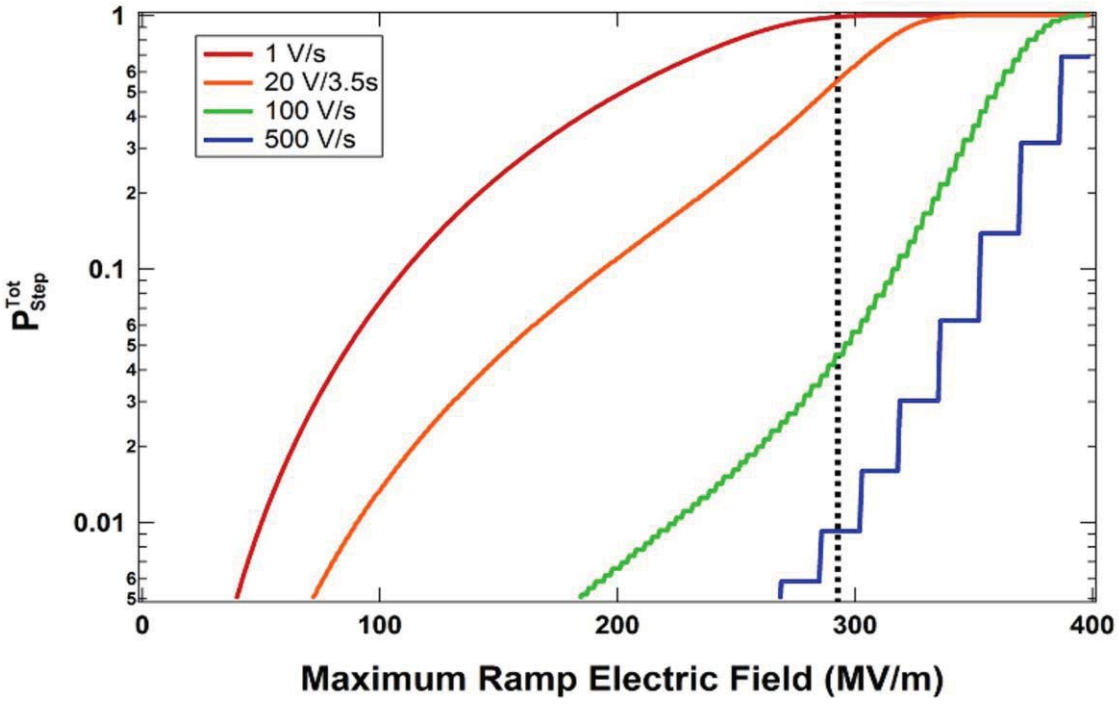

FIG. 3.2. Cumulative probability of breakdown during the voltage step-up process as a function of ramp maximum electric field. Results shown are based on Eq. 3.7 using material properties from fits to LDPE breakdown data for four ramp rates up, including the typical experimental ramp rate of 20 V per 3.5 s and the ASTM upper bound of ramp rates, 500 V/s. The vertical dashed line indicates the Weibull scale parameter corresponding to the 63.2% likelihood of breakdown from the 20 V per 3.5 s data—293 MV/m.

A more complete description of the breakdown probability as a function of ramp rate than Eq. 3.5 would require consideration of Eq. 3.7. Unfortunately, the breakdown voltage V_{ESD} as a function of $\Delta V/\Delta t$ is impossible to determine analytically. Given changes in either ΔV_{step} or Δt_{step} only, it should be possible to fit data using numerical schemes. Similarly, an analytic solution for Eq. 3.7 may be possible in the product calculus limit of a continuous ramp rate $V/\Delta V \to \infty$. This could be a topic for future theoretical work.

Finally, the probability of breakdown occurring in a SVET test over an elapsed time $t_{elapsed} > N_{step}\Delta t_{step}$ due to either a breakdown during ramping or at V_{static} is the sum of Eqs. 3.1 and 3.7:

$$P_{SVET}^{Tot}\left(\Delta t_{elapsed}, \Delta t_{step}, N_{step}, \Delta V_{step}, T\right) = P_{def}^{Tot}\left(\Delta t_{elapsed} - N_{step}\Delta t_{step}, N_{step}, T\right) +$$

$$P_{step}^{Tot}\left(\Delta t_{step}, N_{step}, \Delta V_{step}, T\right) = \left(\frac{2k_bT}{h/\left(\Delta t_{elapsed} - N_{step}\Delta t_{step}\right)}\right)\sum_{i=HI,LO}\exp\left[\frac{-\Delta G_{def}^{i}}{k_bT}\right]\sinh\left[\frac{\epsilon_0\epsilon_r\left(\frac{N_{step}\Delta V_{step}}{d}\right)^2}{2N_{def}^{i}k_bT}\right] +$$

$$1 - \prod_{j=1}^{N_{step}}\left[1 - \left(\frac{2k_bT}{h/\Delta t}\right)\sum_{i=HI,LO}\exp\left[\frac{-\Delta G_{def}^{i}}{k_bT}\right]\sinh\left[\frac{\epsilon_0\epsilon_r\left(\frac{j\Delta V_{step}}{d}\right)^2}{2N_{def}^{i}k_bT}\right]\right] \quad 3.8$$

In this case we identify $t_{en}^{Tot} = \Delta t_{elapsed} - N_{step}\Delta t_{step}$ and solving for t_{en} we find

$$t_{step-en}^{Tot}\left(\Delta t_{step}, N_{step}, \Delta V_{step}, T\right) = \left(\frac{h}{2k_bT}\right)\left[\sum_{i=A,B}\exp\left[\frac{-\Delta G_{def}^{i}}{k_bT}\right]\sinh\left[\frac{\epsilon_0\epsilon_r\left(\frac{N_{step}\Delta V_{step}}{d}\right)^2}{2k_bT\,N_{def}^{i}}\right]\right]^{-1} \times$$

$$\left\{\prod_{j=1}^{N_{step}}\left[1 - \left(\frac{2k_bT}{h/\Delta t}\right)\sum_{i=HI,LO}\exp\left[\frac{-\Delta G_{def}^{i}}{k_bT}\right]\sinh\left[\frac{\epsilon_0\epsilon_r\left(\frac{j\Delta V_{step}}{d}\right)^2}{2N_{def}^{i}k_bT}\right]\right]\right\} = t_{en}\left(\Delta t_{step}, N_{step}, \Delta V_{step}, T\right) \times$$

$$\left\{\prod_{j=1}^{N_{step}}\left[1 - \left(\frac{2k_bT}{h/\Delta t}\right)\sum_{i=HI,LO}\exp\left[\frac{-\Delta G_{def}^{i}}{k_bT}\right]\sinh\left[\frac{\epsilon_0\epsilon_r\left(\frac{j\Delta V_{step}}{d}\right)^2}{2N_{def}^{i}k_bT}\right]\right]\right\} \quad 3.9$$

This correction for the ramp rate will be shown to be small for the data in section 5.4.1.2. Section 5.4.1.1 compares Eqs. 3.3 through 3.7 to breakdown data at several applied ramp rates in four example polymers.

3.2. Effects of Considering Recoverable Defects

Let us examine what happens if we allow the defect density N_{def} to change. Granted, in many cases N_{def} may be well approximated as a constant, but in cases of exposure to radiation, active chemistry,

or thermal annealing of defects N_{def} might change considerably. For now, to simplify the math, we will only consider one defect species since adding another is straightforward. These would be unoccupied or low-occupancy defects and the interactions between any charges in the material are negligible compared to the effect of the applied field. In the limit of very low defect densities, we would expect the probability of breakdown to decrease since transport is less likely between more distant trap states. Conversely, at very high densities, the energy gained by a hop in the direction of an applied field would not be very different from that of a hop against the field, decreasing the net probability for hopping with defect spacings from some maximum value at a finite field and temperature.

However, we see that in Eq. 2.10 $P_{def}(N_{def}) \propto \sinh\left[\frac{\epsilon_0\epsilon_r F^2}{2k_b T N_{def}}\right]$, meaning that although $P_{def}(N_{def}) \to 0$ as $N_{def} \to \infty$ as expected, $P_{def}(N_{def})$ can only increase with decreasing N_{def}. Perhaps even more troubling is the endurance time Eq. 2.11, $t_{en}(N_{def}) \propto \operatorname{csch}\left[\frac{\epsilon_0\epsilon_r F^2}{2k_b T N_{def}}\right]$, which goes to zero at zero defects and infinity at large defect densities. This behavior is exactly opposite of what we expect. While the energy gained by charges hopping over longer distances does increase, the likelihood of such long hops must decrease at large distances. We see that there is nothing built into the theory to account for tunneling probability dying off with decreasing N_{def}.

The natural place to expect to find the anticipated but missing limiting behavior is in the tunneling frequency factor ν since this ought to decrease with decreasing N_{def}. In the literature regarding MAH, the Crine Model, or other related models, ν is invoked with a rough order of magnitude estimate of the related frequency (Wintle, 1983) or said to be proportional or about equal to $\frac{k_b T}{h}$ where h is Planck's constant (Crine*, et al.*, 1989; Lewis*, et al.*, 1996; Parpal*, et al.*, 1997; Andersen*, et al.*, 2015). If any physical argument is stated, it is said to be related to the phonon frequency. Considering the expected limiting behavior with defect density N_{def}, it becomes a glaring omission to exclude it from ν if N_{def} is not effectively constant.

For MAH, which had a similar problem in its earliest formulations, it is sufficient to consider a frequency ν that takes into account the tunneling probability as a function of distance. Considering that the

frequency factor should fall off like the transmission probability of tunneling through a square barrier of length a_{def} then

$$\nu(a_{def}) \approx \frac{k_bT}{h} \exp\left(-2a_{def}\sqrt{2m_e(\Delta G_{def} - k_bT)/\hbar^2}\right) \quad 3.10$$

Now, so long as $2\sqrt{2m_e(\Delta G_{def} - k_bT)/\hbar^2} > \frac{q_eF}{2k_bT}$, one observes the desired limiting behavior for MAH. Also, if $k_bT \ll \Delta G_{def}$, the thermal energy term in Eq. 3.10 may be neglected. In simplified notation by combining constants $A = 2\sqrt{2m_e(\Delta G_{def} - k_bT)/\hbar^2}$ and $B = \frac{q_eF}{2k_bT}$, $e^{-Aa_{def}}$ shrinks faster than $\sinh(Ba_{def})$ grows so long as $A > B$. We would expect B to be the largest close to breakdown, and even with fairly extreme values of F = 300 MV/m, assuming 3.65 eV C-C bonds for ΔG_{def}, and room temperature, we get $\frac{A}{B} \approx 2$ indicating that the correction results in the desired behavior given any reasonable conditions.

While this correction to ν does not build in requirements of $\Delta G_{def} > k_bT$ and $\Delta G_{def} > q_e a_{def} F$, it represents a significant conceptual improvement to MAH. Unfortunately, this correction is insufficient to correct the Crine model in three dimensions; however, the same correction would work on the earliest versions of the Crine model that consider only the defect spacing a_{def} (Crine*, et al.*, 1989). The problem arises when we consider the 1-D Maxwell stress tensor rather than the energy gained in a hop from one defect to the next. The argument of the sinh function is $\frac{\epsilon_0\epsilon_r F^2}{2k_bTN_{def}}$ rather than $\frac{q_e a_{def} F}{2k_bT}$. Recalling $\Delta V_{def} = (a_{def})^3 \equiv 1/N_{def}$, the same correction $P_{def}(N_{def}) \propto \exp\left(-\left(N_{def}^{\frac{-1}{3}}\right)\right)\sinh\left[\frac{\epsilon_0\epsilon_r F^2}{2k_bTN_{def}}\right]$. In short, the exponential as written cannot dominate the hyperbolic sine and we still have $P_{def}(N_{def}) \to \infty$ as $N_{def} \to 0$ which does not make sense.

Examining hops in three dimensions, even those not necessarily to the nearest neighboring defect, in other words VRH, does not give the desired limiting behavior either. The failure with VRH comes from distances cubed and densities (rather than cubed roots of densities) in the energy factor $w = \frac{3}{4\pi a_{def}{}^3 n(\mathcal{E}_f)}$ for $\nu \propto \exp\left(-Aa_{def} - \frac{w}{k_bT}\right)$ (Mott, 1969; Zallen, 1983; Boer*, et al.*, 2002). This results is an exponent of the

form $-\frac{A}{a_{def}}-\frac{{a_{def}}^3}{B}$ which does not improve the limiting behavior. This also ignores the part of w that depends on the defect density of states $n(\mathcal{E}_f)$, the defect energy density within a few k_bT of the Fermi level. For our purposes this is essentially $N_{def}\Delta G_{def}$. In any case, regarding the average hopping distance, one gets $\nu \propto \exp\left({N_{def}}^{\frac{-1}{4}}\right)$ which is the standard hopping frequency factor for VRH yet again (Boer*, et al.*, 2002). Unfortunately, this solution does not result in the limiting behavior we expect.

The simplest form to get the behavior we expect—though otherwise physically unjustified apart from similarities to the MAH fix—would be

$$\nu \propto \frac{k_bT}{h/\Delta t}\exp\left(\frac{-N_{def0}}{N_{def}}\right) \tag{3.11}$$

where N_{def0} is the undisturbed intrinsic defect density (field, dose, and temperature are zero). In this way, unless the applied field is too strong, we will expect the probability of breakdown to decrease with decreasing density. In addition, when the density of defects is not changed significantly, our original theory is only altered by a small constant factor. If we require our formula to reduce to the previous form of the Crine model when the defect density does not change, we could say

$$\nu = \frac{k_bT}{h/\Delta t}\exp\left(1-\frac{N_{def0}}{N_{def}}\right). \tag{3.12}$$

The adjustments of Eq. 3.11 or Eq. 3.12 give endurance times going to infinity at very low and very high defect densities with a minimum at some finite density. In any case, we see that the Crine model and dual-defect model of breakdown fail to describe the expected limiting case for the low defect density limit without such a correction. It is straightforward to see that so long as the fraction of total bonds in a defect mode is small, this correction (either Eq. 3.11 or Eq. 3.12) will be small as well.

The use of the 1-D Maxwell stress has long been debated and continues to be a disputed topic in the literature (Lewis*, et al.*, 1996; Crine, 1999; Palit, 2014; Crine, 2016b). It is interesting to note that Crine's most recent published work rejects the 1-D Maxwell stress as the physical mechanism for bond stressing in favor of electrostriction—a mechanical deformation of dielectrics related to the square of the polarization and often assumed to be a small enough effect to safely ignore (Crine, 2013; 2016b). The 1-D Maxwell stress is the very assumption that caused the theoretical difficulties outlined above. In these recent

works, he attempts to reconcile discrepancies between his model and some experimental data by considering electrostriction despite continuing to refer to that model and this field of study in general as poorly understood and confusing (Crine, 2016b). Some of the deviations he shows from the F^2 dependence of the Maxwell stress could be bimodal in agreement with the dual-defect model, but the data are too sparse for meaningful fits with the dual-defect model. Given the disputations regarding this point of the theory, adding the somewhat *ad hoc* correction Eq. 3.12 to get the expected physical limiting behavior is perhaps justifiable.

An important consequence of the probability of breakdown vanishing in the limit of either few or many defects is that there must be a peak in breakdown probability at some critical defect density. This peak marks a resonance in the hopping or tunneling probability of charges propagating through defect states. Fig. 3.3 plots this relationship. In region A, as the defect density decreases, trap isolation can dominate and the likelihood of breakdown vanishes despite the large energy gained when hops occur. In region B, as the defect density increases, breakdown likelihood again decreases both increasing the time charges spend in trap states and decreasing the energy gained by hops. This model predicts that for dielectrics subject to trap-creating radiation the risk of ESD can decrease with increasing dose after the peak defect density has been reached. Such behavior is analogous to Paschen's law for dielectric breakdown in gas. In gas at very low pressure, there are not enough molecules to cause avalanche ionization. Conversely, at high pressure charge moving between gas molecules, on average, does not gain much energy before impact. This results in a product of pressure and electrode distance with a minimum breakdown potential where avalanche ionization is most probable. Indeed, comparisons between Paschen breakdown and breakdown in solids are nothing new (Ridley, 1975).

3.2.1. Dynamic Breakdown Models

Having examined what happens if the defect density changes significantly, let us examine how the defect density N_{def}^{i} is effected by temperature and electric field. The rate of change of the defect density must be related to the rate of defect creation minus the rate of annihilation (Lewis*, et al.*, 1996). So let us

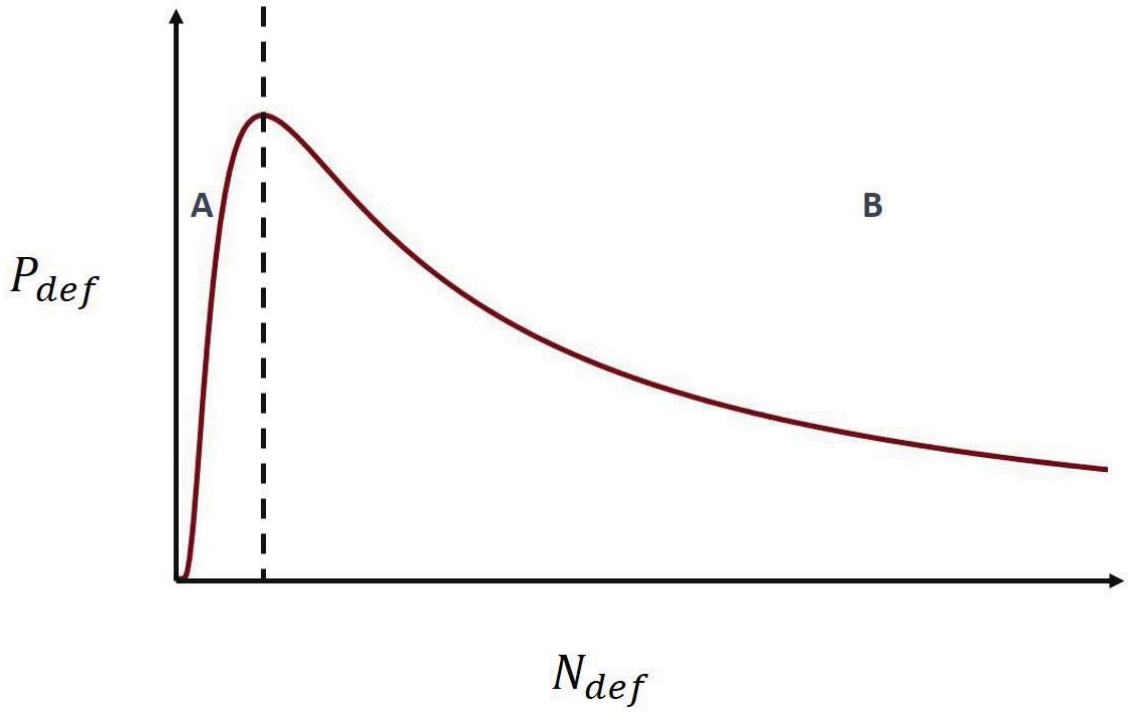

FIG. 3.3. Plot of the probability of breakdown P_{def} versus defect density N_{def} holding all other parameters constant. The dashed vertical line marks the peak of the distribution and the resonance for breakdown to occur. Region A left of the peak is where defect isolation dominates. Region B to the right of the peak is the trap-dominated region.

consider a rate of creation operator K_{def}^{+i} acting on available bonds and an annihilation-rate operator K_{def}^{-i} acting on the existing defects

$$\frac{dN_{def}^{i}(t)}{dt} = \left[N_{bond}^{i} - N_{def}^{i}(t)\right] \cdot K_{def}^{+i}(F,T) - N_{def}^{i}(t)(t) \cdot K_{def}^{-i}(F,T) = N_{bond}^{i} K_{def}^{+i} - N_{def}^{i}(t)\left[K_{def}^{+i} + K_{def}^{-i}\right]. \quad 3.13$$

For now, let us not worry about the form of $K_{def}^{\pm i}(F,T)$. Equation 3.13 can have solutions of the form

$$N_{def}^{i}(t) = \frac{K_{def}^{+i} N_{bond}^{i}}{K_{def}^{+i} + K_{def}^{-i}}\left(1 + e^{-\left[K_{def}^{+i} + K_{def}^{-i}\right]t}\right). \quad 3.14$$

The steady-state solution for this as $t \to \infty$ is simply

$$N_{def}^{i} = \frac{K_{def}^{+i} N_{bond}^{i}}{K_{def}^{+i} + K_{def}^{-i}}. \quad 3.15$$

At this point we need to discuss the form of $K_{def}^{\pm i}(F,T)$. To get this far we have assumed that $K_{def}^{\pm i}(F,T)$ does not depend on time or defect density. If applied field or temperature changes in time then this is clearly not the case but if we assume that they change very slowly, it may not be a bad approximation. Considering that defects are thermally switched on and off and depending on defect energy and applied field, our operator becomes (Lewis*, et al.*, 1996; Crine, 1999; Andersen*, et al.*, 2015)

$$K_{def}^{\pm i}(F,T) = \frac{k_b T}{h} \exp\left[\frac{-\Delta G_{def}^{i} \pm \frac{1}{2}F(t)^2 \epsilon_0 \epsilon_r \Delta \mathrm{V}_{def}^{i}}{k_b T}\right]. \quad 3.16$$

It is clear, assuming $\Delta \mathrm{V}_{def}^{i} = \frac{1}{N_{def}^{i}}$ (as stated before), that Eq. 3.15 has not been solved for $N_{def}^{i}(t)$, and we have violated basic rules of solving differential equations by ignoring the time dependence of the creation and annihilation operators. While the time dependence of slowly varying temperature or electric field might be ignored, $K_{def}^{\pm i}(F,T)$ contains $N_{def}^{i}(t)$, the very term we are solving for. Unfortunately, this complicates Eq. 3.13 to the point of where it is unsolvable analytically. Numerical methods would only be useful for very specific cases where the material properties and extrinsic conditions are known. Crine has published other expressions for N_{def}^{i}, but these also depend on $\Delta \mathrm{V}_{def}^{i}$, which he agrees in later work is, or at least may be, the inverse defect density, resulting in circular reasoning (Crine, 2002a; 2005a; 2007).

Alternatively, let us consider the steady-state behavior of $N_{def}^{i}(F,T)$ from the beginning rather than starting with the differential equation. Let us suppose that

$$N_{def}^{i}(F,T) = N_{def0}^{i} + N_{T}^{i}(T) + N_{F}^{i}(F) \quad 3.17$$

where any change in defect density due to external dose is contained in the initial defect density N_{def0}^{i}.

For $N_{T}^{i}(T)$, let us consider how many phonons we expect to have in the equilibrium state at the defect energy. The average occupancy of phonons of energy is simply the Planck distribution (Kittel, 1966). Considering the number of phonons at the defect energy ΔG_{def}^{i} we find

$$\langle n\left(\Delta G_{def}^{i}, T\right)\rangle = \frac{1}{\exp\left(\frac{\Delta G_{def}^{i}}{k_b T}\right) - 1}. \quad 3.18$$

Equation 3.18 is plotted in Fig. 3.4. Since we assume $\Delta G^i_{def} > k_b T$, the occupancy must be less than one. We see that this phonon mode is unlikely over the range of realistic temperatures; however, there are many bonds in a material. Consider that the defect density could be approximated as product of the available bond density N^i_{bond} and the equilibrium number of phonons that can create defects $\langle n \rangle$.

$$N^i_{def}(T) = N^i_{bond}\langle n \rangle = \frac{N^i_{bond}}{\exp\left(\frac{\Delta G^i_{def}}{k_b T}\right)-1} \tag{3.19}$$

For $N^i_{bond} > 10^{22}$, we get realistic LO-type defect densities using Eq. 3.19 (see 3.1.1, 6.2, and 7.2.2) (Andersen*, et al.*, 2015).

Adding the field dependence is tricky since the obvious place to add it is not in a separate term as in Eq. 3.17. Given that $\mathcal{E}_{strain} = \frac{\epsilon F^2}{2N_{def}}$ we have the same issue as above with circular math. A possible solution (considering only the smaller numerator term since it will dominate) is to use the approximation $\mathcal{E}_{strain} = \frac{\epsilon F^2}{2N^i_{def0}}$ resulting in

$$N^i_{def}(T) = N^i_{bond}\langle n \rangle = \frac{N^i_{bond}}{\exp\left(\frac{\Delta G^i_{def} - \frac{\epsilon F^2}{2N_{def}}}{k_b T}\right)-1}. \tag{3.20}$$

For either Eq. 3.19 or Eq. 3.20, $N^i_{def}(T)$ can only increase with increasing temperature. This still does not seem to capture the original conceptual model we have of defect annealing dominating at high temperatures and stopping breakdown. On the other hand, increased defect density means more trapping and less energy gained by hops between traps (region B in Fig. 3.3). This effect also decreases breakdown probability holding other factors constant.

By examining the creation and annihilation operators (Eq. 3.16), we can see if the limiting behavior described above makes sense. Note that

$$\frac{K^{+i}_{def}}{K^{-i}_{def}} = \exp\left[\frac{F(t)^2 \epsilon \Delta \mathrm{V}^i_{def}}{k_b T}\right] \geq 1, \tag{3.21}$$

so we see that in all cases $K^{+i}_{def} \geq K^{-i}_{def}$. Approaching zero electric field or high thermal energy, we see that

$$\frac{K^{+i}_{def}}{K^{-i}_{def}}\left(\frac{F(t)^2 \epsilon \Delta \mathrm{V}^i_{def}}{k_b T} \to 0\right) = 1 \tag{3.22}$$

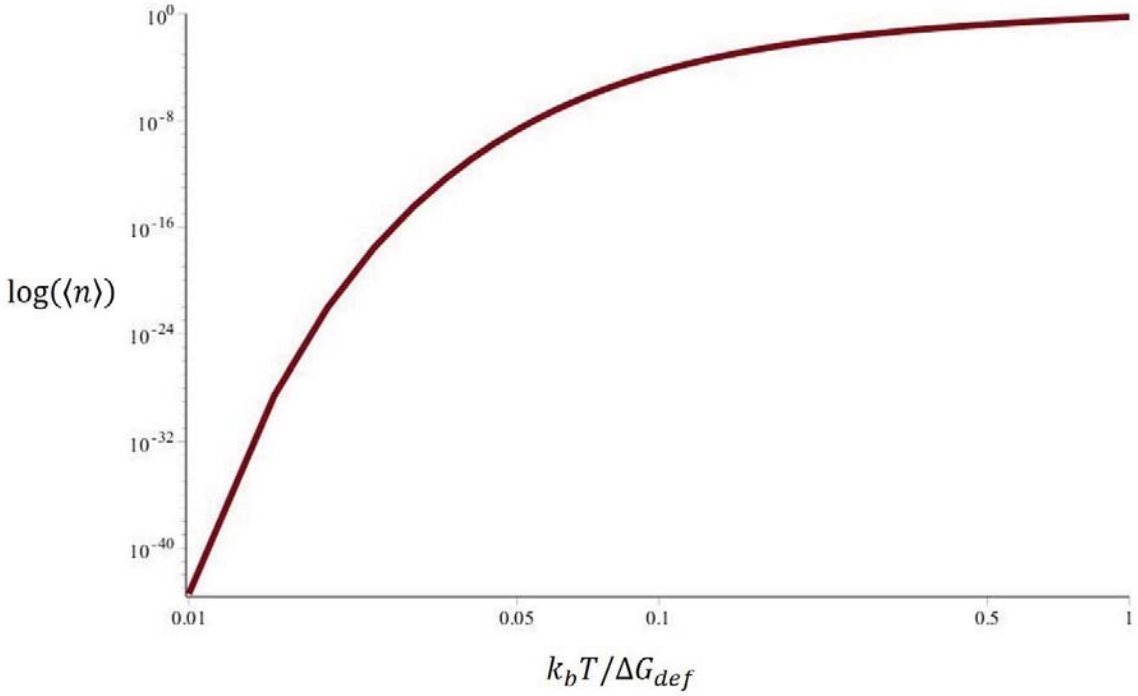

FIG. 3.4. The phonon occupancy, or alternatively the fraction of available bonds in the defect state as a function of thermal energy (corresponding with temperatures up to ~470 K). This assumes that the defect energy on the order of 0.1 eV.

and there is an equilibrium between creation and annihilation. At zero applied field, this is true regardless of finite temperature. From Eq. 3.13 we see that defect creation will tend to dominate unless there are more defects than available bonds, which seems unlikely. This agrees with the steady state behavior predicted in Eqs. 3.19 or 3.20.

For ΔG_{def}^{HI} we assume $\Delta G_{def}^{HI} \gg F(t)^2 \epsilon \Delta \mathrm{V}_{def}^{i}$ and $\Delta G_{def}^{HI} \gg k_b T$ so $K_{def}^{+HI} \approx K_{def}^{-HI}$ and we see that we can indeed safely ignore defect creation and recovery rates for the high-energy defects.

Let us revisit Eq. 3.13 for $\frac{dN_{def}^{LO}(t)}{dt}$ considering $K_{def}^{+LO} \gg K_{def}^{-LO}$.

$$\frac{dN_{def}^{LO}(t)}{dt} = K_{def}^{+LO}\left[N_{bonds}^{LO} - N_{def}^{LO}(t)\right] = \frac{k_bT}{h}\left[N_{bonds}^{LO} - N_{def}^{LO}(t)\right]\exp\left[\frac{-\Delta G_{def}^{i} + \frac{1}{2}F(t)^2\epsilon/N_{def}^{LO}(t)}{k_bT}\right]. \quad 3.23$$

The solution to this equation is $N_{def}^{LO}(t) = N_{bonds}^{LO}$—which we know cannot be right—but because in this approximation defect annihilation is ignored, this result makes sense because only defect creation was allowed so eventually all available bonds will be in the defect mode.

Although we have not solved the differential equation Eq. 3.13 for how the defect density changes over time, by examining the creation and annihilation operators and by considering steady-state behavior it can be shown that in general, defect creation tends to dominate over defect recovery, but that defect recovery should not be ignored as in Eq. 3.23. The difficulty in obtaining exact solutions lies in the fact that the rate of defect creation and recovery depends on the defect density itself.

3.2.2. DC Partial Discharge

In addition to describing a physical model of dielectric breakdown, the dual-defect model can be applied to the problem of DCPD as well. The field of DCPD theory and application is woefully behind that of ac partial discharge (ACPD) (Crine, 2005b; Vu*, et al.*, 2013; Czaszejko, 2014; Trnka*, et al.*, 2014; Corr*, et al.*, 2016). Fig. 3.3 shows that as the defect density changes away from the resonance, the likelihood of breakdown tends to move toward zero. One effect of this could be that, as a discharge begins to propagate through a material, local heating thermally creates many LO type defect sites and, with the sudden increase in N_{def}^{LO} and subsequent trapping, the discharge can no longer propagate. On the other hand, if defect annihilation dominates to where N_{def}^{LO} moves below the resonance, defect isolation could also stop the motion of charge. Either charge trapping or trap isolation due to variations in N_{def}^{LO} could result in a partial discharge rather than a complete destructive breakdown. We have shown that in general that defect creation tends to dominate. Later, Chapter 4 will discuss observations that seem to match this description.

Alternately, one might think of a lattice of defect sites with the density of high-energy defects near, but below, the percolation threshold. While high-energy defects are largely independent of temperature, their density could be increased through radiation damage or through prolonged exposure to F field stress (the latter is the essence of endurance time tests). Additional low energy defects could act in concert with the high-energy defects to complete a percolation path. However, these low energy defects would have small average lifetime and be much more dependent on T. The generation of such defects

would follow an Arrhenius behavior, much like the generation of phonons in a periodic crystalline lattice (Kittel, 1966) or the temperature dependence of photon emission in cathodoluminescence (Jensen and Dennison, 2015). Thus, completion of the percolation path would be expected to increase with increasing T due to defect recovery, but would be transient.

More sophisticated models would have to consider both spatial and energetic distributions of these defects, even distributions that change with temperature, dose, and stress imposed on the materials while under field F, or the time t a material is exposed to such stress.

3.3. Summary of Theoretical Work

In this chapter, the dual-defect model of electrical aging in HDIM has been outlined. This model is a simple extension of mean-field theory outlined in the previous chapter. Rather than considering only the average of the entire defect DOS, the dual-defect model considers the average contribution of two classes of defects, namely high energy chemical defects and low energy physical defects. The dual defect model may be used to describe the probability of breakdown due to intrinsic material properties and extrinsic conditions (Eq. 3.1). It can also be used to estimate the time to breakdown, (Eq. 3.2), and the likelihood of breakdown due to a voltage ramp-up, (Eq. 3.7). We have discussed other ramp rate effects in 3.1.2. Finally, to the extent possible, we have examined the effects of considering defect creation and recovery for the low-energy defects and how the variable nature of these defects with T and F leads to a candidate physical explication of DCPD.

CHAPTER 4

EXPERIMENTAL METHODS

Having proposed a new theory of dielectric breakdown—the dual defect model—we turn our attention to how this model, and indeed any model of breakdown, should be tested in the laboratory. This chapter describes both general considerations for performing breakdown tests, and the specific experimental details of the MPG experiments used to generate the data discussed in this dissertation. Chapter 4 begins with a general discussion of ESD test configurations and how they relate to the models outlined in Chapters 2 and 3, then transitions into a technical description of the MPG ESD test setup and how it is used.

The tests described here are for the parallel-plate geometry test method, as shown in Fig. 4.1. The dielectric to be measured is sandwiched between two metal plates and a voltage is applied until breakdown occurs. Many dielectric breakdown test systems rely primarily on such leakage current measurements to identify breakdown, particularly those following the ASTM D3755-14 Standard Test Method for Dielectric Breakdown Voltage and Dielectric Strength of Solid Electrical Insulating Materials Under Direct-Voltage Stress (ASTM D 3755-14, 2014). Such measurements are critical for applications including high voltage direct current (HVDC) power, high voltage switching and control, microelectronics, spacecraft charging induced ESD mitigation, and advancing the understanding of breakdown physics in disordered dielectrics (Andersen*, et al.*, 2015; Andersen*, et al.*, 2017). NASA handbooks recommend using the ASTM D3755 test method for dielectric breakdown testing of spacecraft dielectrics (NASA HDBK-4002, 1999; NASA HDBK-4002A, 2011; Garrett and Whittlesey, 2012).

Other ESD test methods used in spacecraft applications include the electron beam exposure method and the human body model (ECSS-E-ST-20-08C, 2012; Garrett and Whittlesey, 2012; Wilson*, et al.*, 2013b; Green and Dawson, 2015). While the electron beam method is a better approximation of the space environment, it introduces enough experimental difficulty to make fitting data to the models presented here unrealistic (*e.g.,* one cannot measure surface potential without blocking the electron beam). The human body model is an impulse method more suited for components level testing, and in any case, does not model prolonged exposure of the lifetime to breakdown problem. It is also interesting to note that

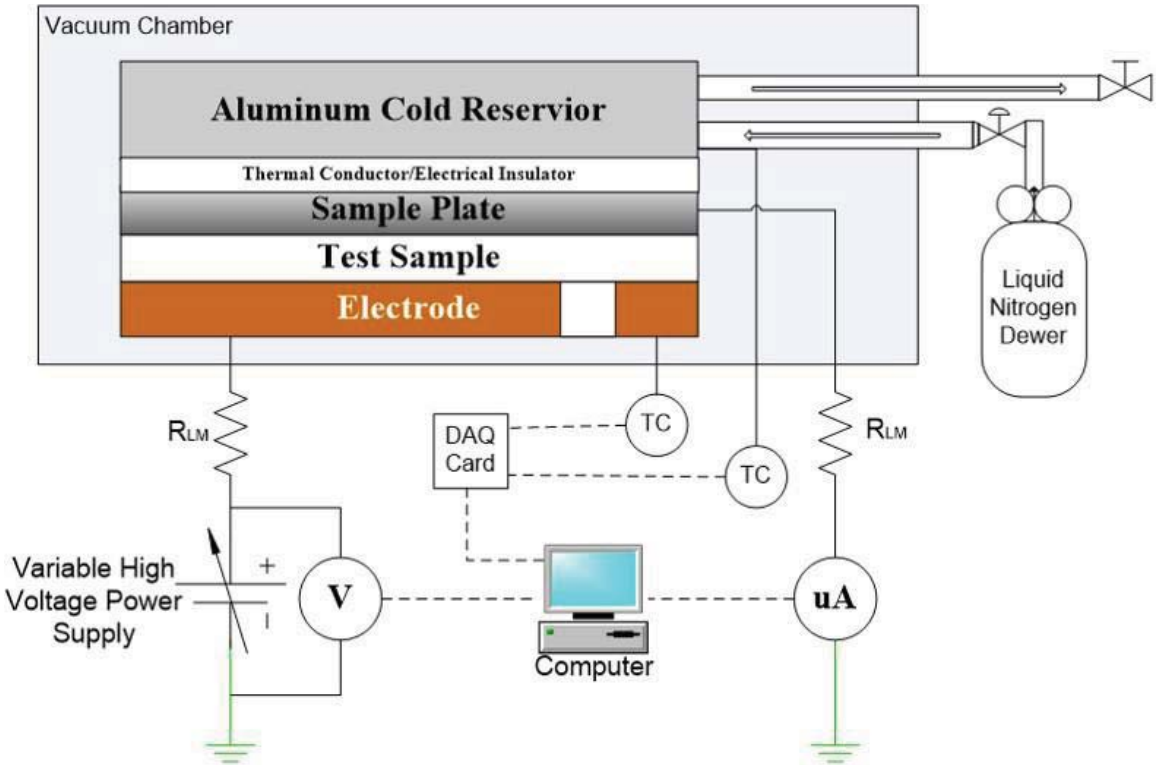

FIG. 4.1. Block diagram of ESD test apparatus. Shown are a simple parallel-plate capacitor sample geometry with high voltage power supply, a cryogenic reservoir in thermal contact with sample plate, plus computer-automated voltage, current and temperature sensors.

the electron beam method produces discharges without easily visible breakdown damage on test samples (Jensen*, et al.*, 2013). In the context of spacecraft charging then, ESD includes both dielectric breakdown and partial discharge (PD).

4.1. Definition of Breakdown

Prior to outlining the experimentation, it is important to define what is being measured. Unfortunately, the imprecise definition of breakdown in the ASTM D3755-14 standard can cause misidentification of breakdown. This standard recommends identifying breakdown with a breaker or fuse that is tripped by a sudden rise in leakage current at breakdown, *i.e.*, an arbitrary leakage current threshold. If the recommended test circuit current sensing element threshold is set too high, breakdown may occur undetected. Conversely, false positives may result from designating a low current threshold.

An operational definition of breakdown that is much less sensitive to these pitfalls is outlined herein. I propose an improved definition of breakdown based on the average rate of change of the leakage current with increasing voltage, rather than a simple current threshold, avoiding ambiguous association with anomalies in current traces. For tests that continuously monitor leakage current, breakdown can be detected by a transition from negligible current to an ohmic slope defined by the circuit's current-limiting resistors. In practice, a fixed current threshold may be inadequate to define dielectric breakdown. Field-enhanced conductivity, partial discharge, surface flashovers, incomplete breakdowns, and other phenomena may further obscure the characteristic dielectric breakdown signature. In Section 4.6.4, the MPG breakdown criterion is discussed in detail. Different types of pre-breakdown anomalies in current traces can now be clearly identified and studied, in addition to the breakdown itself. Alternatively, by Ohm's law, one could consider the voltage drop across the test sample as a function of time as an indicator of breakdown, *i.e.*, at breakdown the voltage drop on the sample drops dramatically without recovery.

4.2. Voltage Step-up to Breakdown Tests

Here we begin to discuss methods used to test breakdown theories, especially those in Chapters 2 and 3. One standard breakdown test method is the voltage step-up test (ASTM D 3755-14, 2014). In these tests, the sample is subjected to voltage that increases incrementally until breakdown occurs. Unless otherwise stated, the applied voltage refers to the voltage applied to the entire test circuit. This is the test type shown in Fig. 4.2 as well a Fig. 4.7 through Fig. 4.10.

Eq. 3.7 can be re-written as

$$P_{step}^{Tot}(F,r,T) = 1 - \prod_{j=1}^{F/d\cdot\Delta V_{step}} \left[1 - P_{def}^{Tot}\left(\Delta t_{step}, \frac{j\Delta V_{step}}{d}, T\right)\right] \quad 4.1$$

and can be used to fit an ensemble of such measurements. This explicitly predicts the probability of breakdown as a function of applied field $\left(N_{step} = F/\left(d\cdot\Delta V_{step}\right)\right)$, voltage ramp rate $\left(r = \Delta V_{step}/\Delta t_{step}\right)$, and temperature T. The other material properties such as defect densities and energies are contained in P_{def}^{Tot}. Chapter 5 will compare the Crine model to the dual defect model for voltage step ups by comparing fits to data using P_{def}^{Tot} (Eq. 3.1) for the dual defect model and $P_{def}^{Tot} \to P_{def}$ (Eq. 2.10) from the Crine model. These fits will also be compared to empirical Weibull fits for this same test type.

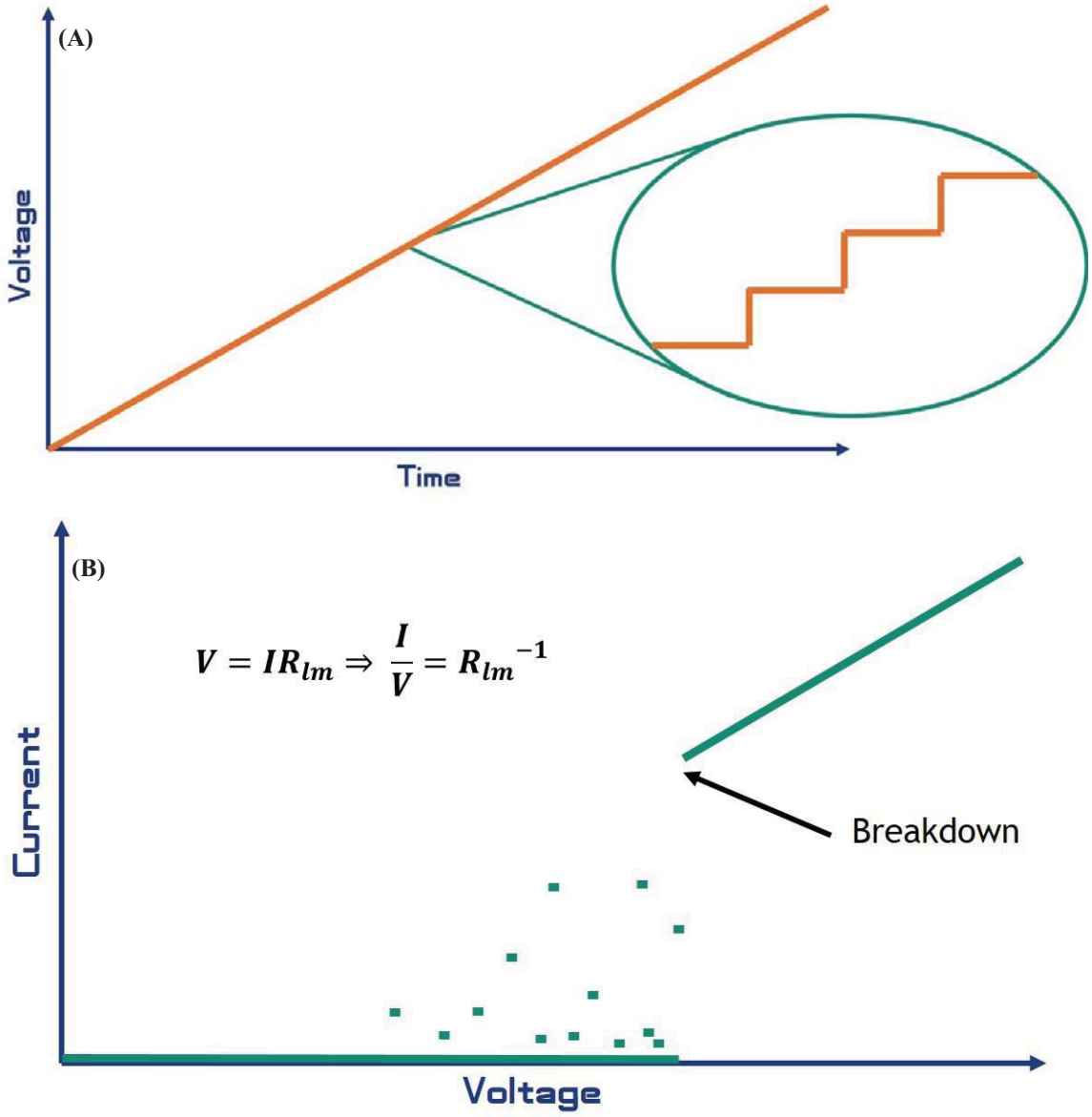

FIG. 4.2. Voltage step-up test method. (A) The applied voltage increases over time until the test is ended. The MPG standard ramp rate is stepwise 20V/ 4s using a 30kV dc power supply. Tests of the voltage ramp rate dependence of breakdown are simply voltage step-up tests with either faster or slower ramp rates. (B) Current is measured as the applied voltage increases. Before breakdown, little or no current is measured. After breakdown current increases linearly according to Ohm's law.

This approach requires assuming that the empirical cumulative distribution (ECD) of the tests is a reasonably good approximation for the true underlying cumulative probability distribution (see Section 5.2). This assumption improves with increasing test number, roughly as the square root of the test number.

4.3. Voltage Ramp-rate Dependence of Breakdown Tests

Voltage step-up to breakdown tests can be done at different ramp rates to examine the ramp rate dependence discussed in 3.1.2 and shown in Fig. 4.2, Fig. 4.8, and Fig. 4.9. Due to the stochastic nature of ESD, several tests should be done at each ramp rate of interest to get decent statistics. Eq. 3.3 through Eq. 3.5 predict how the nominal breakdown field (the mean or Weibull scale parameter field) changes with ramp rate r. Equation 4.1 can be used in a numerical scheme to fit data so long as either the voltage step ΔV_{step} or time step Δt_{step} are the same for each ramp rate studied (unless one has enough data to do meaningful fits in three-dimensional space). A numerical scheme is necessary to extract how F at breakdown changes with ramp rate. If comparisons are to be made to empirical models using this numerical method, P_{step}^{Tot} must be chosen to match the statistics used in those models. For example, when comparing average breakdown fields at different ramp rates, $P_{step}^{Tot} = 0.5$, or if Weibull statistics are to be used, $P_{step}^{Tot} = 0.632$. A study of this type is presented in 6.2.3. The numerical scheme for using Eq. 4.1 is found in Appendix C.

4.4. Static Voltage Endurance Time Tests

Static voltage endurance time (SVET) are conducted by incrementing the applied voltage to a plateau voltage V_{static}, and then maintaining this static electric field across the sample until complete electrostatic breakdown occurred as shown in Fig. 4.3. Typical static voltages for the endurance time experiments described here were in the range of 4 kV to 9 kV. These values yielded endurance times from a few minutes to a few days. The appropriate value of the endurance time, as determined from the elapsed time as logged by the data acquisition program measured from when the initial voltage was applied, is discussed in 5.4.1.2 and 6.2.2. SVET measurements directly measure the endurance time, t_{en} to electrostatic breakdown at some subcritical field. SVET test the predictions made by

$$t_{en}(F,T) = \left(\frac{h}{2k_bT}\right) \exp\left[\frac{\Delta G_{def}}{k_bT}\right] \operatorname{csch}\left[\frac{\epsilon_0 \epsilon_r F^2}{2k_bTN_{def}}\right], \tag{2.11}$$

for a single defect model

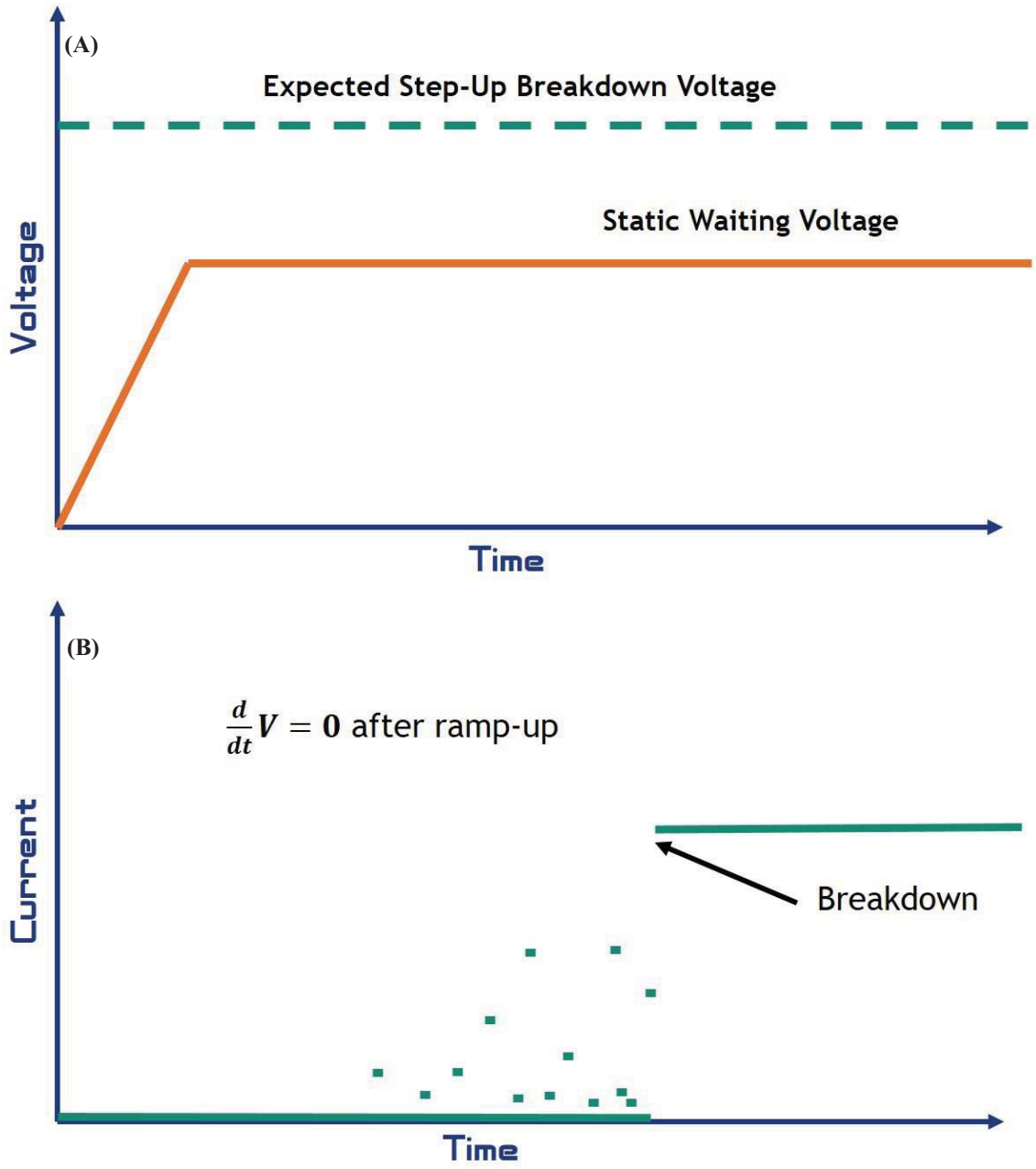

FIG. 4.3. Static Voltage Endurance Time (SVET) test method. (A) The applied voltage increases over time until the waiting voltage is achieved. The static waiting voltage is maintained for the duration of the test. (B) Current is measured throughout the test. Breakdown is marked by a transition to a large, constant, current set by the residual resistance of the test circuit.

$$t_{en}^{Tot}(F,T) = \left(\frac{h}{2k_bT}\right)\left\{\sum_{i=HI,LO} \exp\left[\frac{-\Delta G_{def}^{i}}{k_bT}\right] \sinh\left[\frac{\epsilon_0\epsilon_r F^2}{2N_{def}^{i}k_bT}\right]\right\}^{-1}, \quad 3.2$$

or for the dual-defect model with

$$t_{step-en}^{Tot}(F,T) = t_{en}^{i}(F,T) \times \left\{\prod_{j=1}^{\frac{Fd}{\Delta V_{step}}}\left[1 - \left(\frac{2k_bT}{h/\Delta t}\right)\sum_{i=HI,LO} \exp\left[\frac{-\Delta G_{def}^{i}}{k_bT}\right] \sinh\left[\frac{\epsilon_0\epsilon_r\left(\frac{j\Delta V_{step}}{d}\right)^2}{2N_{def}^{i}k_bT}\right]\right]\right\} \quad 4.2$$

for considering the voltage ramp to the static waiting voltage.

Equations. 2.11, 3.2, and 4.2 (a simplified version of Eq. 3.9) are the predictions of the Crine model, dual-defect model, and the ramp-up to static voltage models respectively. The ramp-up correction could be applied to t_{en} from either Eq. 2.11 or Eq. 3.2.

4.5. Temperature Dependence of Breakdown

Section 2.1.3 outlines how charge transport mechanisms can change significantly with temperature. In 2.2, it was shown how both the Crine and dual-defect models are based on Boltzmann factors for the likelihood of hopping between localized defects and the temperature-dependent phonon spectrum. In a general sense, the temperature dependence predicted by these models is not straightforward, although once specific material properties and extrinsic conditions are identified, the models do make specific predictions for the likelihood of breakdown at any given temperature where the assumptions of the models are not violated (*e.g.*, $k_bT > \Delta G_{def}^{HI}$).

Voltage step-up tests, or even SVET tests, may be performed at desired temperatures to test the temperature dependence of breakdown. In practice, this requires the use of cryogenic fluid such as liquid nitrogen for cooling and vacuum baking for heating. Preliminary results from such tests are discussed in 6.2.4.

4.6. Experimental Procedures

This section will review the hardware and methods used by the MPG to perform each of the tests described above. Detailed operating procedures for operating this equipment and the corresponding software can be found in Appendix A and Appendix C respectively.

4.6.1. Sample Preparation

Good sample preparation and characterization prior to testing is key to good measurements. It has been shown that even batch-to-batch differences in the same material from the same manufacturer may significantly change charge transport properties presumably due to differences in initial defect densities due to sample manufacture and preparation (see 6.2.1) (Saiki*, et al.*, 2015). The effects of unintended electrical aging, contamination, or other damage can drastically effect a material's defect population and therefore, its charge transport properties (Dennison, 2015).

Especially for space missions, it is important to bake test samples *in vacuo* to drive off water and other volatile compounds, which can significantly affect conductivity, work function, and electron emission (Garrett and Whittlesey, 2012; Dekany*, et al.*, 2013; Dennison*, et al.*, 2016a). Only by eliminating extrinsic factors that can effect conductivity and breakdown can one begin to test the intrinsic properties of a material. Details of the MPG sample preparation procedures are given in Appendix A.

4.6.2. Electrostatic Discharge Chamber

This section details the MPG ESD chamber setup. ESD tests were conducted using a modified ASTM method (ASTM D 149-97a, 2004; ASTM D 3755-14, 2014) in a custom, high vacuum chamber ($<10^{-3}$ Pa base pressure using a Pfieffer TSH 071E turbomolecular pump station backed with an oil-free diaphragm pump) (Brunson, 2010). See vacuum diagram in Fig. 4.4 (a). Pressure was monitored near the pumps with a Pfeiffer PKR 251 cold cathode and Pirani full range gauge. Electric fields were applied to the material using a variable high voltage power supply (CPS Precision, Model 130N/1314; 0-30 kV at 500 μA and ripple < 200 mV at full load) in a simple parallel plate capacitor geometry (Fig. 4.1 and Fig. 4.4 (b)). Voltage (V) and current (I) were monitored for the duration of the experiments using two interfaced multimeters (Amprobe®, Model 38XR-A; 100 μV and 100 nA resolution at 2 Hz acquisition rate) under LabVIEW control (details in Appendix C). Voltage is measured using a 1000/1 voltage divider.

(a)

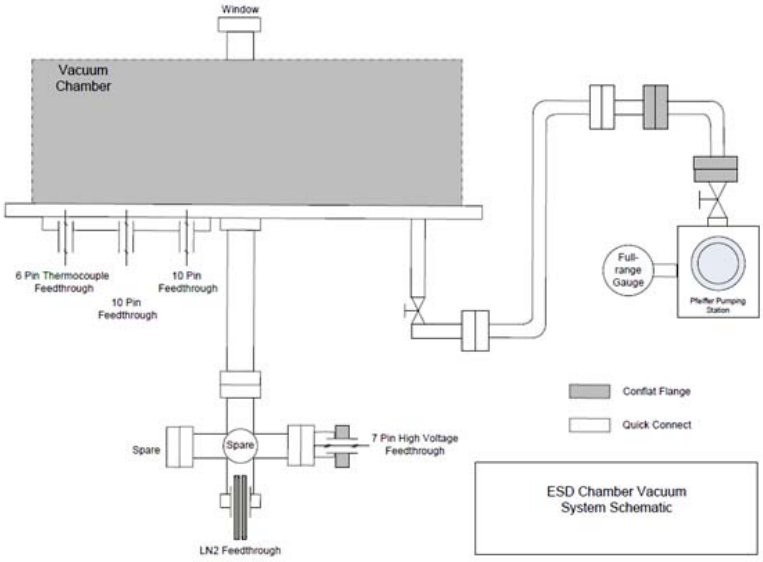

(b)

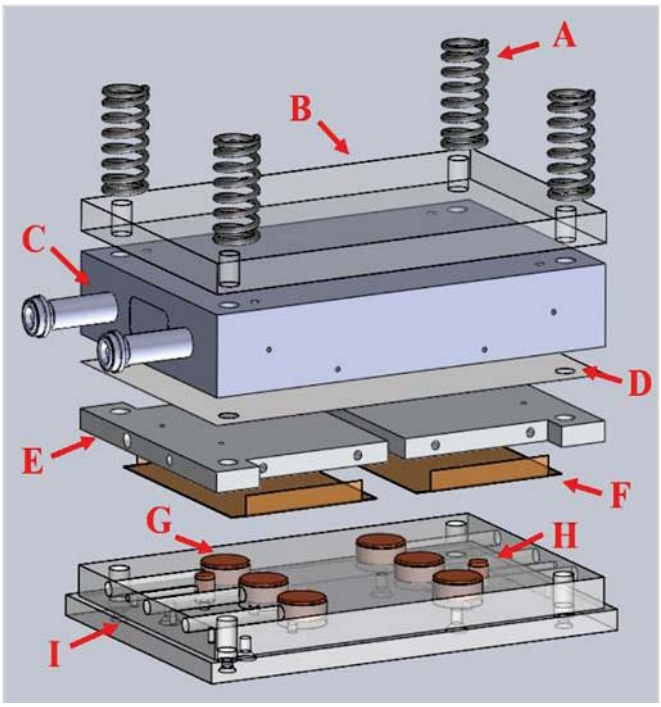

FIG. 4.4. USU ESD system hardware. (a) Vacuum diagram. (b) Exploded view of ESD test assembly showing: (A) Adjustable pressure springs, (B) Polycarbonate insulating layer in cryogenic configuration—located between D and E during room temperature tests, (C) Cryogen reservoir, (D) Thermally conductive, electrically isolating layer, (E) Sample and mounting plate, (F) Sample, (G) HV Cu electrode, (H) Cu thermocouple electrode, (I) Polycarbonate base.

Samples (**F**, in Fig. 4.4 (b)) were clamped between a metal sample mounting plate (**E**) and six highly polished (<200 nm rms surface roughness) 1.98±0.08 cm^2 active area beveled Cu high voltage electrodes (**G**). This allowed testing of six samples during a single vacuum cycle. A spring clamping mechanism (**A**) was employed to apply uniform sample contact pressure of a few hundred kPa, in compliance with standard methods (ASTM D 257-99, 1999). This pressure has been measured with FlexiForce sensors at each electrode as a function of the number of turns applied by a hex key is shown in Fig. 4.5. Test voltages were typically reached by incrementing the applied voltage at ΔV_{step}≈20 V at Δt_{step}≈4 s time intervals up to 15 kV or until breakdown occurred and the test was ended (see Fig. 4.10 (a) with additional details in Appendix C). Current increased significantly at breakdown (typically up to on the order of 10 μA) with leakage current limited by the sum of any residual sample resistance and two in-series current limiting resistors (R_{lm}=100 MΩ each in Fig. 4.1). Given extreme values of the materials tested, the RC time constant τ_{RC} of the system is ≲50 ms, much less than Δt_{step} or the 0.4 s maximum time constant prescribed by the ASTM standard (ASTM D 3755-14, 2014). The active area of the device under test leads to sample capacitance on the order of 250 pF depending on the individual sample thickness and sample permittivity.

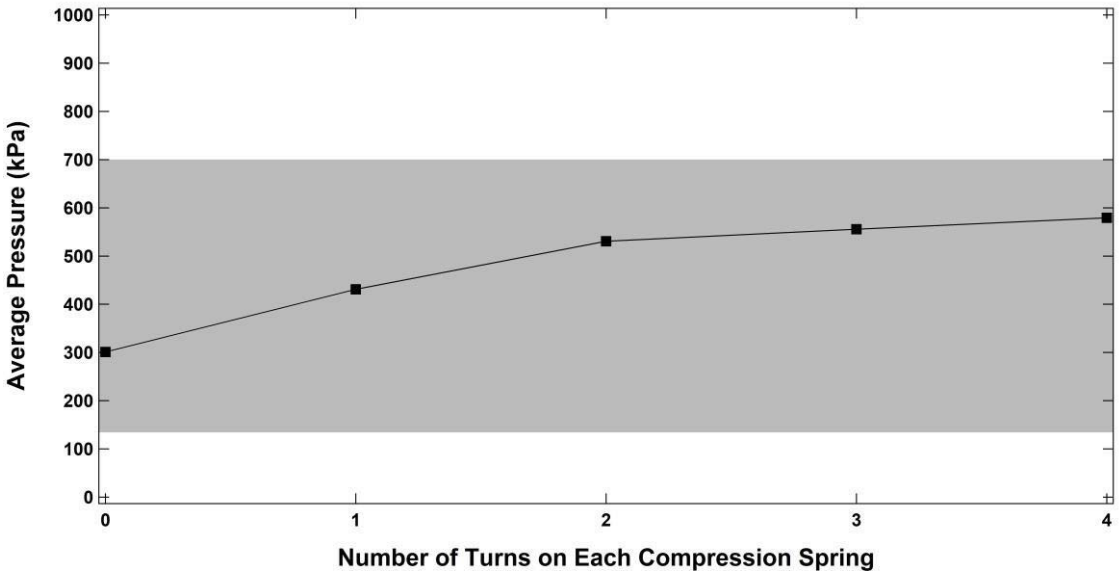

FIG. 4.5. Pressure applied to samples with increasing spring compression. The grey region indicates the recommended range of pressures to ensure good sample contact with electrodes.

Test were typically conducted at room temperature (25±1 °C) (Dekany*, et al.*, 2013), but could be set to range from ~150 K to 360 K. Measurements were made by cooling samples in thermal contact with a liquid nitrogen filled aluminum cryogen reservoir (**C**) or baking the entire chamber for high temperatures. Temperature was monitored with Type K thermocouples attached to two Cu temperature sensors (**H**) in good thermal contact with the sample, but electrically isolated (**I**). Temperatures typically increased less than 0.6 K/min or ≲15 K during a single cryogenic step-up testing cycle. A CHO-THERM layer (**D**) provides good thermal conductivity between the cryogen reservoir and the sample plates while maintaining electrical isolation.

Fig. 4.6 uses a generalized circuit diagram to compare the USU MPG test circuit to other test circuits described with at least some detail (Rowland*, et al.*, 1986; Ho and Jow, 2013; Kerwien*, et al.*, 2016; Ritamäki*, et al.*, 2017b). The addition of a capacitor parallel to the device under test can assist with breakdown, particularly when the power supply cuts out at breakdown. The large-area breakdown method effectively has many parallel test capacitors (Ritamäki*, et al.*, 2017b). The MPG design has received some criticism for having large current limiting resistors. However, we show that the associated concerns are typically negligible in 4.6.5. The ammeter is unique to the MPG setup, and is either replaced by some other triggering mechanism as in (Ho and Jow, 2013; ASTM D 3755-14, 2014) or is omitted altogether with voltage drops serving as detection of breakdown as in (Kerwien*, et al.*, 2016; Ritamäki*, et al.*, 2017b).

4.6.3. Data Processing Software

Details of data processing and storage are detailed in Appendix C but are reviewed briefly here. Voltage, current, and time data generated by the LabVIEW control program are output in a text file. A custom Igor PRO macro uses these files to plot the data (see Fig. 4.7). The user can then identify breakdown (see Section 4.6.4) and other interesting test features, such as voltage ramp rate or pre-breakdown current traces. Data and experiment parameters from each test are entered into a sortable Excel matrix that includes many built-in calculations and error analysis (*e.g.*, breakdown electric field was calculated using the sample thickness and breakdown voltage).

Once series of tests of interest are completed with data entered into the results matrix, macro data analyses could be performed (*e.g.,* dual-defect model fits to a series of tests on a given material). These

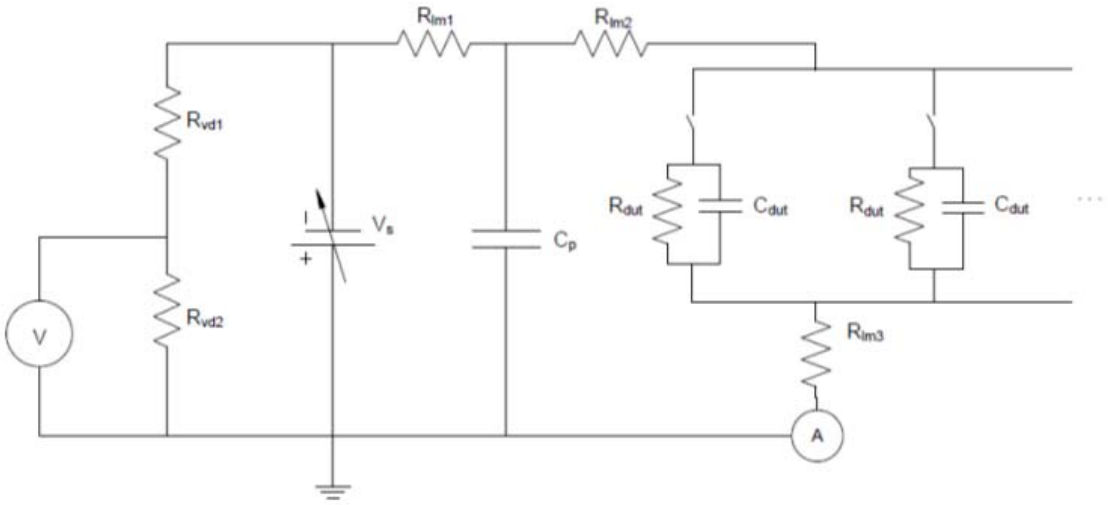

	R_{lm1}	R_{lm2}	R_{lm3}	R_{vd1}	R_{vd2}	C_p	C_{dut}	No. of C_{dut}
Ho 2013	N/A	NONE	NONE	N/A	N/A	NONE	N/A	Many
Kerwien 2016	3 MΩ	NONE	NONE	N/A	N/A	500 pF	N/A	Many
Ritamaki 2017	1 MΩ	10 kΩ	10 Ω	N/A	N/A	100 nF	N/A	Many
Rowland 1986	NONE	NONE	100 kΩ	N/A	N/A	47 µF	N/A	Many
USU MPG	100 MΩ	NONE	100 MΩ	600 MΩ	1 MΩ	NONE	250 pF	2

FIG. 4.6. Generalized breakdown circuit with corresponding available component values from several published test setups (Rowland*, et al.*, 1986; Ho and Jow, 2013; Kerwien*, et al.*, 2016; Ritamäki*, et al.*, 2017b).

analyses are described in detail in Chapter 5 but include statistical Weibull analyses, fitting to theoretical models, and analyses of DCPD.

4.6.4. Breakdown Criteria

This section discusses challenges associated with accurately identifying breakdown using this measurement technique and practical considerations for improving the interpretation of observed phenomena. I propose enhanced breakdown criteria that mitigates the difficulties that have been experienced with identifying breakdown and other features in difficult cases (Andersen and Dennison, 2017). Breakdown can be identified based on the average time rate of change of leakage current as opposed to simply a current threshold. Here dc breakdown tests are emphasized; however, the results may be easily adapted to ac breakdown testing.

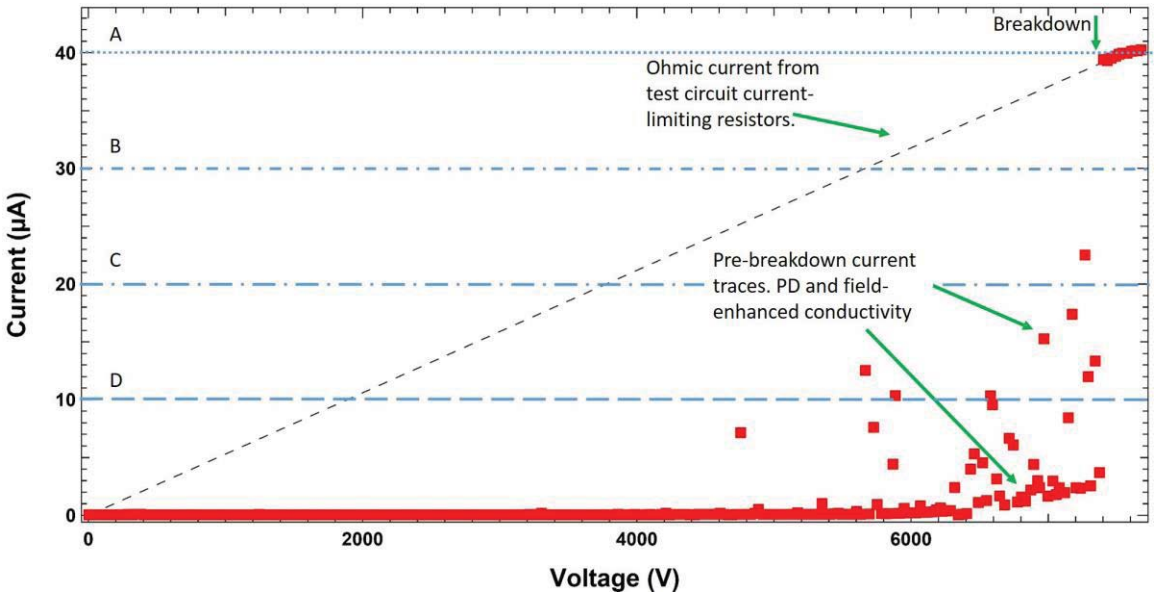

FIG. 4.7. Current traces from a prototypical voltage step-up test in baked polyimide (PI) under vacuum conditions tested at a ~5V/s ramp rate. At low voltages up to ~3 kV, no leakage current is observed. As voltage increases, pre-breakdown current traces are observed. In this test, a clear discontinuity in the observed current occurs at breakdown. Supposing a sensing threshold A (40 μA), the true breakdown voltage would have been missed. At B (30 μA), the true breakdown voltage would be observed for this test. At C and D (20 and 10 μA respectively), partial discharges would erroneously indicate a breakdown voltages below the true value.

To understand the currently accepted breakdown criteria and their limitations let us review a few selected statements from ASTM D3755-14 section 8 Criteria of Breakdown which is the *de facto* standard for dc breakdown tests recommended by NASA space environment effects mitigation guidelines (NASA HDBK-4002A, 2011; Garrett and Whittlesey, 2012; ASTM D 3755-14, 2014). The typographical error in 8.2 is from the original text and therefore has not been corrected.

> "8.1 Dielectric breakdown is generally accompanied by an increase in current in the test circuit that will activate a sensing element such as a circuit breaker, a fuse, or current-sensing circuit. If sensitivity of the element is well coordinated with the characteristics of the test equipment and the material under test, its operation will be a positive indication of breakdown.
>
> 8.2 Failure of a circuit breaker to operate is not be a positive criterion of the absence of breakdown. A breaker can fail to trip because it is set for too great a current or because of

> malfunction. On the other hand, if the tripping circuit is set for too low a current, currents due to leakage or partial discharge (corona) will cause it to trip before breakdown voltage is reached.
>
> 8.3 Observe the specimen during the test to ascertain that tripping of the breaker or current-sensing circuit is not caused by flashover…
>
> 8.4 Observation of actual rupture or decomposition is positive evidence of specimen breakdown. In test position, however, these physical evidences of breakdown are not always apparent. If breakdown is in question, it is common practice to repeat the test on the same specimen. Breakdown is confirmed when reapplication of test voltage results in a substantially lower breakdown voltage."

This breakdown criterion defines breakdown as a sudden increase in observed current above some threshold value implemented in analog hardware. The European standard for such tests has essentially the same requirements for identifying breakdown (IEC 60243-1, 2013; IEC 60243-2, 2013). As the true breakdown threshold is not easy to predict *a priori*, the ASTM standard cautions that a threshold set too low may be sensitive to sub-breakdown current such as PD. On the other hand, if the threshold is set too high, breakdown may occur without reaching the arbitrary current threshold. While post-breakdown observation of visual damage or repetition of the test on a particular sample can sometimes clarify a questionable or missed breakdown event, critical information about the breakdown voltage or time is often lost. Because voltage stress history can affect the breakdown potential (see 3.1.2), previous stress applied to an unbroken sample in an initial test attempt may invalidate subsequent test attempts (Andersen*, et al.*, 2015).

The MPG ESD system continuously monitors the leakage current during HVDC breakdown tests. Even following breakdown, observed currents in this system are generally well below 50 μA, precluding the use of even the smallest commonly available fuses rated down to ~2 mA (Brunson, 2010). The equivalent of a fuse in MPG experiments would be some threshold current value that, if reached, defines breakdown. This criterion alone is insufficient since, as shown in Fig. 4.7, observed pre-breakdown current can—at least temporarily—be a large fraction of the nominal breakdown current set by the current limiting resistors (R_{lm}) in the circuit, shown by a black dashed line. Observed pre-breakdown current traces include

PD and field-enhanced conductivity. Blue dashed lines in Fig. 4.7 show arbitrary current thresholds that would miss the breakdown voltage (A), a threshold that would correctly identify the breakdown voltage (B), and two thresholds (C and D) where PD would have tripped the current sensing element early.

Due to the continuous monitoring of leakage current, in most cases including Fig. 4.7, breakdown is easily visible as a transition from very low current or intermittent PD, to a large current set by the current-limiting resistors R_{lm}. This is especially true at slow voltage ramp rates. We typically recorded the breakdown voltage as the average of the two voltages on either side of this transition. This method of identifying breakdown was severely challenged in less common cases without a clear transition to a smooth ohmic slope, such as those shown in Fig. 4.8.

Figure 4.8 (a) shows two cases that lack a clear transition to breakdown. In both cases, a region of erratic current transients increase well below the expected breakdown. Although one trace has a transition to a smooth breakdown slope, both tests showed visible breakdown damage, confirming breakdown as per ASTM D3755-14 8.4. It is evident that in some cases the breakdown rupture leaves some residual resistance in the circuit with resistance on the same order as the current limiting resistors. Figure 4.8 (b) shows plots for faster ramp rate tests at 125 V/s, 300 V/s, and 500 V/s. At accelerated rates, it can be especially difficult to identify a transition to an ohmic slope, if the expected ohmic slope is even completely achieved. Faster ramp rates also suffer from a decrease in the accuracy of measured breakdown voltage and loss of information about pre-breakdown phenomena (Moser*, et al.*, 2017).

It is apparent that a single threshold current value—independent of applied voltage and other test conditions—is an insufficient breakdown criterion. Furthermore, it is clear that measurements of time- and voltage-dependent current are useful in establishing a more universal and accurate breakdown criterion. A useful criterion for dielectric breakdown must be distinguished from other behaviors, such as:

- PD (transient current spikes through the sample)
- Surface flashover (transient current trace like PD in the leakage current, but where the voltage drops such that the point lies on the R_{lm} ohmic curve indicating current flowing around the sample)

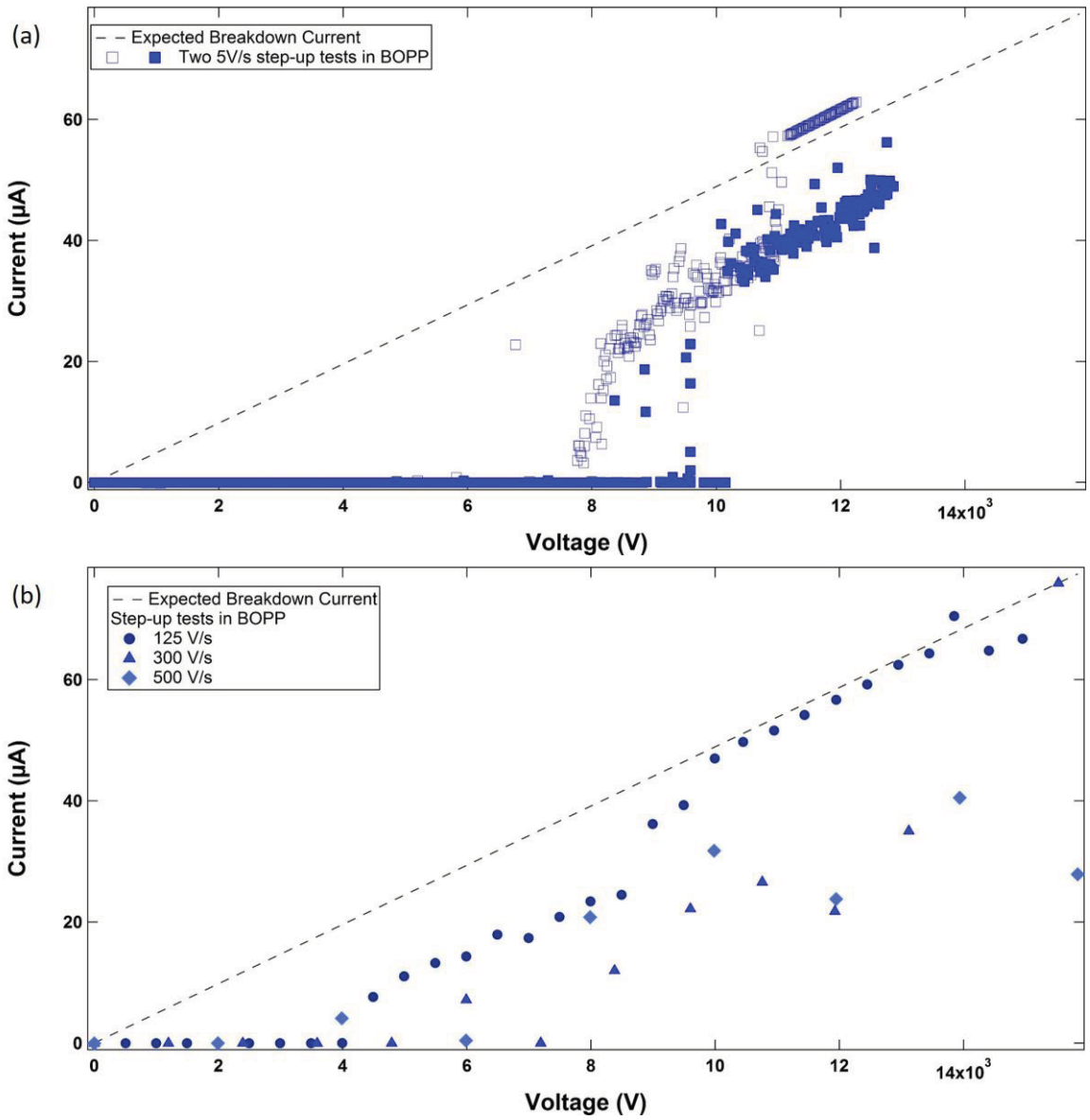

FIG. 4.8. Current traces from example voltage step-up tests in biaxially-oriented polypropylene (BOPP). Dashed lines correspond to Ohms law for the circuit's current limiting resistors. (a) Plot of two step-up tests with ~5 V/s ramp rate. In the test with the open markers, an area of erratic traces proceeds the smooth ohmic slope. The test with solid markers does not transition to a smooth slope. (b) Plot of three step up tests at ramp rates of 125 V/s, 300 V/s, and 500 V/s. In these cases, there is not a clear discontinuity from negligible current to current measurements increasing ohmically with applied voltage.

- Arcing on the external components of the chamber (marked by sudden drops in sustained breakdown currents)

- Field-enhanced conductivity (FEC) (smooth monotonically increasing measureable currents above the noise at higher fields, but not ohmic)
- Current of voltage meter errors that occasionally happen

These pre-breakdown phenomena are discussed in detail in the Section 4.6.5. A definition of breakdown based on rate of change of leakage current, rather than a simple threshold, automatically filters out transient non-breakdown phenomena. In practice, this requires continuous monitoring of leakage current rather than simply a breaker or fuse. For typical high-resistance dielectric thin film samples, minimum current sensitivity needed to observe all the above phenomena depends on electrode geometry and ammeter duty cycle. For the MPG-like setup, less than 100 nA sensitivity is required.

Breakdown is defined by the voltage (or field) at which an insulator no longer blocks significant current flow; therefore, even ohmic-like traces below the expected smooth R_{lm} ohmic behavior must be considered breakdowns. NASA spacecraft charging mitigation guidelines state that insulators are considered at low risk of charging anomalies if bulk resistivity is on the order of 10^{12} Ω·cm or less (NASA HDBK-4002A, 2011). Such materials should have enough conductivity to bleed away charge fast enough to make breakdown very unlikely. Given typical relative permittivity of order 3, our electrode area of 1.98 cm^2 and a typical sample thickness of about 25 μm, this threshold resistivity is equivalent to a sample resistance of ~10^9 Ω compared to the MPG system's R_{lm} ~$2 \cdot 10^6$ Ω (Andersen*, et al.*, 2015). Thus, such nominally safe materials would have slopes on the order of ~10% of the R_{lm} ohmic breakdown curve. This is effectively a voltage-dependent current threshold, where transient currents exceeding this threshold are not considered breakdown.

Based on the considerations outline above, I propose the following improved operational definition of the electrostatic breakdown voltage for step-up tests:

Breakdown voltage can be defined as the average voltage between the last applied voltage with current below 10% of the R_{lm} expected ohmic breakdown curve and the first voltage with current increasing (though not necessarily smoothly) between 10% and 110% of the R_{lm} ohmic breakdown curve.

In some test configurations, such as static voltage endurance time (SVET) tests, current versus time (rather than voltage) or some other variable may be of interest. For SVET tests, current transitions from a baseline to a constant value at breakdown. Any intermediate behavior is likely to happen over such small time increments compared to the SVET wait time that they may be absorbed into the uncertainty without much consequence. There is the possibility of one or more points dropping back below the 10% curve due to external arcing after an apparent breakdown. This happens infrequent and is generally an obvious deviation from a breakdown slope.

Since PD and flashover generally return to the baseline current, they will not qualify as breakdown using this definition. Increases in current significantly steeper than the R_{lm} ohmic curve do not make sense in terms of Ohm's law for our circuit $\left(I \leq \frac{V}{R_{lm}}\right)$. These increases are likely due to the ammeter response to increasingly rapid DCPD—so rapid that return to baseline current may not be observed (see Fig. 4.9 (a)). Most FEC—which is relatively infrequent in MPG tests—will be well below the 10% curve; further, FEC by definition increases supra-linearly with voltage and can therefore be distinguished from breakdown.

Figure 4.9 revisits the same example tests from Fig. 4.8. Regions of current increasing linearly with voltage above the minimum breakdown current (red dashed line) are identified with orange lines. In Fig. 4.9 (a) a grey line indicates a slope corresponding to a resistance much less than R_{lm}. Purple dashed lines connect the last sub-breakdown point to the first point of a breakdown region. The average voltage of these two points—the last measurement of a sample not yet broken down and the first measurement corresponding to a broken down sample—is identified as the breakdown voltage. The voltage difference between these two points contributes to the measurement uncertainty but is often small; especially for slow voltage ramp rates (see Appendix B). Secondary or even tertiary breakdowns can be observed after incomplete breakdowns; however, the initial breakdown is the primary failure. Using this criterion for data with an obvious transition to breakdown, as in Fig. 4.7, does not change the value of the breakdown voltage.

We propose that dielectric breakdown voltage be defined more precisely as the average voltage between the last voltage with current below 10% of the R_{lm} expected ohmic breakdown curve and the first voltage with current increasing between 10% and 110% of the R_{lm} ohmic breakdown curve. This definition

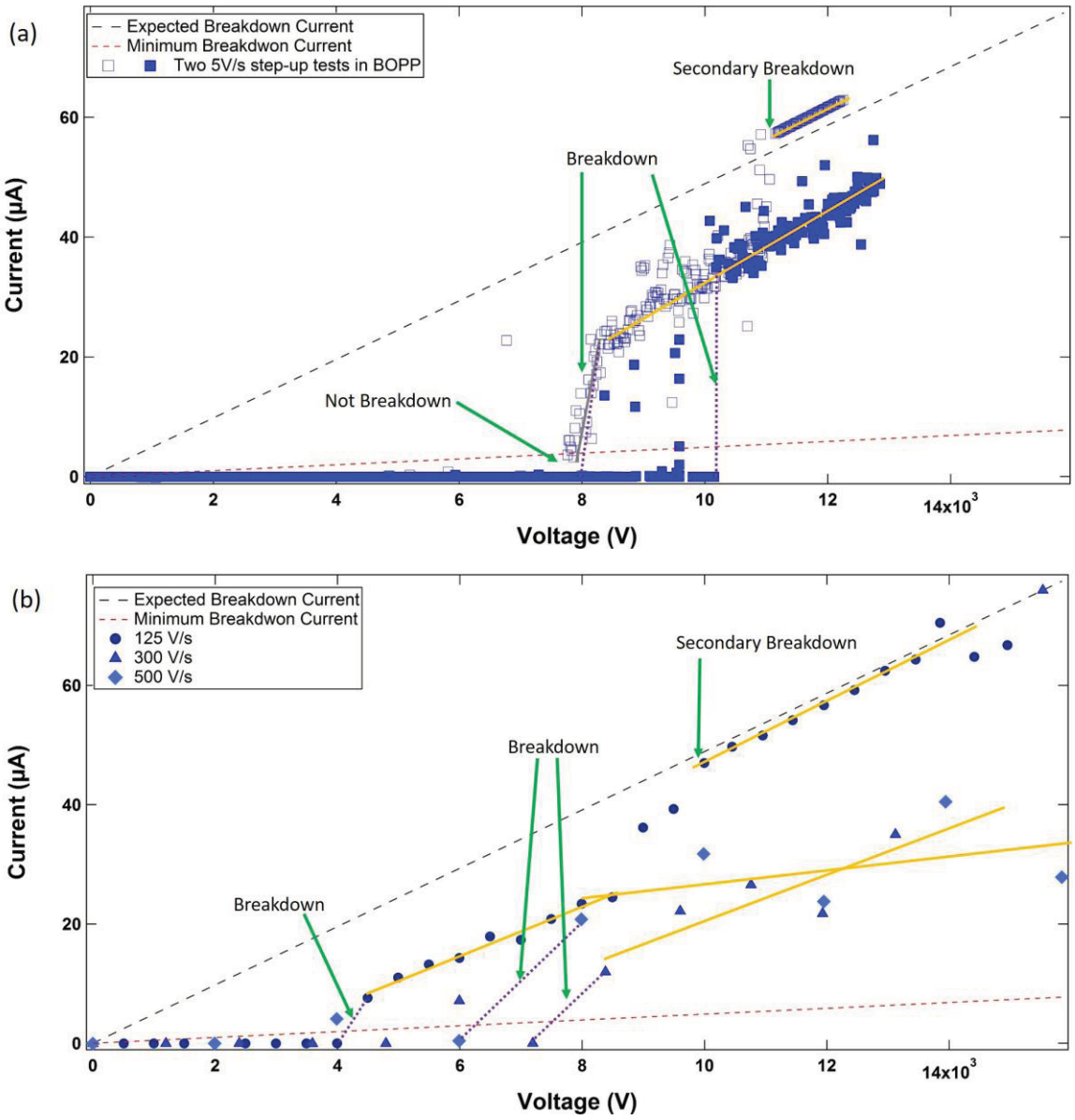

FIG. 4.9. Data from the same tests in Fig. 4.8 with breakdowns identified using proposed criteria. Orange lines are linear fits to breakdown current regions. Purple dotted lines connect the last baseline current datum with the first point corresponding to a measurement of breakdown. The breakdown voltage is the average of these two points with its uncertainty dominated by the spread of these two points. In (a) the grey line has slope corresponding to a resistance much less than the current limiting resistors and therefore cannot be identified as breakdown. Secondary breakdowns to the R_{lm} slope are shown in two cases; however, they are not reported as the primary breakdown.

requires continuous, or at least intermittent, monitoring of low-level leakage currents; it is, however, far less sensitive to false negatives or false positives that may arise from using a breakdown current threshold

criterion as outlined in ASTM Standard D3755. The identification of breakdown in fast voltage ramp-rate tests is also improved.

4.6.5. Observable Phenomena

Having established what constitutes breakdown the various features seen in ESD experiments can more easily be identified. In the previous section, many of these features were anomalies that obscured the identification of breakdown. In this section, they are identified as interesting experimental results thereby undergoing an "anomalous → obvious" transition (Zallen, 1983). Figure 4.10 indicates features observed in typical step-up test I-V curves (labeled **A** through **E**) including those seen frequently only in test systems that measure lower currents and use slower voltage ramp rates. These additional features are often accentuated in log current versus applied voltage curves, such as Fig. 4.10 (b).

As described above, complete dielectric breakdown in the MPG ESD system is indicated by a transition from negligible currents to:

A. *Post-breakdown ohmic current* with slope determined by the current limiting resistors R_{lm} in the test circuit. See Fig. 4.10 (a) and (b).

Typical step-up tests in the USU system for insulating materials with $>10^{16}$ Ω-cm are expected to have steady leakage currents of $<10^{-8}$ A as applied voltages are increased until breakdown, with linearly increasing ohmic currents of $>10^{-5}$ A determined by two 100 MΩ current limiting resistors R_{lm} in series with the sample. For ~90% of highly insulating materials tested, the leakage current below breakdown is below the sensitivity of the ammeter, as seen in Fig. 4.11 (a). Such leakage currents are routinely observed for these materials in high sensitivity constant voltage conductivity test systems (Brunson, 2010; Dekany*, et al.*, 2013; Kiethley Instruments, 2016).

Two related features, which exhibit monotonically increasing current with increasing voltage, well above current sensitivity, are observed in some materials.

B. *Dielectric breakdown with significant residual resistance*. This current steadily increases in an ohmic fashion, but with more resistance than the ESD circuit with no sample present. See Fig. 4.10 (b); also see (Dennison*, et al.*, 2016b). This is interpreted as a partial breakdown of the material, perhaps through only a fraction of the sample

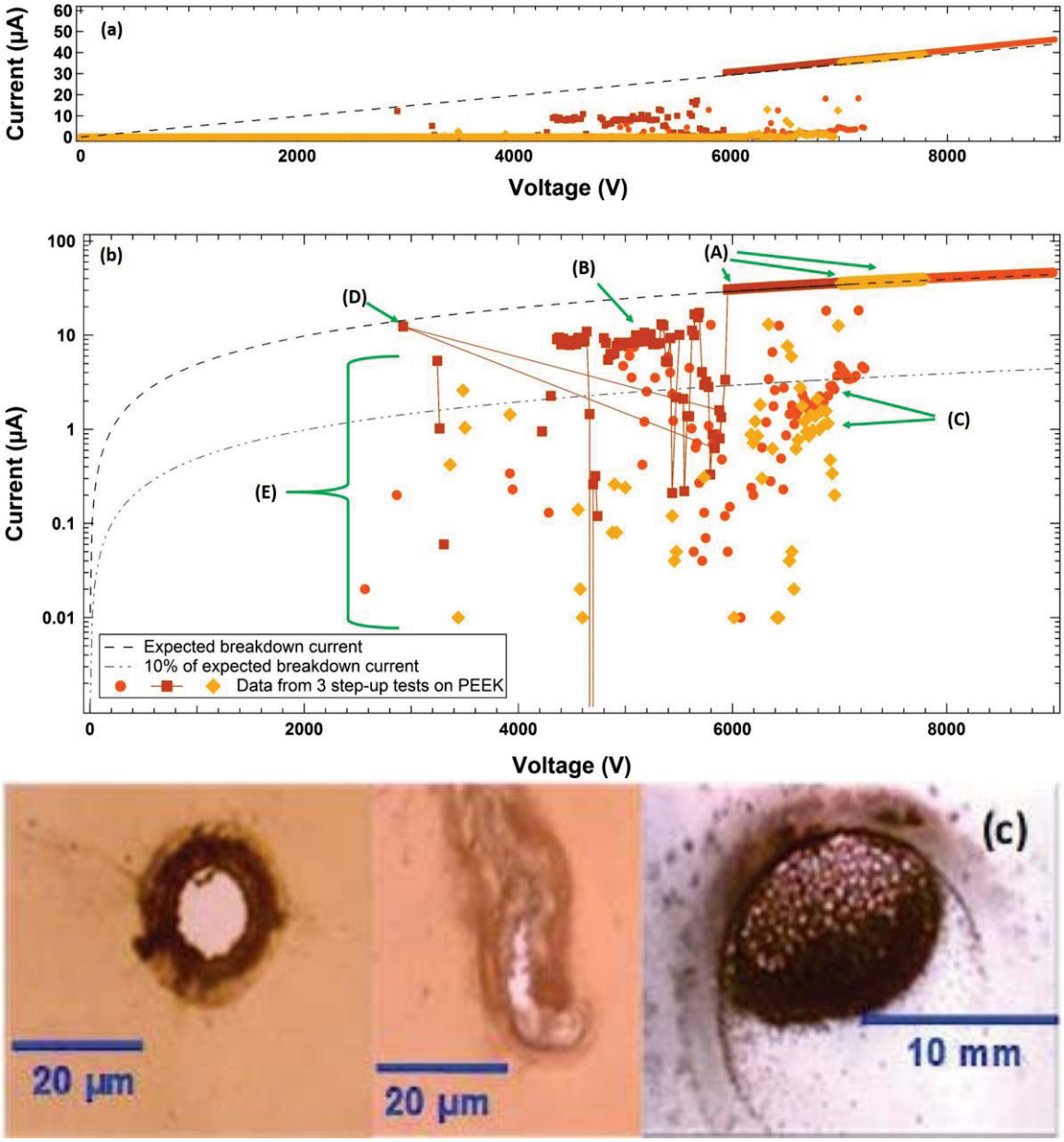

FIG. 4.10. Observed Phenomena. Examples of current traces from three voltage step-up tests on PEEK films together with the expected breakdown current (dashed lines) and 10% of the breakdown current (dot-dashed lines) are shown or reference. (a) Linear I-V plot. (b) Semi-logarithmic IV plot. Plot features are indicated as: (A) Dielectric breakdown marked by transition to a linear ohmic slope corresponding to the circuit's current limiting resistors; (B) Dielectric breakdown with some residual resistance; (C) Field-enhanced conductivity; (D) Surface flashover; and (E) DCPD. (c) Images of post-test breakdown damage sites: the thermoset polymer Kapton E (left) usually breaks down with circular holes, while the thermal plastic LDPE (center) is more irregular. Expanded PTFE (right) can breakdown rather spectacularly due to large amounts of charge stored in the high density of mechanical voids in the material. Note the much larger length scale for the expanded PTFE damage site.

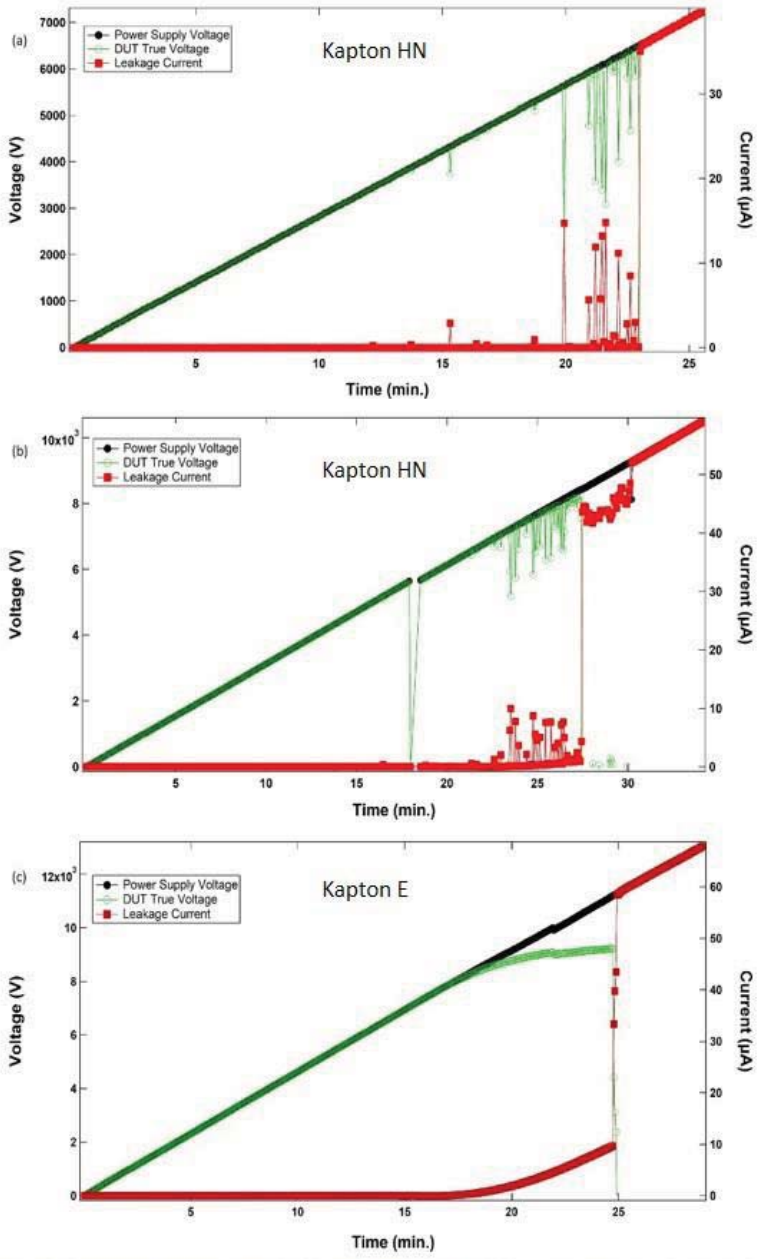

FIG. 4.11. Comparisons of total applied voltage, sample voltage, and leakage current. The device under test (DUT) voltage was calculated using Eq. 4.3. Transient current spikes and voltage drops correspond to PD. (a) Test on Kapton HN with no measureable field-enhanced conductivity. Most tests in materials tested do not exhibit field-enhanced conductivity that we can measure. (b) Kapton HN test with measurable field-enhanced conductivity (FEC) corresponding to only a 2% correction in DUT voltage at V_{ESD}. Most observations of FEC in our setup have similarly negligible effects on the applied voltage. (c) An extreme example of field-enhanced conductivity in a Kapton E test. This material had a greater tendency to exhibit measurable field-enhanced conductivity than other tested materials. While the correct breakdown voltage is still clearly identifiable via Eq. 4.3 (in this case the correction would be ~20%), this would not be considered a successful test.

thickness. Even in cases when there is no transition to *Post-breakdown ohmic current*, after the test there is visible evidence of breakdown on the sample surface, indistinguishable from the damage observed for full breakdowns. Examples of breakdown damage are in Fig. 4.10 (c).

Note that the voltage drop across the sample decreases significantly when this happens. Device under test (DUT) voltage can be obtained using Ohm's law for a series circuit

$$V_{sample} = V - IR_{lm} \tag{4.3}$$

This correction for post-breakdown currents clearly has no effect on the breakdown voltage.

C. *Field-enhanced conductivity* (FEC). Consecutive current measurements increase super-linearly with voltage, at higher voltages near breakdown. See Fig. 4.10 (b). This is attributed to field-enhanced dark current conductivity. Such currents seldom exceed a few percent of the expected breakdown (in ~15% of tests) current and only very rarely exceed 10% of that current (almost exclusively in more conductive materials such as Kapton E) (Wintle, 1983). While FEC is not the target measurement of this system, measurements of currents up to a few μA are consistent with current densities of 10^{-4} to 10^{-2} A/m^2 attributed to FEC (~0.02-2 μA for our electrode area) as reported in the literature (Li*, et al.*, 2015). Equation 4.3 is needed to calculate the voltage drop across the test sample when this occurs. Fortunately, this correction is usually not needed, or is only on the order of only a few percent (Fig. 4.11 (a) and (b), respectively). On the rare occurrence of FEC causing a significant voltage drop across the sample, the test may be invalidated since voltage ramp-up has been arrested (Fig. 4.11 (c)). The voltage drop on the DUT could be mitigated with the use of smaller current limiting resistors, which will be implemented in a planned upgrade to the MPG test system. Experiments with current limiting resistors ranging an order of magnitude smaller to an order of magnitude larger did not show any effect in breakdown voltage or DCPD behavior with the exception that the apparent

DCPD magnitude transitioned from being dominated by the ammeter duty cycle to the being dominated by the limited current.

On rare occasions, breakdowns and transitions to ohmic behavior are observed at very low voltages for a specific sample of a material. See Fig. 5.2 (b) in the Chapter 5. These features are attributed to sample imperfections or damage to the sample surface. Often there is clear evidence in images of the specific sample either before or after the breakdown test showing these sample defects.

Further, most low-ramp-rate step-up tests performed with the MPG system exhibit additional transient current features in breakdown I-V curves, most often with only a single sequential current measurement above the leakage current or current sensitivity level. One such feature is:

D. *Surface Flashover*. Occasionally, a sudden (often-large) voltage drop is measured together with current corresponding to the ohmic current at this reduced voltage. Such surface discharge traces are found to be very infrequent at low pressures $<10^{-3}$ Pa where MPG measurements are typically made, and to increase in frequency more than an order of magnitude as pressure is increased to $\sim10^{0}$ Pa where Paschen discharge is more likely to occur. See Fig. 4.10 (b) and Fig. 4.12 (a). This is interpreted as a brief surface flashover, where current temporarily bypasses the shorted test sample in the circuit.

   On several occasions at which surface flashover features were observed in the I-V curves, there were features observed on the surface indicating arcing at the edges of the samples. Tests at elevated pressure—well beyond typical MPG operating conditions—reveal increased instances of surface flashover in addition to traces that seem to indicate discharges to areas of the chamber not possible in normal pressure ranges. At pressures of only a few torr, breakdown is not observed at all due to Frank-Hertz effect as shown in Fig. 4.12 (b) (Franck and Hertz, 1914). Fig. 4.12 (c) is an example of unusually severe visible damage associated with surface flashover.

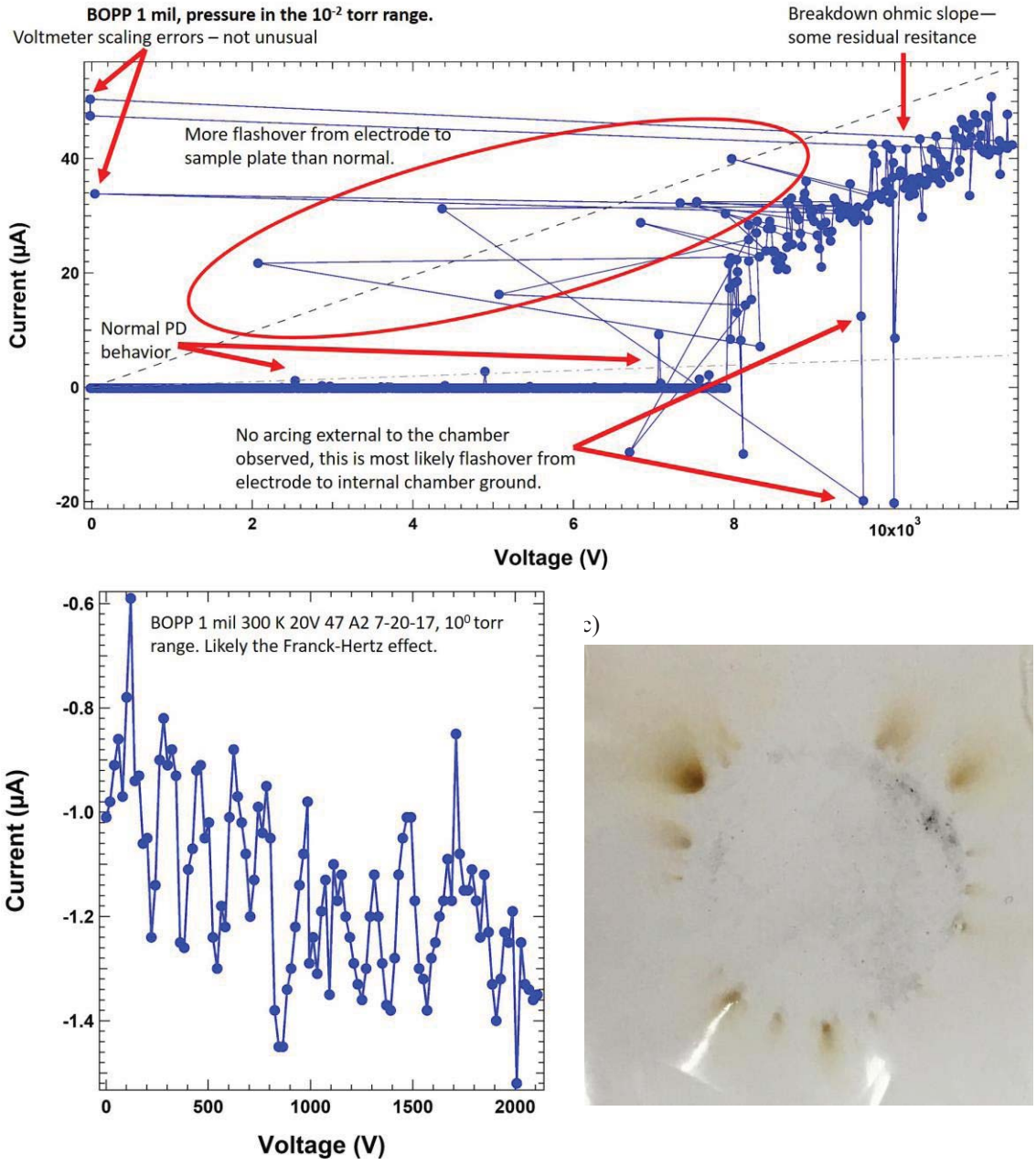

FIG. 4.12. Evidence of surface flashover. (a) Current traces from a test of BOPP with standard test parameters excepting elevated chamber pressure. Typical tests are in the the $\lesssim 10^{-5}$ torr range. This test at $\sim 10^{-2}$ torr shows a much more frequent surface flashover than typical tests, but no atypical DCPD behavior. (b) Test on BOPP with pressure in 10^{0} torr range. Not typical behavior observed but the oscillating negative current is consistent with the Frank-Hertz effect. (c) Damage done by unusually severe surface flashover on LDPE. Notice the outline of the electrode area is clearly visible as is charring extending radially away from the electrode area toward the exposed areas of the aluminum sample mounting.

On very infrequent occasions, very large transient currents are observed, well above the ohmic breakdown curve (see for example, Fig. 4 in (Moser*, et al.*, 2017)). These are attributed to instrumentation malfunctions, such as erroneous readings by the current or voltmeters or the data acquisition card.

By far the most frequent transient current features are those we classify as dc partial discharge (DCPD), labeled **E** in Fig. 4.10 (b). We have previously referred to these DCPD traces as pre-breakdown arcing (Andersen and Dennison, 2014; Andersen and Dennison, 2015b). HVAC partial discharge testing is not performed in the MPG laboratory, which is not yet equipped with an off-the-shelf standard PD monitor typically used for most HVAC and HVDC partial discharge tests performed in other labs (Morshuis and Smit, 2005). Nevertheless, we can clearly distinguish DCPD from other transient features discussed above. No visible damage to the sample has been observed in tests with DCPD terminated prior to breakdown. On average, more than 10 DCPD traces of varying amplitude are observed in a single step-up run. Although these DCPD features can be observed in successive current measurements (particularly at voltage approaching the breakdown voltage), they generally are distinct, single measurements of current that return to the background or field-enhanced conductivity levels for subsequent current measurements. The onset and frequency of these DCPD vary significantly from material to material of the same sample geometry indicating that they most likely depend on the sample material rather than being an artifact of the test apparatus. The easy identification of surface discharges (see D above) adds credence to the notion that DCPD traces must be a bulk phenomenon.

DCPD measured with slow ammeters are more frequent and of higher current amplitude at higher applied fields. Observed DCPD transient current features ranged over two orders of magnitude in current below the breakdown current. This is discussed further in 574.7.

Note that there is a significant the body of published work on DCPD has been done in the context of DCPD in gaseous voids in polymers or at polymer-polymer or polymer-conductor interfaces. In many cases, the test sample thicknesses are on the order of ~10^{-3} m with voids ranging from ~10^{-3} m to ~10^{-4} m (Kazuo, 1978; 1980; Fromm, 1995; Corr*, et al.*, 2016; Imburgia*, et al.*, 2016). Such void dimensions are greater than our sample thickness (~25 μm). The DCPD reported in this dissertation in bulk dielectric thin films are significantly different from such studies on gaseous voids. Studies with gas-filed voids are

conducted near atmospheric pressure. This leads to gas discharge across the voids. Our samples have no such large voids. There may be surface irregularities in the sample and clamped electrodes trapping gas or internal voids in the polymers with dimensions as large as ~10^{-7} m to ~10^{-6} m although we have no direct evidence of their existence or nature. There are also undoubtedly small voids within the bulk polymers, such as gaps between disordered polymer chains on the order of ~10^{-8} m to ~10^{-9} m. Further, our experiments are conducted in ≤ 10^{-3} Pa vacuum so gas filled voids are unlikely. The difference mean that mechanisms for gas discharge across large voids is not necessarily an expected mechanism this study.

4.6.6. Post-Breakdown Cataloging

After samples have been tested, the sample thickness is measured using a computer-interfaced digital micrometer (Mitutoyo IP65 ±1 μm) and optical microscope images are taken of the breakdown sites (see Table A.1). The used samples are then labeled with relevant test and materials parameters and stored in plastic containers in case they are needed again for further analysis. This has been especially useful if any details of an experiment have been called into question. For more details on post-breakdown characterization and storage, see Appendix A and (Hansen, 2014).

4.7. High Temporal Resolution Measurements of Pre-Breakdown Events

As described above, many PD are observed prior to complete dielectric breakdown. To investigate these DCPD with greater time resolution, two additional methods have been employed. First, the test setup was modified to include a 100 MHz oscilloscope (Tektronix TBS 2000 Series) measuring voltage across a 10 kΩ shunt resistor in series with the ESD circuit placed between the ~200 MΩ current limiting resistors and ammeter. Current was monitored as usual at ~2 Hz with the Amprobe® ammeter and at ~10 kHz with the oscilloscope, and the data from both instruments were correlated in time. An example of these measurements is shown in Fig. 4.13 (a). These measurements were not affected by removing the ammeter from the circuit. The decay time for each DCPD is limited by the RC time constant of the measurement circuit (approximately 40 ms). The maximum current is limited by the current limiting resistors and therefore the DCPD amplitude grows with increasing voltage; however, this change is small compared to the differences in DCPD amplitude observed by the ammeter. One of the difficulties of this technique was

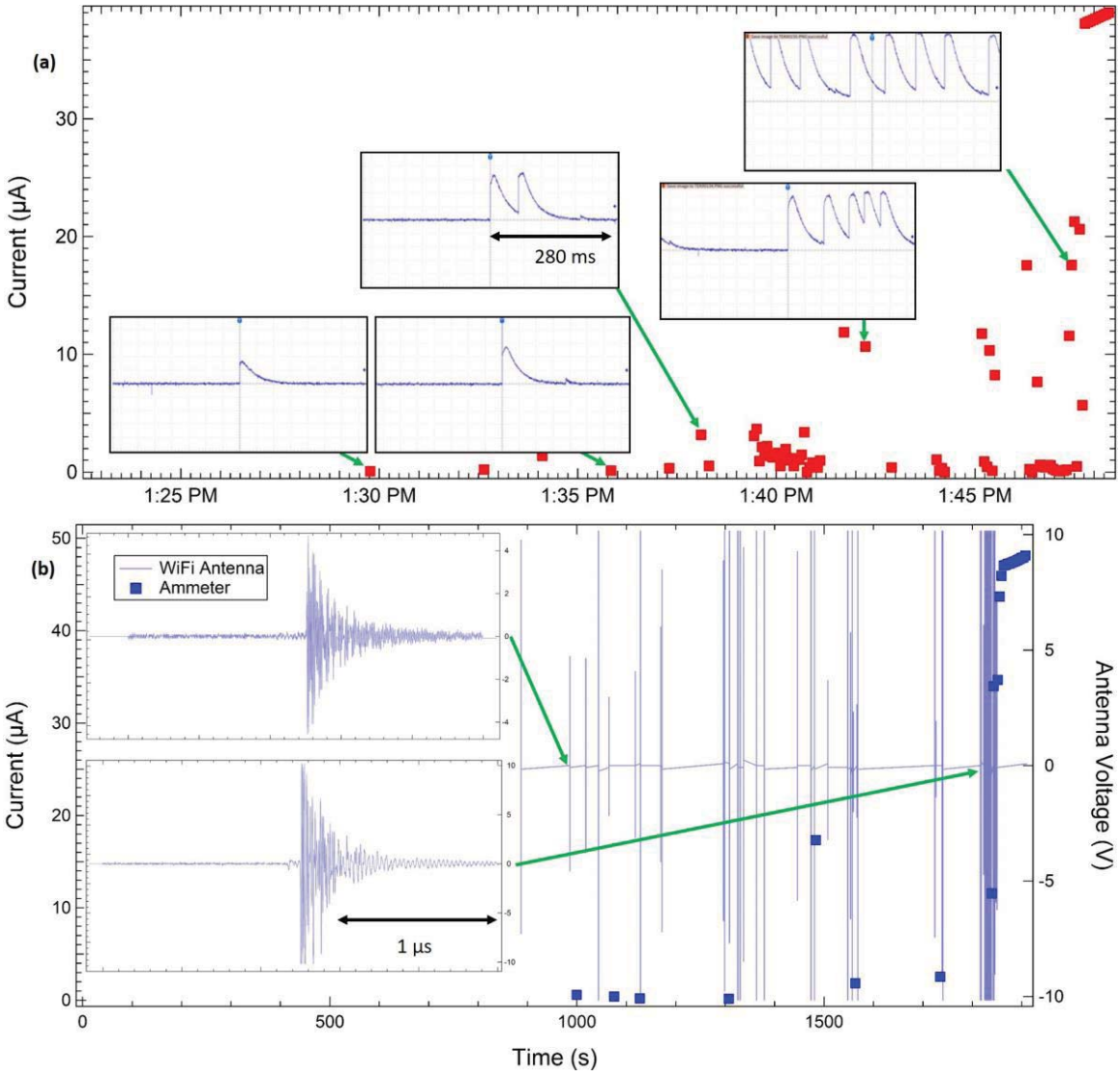

FIG. 4.13. Supplementary measurements of DCPD in voltage step-up tests. (a) DCPD events from a step-up to breakdown test in PI. In-line shunt resistor oscilloscope traces of DCPD were correlated to DCPD as seen by the standard ammeter; five of these are shown here. Large amplitude ammeter events correspond to many DCPD of similar amplitude as seen by the oscilloscope. (b) DCPD measured during a voltage step-up test on BOPP by a 2.4 GHz WiFi antenna connected to a 50 Ω load oscilloscope shunt, together with the standard ammeter curve. The inset shows two examples of individual trigger events. As in (a), larger amplitude ammeter traces correspond to multiple DCPD as seen by the antenna.

the correlation of events seen in the oscilloscope on the order of tens of ms with those seen by the LabVIEW control program which takes one datum every 4s. The duty cycle of the ammeter also meant that sometimes, fast PD would not be recorded by the ammeter. To further exacerbate the problem, the LabVIEW program only recorded time from the beginning of the experiment rather than local time like the

oscilloscope. Cell phone video of both screens running simultaneously allowed for correlation of events seen in both instruments to be made. The setup could surly be improved; however, only a few step-up tests were needed to observe many PD.

The second DCPD supplementary detection technique used was the common RF antenna PD detection method, shown in Fig. 4.13 (b) (Tang*, et al.*, 2006; El-Hag*, et al.*, 2013; Liu*, et al.*, 2015). The short time scales of individual DCPD result in a broad frequency-space signal, and detection antennas cited in the literature observe frequencies from 1 MHz to 5 GHz (Tang*, et al.*, 2006; El-Hag*, et al.*, 2013; Liu*, et al.*, 2015). HVAC partial discharge testing is not performed in our laboratory, which is not yet equipped with an off-the-shelf PD monitor typically used for most HVAC and HVDC partial discharge tests performed in other labs (Morshuis and Smit, 2005). However, ubiquitous 2.4 GHz WiFi antennas fall within the range of typically used DCPD detection antennas. A 2.4 GHz WiFi antenna, placed adjacent to a vacuum chamber glass window, was connected to a 50 Ω load and monitored using an oscilloscope (Tektronix TDS 2014) and custom LabVIEW data acquisition software. While this adaptation of standard PD detection method serves as an independent detection of DCPD in the MPG ESD system and shows that they are much faster than the ESD circuit RC time constant, spectral information and improved timing would require a broad-band antenna and efforts to reduce ringing in the circuit (Chen*, et al.*, 2017).

These experiments confirm our detection of DCPD and show that high-amplitude DCPD, as seen by the ammeter, can represent the current integrated over many DCPD of roughly the same magnitude. This assumption is critical for the analysis discussed in 5.5 and 6.2.5.

CHAPTER 5

ANALYSIS OF ESD AND PD TESTS

"There is terror in numbers" (Huff, 2010). Relating breakdown data to theoretical or even empirical models can be a nontrivial task. Evaluating mathematical theory using experimental data inevitably requires the use of statistical methods. Perhaps the principal numerical terror for the author is unintentionally falling into the following trap—that "if you can't prove what you want to prove, demonstrate something else and pretend that they are the same things. In the daze that follows the collision of statistics with the human mind, hardly anybody will notice the difference" (Huff, 2010). To mitigate such statistical peril, a good scientific theory must make falsifiable predictions (Popper, 1963). The analysis methods presented in this chapter demonstrate how the theoretical models from Chapters 2 and 3 as well as commonly used empirical models of breakdown can be evaluated using data from experiments outlined in Chapter 4. While Chapter 4 explained important details of how individual tests were performed, this chapter discusses the methods used for analyzing and making sense of data from ensembles of tests. The following sections in this chapter describe tools capable of gauging how well theoretical predictions of dielectric breakdown match observations or if they are any good at all. Test data shown in this chapter is primarily for explaining the analysis methods used. For Sections 5.2 through 5.4 the data are from 60 step-up to breakdown tests at room temperature performed on samples of biaxially-oriented polypropylene (BOPP). Results and conclusions of these analyses for four prototypical polymers are presented in Chapter 6 and Chapter 7 respectively.

5.1. Sortable Data Matrix

The most important tool in analyzing ESD data is the ESD Quality Summary Table Excel matrix. This Excel database is the foundation of all MPG ESD analyses. It is the repository of all MPG ESD data and corresponding sample information. Each test results is an entry containing sample information, test parameters, test results, and built in calculations of derived quantities. Adapted from a MPG Excel worksheet for electron-beam measurement data, the ESD Quality Summary Table sorting capabilities allows for the comparison of any test parameters or results of interest. For example, the breakdown fields

for room temperature tests in ascending order from a certain period of time in a given material is easily available for exporting into other programs such as Igor Pro. Any tests with questionable results, perhaps due to operator error, have been highlighted so that they can easily be filtered out. While some entries are specific to individual test types, the following are a few of the primary categories: sample material, sample thickness, test temperature, ramp rate, sample location, bakeout date, test date, chamber pressure, test type, breakdown voltage, breakdown electric field, time to breakdown, etc. Some of these, such as breakdown voltage are calculated quantities. For example, the breakdown voltage is the average of the last voltage before breakdown and the first voltage where breakdown has occurred. Likewise, the breakdown electric field is the quotient of the breakdown voltage and sample thickness.

Derived quantities and their uncertainties are calculated and tabulated automatically. The uncertainty analysis is outlined in Appendix B. Further details on the data and calculations in the ESD Quality Summary Table are provided in Appendix C. At the time of writing, this matrix contains information from nearly 1000 tests performed by various MPG students over the last ten years. Sadly, much of the earliest MPG data has been lost due to poor data management. Although I created this matrix and performed many of the tests therein, it contains results from the efforts of many of my predecessors and is now maintained by students that I have helped train. Whenever major changes or additions are made, new versions are created and old ones are saved as backups lest some mistake corrupt the data or calculations. The analysis in the following sections of this chapter begin with selecting relevant quantities from the ESD Quality Summary Table.

5.2. The Empirical Cumulative Distribution of Events

The results of repeated observations of some event can be represented explicitly by the empirical cumulative distribution (ECD). The ECD estimates the probability of occurrence P of an event as a function of a variable (for now let us assume the electric field F but the same principle applies to many other quantities, *e.g.*, time) based on j data points x_i as (Van der Vaart, 1998)

$$P(F) = \frac{1}{j}\sum_{i=1}^{j} \mathbf{1}\{x_i \leq F\} \text{ where } \{x_i \leq F\} = \begin{cases} 1 & \text{if } x_i \leq F \\ 0 & \text{otherwise} \end{cases}. \quad 5.1$$

Figure 5.1 is an example of an ECD plot It is apparent that Eq. 5.1 is only a valid approximation of the true underlying cumulative probability distribution for large j. Thus, we can empirically estimate the probability of breakdown (or PD) directly from the data given enough tests. The ECD can then be compared to empirical or physical models of the cumulative distribution functions (CDF) of breakdowns. In statistics, often the probability density function (PDF) is used to represent the distribution of an observable. The PDF is simply the derivative of the CDF. For example, the normal distribution is the PDF derivative of the error function—a CDF. For the analysis in this dissertation, it is more convenient to use the CDF. A useful feature of CDFs is that they always range in value from zero to unity as a function of some variable of interest. In other words $P(F)$ is probability distribution such that $0 \leq P(F) \leq 1$.

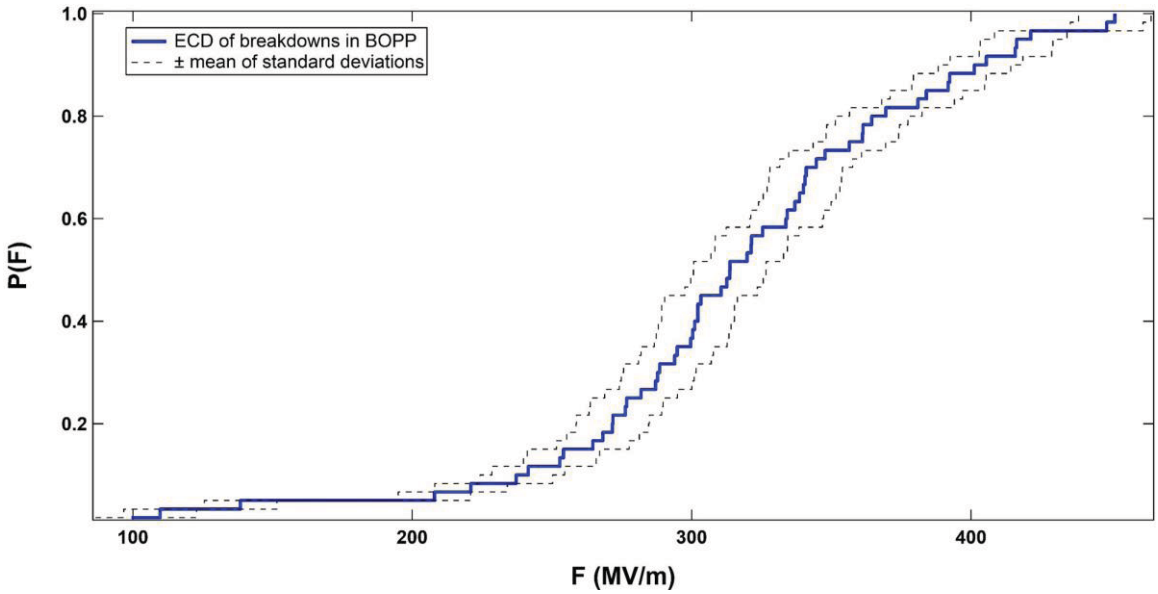

FIG. 5.1. Empirical Cumulative Distribution (ECD) of 60 breakdowns in BOPP. Dashed lines are the same ECD shifted left and right by the average of the uncertainties in the measurements.

Plots of the ECD preclude the use of standard error bars (see further details in Appendix B). Equation 5.1 relies on counting how many events happened below some value of the variable in question. Uncertainties, especially overlapping uncertainties, frustrate any attempts at standard error propagation. However, we estimate the uncertainty in the ECD as the average of the standard deviations of the data. This

is clearly an overestimation of the uncertainty; however, it demonstrates that the ECD is well defined. Fig. 5.1 is an example of an ECD from 60 breakdown tests in BOPP with dashed lines representing our estimate of uncertainty in the ECD.

5.3. Empirical Models of Breakdown

This section reviews the canonical empirical models that are typically used to characterize measurements of dielectric breakdown. These models are various Weibull functions (Dissado and Fothergill, 1992). In many cases of random uncertainties it is assumed that measurements should be normally distributed (Taylor, 1997). At first pass, the uninitiated might suggest reporting the average and standard deviation of breakdown voltages. However; Gaussian statistics are not applicable to failure statistics that need to account for the removal for samples from the test population once they have broken down (Dissado and Fothergill, 1992). The breakdown strength of a dielectric material is often listed in tables as a constant value, occasionally with a note that the value listed corresponds to a certain temperature or thickness (Andersen*, et al.*, 2017). This convenient representation can belie the stochastic nature of breakdown and that, even under ideal conditions, repeated tests result in a distribution of breakdowns with applied electric field.

While fits with empirical models generally lack much, if any, physical insights into a material, they are useful in that they are mathematically simple compared to physics-based models. This facilitates the comparison of different materials, but extrapolation can be risky since it is unclear what physical mechanisms may need to be assumed for the observed behavior to continue into unmeasured territory. Weibull functions are frequently used to describe the probability of dielectric failure due to increasing stress factors. In this study, it models the increasing probability of failure due to ESD with increasing applied field. As with other probability distributions, such as Gaussians, Weibull distributions are characterized by a centroid and a width parameter.

In this section we discuss how the empirical ECD of breakdown data is fit to two-, three-, and five-parameter Weibull functions, using methods similar to prior studies (Dissado and Fothergill, 1992; Chauvet and Laurent, 1993; Rytöluoto*, et al.*, 2015). Further step-by-step details of fitting Weibull functions to data can be found Appendix D. Most Weibull analysis in the literature is done using black box

software packages, such as Weibull++ (Rytöluoto*, et al.*, 2014; Boggs, 2017a). Discussions with several presenters at the Conference on Electrical Insulation and Dielectric Phenomena (CEIDP) where Weibull plots of breakdown tests are a common sight revealed that many researchers rely on software packages without a detailed understanding of how they work. The analysis below was developed independently based on available published literature. A free trial version of Weibull++ was obtained and the resulting calculations agreed with the tools I have developed (more details can be found in Appendix B). Weibull confidence intervals can be made using various methods that are also discussed in Appendix B. Such confidence intervals are purely statistical constructs that do not directly reflect the measured instrumentation uncertainty as much as quantify the stochastic distribution of the measurements. For this reason, we have elected not to use them in this study; opting instead for reporting the uncertainty in the fitting parameters together with the mean measurement uncertainty in each case.

5.3.1. Two-Parameter Weibull Model

The simplest Weibull function of field F has only two parameters F_0 the field corresponding to a 63.2% probability of breakdown, and a width parameter β:

$$P(F) = 1 - \exp\left(-\left[\frac{F}{F_0}\right]^{\beta}\right). \tag{5.2}$$

The width parameter β is at some level related the width of the spatial end energetic distributions of the trap states. In the Crine and dual-defect models, which assume delta function distributions in energy, β must be driven by the width of the spatial distribution of defects, that is the width of the distribution of a_{def}. It is straightforward to linearize this function with the transformation (Chauvet and Laurent, 1993)

$$x = \log(F) \text{ and } y = \log\left[\ln\left(\frac{1}{1-P}\right)\right]. \tag{5.3}$$

One then transforms the ECD of a data set in the same way, and, by fitting it to a line, the Weibull parameters can be extracted. Upon linearization, it often appears that the first few low-probability events at low fields do not follow the same trend as the rest of the data. This could be the result of extrinsic imperfections in some samples or tests (*e.g.*, sample damage or impurities or contamination) resulting in a breakdown at an unusually low field not representative of the material itself. Linear fits in the transformed coordinates (at least in Igor Pro) are sensitive to the inclusion of these outliers. Fitting with Eq. 5.2 to the

untransformed data is less sensitive to the inclusion of these points (Fig. 5.2). For the data shown, the linear fit excluding outliers to the transformed data and the Weibull fit to the untransformed data are the same within the uncertainty of the resulting fitting parameters as in Fig. 5.3. In previous generations, linearization greatly facilitated fitting; however, modern computer fitting packages eliminate the advantage of fitting with linearized data. Plotting in the transformed coordinates is still convenient in that salient features can be more easily identified; however, numerical fitting is better using the untransformed data. Indeed, for more complicated equations in subsequent sections, fitting untransformed data becomes the only practical option. Therefore, future fits will be done to data (excluding obvious outliers) in the untransformed coordinates then the fits will be transformed via Eq. 5.3 for plots. This also simplifies the representation of uncertainty of fitting parameters. In the transformed space the Weibull fit $y = Bx + A$, $B = \beta$ however, $A = \beta \log[F_o]$.

5.3.2. Three-Parameter Weibull Model

Equation 5.2 assumes that the probability of breakdown reaches zero as the field goes to zero. There are indications that there can be a non-zero threshold field for breakdowns (Chauvet and Laurent, 1993; Laurent*, et al.*, 1994; Andersen and Dennison, 2014; 2015b; Andersen*, et al.*, 2015). Incorporating a threshold field into a Weibull distribution Eq. 5.2 requires a third parameter F_s and yields (Dissado and Fothergill, 1992; Chauvet and Laurent, 1993)

$$P(F) = 1 - \exp\left(-\left[\frac{F-F_S}{F_{0-F_S}}\right]^{\beta}\right). \tag{5.4}$$

One can construct a transformation of Eq. 5.4 into a linear form similar to Eq. 5.3, namely (Chauvet and Laurent, 1993)

$$x = \log(F - F_s) \text{ and } y = \log\left[\ln\left(\frac{1}{1-P}\right)\right]. \tag{5.5}$$

However, Eq. 5.5 is not a unique transformation due to the reduction from three parameters to two in a linear transformation. One can iteratively optimize such a fit or instead, as done in this analysis, fit the untransformed data with Eq. 5.4 prior to transforming it via Eq. 5.3. When $F_s = 0$ Eq. 5.4 reduces to Eq. 5.2.

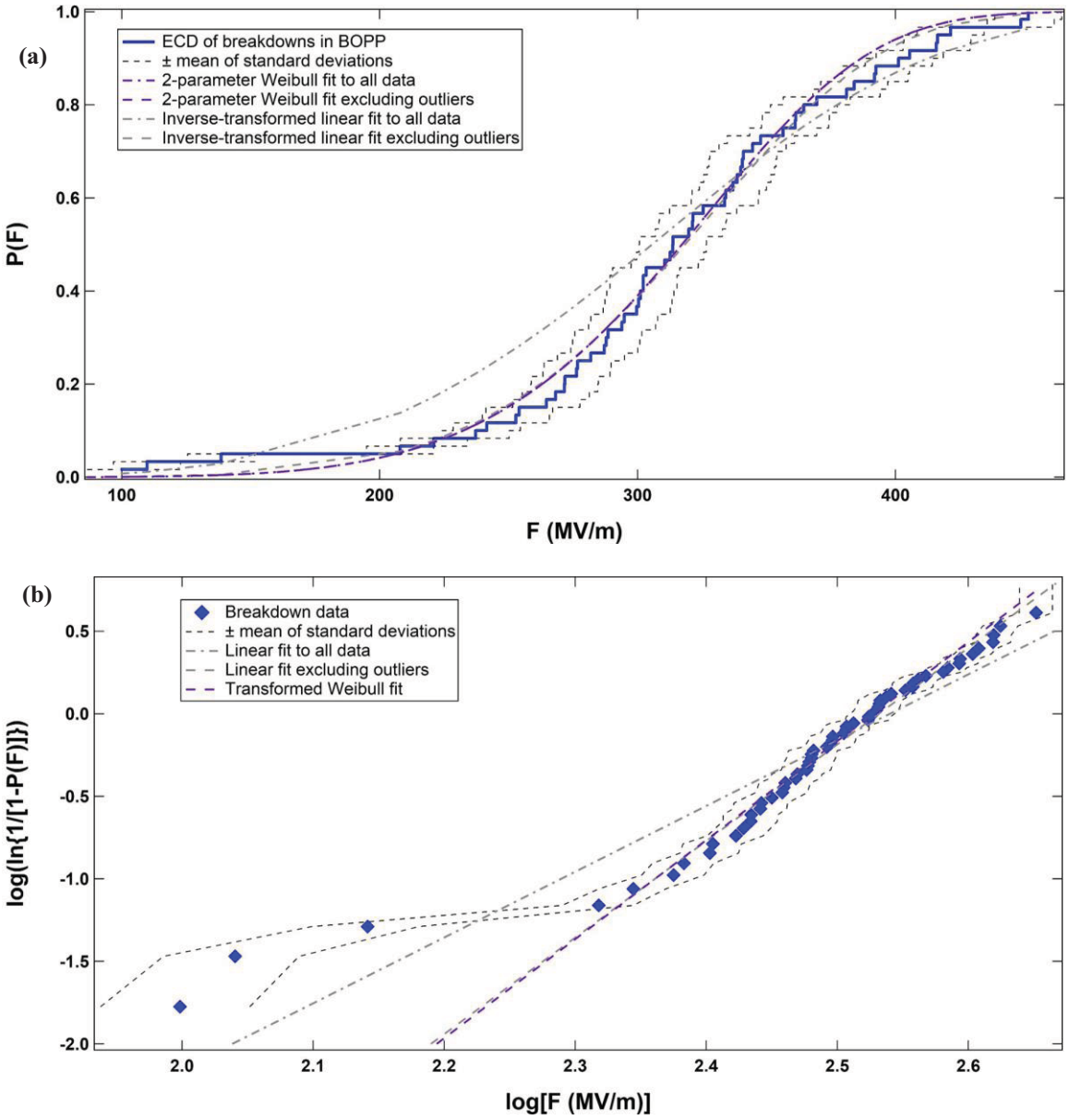

FIG. 5.2. 2-Parameter Weibull Fits. (a) Data shown in untransformed coordinates. Fitting with (e2) gives the same result whether or not the first three points are included hence they are indistinguishable. (b) Data transformed via Eq. 5.3 with linear fits. The transformation shows that the lowest three data do not follow the prevailing trend.

The fitting parameters, due to their clear physical interpretations, are all constrained to be positive ($F_0 > 0, F_s \geq 0, \beta > 0$). Furthermore we require the threshold field to be less than the critical field, *i.e.*, $F_s < F_0$.

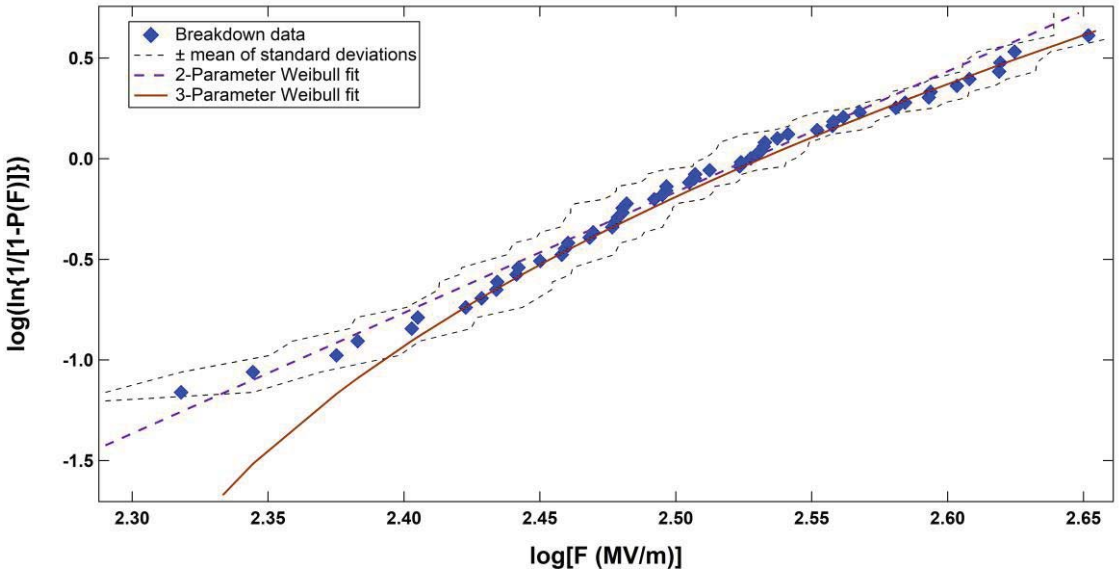

FIG. 5.3. Two- and three-parameter Weibull fits to BOPP breakdown data. Outliers excluded. The best 3-parameter fit deviates significantly from the data at lower fields in this case.

5.3.3. Mixed Weibull Model

Another common fitting method is to mix two or more Weibull distributions as a way to model multiple breakdown modes (Dissado and Fothergill, 1992; Rytöluoto*, et al.*, 2015). Though this will lead to better fits, it is at the expense of an expanded parameter set. As an example, a recent study of a bimodal breakdown distribution in a LDPE nanodielectric composite material was fit to a two-parameter Weibull distribution (Wang*, et al.*, 2014b).

In general, any number S of probability distributions can be mixed using normalization factors n_i and n where the total probability function is

$$P_{mix}(F) = \sum_{i=1}^{S} \frac{n_i}{n} P_i(F) \tag{5.6}$$

where normalization as probability distribution requires

$$\sum_{i=1}^{S} \frac{n_i}{n} \overset{!}{=} 1 \tag{5.7}$$

For the case of $S = 2$, Eq. 5.7 simplifies to

$$P_{mix}(F) = pP_1(F) + (1-p)P_2(F), \tag{5.8}$$

where $0 \leq p \leq 1$ satisfies Eq. 5.7. As an example, the mixture of two 2-parameter Weibull functions is

$$P_{mix}(F) = p\left(1 - \exp\left(-\left[\frac{F}{F_{01}}\right]^{\beta_1}\right)\right) + (1-p)\left(1 - \exp\left(-\left[\frac{F}{F_{02}}\right]^{\beta_2}\right)\right). \quad 5.9$$

Here, p represents the fractional weight of the first two-parameter Weibull distribution, $F_{01}$and F_{02} are their distribution centroids, and β_1 andβ_2 are the corresponding width parameters.

There is no clear way to linearize Eq. 5.9, which is to be expected. If this is a better fit to the data, we would expect to see a mixture of two lines in the coordinate system used in Fig. 5.2 (b). Again, the most straightforward method is to fit the data to the function in question, then transform it via Eq. 5.3 in order to compare it to the other fitting equations. In other words, no data are being fit to linear functions for any of the Weibull distributions; however, data and Weibull fits are plotted in a coordinate system where a 2-parameter Weibull function is linear in order to facilitate visual comparisons. Fig. 5.4 is an example of a mixed Weibull fit to breakdown data in BOPP. One should beware that adding additional fitting parameters may automatically improve fits to data as additional parameters add additional degrees of freedom without necessarily adding any physical insight. This is discussed further in the Chapter 6.

5.4. Fitting with Physical Models

Having outlined how breakdown data can be analyzed with empirical Weibull models, we return to a discussion of comparing theoretical physics-based models to breakdown data. These models are much more complicated than the simple Weibull equations, but our fundamental assumption is that models based on materials physics will be more useful than empirical models for three reasons. First, physical models are more conceptually satisfying than empirical models. Second, explicitly stating physical quantities can guide extrapolation. If an extrapolation extends into a regime where one of the underlying physical assumptions of the model is violated (*e.g.*, the thermal energy is greater than the defect energy), the user can know to mistrust such calculations. Such red flags are not built into empirical models. Third, physics-based models can use results from independent measurements of material properties to make predictions, even before tests are performed.

This section outlines analysis methods using physics-based models. Some of this analysis will utilize Weibull statistics outlined in the previous section.

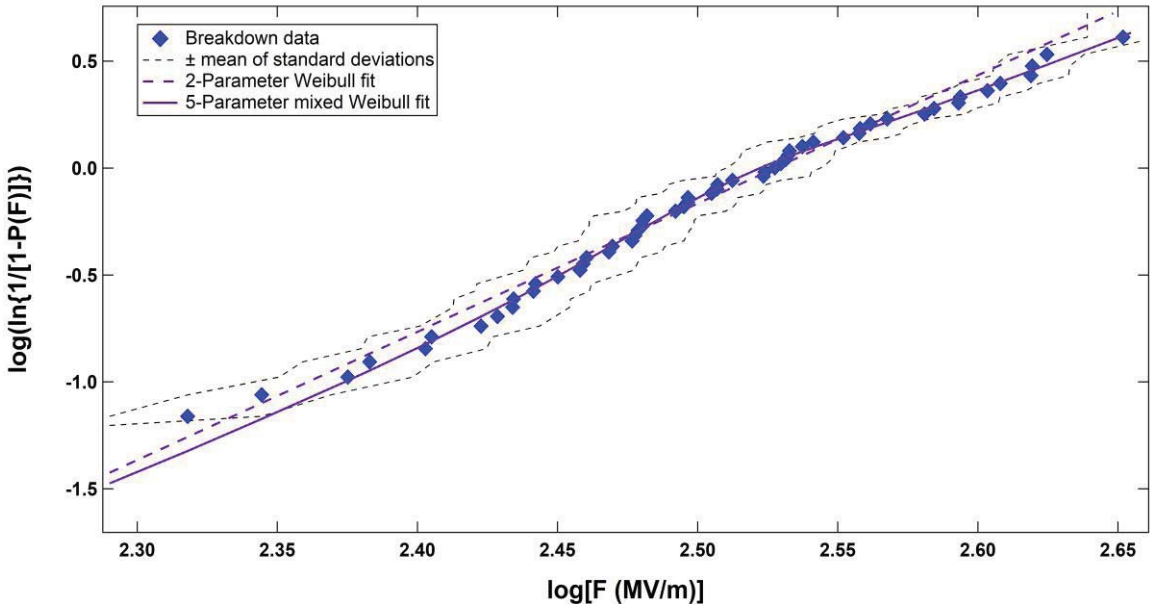

FIG. 5.4. Comparison of a 5-parameter mixed two-Weibull fit to a standard 2-parameter Weibull fit in BOPP. The mixed Weibull clearly follows the data more closely than the 2-parameter fit.

5.4.1. Comparing Crine and Dual-defect Models

The preeminent materials properties based model of dielectric breakdown is the well-known Crine model shown in MPG nomenclature in Eq. 2.11. (Crine*, et al.*, 1989; Dissado and Fothergill, 1992; Martinez-Vega, 2013).

$$t_{en}(F,T) = \left(\frac{h}{2k_bT}\right) \exp\left[\frac{\Delta G_{def}}{k_bT}\right] \operatorname{csch}\left[\frac{\epsilon_0 \epsilon_r F^2}{2k_bTN_{def}}\right], \qquad 2.11$$

Despite the fact that Crine himself is still working to improve and modify his theory to this day, newly proposed models in this field of study should be compared to Crine's canonical model (Lewis*, et al.*, 1996; Palit, 2014; Crine, 2016b). In this section, I will outline the analysis used to compare the Crine model to the dual-defect model proposed in 3.1. The results of this comparison will be discussed in 6.2.

5.4.1.1. Voltage Step-up Test Comparisons

A search of the relevant published literature to date reveals that the Crine model has not been applied to voltage step-up tests. Eq. 2.11 refers to the time endurance problem, discussed in Section 5.4.1.2. To relate the Crine model to the ECD of a set of voltage step-up tests, one must consider Eq. 2.10 and the

likelihood of breakdown due to a voltage step-up process as discussed in 3.1.2. We will continue to refer to the mean-field approximation based theory as the Crine model, despite its novel formulation in this dissertation. Considering only a mean-field approximation as Crine does, we need to consider Eq. 3.7 for only one defect species $P_{def}^{Tot} \rightarrow P_{def}$. This is

$$P_{step}^{Tot}\left(\Delta t_{step}, N_{step}, \Delta V_{step}, T\right) = 1 - \prod_{j=1}^{N_{step}}\left[1 - P_{def}\left(\Delta t_{step}, \frac{j\Delta V_{step}}{d}, T\right)\right]. \quad 5.10$$

We will compare this to the dual-defect model prediction

$$P_{step}^{Tot}\left(\Delta t_{step}, N_{step}, \Delta V_{step}, T\right) = 1 - \prod_{j=1}^{N_{step}}\left[1 - P_{def}^{Tot}\left(\Delta t_{step}, \frac{j\Delta V_{step}}{d}, T\right)\right] \quad 3.7$$

where for two defect species

$$P_{def}^{Tot}\left(\Delta t_{step}, \frac{j\Delta V_{step}}{d}, T\right) = \left(\frac{2k_bT}{h/\Delta t_{step}}\right)\sum_{i=HI,LO}\exp\left[\frac{-\Delta G_{def}^{i}}{k_bT}\right]\sinh\left[\frac{\epsilon_0\epsilon_r\left\{\frac{j\Delta V_{step}}{d}\right\}^2}{2N_{def}^{i}k_bT}\right]. \quad 5.11$$

Equations 5.10 and 5.11 will be compared to the ECD, Eq. 5.1, for several data sets in the Chapter 6. The application of physics-based breakdown theory to voltage step-up tests in this way is, to the best of our knowledge, a novel approach. Fitting with these equations is non-trivial due to the product series. In Igor Pro the standard curve-fitting package does not have sufficient options; it is necessary to create a dummy fit function in the standard curve-fitting interface, then open up the corresponding fitting routine and alter the code. Details of the routine are in Appendix C. To avoid problems with the representation of numbers even with double precision, it is essential to combine as many constants as possible into the fitting parameters, then to back out the desired values after the numerical calculations. To do this we can simplify Eq. 5.11 to

$$P_{def}^{Tot}\left(\Delta t_{step}, \frac{j\Delta V_{step}}{d}, T\right) = \sum_{i=HI,LO}\lambda^i \sinh[\xi^i j^2] \quad 5.12$$

where here

$$\lambda^i = \left(\frac{2k_bT}{h/\Delta t_{step}}\right)\exp\left[\frac{-\Delta G_{def}^{i}}{k_bT}\right] \text{ and } \xi^i = \frac{\epsilon_0\epsilon_r\left\{\frac{\Delta V_{step}}{d}\right\}^2}{2N_{def}^{i}k_bT}. \quad 5.13$$

Of course, for the Crine model assumptions, there would only be one of each combined variable λ and ξ. Therefore, the material temperature, average sample thickness, time at each voltage step, and relative permittivity need to be known to extract the defect energy ΔG_{def}^{i} and defect density N_{def}^{i}. Igor Pro requires initial guesses for any user-defined fitting function, therefore we need physically reasonable ranges for both

λ and ξ. As we are for now only considering only room temperature tests at the MPG standard ramp rate of 20V/4s (or for MPG tests before September 14th, 2015 20V/3.5s due to a LabVIEW glitch) both $T = 298 \pm 1.5$ K (Dekany, *et al.*, 2012) and Δt_{step} are fixed. The relative permittivity ϵ_r and average sample thickness d will be unique to each material but range from 2.4-3.5 and 24-30 μm, respectively, for the materials used in this study. Realistically, we expect the defect energies must fall somewhere between $k_B T$ as a lower bound (~0.03 eV) and the dissociation energy of the strong C-C bonds in a polymer (~3.65 eV) as an upper bound (Phillips, 1983; Andersen, *et al.*, 2015). Estimations of bond densities span orders of magnitude, but reasonable estimations of broken bond densities in LDPE are ~10^{18} bonds/cm^3 and total available bonds are $\gtrsim 10^{22}$ bonds/cm^3 (Andersen, *et al.*, 2015). For λ this range is a staggering ~10^{-54} to ~10^{13}. The variable ξ can range from ~10^{-7} to ~$2 \cdot 10^{-3}$. Splitting these variables into HI and LO defect types we get (assuming at least 0.5 eV between defect types), λ^{LO} ~10^{-29} to ~10^{13} and λ^{HI} ~10^{-54} to ~10^{-29} then for reasonable densities ξ^{LO} ~10^{-7} to ~10^{-4} and ξ^{HI} ~10^{-5} to ~$2 \cdot 10^{-3}$. For Igor Pro, good fits for most materials have been obtained with initial guesses of $\xi \approx 10^{-5}$ and $\lambda \approx 10^{-4}$ corresponding to approximately $\Delta G \approx 1$ eV and $N_{def} \approx 10^{20}$ cm^{-3}. Fig. 5.5 gives an example of such fits for BOPP done in untransformed coordinates then transformed via Eq. 5.3. In this case, both Crine and dual-defect model fits give the same trend line. A discussion of this and fits to other polymers studied is given in the Chapter 6.

5.4.1.2. Static Voltage Endurance Time

In this section, we discuss the evaluation of SVET data. SVET is the most difficult to obtain of the tests discussed in this dissertation, but perhaps the most insightful. SVET data directly probes the lifetime of insulating materials under prolonged electric field stress. Obtaining statistically significant quantities of SVET can be very onerous, even for waiting voltages close to the nominal breakdown data. The 58 SVET tests in LDPE discussed in this dissertation took approximately 68 days of instrument time to collect not counting tests that broke down before reaching the waiting voltage. I am grateful for my predecessors in the MPG who collected the majority of this data. Over a dozen SVET tests have been attempted by the MPG on polyimide (PI), however, only nine have been successful (often breakdown occurs before the waiting voltage is achieved, or the test is terminated prior to breakdown due to scheduling

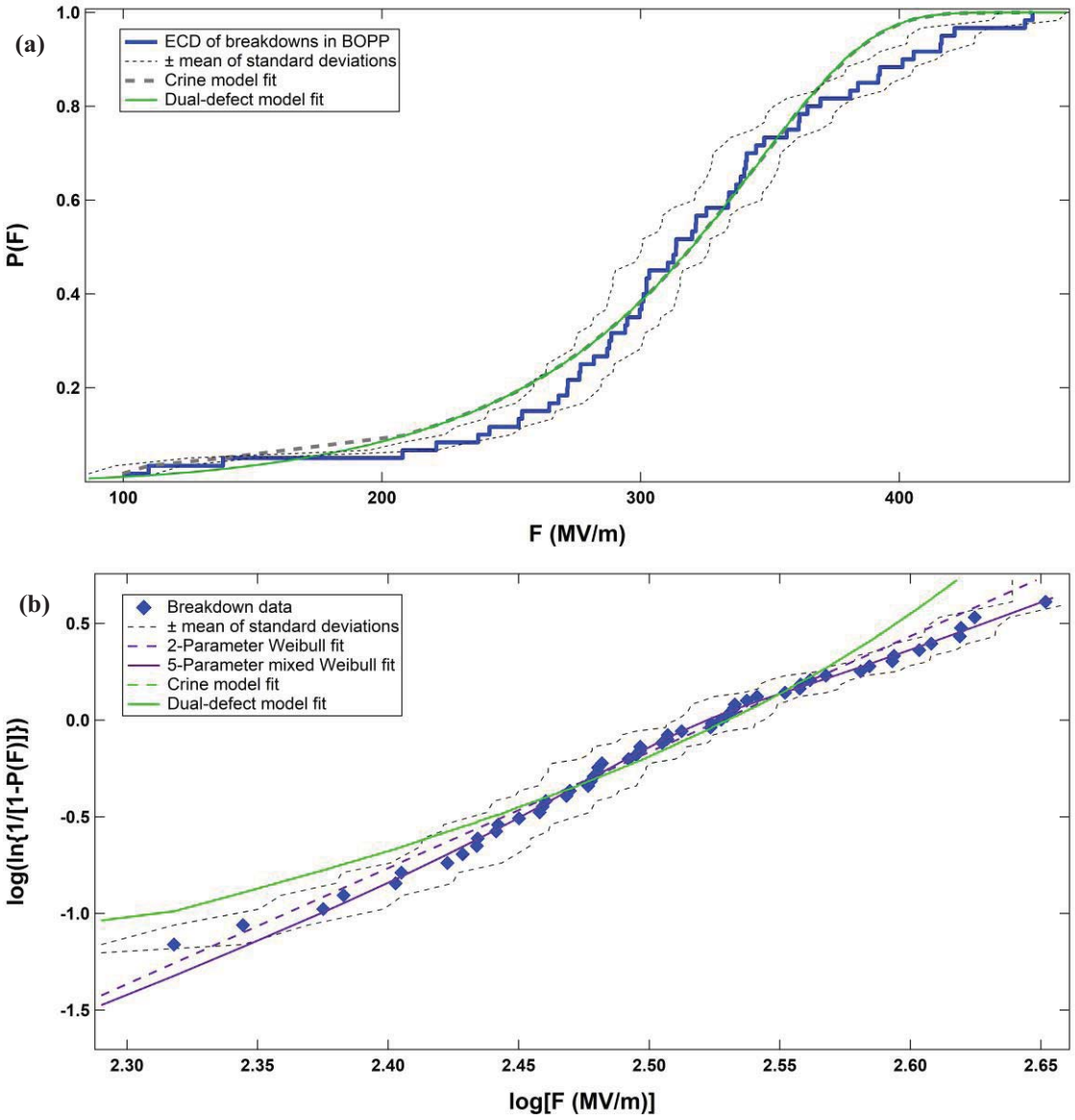

FIG. 5.5. Fits using defect-driven models. In this case, both models result in identical trend lines. (a) Fits and data shown in untransformed coordinates. (b) Data transformed via Eq. 5.3 for easier comparison to Weibull fits.

constraints) and no meaningful analysis can be extracted from these data. There has been much discussion over SVET results in the literature for many materials. In most cases, only ten or so tests of each material are used to establish the authors' conclusions (Dissado and Fothergill, 1992; Crine, 1999; Palit, 2014; Crine, 2016b). Lack of more extensive studies on SVET behavior could be the source of some of the

confusion in the literature. Indeed, I am only able to present SVET data for one material, discussed in more detail in 6.2.2.

For repeated SVET tests at a single waiting voltage one can use a variant of the Weibull statistics I have discussed in 5.3 to analyze the results (Dissado and Fothergill, 1992; Mazzanti, 2017). The tests discussed here were performed over a range of static voltages although some were repeated. Many tests done at each static voltage over a range of voltages would be ideal but very impractical.

In 3.1.2 the complicated complete time endurance equation for a voltage ramp up to a waiting voltage was introduced as

$$t_{step-en}^{Tot}\left(\Delta t_{step}, N_{step}, \Delta V_{step}, T\right) = \left(\frac{h}{2k_bT}\right)\left[\sum_{i=A,B}\exp\left[\frac{-\Delta G_{def}^{i}}{k_bT}\right]\sinh\left[\frac{\varepsilon_0\varepsilon_r\left(\frac{N_{step}\Delta V_{step}}{d}\right)^2}{2k_bT\,N_{def}^{i}}\right]\right]^{-1} \times$$

$$\left\{\prod_{j=1}^{N_{step}}\left[1-\left(\frac{2k_bT}{h/\Delta t}\right)\sum_{i=HI,LO}\exp\left[\frac{-\Delta G_{def}^{i}}{k_bT}\right]\sinh\left[\frac{\epsilon_0\epsilon_r\left(\frac{j\Delta V_{step}}{d}\right)^2}{2N_{def}^{i}k_bT}\right]\right]\right\} = t_{en}\left(\Delta t_{step}, N_{step}, \Delta V_{step}, T\right) \times$$

$$\left\{\prod_{j=1}^{N_{step}}\left[1-\left(\frac{2k_bT}{h/\Delta t}\right)\sum_{i=HI,LO}\exp\left[\frac{-\Delta G_{def}^{i}}{k_bT}\right]\sinh\left[\frac{\epsilon_0\epsilon_r\left(\frac{j\Delta V_{step}}{d}\right)^2}{2N_{def}^{i}k_bT}\right]\right]\right\} \quad 3.9$$

While, it is conceptually more complete to consider the ramp-up process, is it significant and necessary? The product series related to the ramp-up is the primary source of the difficulties in fitting discussed in the previous section. Fig. 5.6 compares SVET predictions with and without this correction, together with the limiting worst case of considering the waiting voltage during the step up process. The black curve assumes no contribution from the ramping process, the yellow curve assumes each ramp step field places as much stress on the material as the static field, and the green curve weights each ramp time interval with the appropriate field-dependent failure probability. The differences between these cases are only visible at the highest waiting fields and are all contained within the estimated uncertainty in the fitting parameters. Note that even at high fields the discrepancy in time to breakdown between the correct (green) curve and the approximate (black) curve is <5% at t_{en}≥1 s and is <20% of the variation due to ±5% uncertainties in the defect energies at t_{en}=1 s or indeed the spread in the data (see Fig. 6.2). Thus, we can safely use Eq. 3.2. for t_{en}^{Tot} without the correction for the ramp-up process—at least for our study on LDPE. This simplifies the fitting of SVET data. The results of this fit are discussed in detail in 6.2.2.

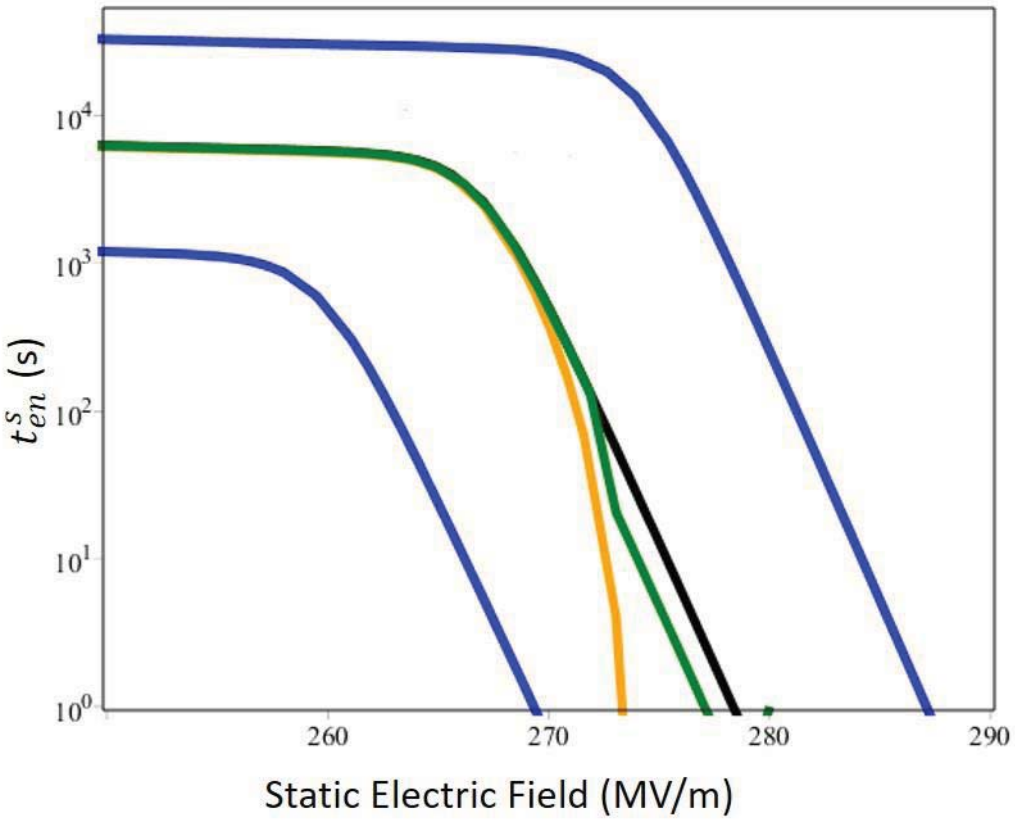

FIG. 5.6. Comparison of various SVET predictions. Traces include the prediction with no correction for the ramp up to the static waiting voltage (black), with the correction (green), and substituting the waiting voltage stress for the ramp-up voltages (yellow). The blue curves represent 5% variations in the black SVET prediction.

5.4.2. Analysis of Tests of Variable Extrinsic Conditions

The probability of breakdown, as predicted by both the Crine and dual-defect models depend significantly on extrinsic material conditions such as the voltage ramp or rather the rate of change of electric field $\frac{F}{\Delta t}$, temperature T, and ionizing radiation that can change N_{def}^i. Empirical models of ramp rate effects were discussed in 3.1.2 in the context of the physical models. The temperature dependence is theoretically very difficult. Except for the leading frequency factor and the product series for the ramp-up, the remainder of the breakdown theory we have discussed is made of various Boltzmann factors. Temperature dependence is featured in each of these terms except the index of the product series. The dominant factor will depend greatly on both the material properties and the other test conditions and good

analytical predictions can only be made when most of these terms are known and constant (although this is not necessarily the case, *e.g.*, the temperature is likely to effect the rate of LO type defect creation and annihilation).

For radiation effects, we have already discussed the effects of changing the defect density in 3.2. Depending the dose rate, we can model such effects as either changes in the initial defect density N_{def0} for slow cumulative effects; otherwise, another term would need to be added to the already difficult differential Eq. 3.13 for changes in the defect populations.

For tests that change the extrinsic conditions of the sample, ideally, many tests at each test conditions are needed to obtain good statistics. For example, Weibull fits to a group of tests at a given ramp-rate yield the Weibull centroid parameter F_0, which is directly comparable for physics-based models with probability set to 63.2%. While large numbers of repeated tests over a range of conditions is ideal, it is often impractical. A limited number of tests may still be sufficient to show changes in breakdown likelihood if the effects are large.

Section 6.2.3 describes a study of tests across several voltage ramp rates for three materials. Section 6.2.4 discusses the MPG measurements at cryogenic and elevated temperatures together with radiation exposure. Due to limited quantities of tests for each value of the varied extrinsic condition, these measurements were analyzed with by comparing F_0 from Eq. 5.2, a two-parameter Weibull fit. The shape parameters were not particularly useful in most cases as it was very sensitive to the number of tests in each condition, which varied significantly. Nevertheless, this is sufficient for investigating dominant trends from preliminary measurements.

5.5. Non-shorting Partial Discharges as Precursors for Breakdown

We now transition into a discussion of the analysis of DCPD as observed during MPG ESD tests. Section 1.1.2 reviewed briefly the need for both improved accelerated ESD test methods and improved theoretical understanding of DCPD. Section 3.2.2 discusses a conceptual model for DCPD related to the dual-defect model of breakdown via LO type recoverable shallow defects. Finally, in 4.6.5 and 4.7 MPG measurements of DCPD are explained. This section focuses on how these measurements of DCPD are characterized and compared to dielectric breakdown events. If DCPD can be shown to be a key indicator of

long-term breakdown behavior, they could be used to greatly expedite the characterization of candidate dielectrics for extreme applications (Andersen and Dennison, 2015b). Finally, the establishment of relationship between breakdown and DCPD may provide insights into the dual-defect model-particularly recoverable defect mechanisms.

5.5.1. Observing DCPD

Typically, measurements of PD and breakdown are independent from one another. This may be because only one or the other phenomena might be the target of a given measurement. For example, test setups may only be sensitive to one of the two phenomena or if a test can detect both one is considered a nuisance. While we acknowledge that there have been other reports of researchers seeing both DCPD and breakdown (Rytöluoto*, et al.*, 2015), this section focuses on why they are not typically reported together. As shown in Fig. 5.7 (a), the observed frequency of the DCPD with the USU MPG setup increase substantially with increasing voltage. For all four materials studied, no DCPD were observed below a threshold voltage. It may be that the apparent threshold is simply a consequence of the fact that the observed rates at threshold voltages predict at most a few DCPD per run.

Given the observed frequency of DCPD for a given material in the USU MPG setup, we can estimate the frequency one would expect to see DCPD for different setups with different hypothetical ammeter duty cycles and voltage ramp rates. Fig. 5.7 (b) shows the estimated DCPD count rate for LDPE and BOPP as a function of voltage ramp rate, given various instrument duty cycles. This count rate is estimated as the product of the average DCPD frequency above DCPD inception, the duty cycle, and duration of a test run (estimated as the ratio between the nominal breakdown voltage and the voltage ramp rate). Given a duty cycle and estimated DCPD frequency, the estimated DCPD count per run decreases with increasing voltage ramp rate. The average estimated DCPD frequencies above inception for each material in Fig. 5.7 (a) are 4.7±0.3 Hz for BOPP, 1.35±0.09 Hz for PI, 0.86±0.04 Hz for LDPE, and 0.54±0.05 Hz for polyether ether ketone (PEEK).

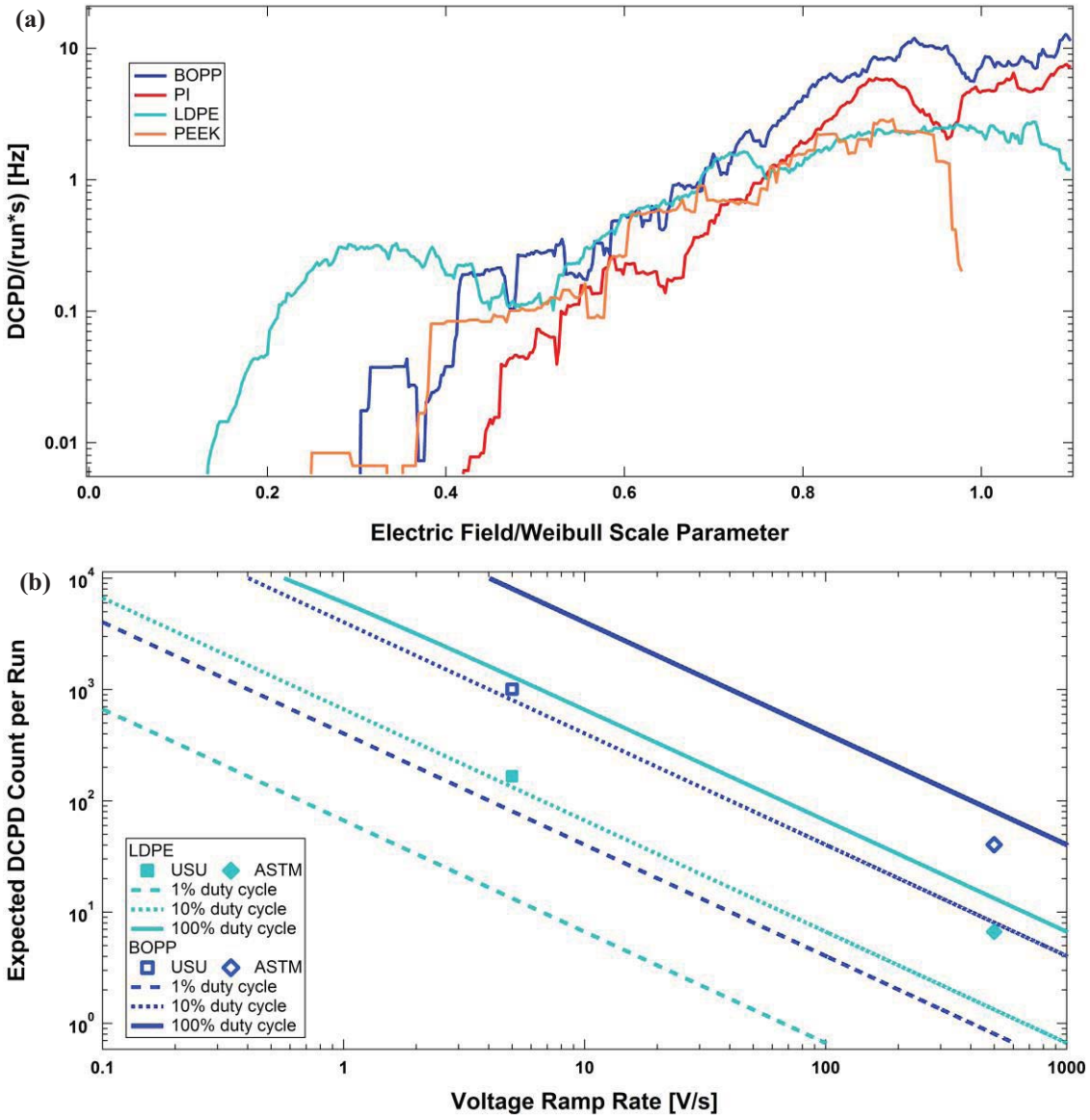

FIG. 5.7. Frequency of DCPD. (a) Estimated frequency of DCPD from data versus applied field scaled by breakdown field, corrected for equipment duty cycle and smoothed with a 500 V boxcar method. (b) Estimated DCPD count measurement for various duty cycles versus voltage ramp rate. Upper blue curves correspond to the material with the highest average DCPD frequency, BOPP. The lower cyan curves represent the estimates for LDPE. Square markers indicate the estimates using the most common USU ramp rate (~5 V/s) and duty cycle (~12%) for BOPP while diamond markers indicate estimates of the ASTM method with a 500 V/s ramp rate and a 50% duty cycle.

The distribution of these DCPD features with applied voltage are clearly stocasitic in nature and vary significantly from material to material, but are consistent for many different step-up tests on the same

materials; again, this strongly suggests that DCPD features are clearly not experimental artifacts (Andersen and Dennison, 2014).

Following is a summary of potential factors in order of likely impact in the distinctiveness of our measurements, or at least reported measurements, of DCPD during breakdown tests:

(i) Continuous monitoring of leakage current (see 4.1). The standard procedure for step-up to breakdown tests recommends the use of a fuse or breaker to indicate breakdown (ASTM D 3755-14, 2014). If leakage current is not monitored continuously then it will be extremely unlikely that DCPD will be observed (Andersen and Dennison, 2017). At most, if the current sensing element has a low tripping threshold, DCPD would result in a false positive in the dielectric breakdown test. Likewise, as shown in Fig. 5.7 (b), setups with poor duty cycles may also struggle to observe DCPD. Likewise, as shown in Fig. 5.7 (b), setups with poor current sensor duty cycles may also struggle to observe DCPD.

(ii) Ammeters used were sensitive down to 10 nA. Depending on the breakdown voltage in a given test, current through our test circuit at breakdown is limited to ~40 μA. With DCPD observations as small as ~0.1 μA, they might easily be missed by a setup exclusively designed to test for dielectric breakdown and only sensitive to higher leakage current amplitudes.

(iii) The use of slower ramp rates than most standard tests (ASTM D 3755-14, 2014). As shown in Fig. 5.7 (b), the estimated DCPD count decreases dramatically with increasing voltage ramp rate. MPG step-up tests, with an average voltage ramp rate of 5 V/s, are likely to see 100 times more DCPD events than using a 500 V/s ramp in a given run. In LDPE, an average of 17 DCPD observations occurred (unadjusted for amplitude). At 500 V/s we would expect fewer than one in twenty tests to include even a single DCPD observation.

(iv) Stepwise ramping with sharp edges in the applied voltage profile used in these tests may trigger more DCPD than a continuous voltage ramp (Wang*, et al.*, 2014a).

(v) Large flat electrode areas, rather than sharp needles often used in breakdown tests (Dissado and Fothergill, 1992). See Fig. 5.8 and Section 4.6.2.

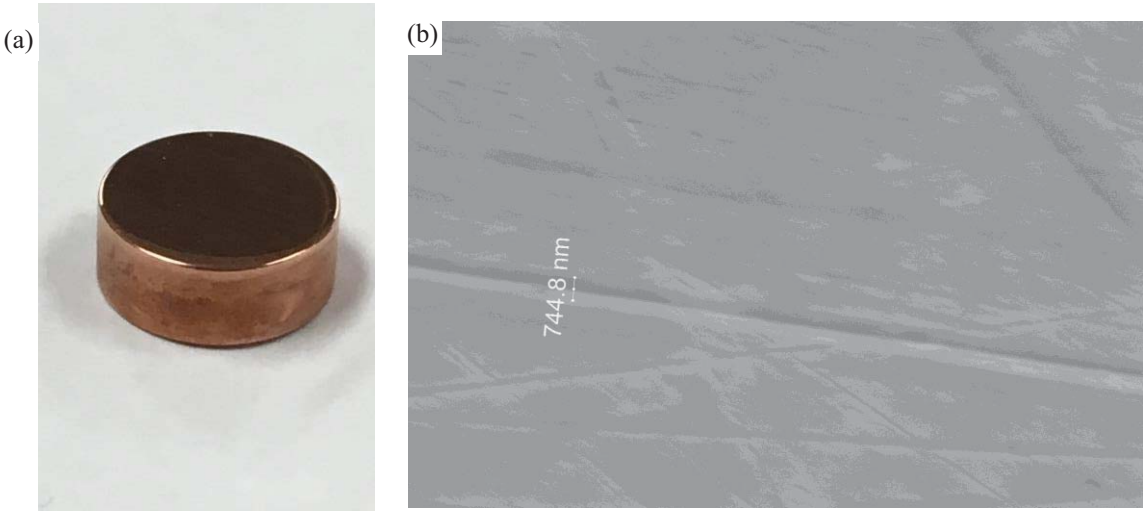

FIG. 5.8. Images of USU MPG high voltage electrodes. (a) Photograph of beveled high voltage electrode. (b) SEM image of polished electrode surface. The largest futures are smaller than 1 μm.

(vi) Beveled electrode edges that minimize edge effects (Chauvet and Laurent, 1993). See Fig. 5.8 and Section 4.6.2.

(vii) Polished electrodes to minimize the effects of protrusions (Arevalo and Dong, 2014; Zavattoni*, et al.*, 2014). See Fig. 5.8 and Section 4.6.2.

(viii) Spring-loaded sample clamping system to maintain a uniform electric field. See Section 4.6.2.

(ix) Samples that extend well beyond the electrode area to reduce surface flashover. See Section 4.6.2.

(x) High quality samples of uniform thickness used to minimize impurities and associated erroneous breakdown. See Appendix D.

(xi) Samples were baked prior to testing, to remove any absorbed water or other volatiles (Zavattoni*, et al.*, 2014). See Section 4.6.1.

(xii) Tests were performed under high vacuum well below pressures with possible Paschen discharges ($<10^{-3}$ Pa base pressure), rather than in oil or some other dielectric medium. See Section 4.6.2.

Having discussed in detail many of the reasons that DCPD are rarely reported in breakdown tests of polymer films we note again that there are other reports of DCPD in thin films. Several studies from the University of Tempere report DCPD in during breakdown tests of thin polypropylene films ranging from 4-25 μm (Rytöluoto and Lahti, 2013; Rytöluoto*, et al.*, 2015; Rytöluoto, 2016; Ritamäki*, et al.*, 2017a; Ritamäki*, et al.*, 2017b). The DCPD they report are in conjunction with the large-area metalized film self-clearing breakdown method. Their reports include DCPD of sufficient energy to vaporize sections of the thin-film electrodes without the observation of a breakdown rupture in the polymer dielectric (Rytöluoto*, et al.*, 2015; Ritamäki*, et al.*, 2017a). Such observations are consistent with the notion of bulk DCPD through dielectric films. A research group at W.L. Gore and Associates, Inc. doing similar large area tests on ~6 μm PTFE and BOPP films do not report DCPD directly, but they do report using filtering criteria to distinguish between breakdowns, DCPD, and flashover events (Kerwien*, et al.*, 2016). In these studies, and indeed breakdown studies in general, transients such as flashover and PD are generally considered a nuisance to be suppressed or filtered out so as not to be misidentified as breakdown (see 4.1 and 4.6.4) (IEC 60243-1, 2013; IEC 60243-2, 2013; ASTM D 3755-14, 2014; Andersen and Dennison, 2017). Although DCPD are not typically the target of dc tests on thin films, such detections have been published independently.

5.5.2. Energy Budget for DCPD and Breakdown Events

In this section, we compare the energy of DCPD events to the energy required to effect the observed damage of breakdown from our ESD tests. We have shown that in 4.7 that the true discharge time in much less than the RC time constant. Let us assume breakdown to be an adiabatic process, *i.e.*, only the energy stored in the DUT capacitor is available to effect a discharge (Boggs, 2017b). One might imagine that perhaps the observed DCPD are simply discharges that should have been breakdowns, but, due to poor apparatus design, died off before complete breakdown due to lack of available energy. Comparing distributions of breakdowns and DCPD (see Sections 5.5.3 and 5.5.4) suggests that this is very unlikely since we already know that DCPD can happen at much higher voltages than the lower end of the

breakdown distribution. Nevertheless, consider the following calculations. The total energy stored in our simple parallel plate capacitor is simply

$$\mathcal{E} = \frac{\epsilon_r \epsilon_0 A V^2}{2d} \tag{5.14}$$

which or a limiting low energy case of our largest thickness (from PI) paired with the smallest relative dielectric constant (from LDPE) is

$$\mathcal{E}(V) \approx 5.66 * 10^{-11}[\mathrm{F}] * V^2 \,. \tag{5.15}$$

By integrating all the current of the smallest discharge in Fig. 4.13 (a) one calculates ~$350 \cdot 10^{-9}$ C. This corresponds to roughly $3.7 \cdot 10^{-4}$ J at 2016 V. Inserting this voltage into Eq. 5.14 yields $3.9 \cdot 10^{-4}$ J. Also, note that fitting the data with an exponential decay yields a time constant of 0.0428±0.001s, in agreement with the calculated RC time constant of ~0.05 s for the MPG ESD circuit. This excellent agreement shows that the DCPD are fully discharging the DUT capacitor. Fig. 4.13 shows that this is the case for DCPD in general over the whole voltage range.

Let us now consider the energy it takes to cause the observed damage that occurs at complete dielectric breakdown (see Fig. 4.10 (c)). At a minimum, this is the decomposition energy of the polymer (which is the same as the enthalpy of formation). One may also consider the decomposition of the elemental constituents together with the heating of the resulting gas into a regime of very good conductivity. This process as described in Bogg's CEIDP Whitehead Lecture is where the first term in the total enthalpy of formation of polyethylene and its constituents and the second term describes the energy needed to heat the resulting gas (Boggs, 2017b).

$$\mathcal{E} = \frac{100\frac{\mathrm{kJ}}{\mathrm{mol}} + 25\frac{\mathrm{kJ}}{\mathrm{mol}}}{14\times10^{-3}\frac{\mathrm{kg}}{\mathrm{mol}}} m + C_V \frac{m}{\rho_m} \Delta T \tag{5.16}$$

Using Boggs' values for volumetric heat capacity C_V=2×106 J·m^{-3}·K^{-1}, and a very large ΔT= 5000K and the mass density of LDPE (ρ_m=962 kg·m^{-3}) we need only to estimate the mass of the material that has been destroyed. Note that more than half the energy required by Eq. 5.16 goes into heating process alone. Optical microscope images of breakdown sites in LDPE show that breakdown volumes range over four orders of magnitude ($\lesssim 10^{-13}$ to $\gtrsim 10^{-10}$ m^{-3} given ~25 μm thick samples and hole diameters ranging from ~10^{-5} to ~10^{-3} m) with no apparent correlation between breakdown field and hole size (see Appendix

A)(Hansen, 2014). For the larger hole sizes on the order of 10^{-11} m^{-3} we see that the adiabatic assumption is violated since Eq. 5.16 yields ~0.18 J corresponding to over 52 kV (the power supply can only apply up to 30 kV and typical breakdowns are less than 10 kV). Perhaps in these cases additional damage is done after the initial breakdown so let us consider the smaller holes of about 10^{-13} m^{-3} in size. Small holes require ~1.8 mJ by Eq. 5.16 corresponding to ~5 kV (~197 MV/m in our geometry) to get that energy in the DUT capacitor Eq. 5.15. These values are roughly consistent for the lower end of the breakdown distribution for LDPE.

As is shown in the Sections 5.5.3 and 5.5.4 (see Fig. 5.11) many DCPD are observed at voltages much larger than 5 kV. Since the observed DCPD energy at a given energy are well approximated by the energy of the DUT capacitor (Eq. 5.14) we can say that most DCPD have more than enough energy to cause destructive breakdown yet do not. In other words, the DCPD cannot be the result of a breakdown that failed due to some limitation of the test circuit (see also Section 4.6.5). What is curious is that the material can withstand such discharges without vaporizing sections of the sample. Nevertheless, this result is consistent with published results of DCPD and breakdown energies with mostly overlapping energy ranges (and DCPD vaporizing sections of thin film electrodes without perforating the dielectric) from the University of Tampere (Rytöluoto*, et al.*, 2015; Ritamäki*, et al.*, 2017b).

5.5.3. Comparing Distributions of Events

In this section, we review the efforts to compare DCPDs to breakdowns. We note again that the setup used for these tests was not originally intended to measure DCPD. Initially, all of the phenomena described in Section 4.6.5 apart from breakdown were unanticipated and puzzling. Nevertheless, the similarities between breakdown and then-termed pre-breakdown arcing event distributions were too obvious to ignore. Even without a clear understanding of the physical origins of pre-breakdown DCPD events, it became clear that if the distribution of breakdowns in test materials could be shown to be approximated well by the distribution of DCPD events versus applied field, this could greatly accelerate the characterization of the breakdown distributions and possible threshold field for materials tested. The destructive nature of step-up to breakdown tests, particularly in the parallel plate configuration, results in a single datum per test. The prospect of accurately determining the distribution of breakdowns, especially the

inception field where breakdowns are least likely to occur, becomes onerous. The popular test method of vapor-deposited electrodes on a large sample sheet allows for multiple breakdowns and increased data collection rates, but it has been shown that these events are not fully independent of each other, possibly skewing these results for predictions of breakdown distributions. (Kerwien*, et al.*, 2016).

After the author's two years of experience with the MPG ESD system initial efforts at comparing these two phenomena were presented (Andersen and Dennison, 2014). At that point in time, we referred to DCPD as "pre-breakdown arcing" or "pre-arcing." This initial analysis was not very rigorous, but led to further development. Fig. 5.9 from that paper shows a representation of data for 89 LDPE and 36 PI (Kapton) step-up tests. In this study, Fig. 5.9 shows the PDF with the fit to the ECD and compares it to a Gaussian fit to the estimated frequency of DCPD in Fig. 5.10. As discussed in Section 5.3 the ECD of breakdown events are not expected to be Gaussian but rather Weibull since each time a sample breaks down, it is removed from the sample population. While this was essentially comparing apples to oranges, it was a step toward more sophisticated methods. Note that the data presented here is not the same population of tests discussed in 5.4.1.1. They include some data that were later shown to contain errors (for LDPE some tests were done with a bad electrode plate design that was identified at a later date), different batches of PI were grouped together, and obviously subsequent tests were not included.

The fraction of total samples broken down versus breakdown field was fit to Eq. 5.2 and is shown in Fig. 5.9 with results in Table 5.1. The onset of breakdowns F_{onset} is defined here as $P(F_{onset}) = 4.6\%$. Similarly, the field at which nearly all breakdowns have occurred, F_{ESD}, is defined as $P(F_{ESD}) = 95.5\%$. In Fig. 5.9 and Fig. 5.10 F_{onset} to F_0 defines the blue region, F_0 to F_{ESD} defines the yellow region, and the red region is defined as field values above F_{ESD}. We noted that the two polymers in Fig. 5.9 exhibit similar high field behavior, which would be expected if HI Type defects are roughly the same for each material. However, F_{onset} and the width of the blue regions in Fig. 5.9 differ significantly, suggesting larger differences in LO Type defects. As expected, F_{onset} is higher for PI (Kapton)—the more rigid of the two materials and therefore larger LO type defect energies—than for LDPE.

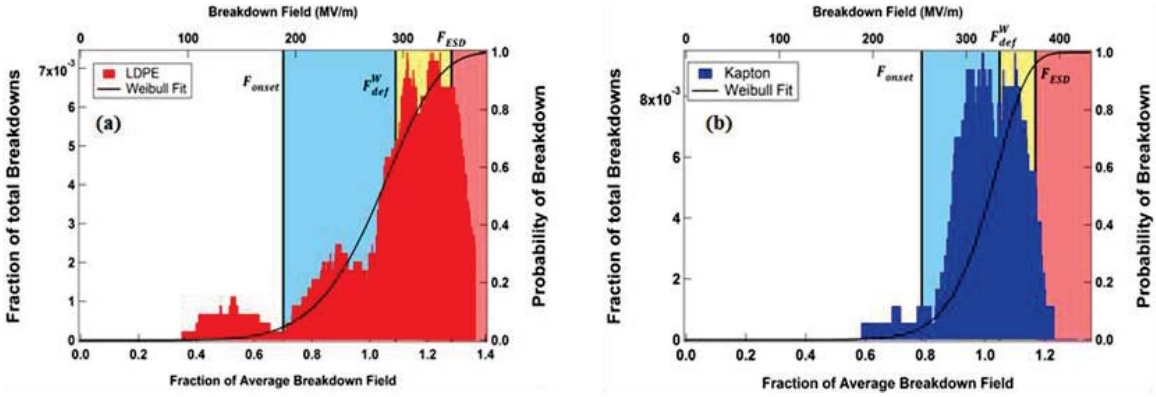

FIG. 5.9. Histograms of the fraction of total breakdowns versus breakdown electric field compared to the probability of breakdown at those fields given by Weibull distributions (black curves) for (a) 89 LDPE and (b) 36 Kapton (PI) step-up breakdown tests. F_{onset} to F_0 defines the blue region, F_0 to F_{ESD} defines the yellow region, and the red region is defined as field values above F_{ESD}.

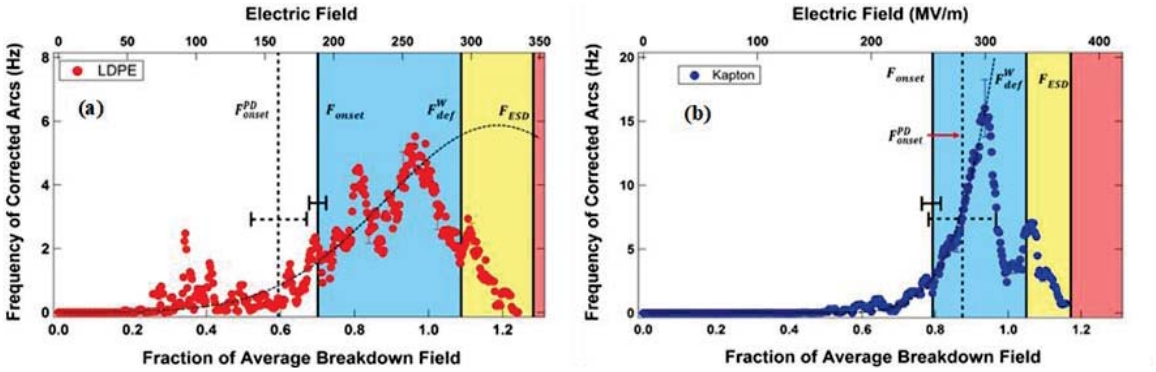

FIG. 5.10. Histograms of the frequency of short duration, recoverable breakdown events or "pre-arcs" observed during step-up breakdown tests for (a) LDPE and (b) polyimide. Frequencies have been corrected as described in the text. Black dashed curves are Gaussian fits, based on Eq. (3). Error bars for F_{onset}^{PD} and F_{onset} are shown. The colored regions match those of Fig. 5.9.

A first pass at a statistical analysis was conducted for the DCPD observed during ESD test before complete breakdown occurs for the same step-up voltage tests in Fig. 5.9 in an attempt to compare the distributions of ESD and DCPD events.

Typical threshold amplitudes for the smallest arcs observed above background noise were 0.09 μA for LDPE and 0.07 μA for PI, as determined from ~0.5 s intervals of current acquired, integrated and averaged by the ammeter over its meter response time of ~0.5 s. Initial oscilloscope DCPD measurements

suggested that the measured arc rate needed to be corrected for multiple short duration arcing events of about the same amplitude occurring within these sampling intervals. The DCPD rates measured with the ammeter were corrected for these multiple DCPD per acquisition time by estimating the number of single arcs in higher current events as the measured current divided by the average ammeter single arc current, estimated as 0.15±0.05 μA. Shapes of the corrected arc rate distributions (see Fig. 5.10) are largely insensitive to the specific choice of single arc current values, *i.e.*, as long as this value was big enough not to include noise and small enough to get most of the events, the shape of the distribution did not change.

Figure 5.10 shows a histogram of number of corrected DCPD events versus applied field divided by the average breakdown field for both LDPE and polyimide step-up tests. These frequency data are fit with a field-dependent Gaussian distribution

$$f(F) = \frac{f_0}{\Delta F\sqrt{2\pi}} exp\left[-\left(\frac{(F-\bar{F})^2}{2\Delta F^2}\right)\right] \quad 5.17$$

centered at the peak in the data $\bar{F} \approx F_0$, with a width $\Delta F = \frac{1}{2}(\bar{F} - F_{onset}^{PD})$, and normalized with f_0 to match the amplitude of the peak. The frequencies have been corrected to reflect only a ~0.5 s ammeter data collection interval per 3.5 s at each voltage. The results are tabulated in Table 5.1.

Table 5.1. Results from preliminary study comparing ESD and DCPD distributions.

	Results of fits to initial breakdown data				**Results of fits to initial DCPD data**			
Material	$\boldsymbol{F_0}$ (MV/m)	$\boldsymbol{\beta}$ (unitless)	$\boldsymbol{F_{onset}}$ (MV/m)	$\boldsymbol{F_{ESD}}$ (MV/m)	$\boldsymbol{f_0}$ (MV/m·s)	$\boldsymbol{\Delta F}$ (MV/m)	$\boldsymbol{F_{onset}^{PD}}$ (MV/m)	$\boldsymbol{\bar{F}}$ (MV/m)
LDPE	293	6.96	189±6	345±17	1200±400	80±10	160 ±20	310±30
PI	336	10.9	253 ±8	373±11	7000±3000	53±3	280 ±30	384±17

The Gaussian fit was used as a first-order approximation to the DCPD rate assuming a random distribution of DCPD events with average breakdown, but does not account for removal of specimens from

the sample population after breakdown. A similar Gaussian distribution of the mean radius of random polymer coils is predicted from random walk models of chain kink density (Zallen, 1983; Cho*, et al.*, 2000). This can be related to the entropic contribution to elastic strain energy for basic theories of rubber elasticity (Anderson*, et al.*, 2004; Trnka*, et al.*, 2014).

We compared F_{onset} to F_{onset}^{PD}. A cursory observation of Fig. 5.9 and Fig. 5.10 suggests that for both LDPE and PI, ESD breakdown can begin to occur at about the same field as DCPD is observed in samples that have not yet broken down. To make initial quantitative comparisons, we assumed a Gaussian probability for DCPD up to where the frequency starts to decrease and a Weibull distribution probability for breakdown. Compare the fields at which there is a ~5% probability of observing either arcing (F_{onset}^{PD}) or breakdown (F_{onset}); for LDPE F_{onset}^{PD}160±20 MV/m ≈ F_{onset}=189±6 MV/m and for polyimide F_{onset}^{PD}=280±30 MV/m= F_{onset}=253±8 MV/m within the uncertainty.

This study of step-up measurements of LDPE and polyimide indicates that the field for the onset of catastrophic ESD breakdown is approximately the as the same field where DCPD begins. This initial study was suggestive, though unsophisticated, and not entirely convincing (Andersen and Dennison, 2014). Clearly, a more sophisticated method to compare the distributions of DCPD and breakdown events was needed.

5.5.4. Quantile-Quantile Analysis Method

After further study and consultation with statisticians, we applied quantile-quantile (q-q) analysis to the problem. Q-q plots directly compare the cumulative distributions of two observables. In section 5.2 we discussed the ECD of events in the context of breakdowns. Likewise, Eq. 5.1

$$P(F) = \frac{1}{j}\sum_{i=1}^{j} \mathbf{1}\{x_i \le F\} \text{ where } \{x_i \le F\} = \begin{cases} 1 & \text{if } x_i \le F \\ 0 & \text{otherwise} \end{cases} \quad 5.1$$

can be applied to DCPD to create a corresponding ECD.

For breakdowns, this calculation is straightforward in that each experiment yields one breakdown at a given field. Counting DCPD is more difficult because they are observed at many amplitudes. In order to more accurately count DCPD, a typical small DCPD value as recorded by the ammeter (0.15 μA) was estimated; larger amplitude arcs were divided by this small DCPD value to determine nearest integer

multiple of DCPD per ammeter measurement time. The shape of the resulting distribution of adjusted DCPD is quite insensitive to the choice of the chosen small DCPD value, so long as this value is above the noise of the system (*i.e.*, $\gtrsim$0.085 μA) and not so large as to eliminate too much data (*i.e.*, $\lesssim$0.5 μA). As shown in Fig. 4.13, the DCPD amplitudes are not strictly the same since they increase with increasing voltage, but their variation is much smaller than the variation in amplitude as recorded by the ammeter so it is not a bad assumption.

Figure 5.11 compares the ECD of 96 breakdown tests in LDPE to the ECD of the 46,057 discretized DCPD events from those same tests. It should be noted that in many voltage step-up tests there is very erratic behavior where the current changes greatly from one measurement to the next without returning to baseline current before clear breakdown occurs. When these traces are too erratic to distinguish between any of the cases described above, any DCPD therein are not countable (Moser*, et al.*, 2015). This tends to occur at the higher fields just before breakdown so many DCPD are likely to be missed this way; therefore, we expect the distribution of DCPD to be somewhat distorted or shifted. This is evident in Fig. 5.11 and its inset. Although the two ECDs in Fig. 5.11 appear to be similar, to camper two sample populations of different sizes to each other, a robust, non-parameterized statistical method was required.

To create a q-q plot it is convenient to begin with comparing ECD plots. In Fig. 5.11 the dashed lines show two examples of quantile matching. For an ECD plot, the y-axis represents the estimated probability of occurrence, or quantile. For each quantile Q_n there is an x-axis value for each ECD plotted. These x-axis pairs for each Q_n become x- and y- values x_n and y_n on the q-q plot. For two samples of different sizes, some type of interpolation is necessary to get matching quantiles. Since there are many more DCPD than breakdowns, the quantiles of DCPD events were linearly interpolated to match the quantiles of the breakdowns. Fig. 5.12 shows the q-q plot corresponding to the ECDs in Fig. 5.11. The results of the q-q analyses will be presented in 6.2.5.

If the underlying distributions are precisely the same, the q-q plot will follow a unitary linear relationship, namely $y = x$. Any other linear q-q plot demonstrates that the two distributions are indeed correlated, while q-q plots deviating significantly from linearly show that the distributions are not correlated (Hoaglin, 1985). Nonzero intercepts indicate that one population is shifted by a constant relative

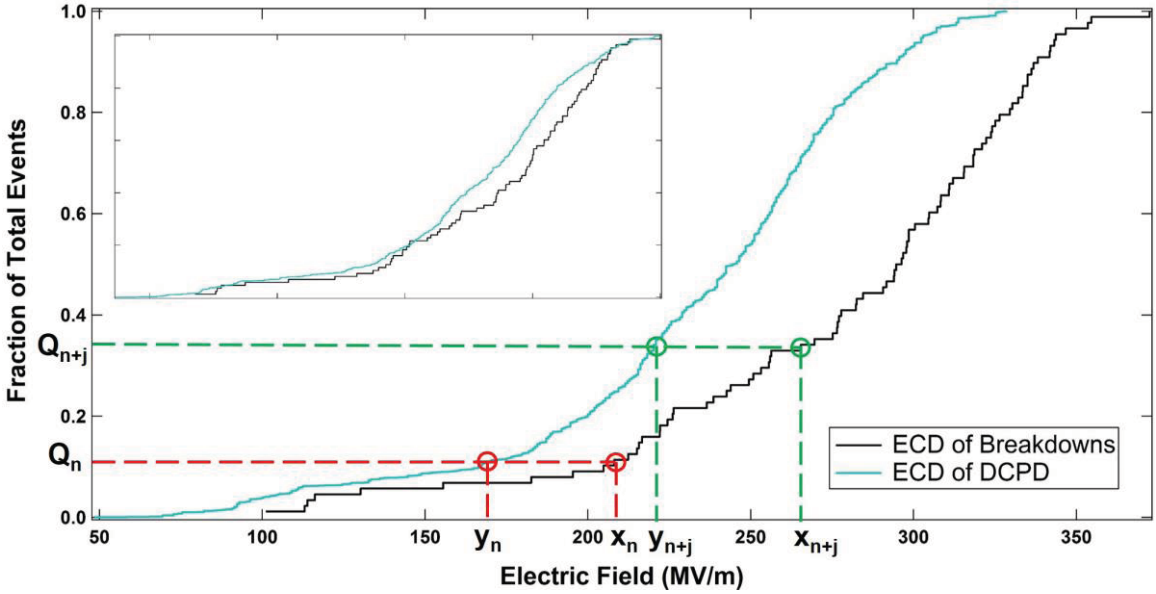

FIG. 5.11. The empirical cumulative distributions (ECD) of breakdown and DCPD events from 96 voltage step-up to breakdown tests in LDPE at room temperature. The inset shows the ECDs normalized to the highest field value for each type. Red and green dashed lines show examples of matching quantiles from two ECDs. For two ECDs plotted together, one quantile—the y-axis value—corresponds to two x-axis values which become the (x, y) pairs on a q-q plot. The ECDs shown here yield the q-q plot Fig. 5.12.

to the other. Slopes other than unity reflect a relative scaling factor between the distributions. The data in Fig. 5.12 are an example of correlated data, and when normalized show that the underlying distribution are practically identical.

The advantage of the q-q plot method is that it results in a non-parametric plot that is easy to interpret qualitatively—if the distributions are correlated, the q-q plot will be linear; otherwise, it will not. The drawback is that for a two-sample q-q plot, quantifying the results becomes more complicated than a simple linear correlation, especially for a q-q plot comparing two data sets rather than a single data set to a known distribution function. Calculating a linear correlation coefficient gives artificially good results due to the sorting in Eq. 5.1 required when creating ECDs for the q-q plot, even for q-q plots that clearly deviate from linear. In our previous publication we erroneously used this method to determine the significance of the fit (Andersen and Dennison, 2015b). The methods that do exist, such as a two-sample Kolmogorov-Smirnov statistic or other methods, result in a confidence interval around the q-q plot that statistically gives a range of confidence of where the data actually are on the plot (Einmahl and McKeague,

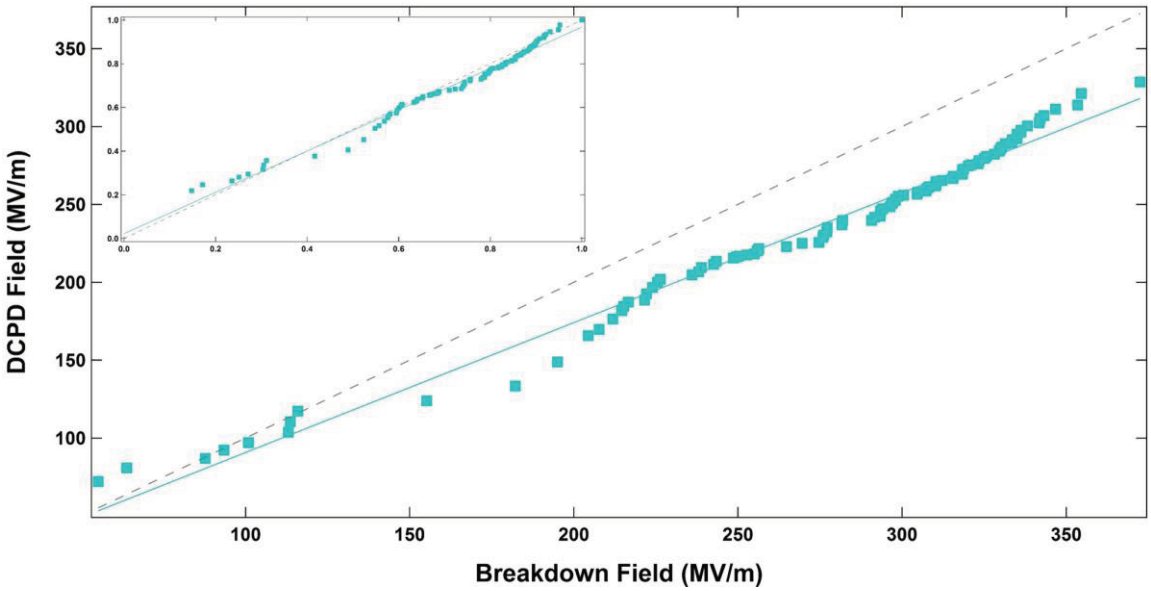

FIG. 5.12. Quantile-Quantile plot based of the ECDs for DCPD and breakdowns from LDPE tests in Fig. 5.11. Dashed black lines are unity slope for reference. The inset is the q-q plot with data normalized to the maximum field for each data type.

1999; Rosenkrantz, 2000; Valeinis*, et al.*, 2010). Further details are in Appendix B. From the author's perspective, such methods are not satisfying measures of the goodness or significance of the linear fit. For the purposes of this study, we contrast the q-q plots comparing DCPD and breakdowns to q-q plots of uncorrelated data in 6.2.5.

CHAPTER 6

RESULTS

This chapter discusses the results of the tests outlined in Chapter 4 that we used to evaluate the theory presented in Chapter 3, analyzed with methods described in Chapter 5. The results are summarized as follows. Voltage step-up tests show reasonable agreement with the dual-defect model proposed in this dissertation (Andersen and Dennison, 2015a; Andersen*, et al.*, 2015). SVET tests on LDPE show very good agreement with the dual-defect model (Andersen*, et al.*, 2015). Voltage ramp-rate tests did not agree well with predictions in a likely refutation of some simplifying assumptions (Andersen*, et al.*, 2016; Moser*, et al.*, 2017). Cursory temperature- and radiation-dependent tests show conceptual agreement with the Crine and dual-defect model (Andersen*, et al.*, 2015; Kippen*, et al.*, 2016). Finally, we show a significant correlation between DCPD and dielectric breakdown (Andersen and Dennison, 2014; 2015b).

6.1. Summary of Data

To date, the MPG has performed roughly 1000 breakdown tests on nearly a dozen different materials since 2007. Of these tests, those in Table 6.1. Detailed materials properties are listed in Appendix D. The SVET tests on LDPE took a total of 68 days of acquisition time. Measured endurance times conducted at electric fields from 180 to 290 MV/m spanned almost five orders of magnitude in time from ~10 s to several days. Many of the PEEK samples were exposed to high-energy β^- radiation, tested at elevated temperatures, or both. Thousands of DCPD measurements—primarily from the tests above—corresponding to hundreds of thousands of DCPD events were used for the q-q analysis.

6.2. Comparison of Empirical and Physical Models to the Breakdown Data

6.2.1. Step-up Test Results

We begin by comparing the ECD of the room temperature voltage step-up tests in BOPP, PI, LDEP, and PEEK to 2-, 3-, and 5- parameter Weibull distributions as shown in Table 6.2

$$P(F) = 1 - \exp\left(-\left[\frac{F}{F_0}\right]^{\beta}\right), \tag{5.2}$$

$$P(F) = 1 - \exp\left(-\left[\frac{F-F_s}{F_{0-F_s}}\right]^{\beta}\right), \tag{5.4}$$

Table 6.1. Summary of tests described in this dissertation.

Material	**No. of room temp. tests**	**No. of SVET tests**	**No. of voltage ramp rate tests**	**No. of temp. or radiation tests.**
BOPP	60	N/A	78	N/A
PI 2008	30	N/A	N/A	N/A
PI 2012-2013	38	N/A	N/A	N/A
PI 2017	29	N/A	29	N/A
LDPE	84	58	14	54 at different temps.
PEEK	11	N/A	N/A	76 at different temps. and doses.

and

$$P_{mix}(F) = p\left(1 - \exp\left(-\left[\frac{F}{F_{01}}\right]^{\beta_1}\right)\right) + (1-p)\left(1 - \exp\left(-\left[\frac{F}{F_{02}}\right]^{\beta_2}\right)\right). \quad 5.9$$

With Weibull fits for different materials, or even different batches of nominally the same material, we can begin to make comparisons. As stated before, F_0 corresponds to the 63.2% probability of breakdown and is reported as the nominal breakdown voltage. While F_0 is important, the shape parameter β is also critical as it indicates the stability of the material or in other words the width of the ECD. Higher values of β correspond to more stable materials. For example, the 2008 and 2017 batches of PI have very similar breakdown voltages but the much lower shape parameter in the 2008 batch indicates a greater likelihood of breakdown at lower voltages. We see that for BOPP and PI 2012-2013 a threshold field for breakdown can be clearly defined. For PEEK, which only had 11 tests, anything more complicated than a two-parameter Weibull is an exercise in futility; there simply are not enough data. Note that the ASTM standard for dc breakdown testing recommends only five tests (ASTM D 3755-14, 2014). Excepting cursory material comparisons, this seems woefully inadequate.

Let us first examine the ballpark breakdown values. Due to its application in the capacitor industry, BOPP breakdown strength has been widely investigated in recent years. Measurements using the large-area self-healing technique report BOPP breakdowns in the range of 500-700 MV/m for capacitor grade films (Xu and Boggs, 2006; Xu, *et al.*, 2008; Li, *et al.*, 2015; Kerwien, *et al.*, 2016; Ritamäki, *et al.*, 2017b). The measured value of $F_0 \approx 336$ MV/m (see Table 6.2) is between these two values, and is closer to the manufacture's value for the material used. However the manufacturer's value of breakdown for the BOPP used for tests at USU is 200 MV/m (Goodfellow Corp., 2017). Upon discussing this discrepancy at a conference it was suggested that the difference in intended material application by the manufacturer—and therefore different manufacturing processes—may explain this deviation (Boggs, 2017a). Additionally, the reported values were done using a very different test method where testing was allowed to continue beyond the initial breakdown (Xu and Boggs, 2006; Xu, *et al.*, 2008; Li, *et al.*, 2015; Kerwien, *et al.*, 2016; Ritamäki, *et al.*, 2017b). It has been shown that small-area tests tend to yield higher breakdown values for the same films compared to large-area tests; however, they acknowledge that this is largely due to increased likelihood of encountering extrinsic week points (Rytöluoto, *et al.*, 2015). For pristine samples, this is less likely to be the case.

For PI, our measurements are consistent with nominal breakdown fields at ~300 MV/m as reported by both the manufacturers and other experimentalists (Haq and Raju, 2006; Diaham, *et al.*, 2010; 2011; Goodfellow, 2016b). Polyethylene on the other hand comes in many flavors including high-density, low-density, and cross-linked and even just LDPE may have varying concentrations of crystalline phase polymer. Unfortunately, while experimental details are often sparse, extensive materials details can be even rarer. Examples of breakdown values with epoxy mold electrode tests report fields approaching 100 MV/m (Sekii and Kazama, 2004; Noguchi, *et al.*, 2008), roughly half of the 200 MV/m quoted by the manufacturer of our samples which is still significantly lower than the F_0 we measure at ~300 MV/m (Goodfellow, 2016a). For our very limited data set at room temperature for unirradiated PEEK we report a nominal breakdown strength of ~200 MV/m compared to the 110-150 quoted by the manufacturer and 400-500 MV/m reported in the literature for capacitor grade films generally with the self-healing method (Ho and Jow, 2009; Pan, *et al.*, 2009; Ho and Jow, 2013; Goodfellow Corp., 2016). Again the breakdown can

Table 6.2. Comparison of Weibull fits to voltage step-up tests.

Material	2-parameter Weibull function	3-parameter Weibull function	5-parameter Weibull function
BOPP	$F_0 = 337.0 \pm 0.8$ MV/m $\beta = 6.0 \pm 0.1$	$F_0 = 335.7 \pm 0.7$ MV/m $F_s = 170 \pm 10$ MV/m $\beta = 2.9 \pm 0.3$	$p = 0.24 \pm 0.05$ $F_{01} = 309 \pm 2$ MV/m $F_{02} = 349 \pm 3$ MV/m $\beta 1 = 13 \pm 2$ $\beta 2 = 5.4 \pm 0.2$
PI 2008	$F_0 = 264 \pm 1$ MV/m $\beta = 4.7 \pm 0.2$	$F_0 = 264 \pm 2$ MV/m $F_s = 0 \pm 90$ MV/m $\beta = 5 \pm 2$	$p = 0.14 \pm 0.03$ $F_{01} = 146 \pm 7$ MV/m $F_{02} = 273 \pm 2$ MV/m $\beta 1 = 10 \pm 8$ $\beta 2 = 6.5 \pm 0.4$
PI 2012-2013	$F_0 = 336.3 \pm 0.9$ MV/m $\beta = 6.6 \pm 0.2$	$F_0 = 336 \pm 1$ MV/m $F_s = 0 \pm 100$ MV/m $\beta = 7 \pm 3$	$p = 0.74 \pm 0.2$ $F_{01} = 330 \pm 5$ MV/m $F_{02} = 344 \pm 5$ MV/m $\beta 1 = 5.3 \pm 0.8$ $\beta 2 = 16 \pm 8$
PI 2017	$F_0 = 272.3 \pm 0.8$ MV/m $\beta = 7.7 \pm 0.2$	$F_0 = 271.1 \pm 0.9$ MV/m $F_s = 150 \pm 20$ MV/m $\beta = 3.2 \pm 0.7$	$p = 0.23 \pm 0.05$ $F_{01} = 230 \pm 1$ MV/m $F_{02} = 282 \pm 2$ MV/m $\beta 1 = 25 \pm 6$ $\beta 2 = 10 \pm 1$
LDPE	$F_0 = 316.4 \pm 0.7$ MV/m $\beta = 4.7 \pm 0.2$	$F_0 = 316.4 \pm 0.8$ MV/m $F_s = 0 \pm 200$ MV/m $\beta = 8 \pm 4$	$p = 0.41 \pm 0.04$ $F_{01} = 282 \pm 7$ MV/m $F_{02} = 323.8 \pm 0.8$ MV/m $\beta 1 = 3.6 \pm 0.3$ $\beta 2 = 17 \pm 1$
PEEK	$F_0 = 200 \pm 2$ MV/m $\beta = 4.9 \pm 0.4$	$F_0 = 200 \pm 2$ MV/m $F_s = 0 \pm 400$ MV/m $\beta = 10 \pm 10$	$p = 0 \pm 100$ $F_{01} = 0 \pm 5000$ MV/m $F_{02} = 0 \pm 2000$ MV/m $\beta 1 = 0 \pm 50$ $\beta 2 = 0 \pm 50$

be highly sensitive to details of the morphology (Ho and Jow, 2013). In the Chapter 6, we discuss in detail the importance of considering material variability.

Figure 6.1 shows the transformed ECD of breakdown data for these four materials together with Weibull and physics-model fits. Although, as shown here, mixed Weibull functions can provide a better fit to some data, it is difficult to infer any physical significance. It is plausible that the better fit is the result of

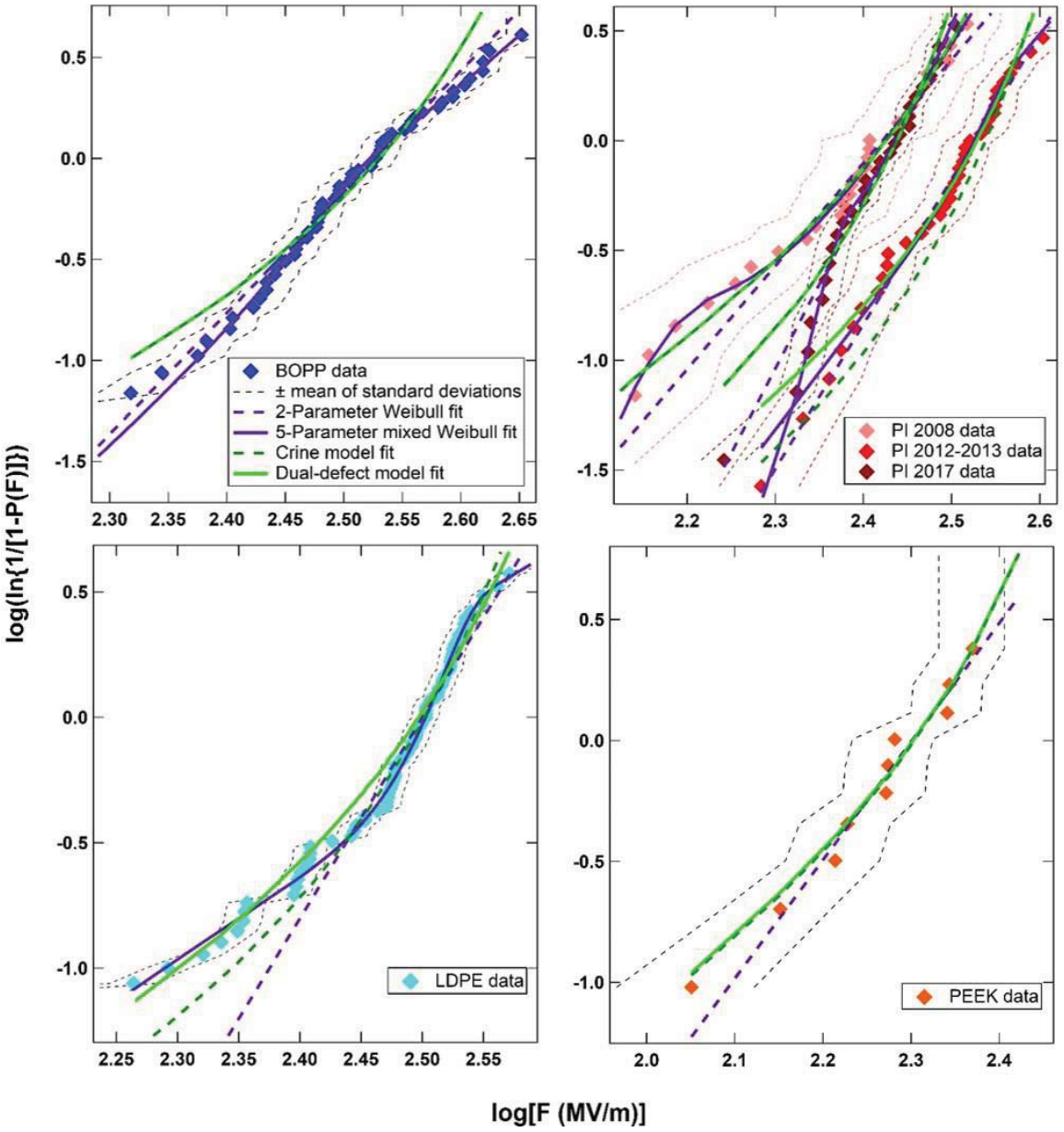

FIG. 6.1. Step-up to breakdown tests together with Weibull and physics-based fits for room temperature tests of (a) BOPP, (b) PI, (c) LDPE, and (d) PEEK. In each case the better of the 2- or 3-parameter Weibull fit (see Table 6.2) is shown.

simply adding more fitting parameters or perhaps there are indeed two breakdown modes or mechanisms requiring a mixture of two distributions. In either case there is not a straightforward way to extract intrinsic parameters of physical interest from the empirical fit (Laurent*, et al.*, 1994). Both the Crine model fits,

$$P_{step}^{Tot}\left(\Delta t_{step}, N_{step}, \Delta V_{step}, T\right) = 1 - \prod_{j=1}^{N_{step}}\left[1 - P_{def}\left(\Delta t_{step}, \frac{j\Delta V_{step}}{d}, T\right)\right], \quad 5.10$$

and the dual defect model fits,

$$P_{step}^{Tot}\left(\Delta t_{step}, N_{step}, \Delta V_{step}, T\right) = 1 - \prod_{j=1}^{N_{step}}\left[1 - P_{def}^{Tot}\left(\Delta t_{step}, \frac{j\Delta V_{step}}{d}, T\right)\right] \quad 3.7$$

result in estimations of defect energy and density. The fitting results are tabulated in Table 6.3.

Table 6.3. Comparison of Crine and dual-defect model fits to voltage step-up tests.

Material	**Crine model**	**Dual-defect model**
BOPP	$\Delta G_{def} = 0.99 \pm 0.01$ eV $N_{def} = (8.2 \pm 0.3) \cdot 10^{19}$cm^{-3}	$\Delta G_{def}^{HI} = 1.1$ eV $N_{def}^{HI} = 8.1 \cdot 10^{19}$cm^{-3} $\Delta G_{def}^{LO} = 1.0$ eV $N_{def}^{LO} = 8.2 \cdot 10^{19}$cm^{-3}
PI 2008	$\Delta G_{def} = 1.0 \pm 0.1$ eV $N_{def} = (9.1 \pm 0.4) \cdot 10^{19}$cm^{-3}	$\Delta G_{def}^{HI} = 1.1$ eV $N_{def}^{HI} = 7.1 \cdot 10^{19}$cm^{-3} $\Delta G_{def}^{LO} = 1 \pm 2$ eV $N_{def}^{LO} = (9 \pm 9) \cdot 10^{19}$cm^{-3}
PI 2012-2013	$\Delta G_{def} = 1$ eV $N_{def} = 1 \cdot 10^{20}$cm^{-3}	$\Delta G_{def}^{HI} = 1.03$ eV $N_{def}^{HI} = 1.3 \cdot 10^{20}$cm^{-3} $\Delta G_{def}^{LO} = 1.02$ eV $N_{def}^{LO} = 1.2 \cdot 10^{20}$cm^{-3}
PI 2017	$\Delta G_{def} = 1$ eV $N_{def} = 6 \cdot 10^{19}$cm^{-3}	$\Delta G_{def}^{HI} = 1.04$ eV $N_{def}^{HI} = 6.5 \cdot 10^{19}$cm^{-3} $\Delta G_{def}^{LO} = 1.02$ eV $N_{def}^{LO} = 6.4 \cdot 10^{19}$cm^{-3}
LDPE	$\Delta G_{def} = 1.02 \pm 0.08$ eV $N_{def} = (4.39 \pm 0.09) \cdot 10^{19}$cm^{-3}	$\Delta G_{def}^{HI} = 1.06$ eV $N_{def}^{HI} = 9.3 \cdot 10^{24}$cm^{-3} $\Delta G_{def}^{LO} = 1.0 \pm 0.2$ eV $N_{def}^{LO} = (3.8 \pm 0.2) \cdot 10^{19}$cm^{-3}
PEEK	$\Delta G_{def} = 1$ eV $N_{def} = 5 \cdot 10^{19}$cm^{-3}	$\Delta G_{def}^{HI} = 1.09$ eV $N_{def}^{HI} = 1.5 \cdot 10^{22}$cm^{-3} $\Delta G_{def}^{LO} = 0.96$ eV $N_{def}^{LO} = 4.8 \cdot 10^{19}$cm^{-3}

Uncertainties are only listed for parameters where the resulting uncertainties were not much larger than the parameters themselves. For such fits, Igor Pro still output repeatable results, even without complete fit convergence after a limited number of iterations. We first note that all results fall into the realm of physically reasonable results based on the range of realistic energies and densities discussed in 5.4.1.1. While the results are all near 1 eV and 10^{20} cm^{-3}, recall that even a few k_bT (~0.03 eV) represent significant differences in transition probabilities and therefore the results show significant variation from one sample to the next. Given that C-C bonds are 3.65 eV, we cannot rule out that two different LO-type defects may be contributing to breakdown if these results are to be taken at face value. As stated earlier, fitting step-up to breakdown data with physics-based equations is novel to the best of our knowledge. The product series used assumes that each step is statistically independent and thus neglects any aging (particularly changes in defect density). Relaxing this assumption would require solving Eq. 3.13 without neglecting the time dependence of $K_{def}^{\pm i}$. For this reason, we cannot expect the results to be exact, only indicative of the underlying physical mechanisms.

In Fig. 6.1, we note that for BOPP, PI 2008, PI 2017, and PEEK, the dual defect model gives essentially the same result as the Crine model. This is also evident in the similarities between the resulting defect energies. Applying Occam's razor, we must conclude that, in these cases we cannot claim any advantage over Crine's mean field approximation. In other words, this suggests that only one defect mechanism dominates for these materials in their corresponding test conditions. This is consistent with others' results for BOPP only showing bimodal behavior after significant thermal aging (Ritamäki*, et al.*, 2017b). For LDPE and PI 2012-13, the dual-defect fit is clearly an improvement over the Crine model fit. In a previous publication we suggested that, for LDPE, that when a mixed Weibull fit is better than a single Weibull fit there must be two underlying defect modes consistent with our dual-defect model of breakdown (Andersen and Dennison, 2015a). In other words, when a mixed Weibull fit is better than a single Weibull fit, we would expect that the dual-defect model fit would be better than a Crine model fit and in LDPE this is indeed the case. For PI 2012-2013 this is also true although the improvements are smaller. Fits to PI 2017 did not corroborate this conclusion, as the mixed Weibull is the best Weibull fit while both physics-based models give essentially the same result. Nevertheless, visually we see that the data for PI 2008 and PI 2017

agree very well at higher fields while deviating at lower fields. This perhaps indicates the same HI defect mechanism but different LO type defects, which seems reasonable for two flavors of the same material. While the physics-model fits do not show this, the mixed Weibull fits are indicative of such behavior. Turning to PEEK, we see that there is not enough data to tell whether any bimodal behavior exists, even with Weibull distributions.

To summarize, Weibull fits to step-up data are simple and practical for comparing materials or test conditions. When mixed Weibull fits are better than single Weibull fits, this may indicate multiple underlying defect mechanisms but in any case, Weibull statistics do not offer any estimations of the material defect energies and densities. Both Crine and dual-defect model fits offer estimates of defect energies and densities. Except in one case in this study, the dual-defect model is a better fit to obviously bimodal data.

6.2.2. Static Voltage Endurance Time Results

In this section, we discuss the results of SVET tests on LDPE. Fig. 6.2 shows the measured data for time to breakdown as a function of applied field for LDPE endurance time tests for the data acquired at 20 V per 3.5 s ramp rate to a static voltage. The green bars on the right axis indicate the time scales in larger units. Error bars in time for the data are less than the size of the symbols, except as shown at t_{en}<200 s. Error bars in electric field are largely determined by the ~2% variations in film thickness.

There is a definite transition between two separate field regimes evident in Fig. 6.2, suggesting that a new composite model is required which incorporates at least two defect mechanisms. The data below ~270 MV/m with endurance times on the order of a few hours to several days were dominated by the recoverable LO type defect processes and can be fit (red dashed curve) by the Crine model,

$$t_{en}(F,T) = \left(\frac{h}{2k_bT}\right) \exp\left[\frac{\Delta G_{def}}{k_bT}\right] \operatorname{csch}\left[\frac{\epsilon_0 \epsilon_r F^2}{2k_bTN_{def}}\right], \qquad 2.11$$

with ΔG_{def}^{LO}=0.95 eV and N_{def}^{LO}=7·10^{21} cm^{-3}. The data above ~270 MV/m with endurance times on the order of ~10 s to ~1 hr can also be fit (blue dashed curve) separately by Eq. 2.11 with ΔG_{def}^{HI}= 3.65 eV and N_{def}^{HI}=1.5·10^{18} cm^{-3}.

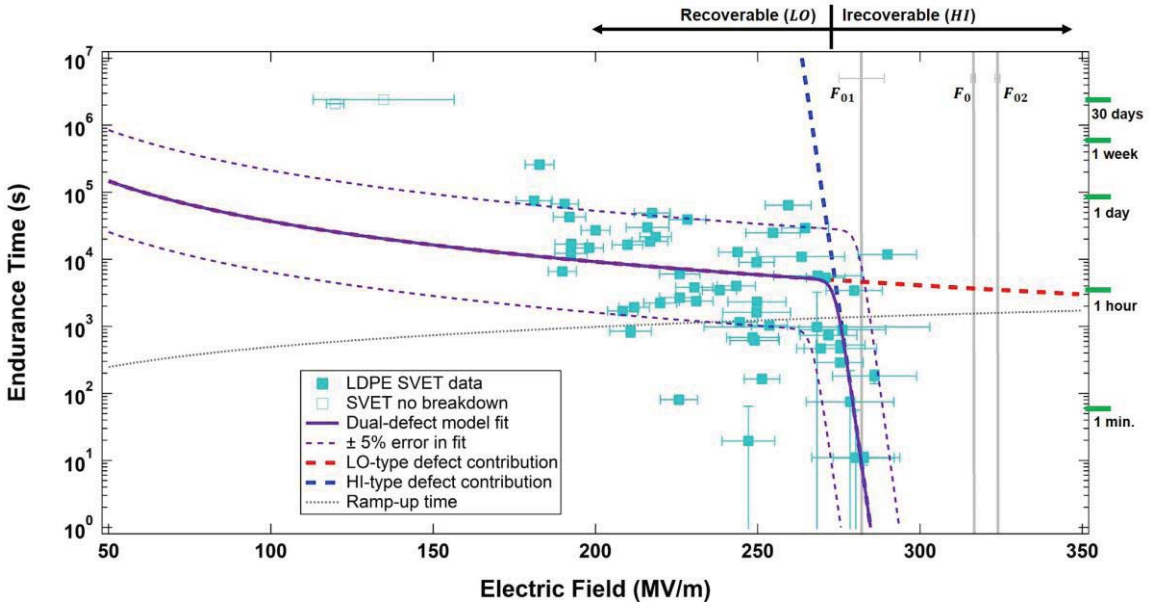

FIG. 6.2. Dual-defect mechanism model fit for endurance time data for LDPE. Data (solid cyan boxes) are fit (purple line) with the dual-defect extension of the Crine model given by Eq. 3.2, with ΔG_{def}^{LO}=0.95 eV, ΔG_{def}^{HI}= 3.65 eV, N_{def}^{LO}=7·10^{21} cm^{-3}, and N_{def}^{HI}=1.75·10^{18} cm^{-3}. The purple dashed lines show a ±5% variation in the ΔG_{def}^{LO} and ΔG_{def}^{HI}. The dashed lines indicates the separate contributions from *HI* (blue) and *LO* (orange) type defects. Two low field tests that were terminated without breakdown (open cyan boxes) are also included. The green bars on the right axis indicate the time scales in larger units. The grey dotted line shows the ramping time to a given field for the data acquired at 20 V per 3.5 s. Error bars in time for the data are less than the size of the symbols, except as shown when t_{en} <200 s. Error bars in electric field are largely determined by the ~2% variations in film thickness. Vertical grey lines correspond to the Weibull breakdown fields from voltage step-up tests.

Unlike the fits to the step-up tests, the defect energies for the fits were based on independent measurements of defect energy values for the fitting parameters and are in excellent agreement with the values discussed in Section 3.1.1.1. For *HI* type irreparable defects, ΔG_{def}^{HI} and N_{def}^{HI} agree with the predicted values N_{def}^{bb}≈1.5·10^{18} broken bonds/cm^3 and ΔG_{def}^{bb}=3.65 eV/bond (see 3.1.1). For *LO* type reparable defects, ΔG_{def}^{LO} and N_{def}^{LO} agree with the predicted values N_{def}^{K}≈3·10^{20} Kuhn pairs/cm^3 and ΔG_{def}^{K}=0.90 eV (see 3.1.1). Errors in the fitting parameters are estimated by assuming a ±5% deviation in the values of ΔG_{def}^{HI} and ΔG_{def}^{LO} used in

$$t_{en}^{Tot}(F,T) = \left(\frac{h}{2k_bT}\right)\left\{\sum_{i=HI,LO} \exp\left[\frac{-\Delta G_{def}^{i}}{k_bT}\right] \sinh\left[\frac{\epsilon_0\epsilon_r F^2}{2N_{def}^{i}k_bT}\right]\right\}^{-1} \quad 3.2$$

to produce the purple curves in Fig. 6.2; these show a maximum deviation in the endurance time of ~1 order of magnitude consistent with a spread in the measured data.

Included in Fig. 6.2 are two SVET tests at low applied field that were terminated prior to breakdown, giving a lower limit on the breakdown time observable at those fields. These are well above the predicted times extrapolated from the fit to the SVET tests with breakdowns. Although more experimentation is needed in this region, these results are consistent with the notion of a minimum threshold field for breakdown presented with published electrokinetic models (Lewis*, et al.*, 1996; Griffiths*, et al.*, 1998).

Note that the endurance time used to generate the purple curve in Fig. 6.2 is approximated as the elapsed time at the static field, and does not include the ramping (step-up) time (shown as the dotted back line). At short elapsed times this slightly overestimates the endurance time by underestimating the time the sample is exposed to a nonzero F. However, as discussed in 5.4.1.2, this effect is negligible compared to the spread in the data. Vertical grey lines corresponding to the Weibull centroid parameters from the fits to voltage step-up tests are shown for comparison. Interestingly F_{02} the critical field for lower-energy subdistribution of breakdowns corresponds with the transition in dominance between the two defect types. This suggests that LO type defects dominate low-field long wait time SVET behavior.

In summary, it is remarkable how well the dual-defect model fits the observed data using independent estimations of defect energies in LDPE (see Table 6.4). The corresponding defect densities are also in good agreement with such estimations. The Crine model can be fit to a portion of the observed data for each defect type, but the predictions clearly deviate significantly over the whole range of measurements. We note that confining fits to step-up tests to use these same energy values results in predictions much narrower than the range of observed results; hence, the different values from fits in the previous section. At lower fields, we note there may be deviation toward a non-zero threshold field, which is not built into the dual-defect or Crine models directly. Nevertheless, this is perhaps the most compelling evidence we present in favor of the dual-defect model.

Table 6.4. Defect energies and densities from SVET fits and independent measurements.

Method	***HI*-type Defects**	***LO*-type Defects**
Estimations from independent materials properties (see 3.1.1)	ΔG_{def}^{bb}=3.65 eV/bond N_{def}^{bb}≈1.5·10^{18} broken bonds/cm^3	ΔG_{def}^{K}=0.90 eV N_{def}^{K}<3·10^{21} Kuhn pairs/cm^3
SVET Fitting Parameters (see Fig. 6.2)	ΔG_{def}^{HI}= 3.65 eV N_{def}^{HI}=1.75·10^{18} cm^{-3}	ΔG_{def}^{LO}=0.95 eV N_{def}^{LO}=7·10^{21} cm^{-3}
Comparison of fitting parameters and independent estimations of materials properties	$\Delta G_{def}^{HI}/\Delta G_{def}^{bb} = 1$ $N_{def}^{HI}/N_{def}^{bb} \approx 1.16$	$\Delta G_{def}^{LO}/\Delta G_{def}^{K} \approx 1.06$ $N_{def}^{LO}/N_{def}^{K} \approx 2.33$

6.2.3. Voltage Ramp Rate Dependence Results

In this section we exam the effect of voltage ramp rate on the breakdown field. Each set of ramp rate tests was compiled into a single graph for each material, showing the breakdown field at that ramp rate. Fig. 3.3 shows the breakdown field versus ramp rate for three polymeric materials: BOPP, PI, and LDPE. The starting point for this study was existing data from our early experiments on Kapton E that we had found to follow Eq. 3.5 reasonably well (Andersen*, et al.*, 2016; Moser*, et al.*, 2017). However, as shown in Fig. 4.10, recent analysis of the Kapton E data has identified unacceptably high field-enhanced current for our circuit, severely altering the voltage ramp rate and for this reason, they cannot be compared to the data shown here. This may explain why Kapton E results did not agree with the general behavior shown in this section.

To review, the voltage ramp rate dependence models considered here are:

(i) the constant value model

$$F_{ESD} = C, \tag{3.3}$$

(ii) the standard empirical model (Dissado and Fothergill, 1992)

$$F_{ESD} \approx \left(\frac{\partial F}{\partial t}\right)^{A/A+B} \text{ or } F_{ESD} = C\left(\frac{\partial F}{\partial t}\right)^{A/A+B}, \tag{3.4}$$

(iii) the simplified physical model based on the Crine model (Andersen*, et al.*, 2016; Moser*, et al.*, 2017)

$$F_{ESD}(r) \approx F_{ESD}(r_0)\sqrt{\gamma \ln\left(r + \sqrt{1 + r^2}\right)} \tag{3.5}$$

and

(iv) the more complicated ramp-up probabilistic model stemming from the Crine assumptions (Andersen*, et al.*, 2016)

$$P_{step}^{Tot}\left(\Delta t_{step}, N_{step}, \Delta V_{step}, T\right) = 1 - \prod_{j=1}^{N_{step}}\left[1 - P_{def}^{Tot}\left(\Delta t_{step}, \frac{j\Delta V_{step}}{d}, T\right)\right]. \quad 3.7$$

Each of these models are used as fits to the data in Fig. 6.3. We see in Fig. 6.3 that the assumption that the breakdown field is constant independent of ramp rate is not a bad model. For each of these data sets, allowing the fitting parameters a and b of the empirical model to be negative, results in reasonable fits as well. Surprisingly, this would predict slightly lower breakdown fields with increasing ramp rate. It should be noted, however, that the uncertainties in a and b are much larger than the best-fit values, effectively reducing Eq. 3.4 to Eq 3.3. For these three materials, both the simplified physical model and the stochastic model are obviously poor fits to the data.

The probabilistic model Eq. 3.7 did not provide a good fit to any of the data, using standard least squares fitting routines. In each case, the modified Igor Pro fitting software returned the error "there may be no dependence on these parameters." We were able to obtain fits with the stochastic model, by restricting the data fit to those tests where the time step Δt_{step}=4 sec was held constant. Fortunately, this was the case for almost all for the data included in Fig. 6.3. Given the poor results and the difficulty involved in developing a Crine-model fitting routine for ramp-rate dependence, dual-defect model fits were not attempted.

The failure of the physics based models likely shows that the assumptions—particularly that each ramp step is independent and that defect densities are constant—made in their formation are not valid for these tests. Relaxing these assumptions would require solutions to the differential Eq. 3.13 discussed in 3.2.1. As shown in Sections 6.2.1 and 6.2.2, theory derived from these same assumptions matched data quite well for voltage step-up tests and very well for SVET tests. Perhaps this improvement is in part because we showed that considering the ramp-up to the static waiting voltage did little to alter the predicted outcome. Here, each voltage step has the same duration in time. One could expect that at low voltages—when the applied field does not distort the defect energy much—there would not be significant changes to the materials defect structure. However, at voltages near breakdown, new defects could be created or even

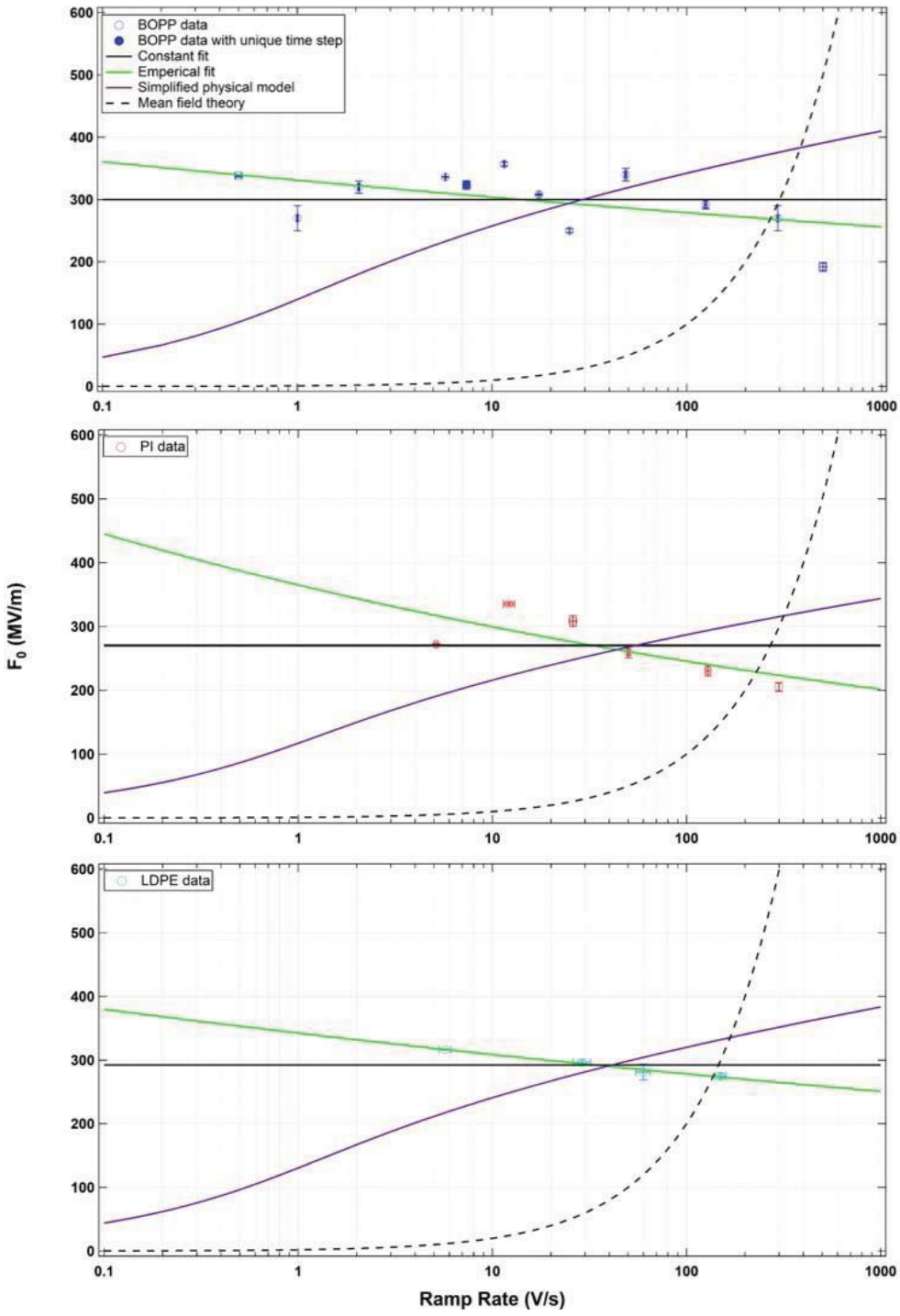

FIG. 6.3. Plots of the Weibull characteristic breakdown field vs voltage ramp rate with constant, empirical and physics-model fits.

annealed via local heating; this contradicts the assumption that each voltage step is independent of the others.

The results of the current study favor the model that breakdown is approximately constant with respect to voltage ramp rate. More testing, especially at slower ramp rates (the most time consuming tests), would be helpful in testing the voltage ramp rate dependence of breakdown. Tests of similar ramp rates using different voltage steps and corresponding time increments would investigate separately the dependence of ΔV_{step} and Δt_{step} in the physics based models,

A significant result, discussed in Section 4.6.4, is that slower ramp rates reveal insightful behavior that is unclear or indistinguishable at faster ramp rates. The most salient result of this study, however, is that slower ramp rates also yield more accurate and precise data simply because the step size is smaller.

6.2.4. Temperature and Radiation Dependence Results

To review the temperature dependence of our model let us review Eq. 3.1 (which reduces to the mean field Crine model for one defect type).

$$P_{def}^{Tot}(\Delta t, F, T) = \sum_{i=HI,LO} P_{def}^{i} = \left(\frac{2k_bT}{h/\Delta t}\right) \sum_{i=HI,LO} \exp\left[\frac{-\Delta G_{def}^{i}}{k_bT}\right] \sinh\left[\frac{\epsilon_0 \epsilon_r F^2}{2N_{def}^{i} k_bT}\right] \qquad 3.1$$

As discussed in Chapter 3, and 5.4.2, temperature place a role in the probability of breakdown as it varies the phonon frequency, the various Boltzmann factors, and the defect density N_{def}^{LO}. Similarly, incident radiation may directly change N_{def}^{i} for either HI or LO species, and, at least during exposure, effect the conductivity through RIC, or even raise the temperature. In this section, we review some preliminary tests on the effects of temperature and radiation on breakdown.

Fig. 6.4 (a) shows data for all MPG ESD tests on LDPE to date (excluding voltage ramp rate tests) across temperatures ranging from ~130 K to ~325 K. Temperature dependent tests are much more time consuming than room temperature tests primarily due to heating and cooling times to reach the target temperature and returning to room temperature for vacuum breaks. Some additional complexity is added by using liquid nitrogen, coolant, or heaters together with temperature monitoring. For this reason, data are particularly sparse at the lowest temperatures. At higher, more accessible temperatures, there is a greater

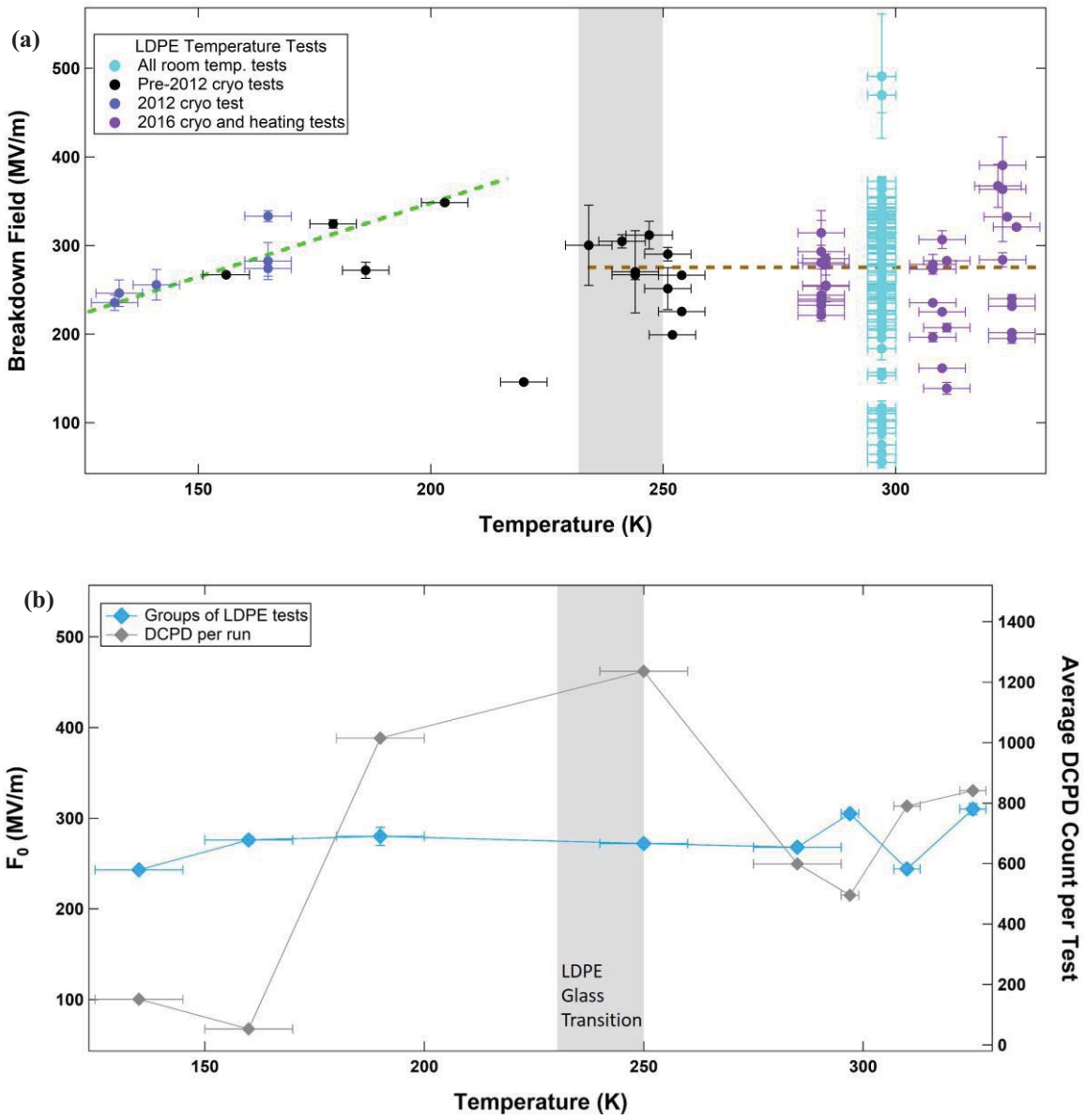

FIG. 6.4. Temperature effects on LDPE. (a) All LDPE standard ramp-up test data across temperatures from ~130 K to ~325 K. (b) Weibull scale parameter and average DCPD count for groups of tests of similar temperatures.

data density but also a greater spread in the data since more tests were done at these temperatures. We present the following two explanations of the observed data in Fig. 6.4 (a).

First, that over the ranges tested there is no significant temperature dependence for LDPE since the spread of data from 55-490 MV/m is large compared to the apparent trend at lower temperatures that only

ranges from 235-348 MV/m. Fig. 6.4 (b) shows only ~20% change in the Weibull characteristic breakdown with temperature. To do even simple Weibull analysis, tests of similar temperatures had to be grouped together, especially at lower temperatures.

Second, we might be beginning to observe a small linear temperature dependence of F_{ESD} for LDPE in the range of ~130 K to ~240 K (dashed green line). There seems to be an abrupt change to a nearly temperature-independent behavior above ~240 K (dashed brown line). These data are consistent with higher temperature measurements by Shinyama (Shinyama and Fujita, 2006) who observed a roughly temperature-independent breakdown field strength of ~450 MV/m over 295 K to 330 K at 1 kV/s ramp rates for similar 25 μm thick LDPE samples; F_{ESD} then decreased linearly to ~250 MV/m at 385 K.

This transition in electric field strength in LDPE may be related to a LDPE structural phase transition (Dennison and Brunson, 2008). This β transition is routinely observed in branched polyethylene, and has been associated with conformational changes along polymer chains in the interfacial matrix of disordered polymers between nanocrystalline regions in the bulk. Similar abrupt (often discontinuous) changes near ~250 K have been seen in prior studies of mechanical and thermodynamic properties (Anderson*, et al.*, 2004) and electron transport properties including dark current conductivity (Dennison and Brunson, 2008; Dennison*, et al.*, 2009) radiation induced conductivity (Dennison*, et al.*, 2007; Dennison*, et al.*, 2009; Gillespie*, et al.*, 2014), loss tangent (Phillips, 1983) and dielectric constant (Phillips, 1983). These changes may result from a discontinuous change in the activation volume at the glass transition to allow a smaller field value to bring about complete breakdown.

Fig. 6.4 (b) also shows the average DCPD count per run versus temperature for LDPE. We see that the discretized DCPD count is significantly reduced <200 at the lowest temperatures. The large discontinuity above ~250 K where the count drops by ~50% and then begins to increase again from ~280 K to ~330 K may be due to the glass transition in LDPE occurring over the temperature range discussed above. Given that we model DCPD as primarily driven by LO type defects, we expect them to vary significantly with temperature as has been observed.

We also examine preliminary tests of breakdown and DCPD in PEEK at elevated temperatures and as a function of β^- dose (acquired at the Idaho Accelerator Center) ranging from ~10 to ~70 MRad

(Kippen*, et al.*, 2017). Given the discussion in 3.1.1 and 3.2 temperature should effect N_{def}^{LO} while dose should effect both N_{def}^{LO} and N_{def}^{HI}. Radiation may also change ΔG_{def}^{HI} by introducing new high-energy defect modes and effecting the average chemical defect energy. Fig. 6.5 (a) shows the average DCPD count per run versus temperature and irradiated dose for PEEK. Like with LDPE, there is a trend to increased DCPD with increasing temperature. For the unirradiated samples, the average DCPD count increased from 1 to 132 as temperature increased from 280 K to 360 K. The DCPD per run also increase significantly with increased dose. For room temperature tests, the DCPD count increased by more than a factor of three at 75 Mrad compared to the unirradiated PEEK. The trend of breakdown field increasing with dose is much clearer than the effect of temperature at a given dose (There is a single outlier at the highest radiation (75 MRad) and temperature (~360 K). Fig. 6.5 (b) shows the breakdown electric field versus temperature and dose from the same tests of PEEK. Note the similarities in the shape overall dose and temperature dependence between breakdown field and DCPD count. The changes in breakdown field in PEEK with dose and temperature range between one and four times the magnitude of the ~20 MV/m average uncertainty in the breakdown fields.

These measurements show that DCDP depend on both temperature and on defect density through radiation dose. As suggested by the discussion in Section 3.2, higher temperatures lead to more low-energy defects and increased likelihood of completing a percolation network leading to more DCPD. Alternately, increased dose increases defect density (especially HI type defects since presumably LO type defects will tend to anneal out over time between irradiation and breakdown measurements), and thereby reduces the density of low-energy defects required to complete the percolation network. The temperature and dose trends in Fig. 6.4 (b) and Fig. 6.5 (a) are qualitatively consistent with the dual–defect model. We expect temperature difference to effect LO type defect processes, especially DCPD and the lower portion of the breakdown distributions. Although it is clear that additional tests are needed to enhance the comparisons presented here, the limited breakdown data at different temperatures and doses indicate trends consistent with expected behaviors. Q-q analyses for the tests at various temperatures and doses described in this section are quite sparse given the limited breakdowns at each unique combination of dose and temperature.

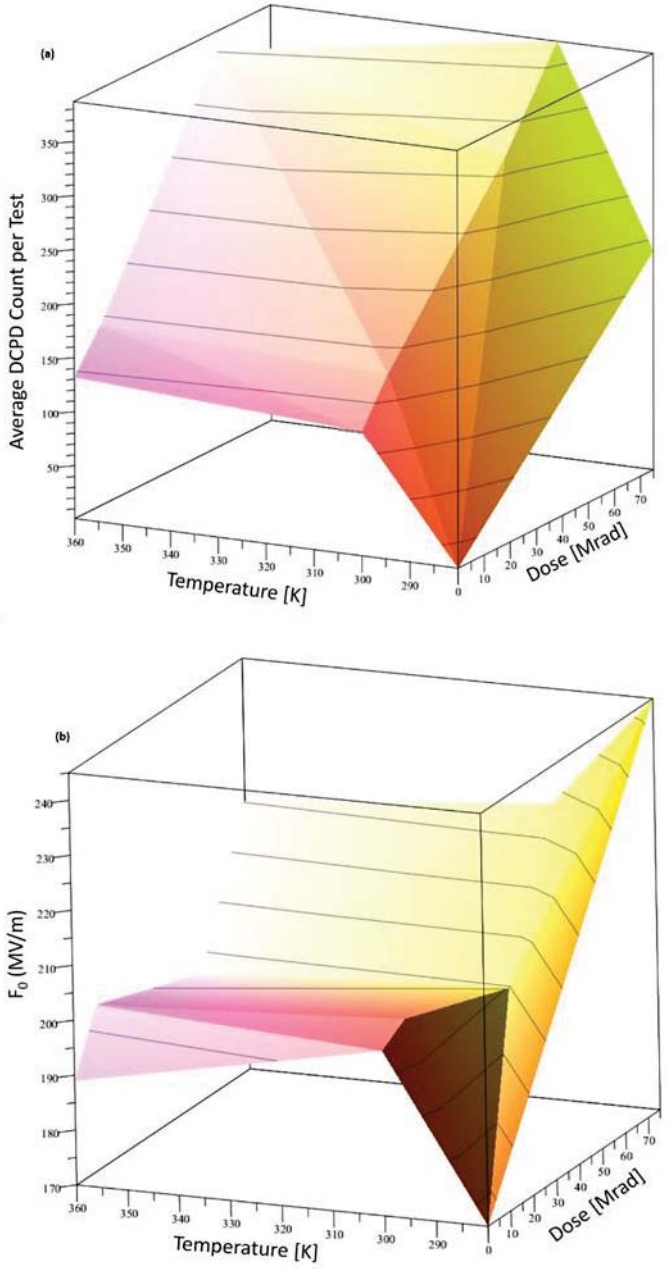

FIG. 6.5. Temperature and dose effects in PEEK. (a) Average DCPD count per run versus temperature and dose for PEEK. (b) Nominal breakdown electric field versus temperature and dose for PEEK. Note the similarities in temperature and dose dependence.

Nevertheless, these appeared to show good correlation except for PEEK samples having been exposed to 75 Mrad.

In summary, for LDPE and PEEK tests discussed here, we see that DCPD are sensitive to temperature and radiation damage. This result agrees qualitatively with the dual-defect model that considers both recoverable and irrecoverable defect species. Both breakdown and DCPD may be affected by the glass phase transition in LDPE. PEEK tests show a significant effect on breakdown with dose, but although there are hints at temperature dependence of breakdown, future tests will be needed to clarify these results.

6.2.5. Comparison of Breakdown and Pre-Breakdown Event Quantiles

We now transition to the results from the q-q analysis explained in 5.5.3. These q-q plots compare the ECDs of breakdown events and the observed DCPD. Fig. 6.6 (a)-(d) contain the q-q plots for DCPD and breakdowns of LDPE, PI, PEEK, and BOPP, respectively. Plots are shown with room temperature data except Fig. 6.6 (c) for PEEK. As shown above, PEEK tests were spread across several temperatures and doses. For PEEK, data from tests done at 360 K are shown. The DCDP count accuracy for the few room temperature tests was reduced due to field-enhanced conductivity and erratic current traces convoluted with the DCPD. Due to the difficulty of counting DCPD between the last baseline current and breakdown, we re-plot the q-q plots normalized to the maximum field value in the insets (Andersen and Dennison, 2015b). Clear outliers in measured breakdown field values, attributed to extrinsic sample damage or instrumentation issues identified above, were neglected in the statistical analysis presented in this study; this represented less than 1% of the tests considered here (Andersen and Dennison, 2015a).

To contrast the q-q plots in Fig. 6.6 observe the two q-q plots of two pairs of arbitrary uncorrelated data sets shown in Fig. 6.7. Fig. 6.7 (a) compares vacuum chamber pressure and sample thickness from the LDPE room temperature data. Fig. 6.7 (b) compares the DCPD events from LDPE to the measured sample thicknesses of PI. Unlike the q-q plots in Fig. 6.6, these clearly do not exhibit a linear trend, indicating that the variables chosen are not correlated, as expected.

It is clear from Fig. 6.6 that the DCPD and breakdowns are related for each of the polymers studied. Except for PI, the normalized q-q plots suggest that not only are the underlying distribution

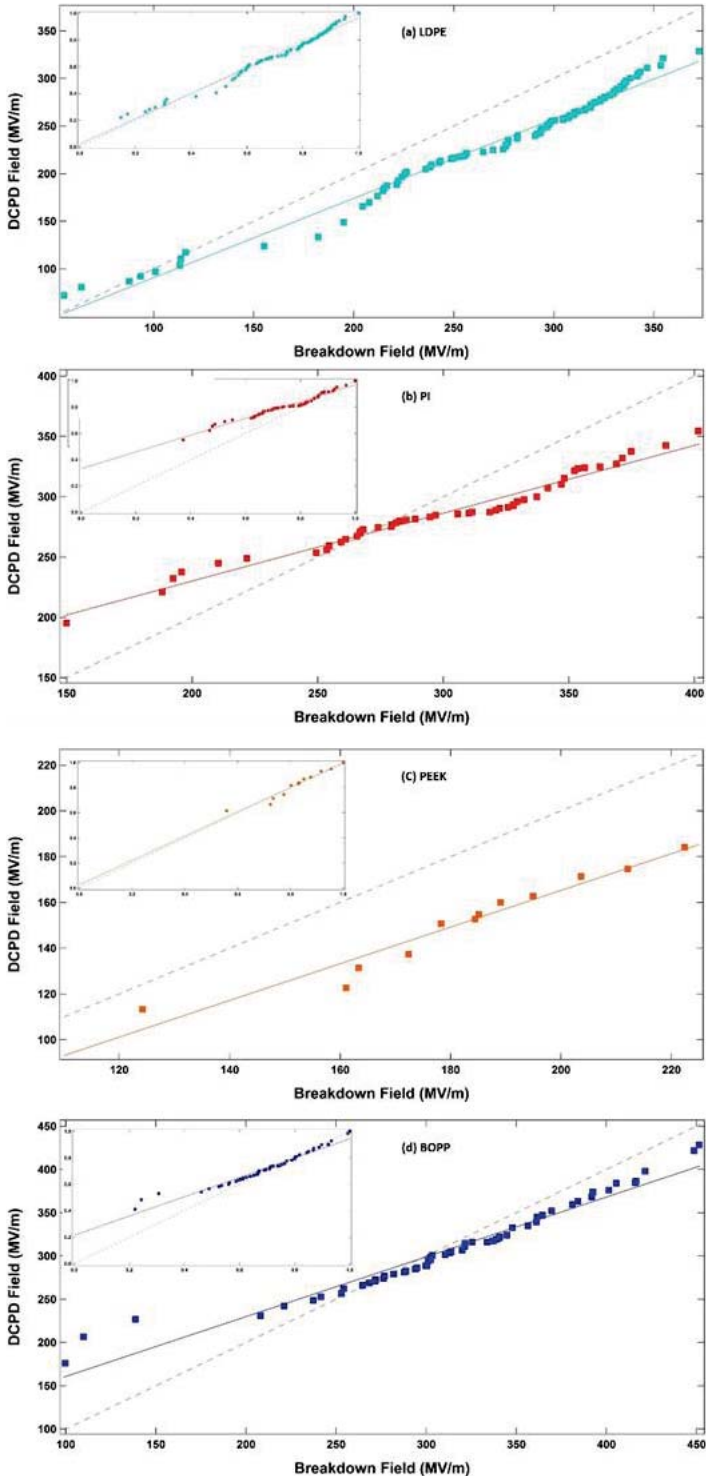

FIG. 6.6. Quantile-Quantile plots of DCPD and dielectric breakdowns with linear fits. Dashed black lines are unity slope for reference. Insets are normalized to the maximum field for each data type. (a) LDPE (b) PI (c) PEEK (d) BOPP.

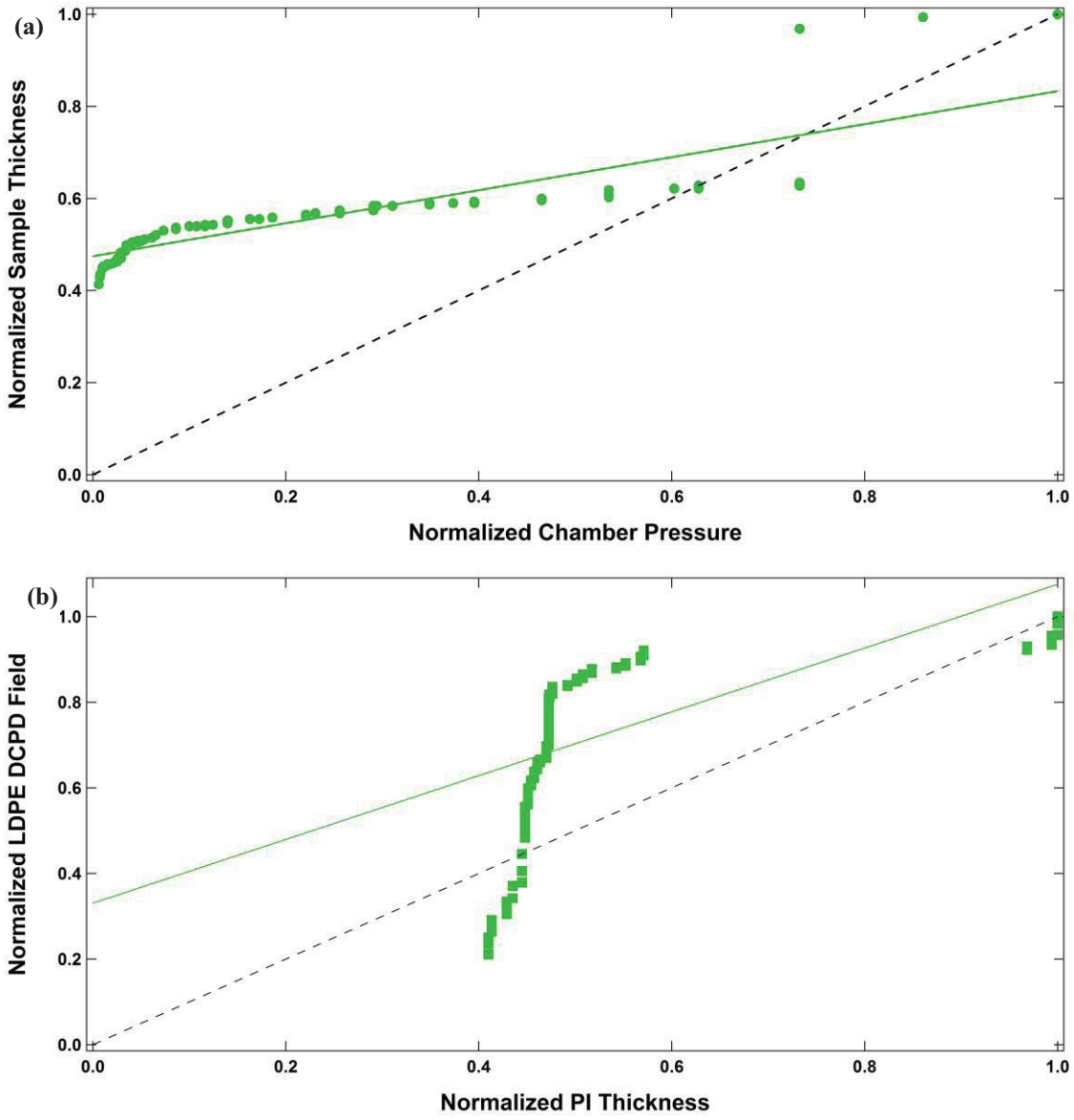

FIG. 6.7. Quantile-Quantile plots of two uncorrelated data sets each and linear fits. Dashed black lines are unity slope for reference. (a) Sample thickness and chamber pressure from a set of breakdown tests. (b) DCPD in LDPE tests and PI sample thickness.

functions of DCPD and breakdowns correlated, they are nearly identical. To show the predictive power of this method, Fig. 6.8 is a q-q plot comparing the DCPD from 5 step-up runs of LDPE to 14 breakdowns from different tests from the same batch of material. Unlike the plots in Fig. 6.6, the DCPD used are not from the same runs as the breakdowns to which they are compared. Although there is a single outlier at

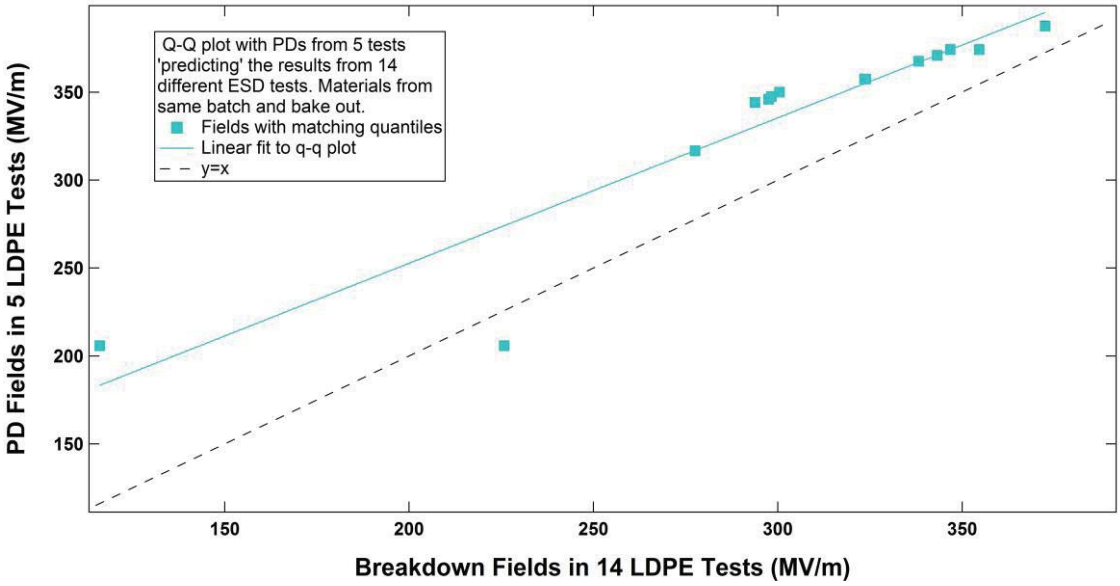

FIG. 6.8. Quantile-Quantile plots of DCPD and breakdowns from different tests with linear fit. Dashed black line is unity slope for reference.

~230 MV/m, this exercise strongly suggests that there is a fundamental underlying relationship between the likelihood of DCPD and the likelihood of dielectric breakdown. Comparing DCPD to breakdowns from different batches do not yield linear q-q plots.

Given that many DCPD are observed during a single breakdown test, using the DCPD distribution as an estimate for the distribution of breakdowns, the characterization of HVDC insulating material, especially the inception field, can be greatly expedited. With further development, the correlation of DCPD and breakdown could be applied to condition monitoring diagnostic techniques similar to those used to detect and localize ACPD (Zhu*, et al.*, 2017). This connection between DCPD and breakdown may be the most significant result of this dissertation.

CHAPTER 7

CONCLUSIONS

This final chapter provides of summary of the context and conclusions drawn from the work in this dissertation. This will include a discussion of the contributions to the theoretical descriptions of breakdown and dc partial discharge (DCPD), comments on how the work here effects the application of this work—particularly in the field of spacecraft charging, and potential future work related to the research presented here.

7.1. Physical Insights in Context of the Others' Work

This dissertation is primarily concerned with what we call the dual-defect model of electrical aging. The term electrical aging encompasses dielectric breakdown, DCPD, and the variable nature of the material itself due to fluctuations in defect density allowed under the theory. As we have shown, our model is a simple extension of Crine's mean field theory for electrical aging that can be derived from thermally assisted hopping transport in highly disordered insulating materials (Miller and Abrahams, 1960; Ambegaokar*, et al.*, 1971; Crine*, et al.*, 1989; Crine, 1999). We simply consider the mean contributions of two defect species rather than one—or the average contribution of all defects—and allow the lower energy of the two defect types to vary significantly with temperature and electric field stress.

The notion of two defect flavors, physical and chemical or deep and shallow, or HI and LO as they have been referred to here, is not in itself novel, even in terms of aging models with static defect density (Chen, 2014). The uniqueness of the physical theory is from: (i) applying two defect types to a Crine-like model, and (ii) in such a model allowing for variable defect densities. To be fair, we do not always use both of those assumptions simultaneously in every case presented here due to the difficulty in solving the differential equation Eq. 3.13 for the time evolution of the defect density. Lewis' model is conceptually similar for a single variable defect type. However, as we have shown, ignoring the time dependence of the defect creation and annihilation operators invalidates his and other similarly simple results (Lewis*, et al.*, 1996).

Without correcting for the variable nature of defects, the limiting behavior of the Crine model is shown to be non-physical, (see Section 3.2). Crine himself in his most recent published work acknowledges that the state of the theory is very incomplete (Crine, 2016b). Other recent work in this area has included phenomenological computer modeling of breakdown (Palit, 2014). While we do not claim that the dual-defect model is not without limitations (*e.g.*, it fails to predict observed ramp rate data), it represents a significant contribution to the theory of aging and breakdown in HDIM and has already been recognized as such in a new book on the topic (Raju, 2016). While it is still an approximation, we have shown in several cases that it is an improvement over the simpler mean field approximation.

We present what is perhaps the first physics-based modeling of voltage step-up tests. Although the results between static voltage endurance time (SVET) and step-up tests in LDPE are not in perfect agreement, this represents a step toward establishing an equivalence between the two methods (Dissado and Fothergill, 1992). To the best of our knowledge, we also present what is the first theoretical description of dc electrical aging that encompasses both dielectric breakdown and DCPD.

7.2. Important Applications

Apart from the contributions to the physics theory of aging in HDIM, this work has many practical applications. The practical improvements or potential improvements stemming from this work are outlined in this section.

7.2.1. Considerations for DC Dielectric Breakdown Testing

Sections 4.1 and 4.6.4 outline the operational definition of breakdown developed for MPG ESD testing (Andersen and Dennison, 2017). This definition based on a voltage-dependent threshold together with the requirement of sustained ohmic breakdown current is much less sensitive to false positives and false negatives cited in the ASTM standard test method (ASTM D 3755-14, 2014). The phenomena that might otherwise cause false positives such as DCPD or flashover are now clearly identifiable. This test method requires continuous or at least intermittent active current monitoring rather than a fuse or breaker that will trip with elevated leakage current.

Additionally, we show that for step-up tests, slow ramp rates at ~1% of the recommended 500 V/s greatly improve the precision and accuracy of tests, due primarily to simply having smaller voltage step sizes.

In Section 6.2.1, we show that there can be significant variation in results for nominally the same material. This underscores the need, especially for very sensitive applications, to test the material from the same manufacturer and preferably, the same batch of materials as what will be used in application to the extent possible. More comments on this are in the Section 7.2.2.

7.2.2. Considerations for Spacecraft Charging Mitigation

The primary context for the USU materials physics group (MPG) research for over the past two decades has been spacecraft charging effects. To that end, most of the work done in this dissertation was with this application in mind. This section reviews considerations stemming from the work done in this dissertation that should be of interest to space environment effects engineers.

The risk presented by electrostatic discharge (ESD) varying greatly from mission to mission depending on the specific space environment conditions and spacecraft configuration and relevant time scales range from hours (orbital periods) to decades (mission lifetimes) (Dennison, 2015). Depending on the space plasma environment, material selection, material thicknesses (either thin films and coatings or virtual capacitors set by charge deposition and range) potentials may range from hundreds of volts to tens of kilovolts (Dennison, 2015). Spacecraft charging effects mitigation standards offer the following guidelines for spacecraft modelers to design spacecraft systems to be immune to the effects of expected ESD pulse characteristics and frequencies:

- Refer to a table of breakdown voltage values for common insulators measured using standard methods (NASA HDBK-4002A, 2011; Garrett and Whittlesey, 2012; ASTM D 3755-14, 2014).
- For materials not listed in available tables use a conservative estimate. Spacecraft charging standards estimate minimum breakdown thresholds—below which spacecraft are assumed to be safe from ESD—over a wide range of 1 to 20 MV/m (Rodgers and

Hilgers, 2003; NASA HDBK-4002A, 2011; Garrett and Whittlesey, 2012; JERG-2-211A, 2012).

- Test specific materials and components to be used to determine breakdown thresholds and add a safety margin either by testing in conditions exceeding expected worse case scenarios or simply assuming the thresholds stated above (Rodgers and Hilgers, 2003; NASA HDBK-4002A, 2011; Garrett and Whittlesey, 2012; JERG-2-211A, 2012).
- Given a breakdown voltage threshold, use spacecraft charging software to estimate the time the spacecraft will spend at potentials at or exceeding the threshold value and assess the ESD threat for the mission (Rodgers and Hilgers, 2003; ISO, 2011; NASA HDBK-4002A, 2011; Garrett and Whittlesey, 2012; JERG-2-211A, 2012).

As we have shown, dielectric breakdown is a complicated, stochastic, process. In the cases of sensitive missions and/or extreme charging environments, the concept of dielectric strength may not be well approximated by a constant value. Nevertheless, breakdowns strengths are most often represented by a single value, perhaps with the occasional caveat that it may depend on thickness or temperature (NASA-CR-149341, 1972; NASA-CR-165590, 1982; Cho*, et al.*, 2005; NASA HDBK-4006; ISO 11221, 2011; NASA HDBK-4002A, 2011; Garrett and Whittlesey, 2012). Concurrently, guidelines and relevant literature also strongly advise that materials be tested for their specific application (NASA-CR-149341, 1972; Ferguson, 2007; ISO 11221, 2011; NASA HDBK-4002A, 2011; Garrett and Whittlesey, 2012; JERG-2-211A, 2012). We now briefly discuss how physical theories of breakdown can improve mission relevance of tests, what tests to consider, and how to interpret their results.

As presented As presented in Chapters 2 and 3, physical models of conductivity and breakdown in insulating materials are driven by the distribution of electronic defect energies and densities, temperature, applied electric field, the time over which a given set of conditions persists, and the history of the materials (aging). Assuming static, intrinsic, defect energies and densities, the breakdown strength may vary significantly with extrinsic conditions such as temperature and charging rate. One should also be aware of aging effects, contamination, or even variations in manufacturing methods or conditions as any of these can significantly alter defect populations and therefore charging properties (Dennison, 2015; Saiki*, et al.*,

2015). Breakdown field strengths can evolve as the interaction with the space environment modifies the defect distributions and conductivity. For example, radiation damage from the space environment can introduce new defects and increase the defect density, thereby affecting the distributions of ESD events. For most space missions it is important to bake test samples *in vacuo* to drive off water and other volatile compounds which can significantly affect conductivity, work function and electron emission (Garrett and Whittlesey, 2012; Dekany*, et al.*, 2013; Andersen*, et al.*, 2015; Dennison*, et al.*, 2016a). Given these effects, consider the following:

A. Zeroth Order Breakdown Testing

Look Up a Number. Spacecraft charging standards from different space agencies estimate a lower bound for ESD threshold fields below which the risk of ESD is insignificant (Rodgers and Hilgers, 2003; NASA HDBK-4002A, 2011; Garrett and Whittlesey, 2012; JERG-2-211A, 2012). Although these recommended values range over an order of magnitude, it is noteworthy that they represent an ESD design criterion that does not depend on temperature, charging history, or even material!

To estimate such an absolute lower bound in the electric field physically needed to achieve breakdown, we assume that breakdown is a cascade process where a liberated charge (*e.g.*, an electron) q_e must gain enough energy $\Delta\mathcal{E}$ through its motion over a distance a through an electric field F_{min} to liberate additional charges upon impacting another defect. This threshold field is given in one dimension by

$$F_{min} = \frac{\Delta\mathcal{E}}{q_e a}. \tag{7.1}$$

it is reasonable to assume that the lowest possible defect energies that could contribute to ESD must greater than a few $k_b T$ at room temperature, *i.e.*, >0.1 eV. Assuming a maximum average defect spacing, a, smaller than 10^{-7} m gives, as a limiting case, that electric fields below 1 MV/m can be considered safe for insulators in general. This agrees with the lowest value cited in a charging standard (JERG-2-211A, 2012). For fields above 1 MV/m more consideration is required. Turning from extreme cases to more realistic estimates, one can expect ionization energies of 1-10 eV and defect spacings closer to ~10^{-8} m, resulting in minimum breakdown fields on the order of 10-100 MV/m.

The next logical step might be to be look up the tabulated dielectric strength of the material in question. Materials manufacturers, spacecraft charging standards, and other sources list tables of dielectric

strengths for many insulating materials. *Caveat emptor*! These sources most often lack even basic experimental details (*e.g.*, test method used, sample preparation, temperature or voltage ramp rate) needed to gauge their relevance for a given space mission. Consider Fig. 7.1, which compares breakdown field estimates for three common insulating polymers, LDPE, BOPP, and Kapton HN (PI). Fig. 7.1 (a) shows the manufacturer's published values for breakdown for 25 μm films of these polymers; other than noting substantially lower values for these materials in bulk rather than in thin films, no uncertainties, qualifiers, sample preparation (*e.g.*, cleanliness or vacuum bake out) or test methods are stated explicitly (Goodfellow, 2016a; 2016b; 2016c). Handbook values can be useful for some applications, or as a starting point for comparing materials, but there are simply too many variables to take handbook values for granted when materials are to be used on sensitive space missions.

It is impossible to perfectly simulate both flight conditions and mission durations on the ground; however, considering mission conditions and possible changes in material properties over mission lifetimes can guide accelerated test methods. Taken together, tests such as the following begin to predict how materials' likelihood for dielectric breakdown can change with different conditions.

B. First Order Breakdown Testing: Voltage Step-Up Tests

First, establish a nominal room temperature breakdown field using voltage step-up to breakdown tests with a moderate ramp rate (Moser*, et al.*, 2017). Industry standard test configurations subject samples to up to 500V/s (NASA HDBK-4002A, 2011; ASTM D 3755-14, 2014). Not only is this charging rate orders of magnitude faster than any realistic operational condition encountered by spacecraft (NASA HDBK-4002A, 2011; Garrett and Whittlesey, 2012), but accuracy and precision of such tests suffer significantly as a result (Moser*, et al.*, 2017). Standard ESD tests performed by the MPG typically use a conservative, though still very rapid compared with space applications, ramp rate of 20V/4s at room temperature (see Chapter 4).

The careful interpretation of voltage step-up tests is important for estimating the fields at which ESD is likely to occur. At least 50 of our standard ESD tests were performed on each of the materials in Fig. 7.1; Fig. 7.1 (b) shows the averages and standard deviations together with error function fits to the data. This method assumes a Gaussian distribution of the results.

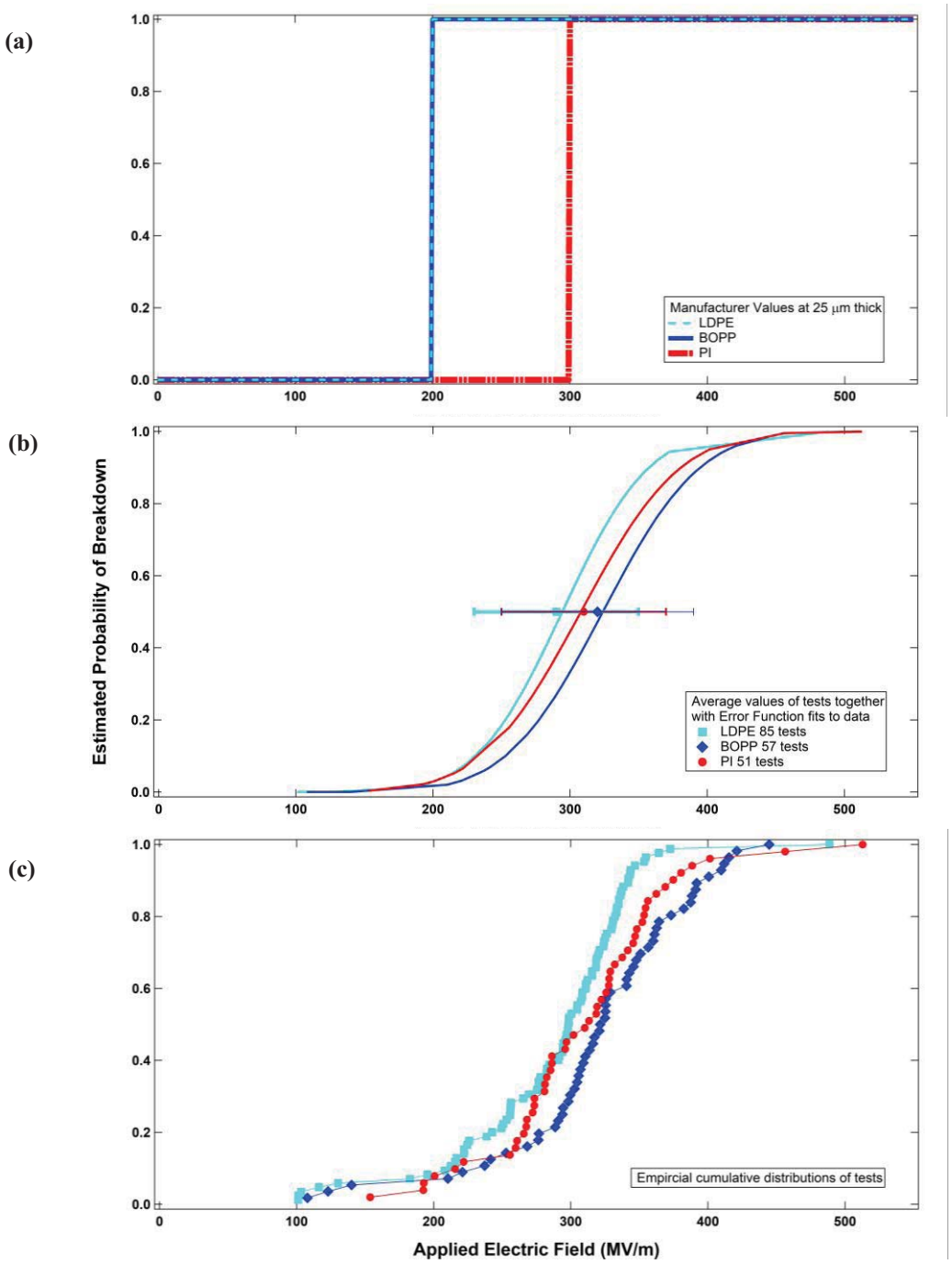

FIG. 7.1. Successively more accurate representations of dielectric strength for LDPE, BOPP, and PI (Kapton). (a) Manufacturer values (see Appendix D). (b) Averages and standard deviations with underlying error function fits to USU step-up tests. (c) Empirical cumulative distributions of USU step-up tests.

Figure 7.1 (c) is the empirical cumulative distribution (ECD) of the results. For each material, the ECD predicts higher probability of breakdown at lower fields than predicted by a Gaussian or other symmetrical distributions. A well-chosen physics model or a Weibull distribution would be better-suited fitting function for modeling this behavior (see Chapter 5). Thus, a more accurate average breakdown threshold may be significantly lower than what one would expect from application of just an average and standard deviation of voltage step-up test results. This has important consequences in establishing the highest acceptable field in a given spacecraft or component design, especially for missions with long duration or for low tolerance of the number of acceptable ESD events. That is, even low probability events at low fields can pose unacceptable risks for long missions or for low fault tolerance systems. This reinforces the importance of measuring and considering a field-dependent probability distribution of breakdown strength over a single average value.

C. Second Order Testing: Varying Key Test Parameters

Given this baseline, voltage step-up tests at different temperatures, radiation doses, or different ramp rates can be done to determine the dependencies of the material in question (see 4.4, 4.5, and 5.4.2). For example, SVET experiments hold a sample below its nominal breakdown voltage and measure the time to breakdown. Samples held at subcritical voltage for prolonged times—as will typically be encountered in space applications—can eventually breakdown. In essence, SVET tests determine the time a sample must be held at a given subcritical field before a significant probability of breakdown is reached. See Fig. 6.2. The time required to obtain these data was 68 days of instrument time making it likely to be impractical to obtain such results for many different candidate spacecraft materials. Results from smaller data sets at fields near the nominal electrostatic breakdown field can be fit to empirical or physical models in order to extrapolate the results to the comparatively very slow ramp rates and much longer times typical of spacecraft missions.

An important open question in the study of ESD is whether there is a threshold field below which breakdown will not occur (Crine, 2005b). Measurements shown in Fig. 6.2 taken at fields below 130 MV/m did not observe breakdown for several weeks, suggesting that there may be a threshold field below 17

MV/m for LDPE. Unfortunately, the time required to obtain the data necessary to definitively establish such threshold fields can be extremely long.

Arcing tolerances and risks will depend on individual spacecraft or systems and space environments. Therefore, modelers will have to ask themselves how much risk they can tolerate and how much testing is feasible given budget and time constraints.

In summary, we offer the following considerations when selecting breakdown thresholds for use in models.

- Define your mission parameters and requirements then tailor ESD tests, together with materials and components, to be as close to worst case flight conditions as possible. Dielectrics that will experience fields less than 1 MV/m are very unlikely to be at risk for ESD.
- Handbook values for breakdown are not wrong, but they were often developed for very different applications (*e.g.*, breakdown tests in oil with a pin electrode at 500V/s). However, these handbook test values are often inappropriate for spacecraft charging applications, or should at least be used with great care.
- Breakdown is not well characterized by as single number. Consider a probability distribution that depends not only on the material, but also on the conditions it is subjected to over time (Andersen and Dennison, 2015a; Andersen*, et al.*, 2015; Dennison, 2015; Saiki*, et al.*, 2015). The acceptable probability for a given mission needs to be determined by considering mission objectives and ESD tolerances.
- Taken together, SVET tests, tests at different ramp-rates, total radiation doses, and temperatures, can be used to more accurately estimate material behaviors, particularly at subcritical fields, extended radiation exposure times, slower ramp rates of field build up, and different temperatures.
- Physics-based or even well-chosen empirical models can estimate behavior of materials for times and conditions not achievable with testing of materials through judicious extrapolation (Andersen and Dennison, 2015a; Andersen*, et al.*, 2015; Dennison, 2015).

7.2.3. Potential for Highly Accelerated DC Dielectric Strength Testing

We have shown several materials have been observed to exhibit a phenomenon that may serve as an early indicator of electrical breakdown (see 4.6.5, 4.7, 5.5, and 6.2.5). Q-q analysis shows that DCPD correlate strongly to the distribution of ESDs (6.2.5). Given that there are most often many non-shorting dc partial discharges per destructive breakdown test, measurements of the distribution of non-shorting dc partial discharges with applied field could be used as an accelerated means of estimating ESD threshold fields. If resources for only a few voltage step-up tests are available, the destructive breakdowns alone are unlikely to yield information about the threshold field (as seen in Fig. 7.1 (c) only a small fraction of total events occur at the lowest fields). However, the numerous non-shorting dc partial discharges are much more likely to reveal lower fields with small likelihoods of breakdown but that become more and more significant at long endurance times. One possible method of establishing the threshold for DCPD, and therefore breakdown, would be to repeatedly ramp up through voltages where both DCPD and breakdown are relatively unlikely but still possible. An example of such a test is shown in Fig. 7.2 (a). In this test, a sample of 25 μm LDPE was ramped up to 4000 V ten times. Note that less than 12% of DCPD in such LDPE films are observed below 4000 V (157.5 MV/m). The lowest voltage of a DCPD trace was 3081 V (121.3 MV/m), which would have less than a 9% chance of occurrence in a standard destructive tests based on the cumulative distribution of events for LDPE used in 6.2.5. Figure 7.2 (b) is a histogram of the observed DCPD in each ramp-up, corrected for the large-amplitude events encompassing multiple fast DCPD as discussed in Section 4.7. It appears that the DCPD count per run is decreasing exponentially with successive ramp-ups, which might make these tests less effective. However, if the second ramp-up is an anomaly, that may not be the case. Additional tests are needed to establish whether DCPD consistently decrease with successive ramp-ups. While this is only a preliminary test, such a method could be used to improve estimations of DCPD and breakdown thresholds especially if only a small number of samples are available for testing.

7.3. Summary of Dissertation

Having (nearly) come to the end of this dissertation, what follows in this section is a summary of the key points in each chapter.

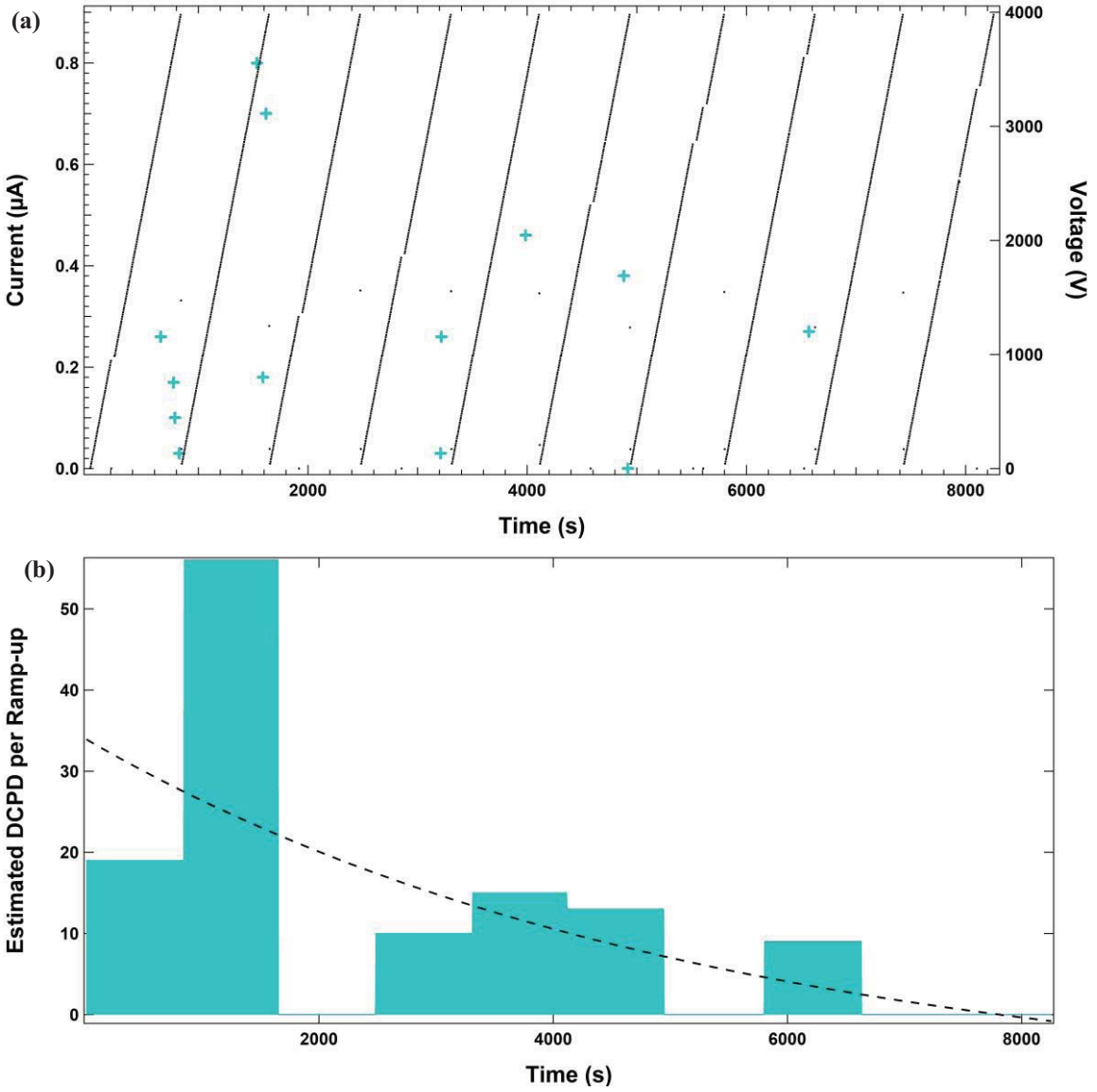

FIG. 7.2. Non-destructive test of LDPE to probe DCPD at lower voltages. (a) Ten voltage ramp-ups to 4000 V (black dots) together with DCPD traces (cyan crosses). (b) Histogram of corrected DCPD with one bin per voltage ramp-up and an exponential decay fit (black dash). In step-up to breakdown tests, only ~12% of DCPD happen below 4000 V. The traces with the smallest voltage (3081 V) has less than a 9% chance of occurrence in a destructive test.

Chapter 1: Introduction. This short chapter is an introduction to the importance and difficulty of researching dc electrical aging of HDIM. From a scientific perspective, HDIM are an interesting and difficult problem due to the complexity inherent in a lack of any long-range structure to the material. Approximations are needed to provide theoretical descriptions and a balance must be sought between

theories that work reasonably well and the complexity that comes with considering which assumptions to make. This work is primarily concerned with spacecraft charging applications, as ESD is the primary cause of spacecraft failures and anomalies due to the space environment. Other uses include estimating the lifetime of dielectrics for HVDC power applications and micro- or nanoelectronics.

Chapter 2: Theoretical Background. After a brief review of band theory in crystalline solids, a review of the physics of charge transport in amorphous solids is presented. Conductivity in HDIM is a function of the spatial and energetic density of states of localized defect states and temperature. By considering a mean field theory of runaway thermally assisted hopping, one can derive the canonical physics-based model of dialectic aging—the Crine model.

Chapter 3: Theoretical Development. A simple extension of the mean field theory is presented that considers two defect species rather than one. These defect types are high-energy (deep) chemical defects and low-energy (shallow) physical defects. Low-energy defects may be close enough to the thermal energy so that they have considerable creation and recovery rates. This theory is used to predict the time to breakdown for SVET tests and the likelihood of breakdown during a voltage step-up test. Voltage ramp-rate effects are also considered. Considering recoverable defects leads to a correction in the limiting behavior of the breakdown theory and a conceptual physical model for dc partial discharge (DCPD).

Chapter 4: Experimental Methods. The test equipment and test procedure for dielectric breakdown tests are outlined. Each test configuration is discussed in context with the relevant theory. An enhanced operational definition of breakdown is outlined. Observed phenomenon are discussed, with particular attention given to DCPD. Supplementary measurements of DCPD observed during breakdown tests are presented.

Chapter 5: Analysis. This chapter outlines the methods used to evaluate ensembles of tests. Methods for empirical Weibull fits and physics-model fits are discussed. We discuss the q-q analysis for comparing DCPD and breakdown events.

Chapter 6: Results. The results of the statistical comparisons of the theoretical models to the experimental data are presented. Fits to voltage step-up tests resulted in physically reasonable values with physics-based fits. SVET data for LDPE showed excellent agreement with the dual-defect model presented.

Voltage ramp-rate dependent tests did not agree will with the theoretical predictions. Initial results for temperature and radiation-dependence are discussed in context of the theory. Finally, we show excellent agreement between the distributions of breakdown and DCPD events for four polymers.

Chapter 7: Conclusions. The dual-defect model is a significant contribution to the advancement of the physics of aging in HDIM. Without adding too much complexity, it offers significant improvements in many cases over the single defect mean-field approximation. The correlation of DCPD and breakdown events may lead to substantial improvements in material characterization. Considerations for testing for terrestrial and space-bound applications are discussed. A roadmap for future work in this field is presented.

Appendix A: Instrumentation Procedures. Detailed instructions are outlined that cover sample preparation, testing, and long term storage. The proper use, maintenance, and troubleshooting the relevant Materials Physics Group equipment is described.

Appendix B: Error Analysis. This describes the estimation of experimental uncertainties and their propagation into calculations. Statistical confidence intervals for empirical cumulative distributions are discussed.

Appendix C: Details of Data Acquisition and Processing Software. This appendix outlines the flow of data and the software used to acquire and processes it. The processing of individual test results and the details of synthesizing groups of tests is described.

Appendix D: Materials Data. Manufacturers' values for relevant physical properties are listed for the materials used in this dissertation.

7.4. Future Work

It seemed that most questions, when answered, lead to further questions. This section outlines some of the questions that have been raised during this research that time and resources did not allow to be addressed and must be left to future work. This section will serve as a roadmap for further research in this area, particularly by members and future members of the MPG.

7.4.1. Theoretical Work

This dissertation has shown both advantages and disadvantages to the dual-defect model. The area with the poorest agreement between predictions and results was the ramp-rate predictions (see 6.2.3). The product series used in

$$P_{step}^{Tot}\left(\Delta t_{step}, N_{step}, \Delta V_{step}, T\right) = 1 - \prod_{j=1}^{N_{step}}\left[1 - P_{def}^{Tot}\left(\Delta t_{step}, \frac{j\Delta V_{step}}{d}, T\right)\right] \quad 3.7$$

assumes that each voltage step is independent of all others and does take into account changes in defect concentrations. To relax this assumption, one must solve

$$\frac{dN_{def}^{i}(t)}{dt} = \left[N_{bond}^{i} - N_{def}^{i}(t)\right] \cdot K_{def}^{+i}(F,T) - N_{def}^{i}(t)(t) \cdot K_{def}^{-i}(F,T) = N_{bond}^{i}K_{def}^{+i} - N_{def}^{i}(t)\left[K_{def}^{+i} + K_{def}^{-i}\right] \quad 3.13$$

without ignoring the critical time dependence of Eq. 3.16 inherent in ΔV_{def}^{i}, considered here as $\Delta V_{def}^{i} = \left(N_{def}^{i}\right)^{-1} = \left(a_{def}^{i}\right)^{3}$.

$$K_{def}^{\pm i}(F,T) = \frac{k_b T}{h}\exp\left[\frac{-\Delta G_{def}^{i} \pm \frac{1}{2}F(t)^2\epsilon_0\epsilon_r\Delta V_{def}^{i}}{k_b T}\right] \quad 3.16$$

As discussed in 3.2.1, this would require numerical techniques with results highly dependent on both the individual material in question through ΔG_{def}^{i}, N_{def}^{i}, and extrinsic considerations such as temperature and applied field. Attempts to date to create such a numerical routine have not yet been successful and have had to be left for future work.

Solving this differential equation will allow one to consider materials as truly dynamic defect density dependent on t, F, and T ($N_{def}^{i}(t,F,T)$) could be one way to characterize the effect of aging on a material. Given, $N_{def}^{i}(t,F,T)$, one could trivially update predictions to Eq. 3.7 or indeed the SVET equation, Eq. 3.2. It is likely that such an improvement may reconcile the discrepancies between defect energies derived from step-up tests and SVET tests that we see. Additionally, one might directly predict and model DCPD, as changes in $N_{def}^{i}(t,F,T)$ will affect the likelihood of breakdown as discussed in 3.2.

There is still disagreement on the physical process that deforms the defect energy when an external electric field is applied (see 3.2.1). To summarize, proposed mechanisms include simply the energy gained by the motion on an electron in an applied field $\left(\frac{1}{2}q_e a_{def}F\right)$, the 1D Maxwell stress

($\frac{\epsilon_0 \epsilon_r F^2}{2k_b T N_{def}}$ as used in this dissertation), or electrostriction which grows faster than F^2 (Crine, 2016b). Related questions are clearly establishing nature of ΔV_{def}^{i} (which we have assumed to be in inverse defect density but this is not always clear in the literature) (Crine, 2007; 2016b), and explicitly building into the theory a physics-based threshold field at which the static voltage endurance time goes to infinity or the probability of breakdown goes to zero.

7.4.2. Recommended ESD System Upgrades

The following are recommended upgrades to the USU MPG ESD test system as resources become available.

- Smaller current limiting resistors, approximately 20-40 MΩ. This would reduce the voltage drop due to field-enhanced conductivity (see 4.6.5) by an order of magnitude. Although this is rarely an issue, it would be better to mitigate it if materials with significant field-enhanced conductivity (*e.g.*, Kapton E) are to be tested. Reducing the current limiting resistance also reduces the instrumental response time constant.
- More sensitive ammeter, down to 0.001 μA for improved sensitivity to DCPD and field-enhanced conductivity. Faster ammeter response would be desirable; this would allow smaller voltage increments to be used at a given ramp rate and permit multiple current measurements over a given ramp time increment.
- Feedthroughs, particularly power and TC feedthroughs, rated to higher voltages to increase the voltage range of the setup without external arcing. The present configurations limit the maximum applied voltage to ~13-15 kV rather than the 30 kV power supply limit. This would allow testing of thicker samples.
- Thermocouple multiplexer for automated temperature measurements.
- Multiple *in-situ* RF antennas and oscilloscope for PD detection and localization. A broadband antenna such as a Rogoswski coil would enable spectral analysis in addition to detection (Chen*, et al.*, 2017).

- Additional vacuum gauge on the chamber side of the main valve. This would improve measurements of pressure in the chamber itself rather than at the pump and allow for improved leak checking.
- Include DUT voltage plots (*e.g.*, Fig. 4.11) as a standard output of the MPG analysis macro. This would automatically correct for any issues, though rare, when the DUT voltage does not match the output voltage.
- Addition of a second parallel test apparatus would double sample throughput.

Additionally, an second test setup with the capability to do large-area breakdown tests (Xu*, et al.*, 2008; Rytöluoto and Lahti, 2013; Rytöluoto*, et al.*, 2015; Kerwien*, et al.*, 2016; Rytöluoto, 2016; Ritamäki*, et al.*, 2017b). Such a setup would allow us to directly compare our existing tests to this popular new method. Such a chamber could be the first for *in vacuo* large-area self-healing breakdown measurements. To my knowledge, the large-area self-healing film electrode method has not yet been applied to SVET tests. While it is not completely clear that non-destructive tests comply with the assumptions of Weibull statistics of independent different discharge events, they may be ideal for SVET measurements, as the test would continue with multiple breakdowns until the electrodes are spent. This could be very helpful for accelerating what is perhaps the most difficult and time-consuming breakdown test type. Note that in this test method, it is more difficult to distinguish DCPD and breakdown (Rytöluoto and Lahti, 2013; Ritamäki*, et al.*, 2017b).

7.4.3. Experimental Work at USU

There is practically no end to the tests that would be interesting to do. Of particular interest might be ceramic or glassy materials, multilayer dielectrics, or nanodielectrics. Testing new materials or, even additional tests of previously tested materials, would surely yield interesting results provided sufficiently many tests are done for each type to get decent statistics (see the results for PEEK in 6.2.1). Given the results of the work presented in this dissertation, the following are suggested to be pursued first by the MPG:

- As implied by the preceding section, it would be helpful to use multiple RF antennas to locate DCPD. Sub-nanosecond time resolution would be needed to obtain spatial

resolutions on the order of centimeters. This would be possible with 10 GHz multi-channel storage oscilloscope. While one could say where in the plane of the sample a DCPD would occur, this method would not be capable of finding at what depth in the sample DCPD occur. If broadband antennas are used, spectra may provide further insights into DCPD.

- Section 6.2.4 presents the results of preliminary tests on the effects of temperature and radiation. Further tests at different temperatures and total ionizing doses are needed to confirm the trends hinted at in this section. Particularly of interest, is the identification of the glass phase transition and its effect on the temperature dependence of breakdown starting with more temperature-dependent tests of LDPE. Tests of irradiated samples as a function of time after applied dose could probe defect recovery effects.
- In 3.2 we consider the dynamic nature of the materials yet we do not consider the variability of the relative permittivity ϵ_r. While this is not likely to be a large effect, the MPG has recently acquired the capability to directly measure ϵ_r and it would be interesting to compare it for aged (voltage increased to DCPD levels but tests stopped prior to breakdown) and un-aged samples. This could compliment breakdown and conductivity measurements on the effect of temperature, total ionizing dose, and dose rate through the modification of the defect density.
- The MPG has a significant library of optical microscope images of breakdown sites (see Appendix A). To date, no damage has been observed for samples that have exhibited DCPD, but have testing terminated prior to breakdown. It would be interesting to compare SEM images of untested samples, aged samples (DCPD, but no breakdown), and breakdown damage.
- In section 5.5.2 we noted that many of the larger breakdown damage sites violate the adiabatic breakdown assumption. More work needs to be done to look at the breakdown site size and shape trends. A continuation of Hansen's study of the characteristics of

breakdown damage in different materials with comparisons of materials, temperatures, and post-breakdown behavior may be of interest (Hansen, 2014).

- To continue the study presented in 6.2.3, additional voltage ramp rate tests, especially similar ramp rates at different profiles (*e.g.*, 20 V per 4 s, 5 V per s, 100 V per 20 s).
- Static voltage endurance time (SVET) tests in LDPE showed the best agreement to the dual-defect model of any test presented in this dissertation (see 6.2.2). Nevertheless, more LDPE tests at lower waiting voltages are needed to probe the existence of a threshold field. SVET tests on other materials, especially other materials described in this dissertation such as PI, BOPP, and PEEK, would be valuable in generalizing the result reported for LDPE to other materials.
- More tests for DCPD at low field with low probability of occurrence (see Fig 7.2) to study the threshold field. Confirmation that multiple scans for DCPD can be taken on a single sample for subcritical field ramps may lead to a new test method. Possible test configurations include repeated ramp-ups, ramping up then ramping down, or low-voltage SVET tests to observe DCPD.

7.4.4. Round Robin Tests: DCPD and Breakdown Correlation

While 6.2.5 demonstrates a strong correlation between DCPD and breakdown events in four materials, this is the first such study. There has been significant discussion in the community as to the merits of such tests, the physical origins of DCPD events, and the proposed correlation of DCPD with breakdown field distribution (Rytöluoto, 2016; Andersen and Dennison, 2017; Boggs, 2017a). Before DCPD distributions can truly be considered proxy for ESD distributions, this would have to be established by studies at other institutions by other research groups. We call on other researchers with the capability of detecting DCPD during voltage-step-up tests to compare the distributions of DCPD and breakdown. Given a successful Round-Robin tests campaign, the results could lead to a new standard method for highly accelerated characterization of the likelihood of breakdown under dc fields for dielectric materials.

REFERENCES

Ambegaokar, V., B. Halperin, and J. Langer, 1971, "Hopping conductivity in disordered systems," Phys. Rev. B **4**, 2612.

Andersen, A., and J. Dennison, 2014, "Pre-breakdown Arcing and Electrostatic Discharge in Dielectrics under High DC Electric Field Stress," in *Electrical Insulation and Dielectric Phenomena, 2014. CEIDP 2014. Annual Report Conf. on Electrical Insulation and Dielectric Phenomena*, p. 63-66.

Andersen, A., and J. R. Dennison, 2015a, "Mixed Weibull distribution model of DC dielectric breakdowns with dual defect modes," in *Electrical Insulation and Dielectric Phenomena, 2015. CEIDP 2015. Annual Report Conf. on Electrical Insulation and Dielectric Phenomena*, p. 570-573.

Andersen, A., and J. R. Dennison, 2015b, "Pre-breakdown arcing as proxy for DC dielectric breakdown testing of polymeric insulators," in *Electrical Insulation and Dielectric Phenomena, 2015. CEIDP 2015. Annual Report Conf. on Electrical Insulation and Dielectric Phenomena*, p. 574-577.

Andersen, A., and J. Dennison, 2017, "An Enhanced Operational Definition of Dielectric Breakdown for DC Voltage Step-up Tests," in *Electrical Insulation and Dielectric Phenomena, 2017. CEIDP 2017. Annual Report Conf. on Electrical Insulation and Dielectric Phenomena*, p. 433-436.

Andersen, A., J. R. Dennison, A. M. Sim, and C. Sim, 2015, "Measurements of Endurance Time for Electrostatic Discharge of Spacecraft Materials: A Defect-Driven Dynamic Model," IEEE Trans. on Plasma Science **43**, 2941-2953.

Andersen, A., K. Moser, and J. Dennison, 2016, "Voltage Ramp-rate Dependence of DC Breakdown in Polymeric Insulators: Physical Models versus Data," in *Electrical Insulation and Dielectric Phenomena, 2016. CEIDP 2016. Annual Report Conf. on Electrical Insulation and Dielectric Phenomena*, p. 494-496.

Andersen, A., K. Moser, and J. Dennison, 2017, "Perspectives on the Distributions of ESD Breakdowns for Spacecraft Charging Applications," IEEE Trans. on Plasma Science **45**, 2031-2035.

Anderson, J. C., K. D. Leaver, R. D. Rawlings, and P. S. Leevers, 2004, *Materials Science for Engineers, 5th Edition* (CRC Press, London).

Anderson, P., and N. Mott, 1978, "Nobel lecture in physics for 1977," Rev. Mod. Phys. **50**, 191-208.

Anderson, P. W., 1958, "Absence of Diffusion in Certain Random Lattices," Phys. Rev. **109**, 1492-1505.

Arevalo, L., and W. Dong, 2014, "Effect of high dielectric protrusions on the breakdown phenomena of large electrodes under positive switching impulses," in *Electrical Insulation and Dielectric Phenomena, 2014. CEIDP 2014. Annual Report Conf. on Electrical Insulation and Dielectric Phenomena*, p. 51-54.

Ashcroft, N. W., and N. D. Mermin, 2005, *Solid State Physics* (Holt, Rinehart and Winston, New York).

ASTM D 257-99, 1999, *Standard Test Methods for DC Resistance or Conductance of Insulating Materials* (American Society for Testing and Materials, West Conshohocken).

ASTM D 149-97a, 2004, *Standard Test Method for Electric Breakdown Voltage and Dielectric Strength of Solid Electrical Insulating Materials at Commercial Power Frequencies* (American Society for Testing and Materials, West Conshohocken).

ASTM D 3755-14, 2014, *Standard Test Method for Dielectric Breakdown Voltage and Dielectric Strength of Solid Electrical Insulating Materials Under Direct-Voltage Stress* (American Society for Testing and Materials, West Conshohocken).

Belmont, M., 1975, "The capture cross section of a dipole trap," Thin Solid Films **28**, 149-156.

Boer, K. W., C. P. Poole, and J. P. Heremans, 2002, *Survey of semiconductor physics* (John Wiley & Sons New York).

Boggs, S., 2017a, personal communication.

Boggs, S. A., 2017b, "Research in the age of numerical simulation," IEEE Elect. Insul. Mag. **33**, 8-16.

Brunson, J., 2010, "Hopping conductivity and charge transport in low density polyethylene," PhD disseration (Utah State University).

Cavallini, A., P. Morshuis, and G. C. Montanari, 2016, "Call for papers: High Voltage Direct Current (HVDC) insulation and diagnostics," IEEE Trans. Dielectr. and Electr. Insul. **23**, 3779-3779.

Chauvet, C., and C. Laurent, 1993, "Weibull statistics in short-term dielectric breakdown of thin polyethylene films," IEEE Trans. Electr. Insul. **28**, 18-29.

Chen, G., 2014, "The missing link - The role of space charge in polymeric insulation lifetime," in *Proc. of 2014 International Symposium on Electrical Insulating Materials*, p. 12-16.

Chen, S., L. Zhu, S. Ji, and X. Liu, 2017, "Detection of Series DC Arc Fault using Rogowski Coil," in *Electrical Insulation and Dielectric Phenomena, 2017. CEIDP 2017. Annual Report Conf. on Electrical Insulation and Dielectric Phenomena*, p. 401-404.

Chinh, D., J. L. Parpal, and J. P. Crine, 1996, "Electrical aging of extruded dielectric cables: review of existing theories and data," IEEE Trans. Dielectr. and Electr. Insul. **3**, 237-247.

Cho, H., Y. C. Kim, S. O. Kim, and I. J. Chung, 2000, "Persistence length calculation from light scattering and intrinsic viscosity of dilute semiflexible polyimide solutions with different degree of imidization," Korea-Australia Rheol. J. **12**, 69-76.

Cho, M., S. Kawakita, M. Nakamura, M. Takahashi, T. Sato, and Y. Nozaki, 2005, "Number of Arcs Estimated on Solar Array of a Geostationary Satellite," J. Spacecr. Rockets **42**, 740-748.

Corr, E., W. H. Siew, and W. Zhao, 2016, "Long term testing and analysis of dielectric samples under DC excitation," in *Proc. of 2016 IEEE Electrical Insulation Conf. (EIC)*, p. 484-487.

Crine, J.-P., J.-L. Parpal, and C. Dang, 1989, "A new approach to the electric aging of dielectrics," in *Electrical Insulation and Dielectric Phenomena, 1989. CEIDP 1989. Annual Report Conf. on Electrical Insulation and Dielectric Phenomena*, p. 161-167.

Crine, J. P., 1999, "Comparison between Lewis and Crine models for the electrical aging of dielectric polymers," in *Electrical Insulation and Dielectric Phenomena, 1999. CEIDP 1999. Annual Report Conf. on Electrical Insulation and Dielectric Phenomena*, vol.2, p. 508-511.

Crine, J. P., 2002a, "Aging and polarization phenomena in PE under high electric fields," IEEE Trans. Dielectr. and Electr. Insul. **9**, 697-703.

Crine, J. P., 2002b, "Electrical aging and breakdown of crosslinked polyethylene cables," in *Electrical Insulation and Dielectric Phenomena, 2002. CEIDP 2002. Annual Report Conf. on Electrical Insulation and Dielectric Phenomena*, p. 23-26.

Crine, J. P., 2005a, "Influence of electro-mechanical stress on electrical properties of dielectric polymers," IEEE Trans. Dielectr. and Electr. Insul. **12**, 791-800.

Crine, J. P., 2005b, "On the interpretation of some electrical aging and relaxation phenomena in solid dielectrics," IEEE Trans. Dielectr. and Electr. Insul. **12**, 1089-1107.

Crine, J. P., 2007, "A molecular model for the electrical aging of XLPE," in *Electrical Insulation and Dielectric Phenomena, 2007. CEIDP 2007. Annual Report Conf. on Electrical Insulation and Dielectric Phenomena*, p. 608-610.

Crine, J. P., 2013, "An electrical aging model including Kramers friction, phonon vibrations and electrostriction," in *Proc. of 2013 IEEE International Conf. on Solid Dielectrics (ICSD)*, p. 283-286.

Crine, J. P., 2016a, "Influence of temperature and elastic properties on some polymer relaxations," in *Proc. of 2016 IEEE International Conf. on Solid Dielectrics (ICSD)*, p. 1-4.

Crine, J. P., 2016b, "Role of electrostriction on the electrical aging of polymers," in *Proc. of 2016 IEEE International Conf. on Solid Dielectrics (ICSD)*, p. 685-688.

Czaszejko, T., 2014, "High-voltage testing fundamentals: a cable testing perspective," IEEE Elect. Insul. Mag. **30**, 7-13.

Dang, C., J.-L. Parpal, and J.-P. Crine, 1996, "Electrical aging of extruded dielectric cables: review of existing theories and data," IEEE Trans. Dielectr. and Electr. Insul. **3**, 237-247.

Dekany, J., A. Sim, J. Brunson, and J. Dennison, 2012, "Electron Transport Models and Precision Measurements in a Constant Voltage Chamber," in *Proc. 12th Spacecraft Charging Technology Conf.*, Kitakyushu, Japan.

Dekany, J., A. M. Sim, J. Brunson, and J. R. Dennison, 2013, "Electron Transport Models and Precision Measurements with the Constant Voltage Conductivity Method," IEEE Trans. on Plasma Science **41**, 12.

Dennison, J., J. Christensen, J. Dekany, C. Thomson, N. Nickles, R. E. Davies, M. Belhaj, K. Toyoda, K. Kawasaki, and I. Montero, 2016a, "Absolute electron emission calibration: round robin tests of Au and graphite," in *Proc. 14th Spacecraft Charging Technology Conf.*, Noordwijk, The Netherlands.

Dennison, J., J. Gillespie, J. Hodges, R. Hoffmann, J. Abbott, and A. W. Hunt, 2007, "Radiation induced conductivity of highly-insulating spacecraft materials," *Proc. 10th Spacecraft Charging Technology Conf.*, Biarritz, France.

Dennison, J., J. C. Gillespie, A. Andersen, A. E. Jensen, G. Wilson, J. Dekany, A. M. Sim, and R. Hoffmann, 2016b, "Synergistic Models of Electron Emission and Transport Measurements of Disordered SiO_2," in *Proc. 14th Spacecraft Charging Technology Conf.*, Noordwijk, The Netherlands.

Dennison, J. R., 2015, "Dynamic Interplay Between Spacecraft Charging, Space Environment Interactions, and Evolving Materials," IEEE Trans. on Plasma Science **43**, 2933-2940.

Dennison, J. R., and J. Brunson, 2008, "Temperature and Electric Field Dependence of Conduction in Low-Density Polyethylene," IEEE Trans. on Plasma Science **36**, 2246-2252.

Dennison, J. R., A. Evans Jensen, G. Wilson, J. Dekany, C. W. Bowers, and R. Meloy, 2013, "Diverse electron-induced optical emissions from space observatory materials at low temperatures," in *Proc. of SPIE 8863, Cryogenic Optical Systems and Instruments*, p. 88630B-88630B-15.

Dennison, J. R., B. Jerilyn, H. Steven, G. Jodie, D. Justin, S. Charles, A. Dan, and S. Alec, 2009, "Engineering Tool for Temperature, Electric Field and Dose Rate Dependence of Low Conductivity Spacecraft Materials," in *Proc. 47th AIAA Aerospace Sciences Meeting including The New Horizons Forum and Aerospace Exposition*, p. 15.

Diaham, S., S. Zelmat, M.-L. Locatelli, S. Dinculescu, M. Decup, and T. Lebey, 2010, "Dielectric breakdown of polyimide films: Area, thickness and temperature dependence," IEEE Trans. Dielectr. and Electr. Insul. **17**, 18-27.

Dissado, L. A., and J. C. Fothergill, 1992, *Electrical Degradation and Breakdown in Polymers* (The Institution of Engineering and Technology, London, UK).

DuPont Document K-15345-1, 2011, *DuPont Kapton HN Polyimide Film, H-38479, Bulletin GS-96-7* (DuPont, Circleville, OH, USA).

ECSS-E-ST-20-08C, 2012, *Space engineering: Photovoltaic assemblies and components* (European Cooperation for Space Standardization ECSS, Noordwijk, The Netherlands).

Einmahl, J. H., and I. W. McKeague, 1999, "Confidence tubes for multiple quantile plots via empirical likelihood," Ann. Stat. **27**, 1348-1367.

El-Hag, A. H., N. Qaddoumi, R. Mourtada, E. A. Murawwi, A. Nimer, K. AlMazam, M. Hirzallah, and A. Huwair, 2013, "Multi-purpose RF antenna for partial discharge and oil quality monitoring," in *Proc. 3rd International Conf. on Electric Power and Energy Conversion Systems*, p. 1-5.

Elliott, S. R., and S. Elliott, 1990, *Physics of amorphous materials* (Longman Scientific & Technical, Essex).

Eyring, H., H. Gershinowitz, and C. E. Sun, 1935, "The absolute rate of homogeneous atomic reactions," J. Chem. Phys. **3**, 786-796.

Ferguson, D. C., 2007, "The New NASA-STD-4005 and NASA-HDBK-4006, Essentials for Direct-Drive Solar Electric Propulsion," in *Proc. 30th International Electric Propulsion Conf.*, p. 4.

Ferguson, D. C., and G. B. Hillard, 2011, in *Spacecraft charging, arcing, and sustained arcs in low earth orbit,* Spacecraft Charging (American Institute of Aeronautics and Astronautics, Inc., Reston, VA), p. 29-73.

Ferguson, D. C., S. P. Worden, and D. E. Hastings, 2015, "The Space Weather Threat to Situational Awareness, Communications, and Positioning Systems," IEEE Trans. on Plasma Science **43**, 3086-3098.

Franck, J., and G. Hertz, 1914, "Über Zusammenstöße zwischen Elektronen und Molekülen des Quecksilberdampfes und die Ionisierungsspannung desselben," Verhandlungen der Deutschen Physikalischen Gesellschaft **24**, 457-467.

Frederickson, A., and J. Dennison, 2003, "Measurement of conductivity and charge storage in insulators related to spacecraft charging," IEEE Trans. on Nuclear Science **50**, 2284-2291.

Fromm, U., 1995, "Interpretation of partial discharges at dc voltages," IEEE Trans. Dielectr. and Electr. Insul. **2**, 761-770.

Garrett, H. B., and A. C. Whittlesey, 2012, *Guide to mitigating spacecraft charging effects* (John Wiley & Sons, Hoboken, NJ).

Gillespie, J., 2013, "Measurements of the Temperature Dependence of Radiation Induced Conductivity in Polymer Dielectrics," Masters thesis (Utah State University).

Gillespie, J. C., J. Dennison, and A. M. Sim, 2014, “Density of state models and temperature dependence of radiation induced conductivity,” in *Proc. 13th Spacecraft Charging Technology Conf.*, Pasadena, CA.

Goodfellow, 2016a, "Polyethylene - Low Density - Film," http://www.goodfellowusa.com/catalog/GFUS4I.php?ewd_token=4a5spJfBMQrycg70gwYgmSAJWJrK8Z&n=cAExnCoaVy0fzR8AiIztidPI3brmyE

Goodfellow, 2016b, "Polymimide - Film," http://www.goodfellowusa.com/catalog/GFUS4I.php?ewd_token=TgmK8AfjlZnTQ7V8YgazgYO7hJ10IP&n=DDBQ7AyextX8s5uyJM6RdP5JX7P5Wb

Goodfellow, 2016c, "Polypropylene - Film," http://www.goodfellowusa.com/catalog/GFUS4I.php?ewd_token=OZhTudvso7EeohXOoDi5l9yWssBALg&n=hOpHJQMIURvoD7DDkkjGiVqPYjhyej

Goodfellow Cambridge Ltd., Jan. 20, 2006, *Material Information—Polyethylene, Low Density LDPE* (Goodfellow Cambridge Ltd., Devon).

Goodfellow Corp., 2016, *Standard Price List for Polyetheretherketone*, (Goodfellow Corp., Coraoplolis PA).

Goodfellow Corp., 2017, *Standard Price List for Polypropylene*, (Goodfellow Corp., Coraoplolis PA).

Grant, P. M., C. Starr, and T. J. Overbye, 2006, "A Power Grid for the Hydrogen Economy," Sci. Am. **295**, 76-83.

Green, N., W., and S. F. Dawson, 2015, "Electrostatic Discharge Testing of Carbon Composite Solar Array Panels for Use in the Jovian Environment," in *Proc. AIAA SPACE 2015 Conf. and Exposition*, p. 4558.

Griffiths, C., J. Freestone, and R. Hampton, 1998, "Thermoelectric aging of cable grade XLPE," in *Conf. Record of the 1998 IEEE International Symposium on Electrical Insulation*, p. 578-582.

Hansen, S., 2014, "Electrostatic Breakdown Analysis," BS thesis (Utah State University).

Hansen, S., J. Dennison, and A. Andersen, 2014a, "Electrostatic Discharge Breakdown Analyses," in *Utah State University Student Showcase*, Logan, UT.

Hansen, S., J. Dennison, and A. Andersen, 2014b, "Electrostatic Discharge Breakdown Analyses," in *American Physical Society Four Corners Section Meeting*, Orem, UT.

Haq, S. U., and G. G. Raju, 2006, "DC breakdown characteristics of high temperature polymer films," IEEE Trans. Dielectr. and Electr. Insul. **13**, 917-926.

Heo, J.-H., J. Salas, and K.-D. Kim, 2001, "Estimation of confidence intervals of quantiles for the Weibull distribution," Stochastic Environmental Research and Risk Assessment **15**, 284-309.

Ho, J., and R. Jow, 2009, "Characterization of high temperature polymer thin films for power conditioning capacitors," in *Army Research Lab ADELPHI MD Sensors and Electron Devices Directorate*.

Ho, J., and T. R. Jow, 2013, "Effect of crystallinity and morphology on dielectric properties of PEEK at elevated temperature," in *Proc. of 2013 IEEE International Conf. on Solid Dielectrics (ICSD)*, p. 385-388.

Hoaglin, D. C., 1985, "Using quantiles to study shape," Exploring data tables, trends, and shapes 417-460.

Hoffman, R., J. Dennison, and J. Albertsen, 2009, "Flux and Fluence Dependence of Electron Emission for High-yield, High-resistivity Materials: Implications for Spacecraft Charging." in *Proc. of the 47th American Institute of Aeronautics and Astronomics Meeting on Aerospace Sciences*.

Huff, D., 2010, *How to lie with statistics* (WW Norton & Company, New York, NY).

IEC 60243-1, 2013, *Electric strength of insulating materials - Test methods - Part 1: Tests at power frequencies* (Czech Institute for Standardization, Geneva).

IEC 60243-2, 2013, *Electric Strength of insulating materials - Test methods - Part 2: Additional requirements for tests using direct voltage* (Czech Institute for Standardization, Geneva).

Imburgia, A., P. Romano, F. Viola, A. Madonia, R. Candela, and I. Troia, 2016, "Space charges and partial discharges simultaneous measurements under DC stress," in *Electrical Insulation and Dielectric Phenomena, 2016. CEIDP 2016. Annual Report Conf. on Electrical Insulation and Dielectric Phenomena*, p. 514-517.

ISO 11221, 2011, *Space Systems – Space Solar Panels – Spacecraft Charging Induced Electrostatic Discharge Test Methods* (International Organization for Standardization, Geneva).

Jensen, A. E., J. Dennison, J. Dekany, and G. Wilson, 2013, "Nanodielectric properties of high conductivity carbon-loaded polyimide under electron-beam irradiation," in *Proc. of 2013 IEEE International Conf. on Solid Dielectrics (ICSD)*, p. 730-735.

Jensen, A. E., and J. R. Dennison, 2015, "Defects Density of States Model of Cathodoluminescent Intensity and Spectra of Disordered SiO2," IEEE Trans. on Plasma Science **43**, 2925-2932.

JERG-2-211A, 2012, *Spacecraft Charging and Discharging* (Japan Aerospace Exploration Agency, Tsukuba, Japan).

Kao, K. C., 2004, *Dielectric phenomena in solids* (Elsevier Academic Press, San Diego).

Kazuo, W., 1978, "D.C. Partial Discharge and Current in Polyethylene," Jpn. J. Appl. Phys. **17**, 483.

Kazuo, W., 1980, "Effect of Ultraviolet Illumination on D.C. Partial Discharge in Polyethylene Vacancies," Jpn. J. Appl. Phys. **19**, 2381.

Kiethley Instruments, 2016, *Lowlevel Measurements Handbook, 7th Edition* (Keithley Instruments Inc., Cleveland).

Kerwien, C. M., D. L. Malandro, and J. R. Broomall, 2016, "Large area DC dielectric breakdown voltage measurement of BOPP and PTFE thin films," in *Electrical Insulation and Dielectric Phenomena, 2016. CEIDP 2016. Annual Report Conf. on Electrical Insulation and Dielectric Phenomena*, p. 486-489.

Kippen, T., A. Andersen, and J. Dennison, 2016, "Temperature Dependency of Electrostatic Breakdown in LDPE and PEEK," in *American Physical Society Four Corner and Texas Sections Meeting*, Las Cruces, NM.

Kippen, T., A. Andersen, and J. Dennison, 2017, "Temperature Dependence of Electrostatic Discharge in Highly Disordered Insulating Polymers," in *American Physical Society Four Corner Section Meeting*, Fort Collins, CO.

Kittel, C., 1966, *Introduction to solid state physics* (John Wiley & Sons, Hoboken, NJ).

Koons, H., J. Mazur, R. Selesnick, J. Blake, and J. Fennell, 1999, "The impact of the space environment on space systems," Aerospace Corp. Technical Operations, El Segundo, CA.

Laurent, C., C. Chauvet, and J. Berdala, 1994, "The significance of the Weibull threshold in short-term breakdown statistics," IEEE Trans. Dielectr. and Electr. Insul. **1**, 160-162.

Lawless, J. F., 1978, "Confidence interval estimation for the Weibull and extreme value distributions," Technometrics **20**, 355-364.

Leach, R. D., and M. B. Alexander, 1995, "Failures and Anomalies Attributed to Spacecraft Charging," NASA Marshall Space Flight Center.

Lewis, T., 2002, "Polyethylene under electrical stress," IEEE Trans. Dielectr. and Electr. Insul. **9**, 717-729.

Lewis, T., J. Llewellyn, M. Van der Sluijs, J. Freestone, and R. Hampton, 1996, "A new model for electrical ageing and breakdown in dielectrics," in *Proc. of 7th International Conf. on Dielectric Materials, Measurements and Applications*, p. 220-224.

Li, Z., H. Uehara, R. Ramprasad, S. Boggs, and Y. Cao, 2015, "Pre-breakdown conduction in polymeric films," in *Electrical Insulation and Dielectric Phenomena, 2015. CEIDP 2015. Annual Report Conf. on Electrical Insulation and Dielectric Phenomena*, p. 872-875.

Liu, J., G. Zhang, J. Dong, and J. Wang, 2015, "Study on miniaturized UHF antennas for partial discharge detection in high-voltage electrical equipment," Sensors **15**, 29434-29451.

Martinez-Vega, J., 2013, *Dielectric materials for electrical engineering* (John Wiley & Sons, Hoboken, NJ).

Mazzanti, G., 2017, "Life and reliability models for high voltage DC extruded cables," IEEE Elect. Insul. Mag. **33**, 42-52.

Miller, A., and E. Abrahams, 1960, "Impurity Conduction at Low Concentrations," Phys. Rev. **120**, 745-755.

Montanari, G., C. Laurent, G. Teyssedre, A. Campus, and U. Nilsson, 2005, "From LDPE to XLPE: investigating the change of electrical properties. Part I. space charge, conduction and lifetime," IEEE Trans. Dielectr. and Electr. Insul. **12**, 438-446.

Morshuis, P. H. F., and J. J. Smit, 2005, "Partial discharges at DC voltage: their mechanism, detection and analysis," IEEE Trans. Dielectr. and Electr. Insul. **12**, 328-340.

Moser, K., A. Andersen, and J. R. Dennison, 2015, "Dependence of Electrostatic Field Strength on Voltage Ramp Rates for Spacecraft Materials," in *American Physical Society Four Corner Section Meeting*, Tempe, AZ.

Moser, K., A. Andersen, and J. R. Dennison, 2017, "Dependence of Electrostatic Field Strength on Voltage Ramp Rate for Spacecraft Materials," IEEE Trans. on Plasma Science **45**, 2036-2039.

Mott, N., 1969, "Conduction in non-crystalline materials: III. Localized states in a pseudogap and near extremities of conduction and valence bands," Philos. Mag. **19**, 835-852.

Mott, N., 1978, "Electrons in glass," Science **201**, 871-875.

Mott, N. F., and E. A. Davis, 2012, *Electronic processes in non-crystalline materials* (Oxford University Press, New York).

NASA-CR-149341, 1972, *High Voltage Design Criteria*, (Boeing Co., Seattle, WA, USA).

NASA-CR-165590, 1982, *Development of electrical test procedures for qualification of spacecraft against EID. Volume 1: The CAN test and other relevant data* (IRT Corp., San Diego, USA).

NASA HDBK-4002, 1999, *Avoiding problems caused by spacecraft on-orbit internal charging effects,* (NASA, Pasadena, CA, USA).

NASA HDBK-4002A, 2011, *Mitigating in space charging effects-a guideline* (NASA, Pasadena, CA, USA).

NASA HDBK-4006, 2007, *Low earth orbit spacecraft charging design Handbook* (NASA, Washington, DC, USA).

Nobel Media AB, 2014, "The Nobel Prize in Physics 1977," http://www.nobelprize.org/nobel_prizes/physics/laureates/1977/.

Noguchi, K., Y. Okamoto, and Y. Sekii, 2008, "Statistical Consideration of Dielectric Breakdown of Polymeric Insulating Material," in *Electrical Insulation and Dielectric Phenomena, 2008. CEIDP 2008. Annual Report Conf. on Electrical Insulation and Dielectric Phenomena*, p. 563-566.

OMEGA, 2018, "Thermocouples: Using Thermocouples in Temperature Measurement," https://www.omega.com/prodinfo/thermocouples.html.

Onsager, L., 1938, "Initial Recombination of Ions," Phys. Rev. **54**, 554-557.

Palit, S., 2014, "Charging and breakdown in amorphous dielectrics: Phenomenological modeling approach and applications," PhD disseration (Purdue University).

Pan, J., K. Li, J. Li, T. Hsu, and Q. Wang, 2009, "Dielectric characteristics of poly (ether ketone ketone) for high temperature capacitive energy storage," Appl. Phys. Lett. **95**, 022902.

Parpal, J.-L., J.-P. Crine, and C. Dang, 1997, "Electrical aging of extruded dielectric cables. A physical model," IEEE Trans. Dielectr. and Electr. Insul. **4**, 197-209.

Peacock, A., 2000, *Handbook of polyethylene: structures: properties, and applications* (CRC Press, New York).

Phillips, P., 1983, in *Morphology and molecular structure of polymers and their dielectric behavior*, Engineering Dielectrics Volume IIA Electrical Properties of Solid Insulating Materials: Molecular Structure and Electrical Behavior, (ASTM Intl.) p. 119.

Popper, K., 1963, *Science: Conjectures and refutations* (Routledge & Kegan Paul, New York, NY)

Raju, G. G., 2016, *Dielectrics in Electric Fields, Second Edition* (CRC Press, Boca Raton).

Reed, C. C., R. Briët, and M. Begert, 2014 “ESD Detection, Location and Mitigation, and Why they are Important for Satellite Development,” in *Proc. 13th Spacecraft Charging Technology Conf.*, Pasadena, CA.

Ridley, B. K., 1975, "Mechanism of electrical breakdown in SiO2 films," J. Appl. Phys. **46**, 998-1007.

Ritamäki, M., I. Rytöluoto, and K. Lahti, 2017a, "High Temperature and Ageing Test Methods to Characterize the Dielectric Properties of BOPP Capacitor Films," in *Electrical Insulation and Dielectric Phenomena, 2017. CEIDP 2017. Annual Report Conf. on Electrical Insulation and Dielectric Phenomena*, p. 266-269.

Ritamäki, M., I. Rytöluoto, K. Lahti, T. Vestberg, S. Pasanen, and T. Flyktman, 2017b, "Large-area approach to evaluate DC electro-thermal ageing behavior of BOPP thin films for capacitor insulation systems," IEEE Trans. Dielectr. and Electr. Insul. **24**, 826-836.

Rodgers, D., and A. Hilgers, 2003 “ECSS-E-20-06 Draft Standard On Spacecraft Charging: Environment-Induced Effects On The Electrostatic Behavior Of Space Systems,” in *Proc. 8th Spacecraft Charging Technology Conf.*

Rongsheng, L., 2013, "Long-distance DC electrical power transmission," IEEE Elect. Insul. Mag. **29**, 37-46.

Rose, A., 1951, "An outline of some photoconductive processes," RCA Review **12**, 362.

Rosenkrantz, W. A., 2000, "Confidence bands for quantile functions: A parametric and graphic alternative for testing goodness of fit," Am. Stat. **54**, 185-190.

Rowland, S. M., R. M. Hill, and L. A. Dissado, 1986, "Censored Weibull statistics in the dielectric breakdown of thin oxide films," J. Phys. C **19**, 6263.

Rytöluoto, I., and K. Lahti, 2013, "New approach to evaluate area-dependent breakdown characteristics of dielectric polymer films," IEEE Trans. Dielectr. and Electr. Insul. **20**, 937-946.

Rytöluoto, I., K. Lahti, M. Karttunen, and M. Koponen, 2015, "Large-area dielectric breakdown performance of polymer films-part i: measurement method evaluation and statistical considerations on area-dependence," IEEE Trans. Dielectr. and Electr. Insul. **22**, 689-700.

Rytöluoto, I., K. Lahti, M. Karttunen, M. Koponen, S. Virtanen, and M. Pettersson, 2014, "Influence of low amounts of nanostructured silica and calcium carbonate fillers on the large-area dielectric breakdown performance of bi-axially oriented polypropylene," in *Electrical Insulation and Dielectric Phenomena, 2014. CEIDP 2014. Annual Report Conf. on Electrical Insulation and Dielectric Phenomena*, p. 655-658.

Rytöluoto, I. J., 2016, "Large-Area Multi-Breakdown Characterization of Polymer Films: A New Approach for Establishing Structure–Processing–Breakdown Relationships in Capacitor Dielectrics," PhD disseration (Tampere University of Technology).

Saiki, T., K. Abe, H. Miyake, Y. Tanaka, and T. Maeno, 2015, "Space charge distribution measurements in insulating materials of commercially available enameled wire," in *Electrical Insulation and Dielectric Phenomena, 2015. CEIDP 2015. Annual Report Conf. on Electrical Insulation and Dielectric Phenomena*, p. 94-97.

Sekii, Y., and T. Kazama, in 2004, "A statistical investigation of dielectric breakdown of low-density polyethylene," in *Proc. of of the 2004 IEEE International Conf. on Solid Dielectrics, ICSD 2004*, p. 83-86.

Shinyama, K., and S. Fujita, 2006, "Mechanical and Dielectric Breakdown Properties Eco-Friendly Dielectric Materials," Int. J. Soc. Mater. Engin. Resorc. **13** 75-80.

Sim, A. M., and J. R. Dennison, 2013, "Comprehensive Theoretical Framework for Modeling Diverse Electron Transport Experiments in Parallel Plate Geometries," in *Proc. 5th AIAA Atmospheric and Space Environments Conf.*, San Diego, CA.

Smirnov, N., 1948, "Table for Estimating the Goodness of Fit of Empirical Distributions," Ann. Math. Stat. **19** 279-281.

Tang, Z., C. Li, X. Cheng, W. Wang, J. Li, and J. Li, 2006, "Partial discharge location in power transformers using wideband RF detection," IEEE Transactions on Dielectrics and Electrical Insulation **13**, 1193-1199.

Taylor, J., 1997, *Introduction to error analysis, the study of uncertainties in physical measurements* (University Science Books, Sausaltio, CA)

Teyssedre, G., and C. Laurent, 2013, "Advances in high-field insulating polymeric materials over the past 50 years," IEEE Elect. Insul. Mag. **29**, 26-36.

Thoman, D. R., L. J. Bain, and C. E. Antle, 1969, "Inferences on the parameters of the Weibull distribution," Technometrics **11**, 445-460.

Torrisi, L., N. Campo, L. Auditore, R. Barna, D. D. Pasquale, A. Italiano, A. Trifirò, M. Trimarchi, and G. D. Marco, 2004, "Mechanical modifications in dense polyethylene induced by energetic electron beams," Radiation Effects & Defects in Solids **159**, 597-606.

Trnka, P., J. Pihera, M. Svoboda, and J. Soucek, 2013, "New challenges in partial diacharge measurements," in *Proc. 2013 IEEE International Conf. on Solid Dielectrics (ICSD)*, p. 75-78.

Trnka, P., M. Sirucek, M. Svoboda, and J. Soucek, 2014, "Condition-based maintenance of high-voltage machines-a practical application to electrical insulation," IEEE Elect. Insul. Mag. **30**, 32-38.

Valeinis, J., E. Cers, and J. Cielens, 2010, "Two-sample problems in statistical data modelling," Mathematical modelling and analysis **15**, 137-151.

Van der Vaart, A. W., 1998, *Asymptotic statistics* (Cambridge university press, Cambridge).

Vu, T. T. N., G. Teyssedre, B. Vissouvanadin, S. Le Roy, C. Laurent, M. Mammeri, and I. Denizet, 2013, "Electric field profile measurement and modeling in multi-dielectrics for HVDC application," in *Proc. 2013 IEEE International Conf. on Solid Dielectrics (ICSD)*, p. 413-416.

Wang, H., P. Zongren, L. Naiyi, Z. Shiling, G. Zihao, and Z. SiYu, 2014a, "Transient electric field calculation of UHV GIS spacer under lightning impulse," in *Electrical Insulation and Dielectric Phenomena, 2014. CEIDP 2014. Annual Report Conf. on Electrical Insulation and Dielectric Phenomena*, p. 542-545.

Wang, Y., G. Chen, and A. Vaughan, 2014b, "Space charge dynamics in silica-based polyethylene nanocomposites," in *Electrical Insulation and Dielectric Phenomena, 2014. CEIDP 2014. Annual Report Conf. on Electrical Insulation and Dielectric Phenomena*, p. 727-730.

Weibull, W., 1951, "A Statistical Distribution of Wide Applicability," J. Appl. Mech. **103**, 293-297.

Wilson, G., J. R. Dennison, A. Evans Jensen, and J. Dekany, 2013a, "Electron Endergy Dependent Charging Effects of Multilayered Dielectric Materials," IEEE Trans. on Plasma Science **41**, 9.

Wilson, G., J. R. Dennison, A. Evans Jensen, and J. Dekany, 2013b, "Electron Energy Dependent Charging Effects of Multilayered Dielectric Materials," IEEE Trans. on Plasma Science **41**, 9.

Wintle, H. J., 1983, in *Conduction Processes in Polymers,* edited by Bartnikas, R. (American Society for Testing and Materials, Philadelphia, PA).

Xu, C., and S. Boggs, 2006, “Measurement of resistive and absorption currents in capacitor films up to breakdown,” in *Proc. 2006 IEEE International Symposium on Electrical Insulation*, p. 249-252.

Xu, C., J. Ho, and S. A. Boggs, 2008, "Automatic breakdown voltage measurement of polymer films," IEEE Elect. Insul. Mag. **24**.

Yoshino, S., and M. Okazaki, 1977, "Numerical Study of Electron Localization in Anderson Model for Disordered Systems: Spatial Extension of Wavefunction," J. Phys. Soc. Jpn. **43**, 415-423.

Zallen, R., 1983, *The Physics of Amorphous Solids* (Wiley, New York, NY).

Zavattoni, L., R. Hanna, O. Lesaint, and O. Gallot-Lavallee, 2014, "Dark current measurements in pressurized SF_6: Influence of relative humidity and temperature," in *Electrical Insulation and Dielectric Phenomena, 2014. CEIDP 2014. Annual Report Conf. on Electrical Insulation and Dielectric Phenomena*,p. 23-26.

Zhu, M.-X., Y.-B. Wang, Q. Liu, J.-N. Zhang, J.-B. Deng, G.-J. Zhang, X.-J. Shao, and W.-L. He, 2017, "Localization of multiple partial discharge sources in air-insulated substation using probability-based algorithm," IEEE Trans. Dielectr. and Electr. Insul. **24**, 157-166.

APPENDICES

APPENDIX A

INSTRUMENTATION PROCEDURES

This appendix contains the detailed procedures for the Materials Physics Group (MPG) electrostatic discharge (ESD) testing. The procedures outline sample preparation prior to testing, test procedures, and post-test sample handling and storage. This document is the cumulative effort of many MPG members including Amberly Evans-Jensen, Anthony Thomas, Charles Sim, Dan Arnfield, Sam Hansen, Steve Hart, Tyler Kippen, and Allen Andersen.

A.1. Sample Preparation

(a) Samples are to be cut, cleaned, and mounted in the sample prep room (SER 217A). Wear gloves throughout preparation.

(b) Create a sample preparation area by laying down an area of aluminum foil, shiny side up, on the clean air bench in SER 217A. When working, the air should be flowing. Replace the white plastic curtain when finished. Ensure that sample preparation area is clean by spraying with methanol and wiping with a Kim wipe (Fig. A.1).

FIG. A.1. Sample preparation area in room 217 A.

(c) Clean all sample plates or other mounting hardware to be used with methanol.

(d) Make sure the recessed portion of the base of the bakeout chamber is clean (except for edges where the O-ring sits). See Fig. A.7.

(e) Gather necessary materials (other than samples) and clean with methanol. These include: knife, screwdriver, HV plates, sample template, rods and nuts for baking (Fig. A.2).

FIG. A.2. Materials needed for sample prep: (left to right) knife, screwdriver, HV plate, and sample template.

A.1.1. Cutting Samples

Samples can be cut individually using a Plexiglas template (far right of Fig. A.2) or with the Creation PCUT CTE630HPGL sticker cutter machine (recommended). Detailed instructions for the sticker cutter can be found on the Big Blue MPF file server under

Z:\Instruction & Procedures\Procedures\Sample Preparation\Sticker Cutter

For manual cutting, please observe the following steps:

(a) Retrieve the sample material, and if necessary, cut off a workable piece (some materials come in large rolls).

(b) If samples are not thin film, they should be cut approximately to 1.75 in. by 2.75 in. This will ensure that they are larger than the electrode guard plates in the CV or ESD chambers.

(c) If samples are thin film, they should be cut using the sample template. Do the cutting in the designated cutting area. Place the template over the sample, and while applying firm pressure to the template, cut around it with the knife.

(d) If samples are stretchy, use extra caution not to stretch the samples. In any case, avoid bending, creasing, or any other physical abuse.

A.1.2. Sample Cleaning and Mounting

(a) Clean the samples in the designated area only.

(b) Spray sample with methanol and gently wipe with a Kim wipe. Repeat for both sides.

(c) Carefully inspect samples for any residual dust particles. Repeat previous step as necessary.

(d) Because many samples charge up and attract dust in the air, turn on the fan on the clean air bench. The switch is under the table on the right side.

(e) If samples are not thin films or are smaller than the standard sample size, this section is not relevant.

(f) Samples are mounted on HV plates, which are used in both the ESD and CV chambers. Two Plexiglas clamps on either end of the plate secure the sample in place (Fig. A.3).

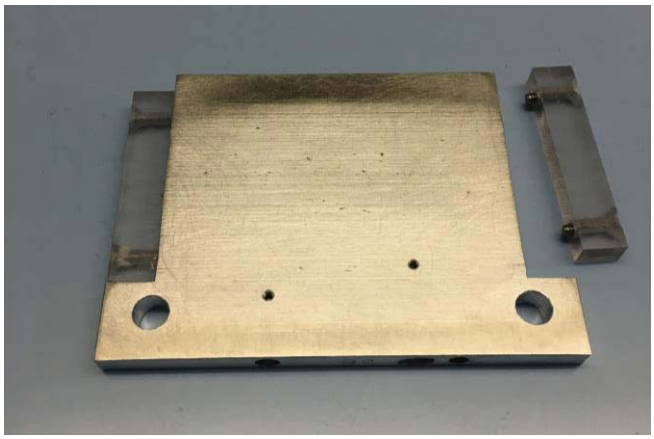

FIG. A.3. HV plate showing mounting clamp.

(g) It is easiest not to remove the clamps, but rather to loosen them, and insert the sample.

(h) Insert the sample on one end of the HV plate and tighten. (Fig. A.4) Insert in other end. Pull the sample taut (but do not overdo it) and tighten the other end. Avoid touching the central regions of the sample during this process.

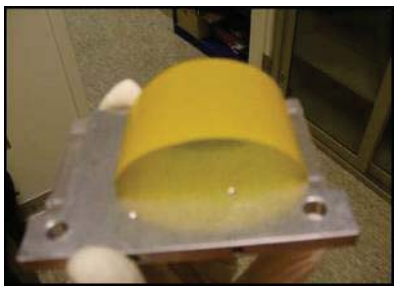

FIG. A.4. Sample mounted halfway.

(i) Stack multiple plates together on the stacking plate and fasten samples on the stack mounting jig with one nut at the top of each rod, as shown in Fig. A.5. Up to 20 sample plates can be mounted this way at one time.

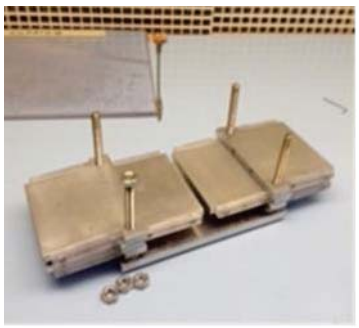

FIG. A.4. Baking stack being built.

A.1.3. Bakeout

(a) Place all samples in the center of the bakeout chamber (Fig. A.6). If samples are not mounted, ensure that they are in sufficient contact with the chamber to ensure efficient heat transfer.

(b) From here on, avoid touching samples; gloves may be removed.

(c) The O-ring in the bakeout chamber does not fit well. Do not place it in the groove in the lid (the O-ring does not like to stay there and you risk dropping a greasy O-ring on your samples when putting the lid on). Rather, place it in the base, making sure it is seated an even distance from the edge. See Fig. A.7.

FIG. A.6. Bakeout chamber.

FIG. A.7. O-ring seated around recessed portion of base of chamber.

(d) Gently place the bakeout chamber lid on the base. Rotate it back and forth a few degrees to ensure that the O-ring is seated well.

(e) Start the diffusion pump system as follows. This will prepare the pump system while it is isolated from the sample chamber.

i. Insert the bakeout chamber into the oven (Fig. A.8). Take care to keep the chamber level. Attach the thermocouple to the bakeout chamber by pinching it beneath nut (Fig. A.10). Attach the vacuum hose using the quick-connect O-ring and clamp (Fig. A.10). Make sure the valve on the chamber is open. Close the oven door. Note: Use caution when opening and closing valves. The slower the better. Do not crank down on the valves. They will strip out. A snug fit will seal just the same as a super tight fit.

ii. Make sure all valves (A, B, C, D) are closed (Fig. A.9).

iii. Turn the "Power" on the pumping station.

FIG. A.8. Oven and pumping station.

FIG. A.9. Pump system valves (center), mechanical pump, bottom.

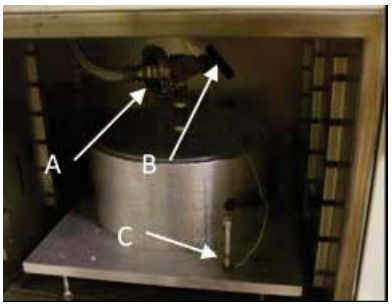

FIG. A.10. Chamber in oven. Note vacuum connection (A), main valve (B), and thermocouple (C).

iv. Switch on the mechanical pump.

v. Note: Ensure the diffusion pump fan comes on when the mechanical pump is turned on (Fig. A.11). Otherwise, the diffusion pump will overheat.

FIG. A.11. Cooling fan and diffusion pump.

vi. Slowly open the foreline valve (A) and evacuate the diffusion chamber.

vii. Continue pumping until TC1 gauge reads approximately 10^{-1} Torr. (TC2 gauge will not be used until crossover). It is best to have the needle buried below this limit, but TC1 Gauge has a lot of noise in it and therefore will usually not stay steady at high vacuum. If the gauge does not read, try unplugging it then plugging it in again.

viii. Turn on the diffusion pump. The pressure may go up a little due to gas molecules being released from the fluid. Let the diffusion pump warm up for 20 minutes before turning on the ion gauge.

ix. Turn on the ion gauge. Note: To ensure the ion gauge is not damaged, make sure the pump has been running for at least 20 minutes before turning it on. If the gauge is not down to at least 10^{-3} Torr, turn off the ion gauge and check the valves to make sure only the foreline valve (A) is open. If you are nervous about damaging the gauge, just turn on the gauge for a couple of seconds to test where the pressure is. Most likely it will be in the correct range because the mechanical pump can get down to 10^{-3} Torr range by itself.

(f) Crossover: This is to be completed after previous start up procedures have been finished for about 20 minutes. This will provide high vacuum for the diffusion pump system to the sample chamber.

i. Ensure the sample chamber vacuum line is connected to the diffusion pump system inlet port on the top of the cart.

ii. Close the foreline valve (A).

iii. Open the rouging valve (B). This will allow the mechanical pump to begin pumping out the sample chamber while isolating the diffusion chamber. If you hear loud and/or high pitched noises from the chamber area there is a major leak indicating a poor seal on the O-ring. If this happens close (B) and open (A). Re-evaluate the O-ring seal. It may just need minor adjustments and/or cleaning and re-greasing. Once the lid is back in place attempt to start back at step (f) ii.

iv. Evacuate (rough) the sample chamber until the TC2 gauge is at least below 10^{-2} Torr. This will ensure the ion gauge will not be damaged. Occasionally this gauge is not responsive. Try unplugging it then plugging it back in or, if

you confirm that the rough vacuum is holding down the chamber lid and you are confident everything is working besides the gauge, wait ~10-15 minutes before proceeding (note that there is some risk when proceeding with a gauge malfunction).

v. Close roughing valve (B).

vi. Open foreline valve (A). TC1 gauge may read a much higher pressure than the diffusion chamber because it is on the backing side of the diffusion pump. This is normal.

vii. VERY SLOWLY open the main high vacuum valve (D). The valve does not need to be open all the way until it stops. A few turns will do. This will create a pumping path from the sample chamber to the diffusion pump and then to the mechanical pump.

viii. Continue watching the gauges for a few minutes to ensure vacuum is still happening. After a short time TC2 gauge should be buried below the zero mark. Turn on the autorange switch for the ion gauge. At this point, refer to Appendix C for the bakeout program instructions. Complete the bakeout before proceeding with vacuum shut down.

(g) Shut Down: This will properly shut down the system so there is no damage to the diffusion pump. Proceed with this section only after the sample oven has cooled to ambient room temperature. Note: Proper cooling of the diffusion pump before exposure to atmospheric pressure is important to the life and stability of the pump fluid. Repeated insufficient cooling periods can be harmful.

a. Option 1: Complete Shutdown

i. Turn off the diffusion pump.

ii. Let the mechanical pump and cooling fan run until the pump is cooled down to room temperature (~20 min.).

iii. Turn off the mechanical pump. The fan will shut off as well.

iv. Backfill to atmospheric pressure through the vent valve (C) located on the upstream side of the diffusion pump. This will ensure that no mechanical pump fluid vapors are swept into the pumping system.

v. Close all valves (A,B,C,D) and turn off the power.

b. Option 2: Quick turnaround

i. Isolation of the diffusion chamber may be desired if a quick turnaround for a re-pumping is needed or the sample chamber needs to be opened before the proper cooling time for the diffusion pump could be achieved. If this is the case, do the following:

ii. Isolate the diffusion chamber by closing the foreline (A) and main high vacuum (D) valves. This can be done before it has cooled.

iii. Turn off the mechanical pump. The fan will shut off as well.

iv. Ensure that only the roughing valve (B) is open. Backfill to atmospheric pressure through the vent valve (C) located on the upstream side of the diffusion pump. Only valves (B) and (C) should be open. This will ensure that no mechanical pump fluid vapors are swept into the pumping system.

v. Once the crossover is complete and the chamber lid is back in place, return to step (f) i. in beginning of the Crossover instructions.

(h) Finishing Bakeout

i. All thin-film samples currently being used need to be baked at temperature for 72 hours (Gillespie, 2013). Time must be allowed for warm-up and for cool-down. Plan accordingly.

ii. If necessary, stop the bakeout program by hitting the 'stop' button, but you should keep collecting data as the chamber cools down.

iii. Turn off the oven. The oven door may be opened for quicker cool-down. Do not continue until the chamber reaches room temperature.

iv. Turn off the diffusion pump. Let it sit for 20 minutes to allow the diffusion pump to be cooled to room temperature.

v. Close the foreline pump and inlet valves (A,D) to isolate the diffusion pump.

vi. Turn off the mechanical pump.

vii. Connect the hose from the nitrogen cylinder to the leak valve at (C). Open the cylinder and begin nitrogen flow. Open main valve (D) to start flow, close it to finish.

viii. Open the leak valve (C) and allow chamber to reach atmospheric pressure.

ix. Close the leak valve (C), close the chamber main valve (D), and stop nitrogen flow.

x. Disconnect the thermocouple and vacuum hose.

xi. Move the chamber to near the glove box. Samples will be stored in a nitrogen environment in the glove box until use. See MPG glove box procedures.

(i) Documenting Sample Preparation and Bakeout

i. Record the bakeout in the bakeout logbook. Include material prepared, plates used, person preparing, date of bakeout, etc. …

ii. Update white boards on the wall in SER 217 (Fig. A.12). Take care not to smudge previous entries.

iii. Fill out the Bakeout Excel sheet. There is a template at Z:\Data & Analysis Folder\Data\Sample Preparation\Sample Bakeout or use the link Bakeout Template and save in the bakeout excel sheet folder for that year.

iv. Save the raw text file in the bakeout file folder for that year.

A.1.4. Storage and Handling

Samples are stored in the dry N_2 glove box (Fig. A.13) until use. The location of all samples that have been prepared is to be recorded on the Sample Board (Fig. A.12) and updated each time a sample

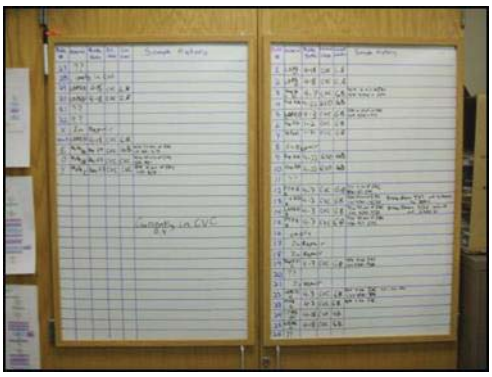

FIG. A.12. Sample board in room 217.

FIG. A.13. Glove box.

location is changed. The sample board is a quick reference for determining the quantity of samples ready to test and the relevant information of samples to be used or currently in use. Any exposure to air during sample relocation and mounting should be minimized. Nitrile gloves should always be used and any contact with the sample material itself should be avoided, even with used samples.

A.2. USU ESD System

WARNING: THE ELECTROSTATIC DISCHARGE CHAMBER OUTPUTS SEVERAL THOUSAND VOLTS! IT CAN BE DANGROUS AND POSSIBLY FATAL IF NOT OPERATED PROPERLY. MAKE SURE ALL CONNECTIONS ARE SECURE AND THE CHAMBER IS PROPERLY GROUNDED BEFORE CONTINUING WITH ANY EXPERIMENTS. REFER TO THE

SCHEMATIC HANGING ON THE WALL NEXT TO THE CHAMBER IF THER ARE ANY DOUBTS ABOUT GROUNDING.

A.2.1. Startup Procedures

A.2.1.1. Room Temperature Tests

Always use nitrile latex gloves when handling the inside of any high vacuum chamber! Contaminates prevent the chamber from reaching optimal, operational pressures. In addition, oil from human skin is a conductor and even a slight amount can create undesired conduction paths.

(a) Attach the red high voltage (HV) lines to the sample plates and note which plate number is attached to which line (Fig. A.14). As a rule of thumb, line A should be attached to the plate which has the smaller number written on it. The two wires for line B (red high voltage and white Teflon) have metal rings around them they will not be mixed up (Fig. A.15). The electrode plate is also etched with A and B sides for reference.

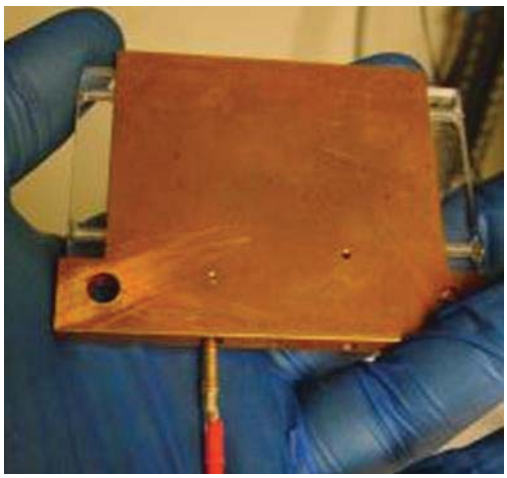

FIG. A.14. Sample plate with high voltage wire attached.

(b) Create the sample stack (bottom to top):

i. Polycarbonate base plate

ii. HV electrode plate

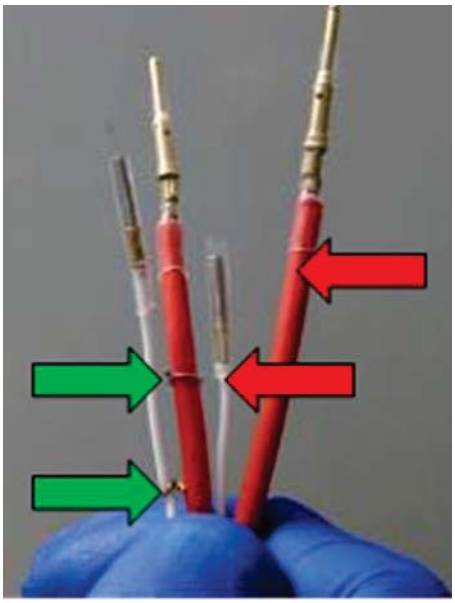

FIG. A.15. High voltage (HV) wires which attach to the sample plates. Note the metal rings on the B HV wires.

iii. Sample plates (sample-side down)

iv. Polycarbonate insulating layer

v. Aluminum cryogenic reservoir

The stack is held together by four custom compression screws (Fig. A.16). When tightening down the compression screws, thread them down until they are just barely catching on the springs. Then, in alternating fashion, screw each down an equal amount of turns using an Allen wrench. About 4 full turns are all that are needed to achieve the right amount of sample contact pressure of a few hundred kPa, in compliance with standard methods (ASTM D 257-99, 1999).

(c) Close the chamber lid and pump down. Check, clean, and regrease the O-ring as needed. Wait until the pressure is around 10^{-5} mbar before operating the chamber. (For reference use the "ESD Chamber Startup Checklist" found at Z:\Instrumentation\Chambers&Systems\ESD\ Documentation\Instructions & Procedures) If the main chamber is under vacuum with the main chamber valve closed but the pumping system is off pump the vacuum system to 10^{0}

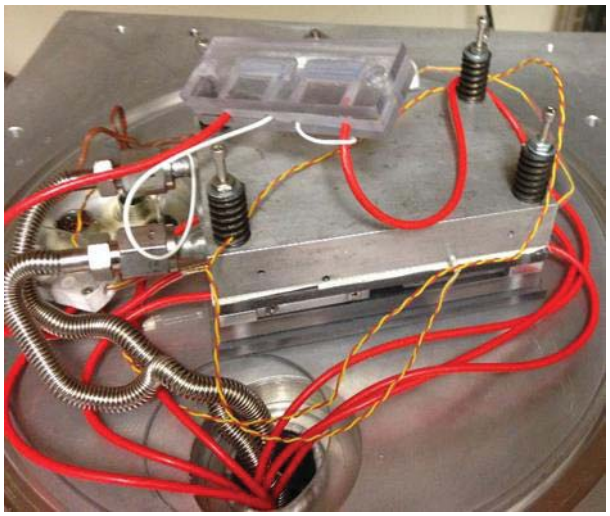

FIG. A.16. The sample stack assembly with compression screws. Compression screws are indicated by the yellow arrows.

mbar or lower before SLOWLY opening the main chamber valve. Do this even if the chamber is under vacuum and only venting is required.

(d) Check the following connections:

i. "HV monitor" port (Fig. A.17 a) to the Meterman set for voltage measurements (Fig. A.17 b)

ii. "Electrode current" port (Fig. A.17 c) to the Meterman set for current meausrments (Fig. A.17 d)

iii. Optical sensors from the top of each Meterman to serial ports of the computer

iv. Ground wire cluster from left feedthrough to the back of the HV switch box (Fig. A.18)

v. Plug the blue wire on the switch box to red "A" dock and the brown ground wire into the black dock, beneath the red "A" dock (Fig. A.19).

(e) Plug the white HV wire into one of the high voltage feed through leads (Fig. A.20).

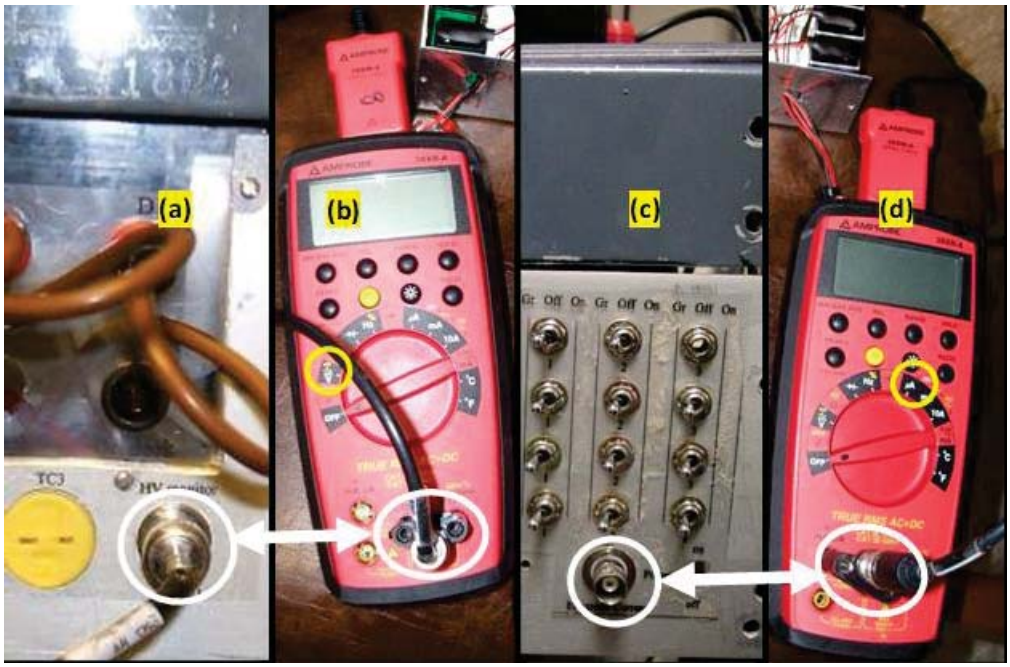

FIG. A.17. ESD Metereman 38XRA multimeters and HV switch box. (a) HV Monitor: the white circle is where the other end of the HV multimeter cable in (b) connects. (b) HV multimeter, the yellow circle indicates the position this meter needs to be set in order to measure voltage. Note the position of the plugs outlined in white. (c) Current monitor connection highlighted in the white circle (d) Current multimeter, the yellow circle indicates the position this meter needs to be set in order to measure current. Note the position of the plugs outlined in white.

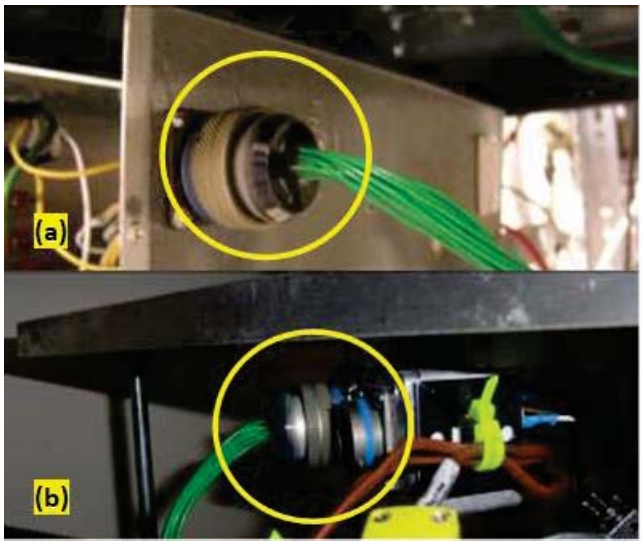

FIG. A.18. (a) Grounding bundle attached to the outside of the ESD switch box. (b) Grounding bundle attached to the outside of the chamber. There is only one way these two connectors (outlined in yellow) will attach to their respective plugs.

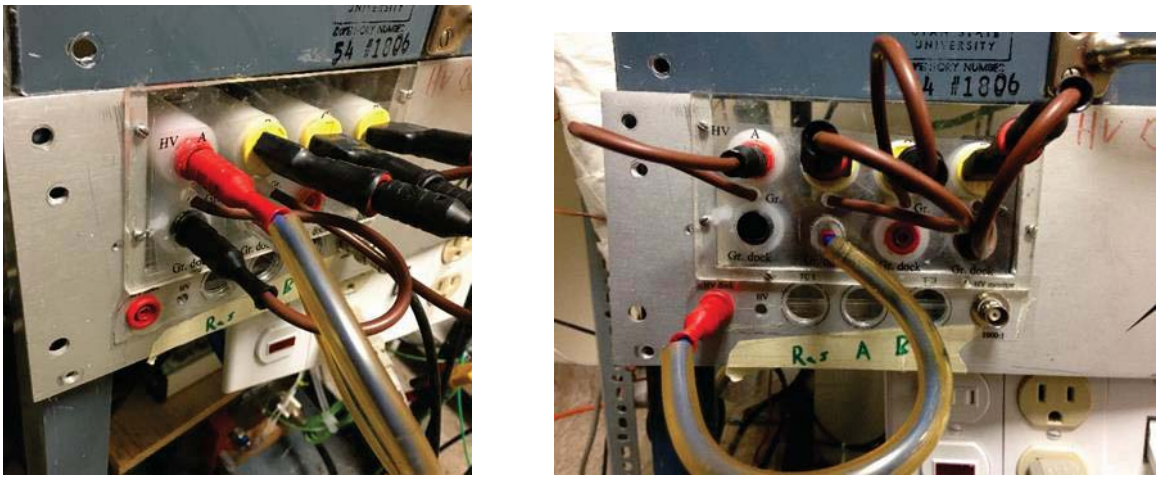

FIG. A.19. Testing position of blue HV wire and grounding wire (left). Blue HV wire plugged into red "HV A" dock. Grounded positions shown right.

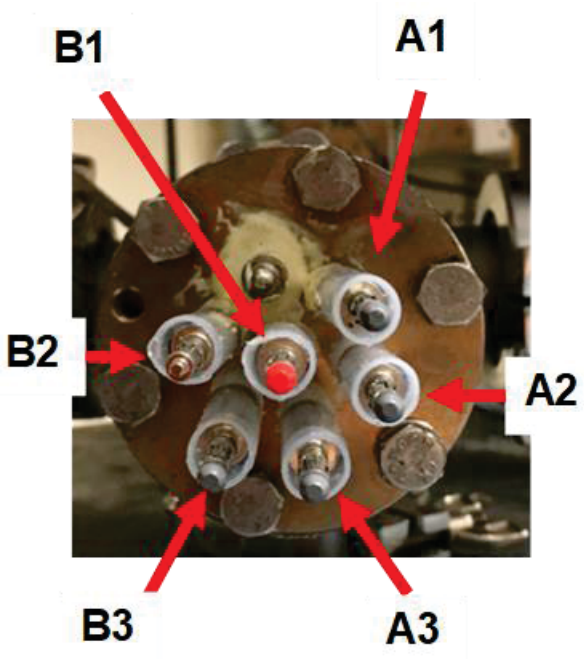

FIG. A.20. High voltage feedthrough to the chamber. The unused feedthrough has been damaged and although it is vacuum safe it is not suitable for ESD tests. B1 is the center pin. Clockwise from the unused pin are A1, A2, A3, B3, and B2.

(f) Cover the leads with the PVC pipe (Fig. A.21). This PVC safety cover is for YOUR (the operator's) protection. DO NOT REMOVE THE COVER DURING ANY HIGH VOLTAGE RUN.

FIG. A.21. High voltage feed through PVC safety cover.

(g) On the HV box, turn on either the first A or the first B switch, depending on which plate is being run (move the switch fully to the right, not to the middle position). (Fig. A.22)

(h) Prepare and start the ESD VI LabVIEW program (see Appendix C).

FIG. A.22. Sample plate switches outlined in white. "A" switch corresponds to sample plate A and the "B" switch likewise corresponds to sample plate B. Only one switch should be in the on position during a run and it should only either be the "A" or the "B" switch.

A.2.1.2. Cryogenic Testing

The setup for a Cryogenic temperature-dependent test is for the most part identical as the room temperature setup above but for one minor modification to the sample stack setup and the addition of extra procedures.

From room temperature setup section, note the following changes:

(a) In part (b) above, the locations of the aluminum cryogenic reservoir and the polycarbonate insulating layer should be swapped. Therefore the sample stack assembly should be (from bottom to top:

i. Polycarbonate base
ii. HV electrode plate
iii. Sample plates (sample-side down)
iv. Aluminum cryogenic reservoir
v. Polycarbonate insulating layer

This is done so that there is better thermal contact and conduction between the sample plates and the aluminum cryogenic reservoir. This helps to cool the sample quickly and efficiently.

(b) Ensure the thermocouple (TC) for the reservoir is attached (Fig. A.23). Also, ensure the TC plugs for the electrode plate are plugged in properly.

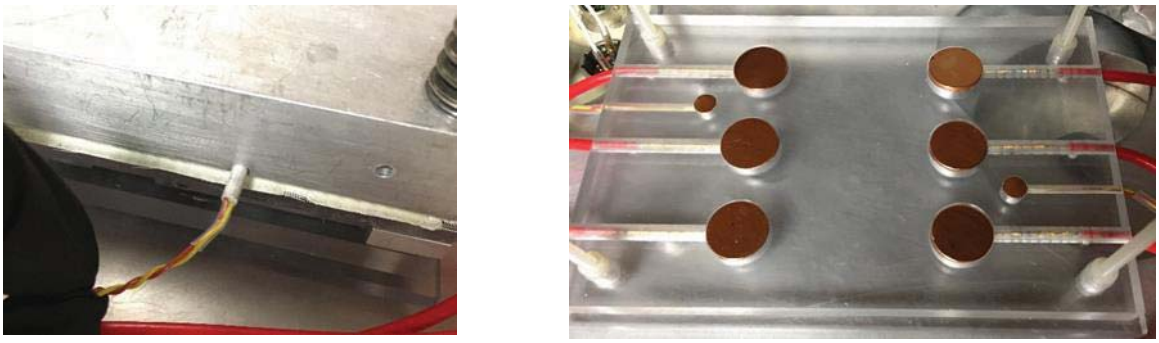

FIG. A.23. TC connections in the ESD chamber. Left- TC partially inserted into cryogenic reservoir. Right- TC electrodes circled in red on the ESD electrode plate.

(c) After the chamber has pumped down, it needs to be backfilled with nitrogen (N_2) gas. This is done because N_2 gas allows cooling by convection. To do this, follow these steps:

i. Ensure the N_2 gas hose is firmly attached to the back of the Pfeiffer turbomolecular pumping station (Fig. A.24).

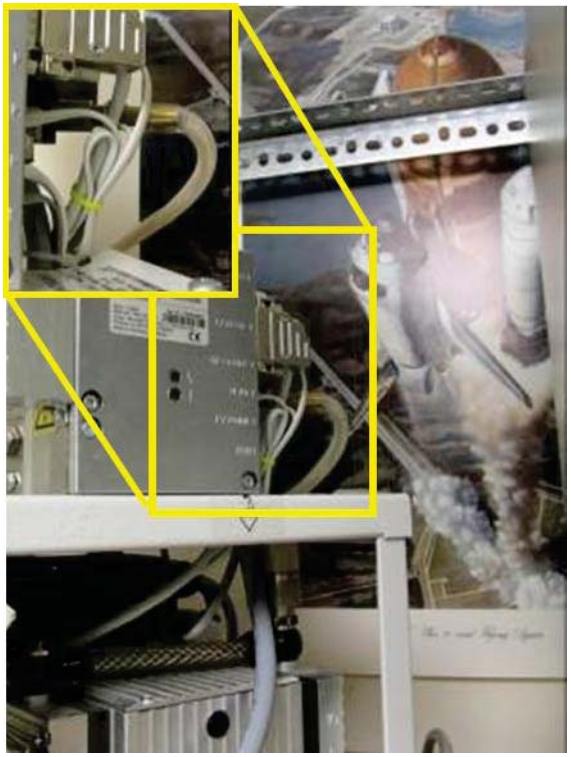

FIG. A.24. N_2 gas hose attached to the back of the Pfieffer TSH 071E turbomolecular pump station.

ii. Open the N_2 gas tank and ensure it is flowing at no more than ~5 psi (Fig. A.25).

iii. Turn off the Pfeiffer turbomolecular pumping station.

iv. Seal the chamber by closing main valve (clockwise) on the underside of the ESD chamber (Fig. A.26) all the way, and then open it by backing off the valve (counter-clockwise) by about three to four turns. This ensures that the chamber can be quickly sealed when the N_2 gas has been injected.

FIG. A.25. N_2 gas tank next to glove box. The tank is controlled by the valve circled in red. Turn it CCW until the gauge circled in red jumps, this gauge indicates the remaining pressure in the tank. The valve in yellow controls the pressure coming out of the tank, which is read by the gauge, circled in yellow. The blue valve directs gas to the ESD and bakeout chambers, while the purple valve directs gas to the glove box.

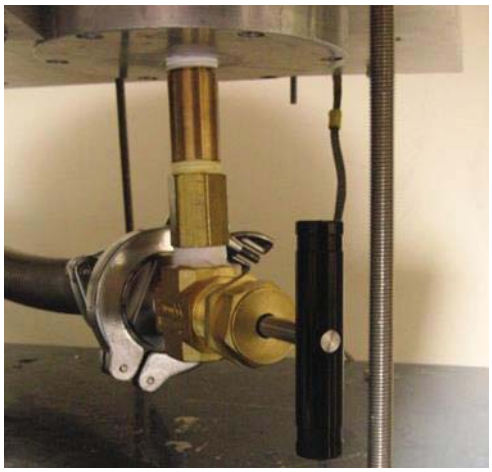

FIG. A.26. ESD chamber main valve.

v. The turbomolecular pump will take about five minutes to wind down if it is running properly. When the turbomolecular pump has wound down and the pressure is high enough (~10^{-1} mbar) the pumping station will begin injecting short bursts of N_2 gas through the gas line attached to the back of

the station to aid in braking the turbomolecular pump and backfilling the chamber with N_2. Injection is indicated by a clicking noise.

vi. Stay close to the chamber (as in do not leave while the turbomolecular pump is winding down) and monitor the pressure. Be prepared to close off the chamber quickly when the pressure has risen to about 10^{-2} mbar. Close the main chamber valve and seal off the chamber completely once the first click of N_2 gas being injected is heard.

vii. The chamber is still kept below atmospheric pressure at this point to prevent frosting on the inside that will ruin high vacuum conditions.

(d) Continue by following rest of the steps as outlined in room temperature setup section.

(e) Follow the same steps outlined in Preparing the ESD VI in Appendix C. It is useful to note in the comments field that this particular breakdown run is a cryogenic breakdown run.

A.2.1.2.1 Chiller Tests

(a) Make certain the coolant lines are connected from the chamber to the reservoir bucket and the chiller's output (Fig. A.27).

(b) Check that there is coolant in the bucket and that it is connected to the pump inlet. If more coolant is needed it is simply antifreeze mixed about 50/50 with water. Also, make sure that the pump outlet is connected to the chiller inlet (Fig. A.27).

(c) Plug the fan into the power strip and make sure that it is on and blowing on the pump. This is important to keep the pump from getting too hot and heating up the coolant.

(d) After the fan is turned on, plug in the pump and turn it on. Make sure that the coolant is flowing through by looking inside the reservoir and checking that coolant is flowing in from the chamber. Double check that there are not any leaks. Next, turn on the chiller using the power switch on the back.

(e) Sample temperatures can be monitored through the yellow TC connections on the front panel of the switch box (Fig. A.18). Be warned that the temperature will first increase for a half an hour or so before it will begin to drop.

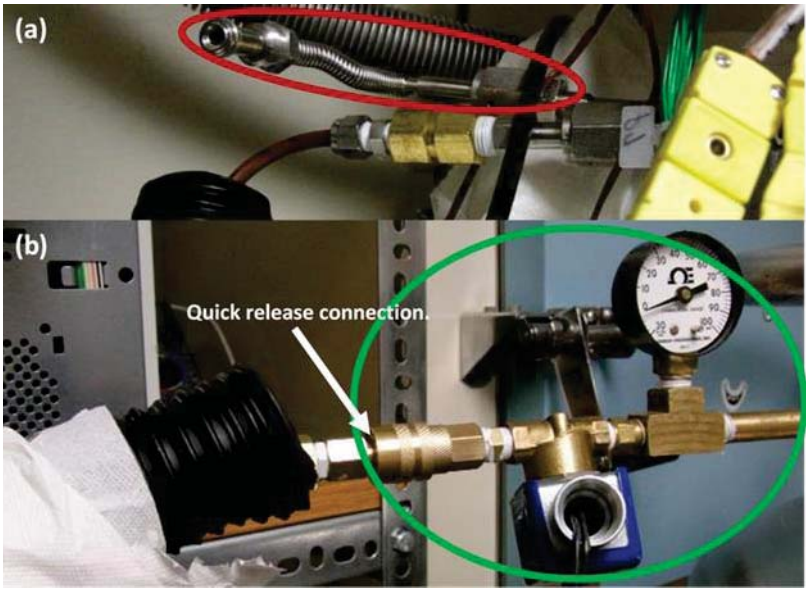

FIG. A.27. (a) lN$_2$ hose connected to the back of the ESD chamber. Circled in red is where the lN$_2$ comes out of the chamber. (b) lN$_2$ hose connected to the valve control (circled in green) of the lN$_2$ dewar. A quick release connector (black arrow) connects the hose to the chamber.

(f) Once the temperatures of the samples and the cryogenic reservoir have bottomed out (*i.e.*, has not changed more than ±2 °C in 15 minutes), then the chamber can be pumped down and cryogenic tests begun. You will leave the pump running during the cryogenic tests. Follow these procedures when pumping down and re-opening the ESD chamber to the pump:

   i. DO NOT OPEN THE CHAMBER VALVE FIRST.

   ii. Turn on the Pfeiffer turbomolecular pumping station.

   iii. Wait until the pressure has reached AT LEAST 10^{-1} mbar or less.

   iv. Open the main chamber valve (Fig. A.26) by turning it counterclockwise.

   v. Once the pressure in the chamber has reached $\leq 10^{-5}$ mbar, the tests may proceed.

(g) Indicate the time and temperature on the table of the beginning of the test run. Also make sure that the sample type, plate number (if applicable), and electrode position are noted as well.

(h) Proceed with steps (a)-(h) outlined in the room temperature test section above.

(i) When the sample has broken down, collect ~10-15 points beyond the breakdown point to ensure it has properly broken down. In addition, mark the time and temperature on the table at which it broke down, also a rough estimate of the voltage from the graph in the LabVIEW program.

(j) If multiple cryogenic runs are being done, one right after another, continue the same process as outlined above.

A.2.1.2.2 Liquid Nitrogen Tests

Cooling with liquid nitrogen (lN$_2$) can begin once the chamber has been backfilled with N$_2$ gas.

(a) Make certain the lN$_2$ hose is firmly attached to the ESD chamber and the lN$_2$ dewar, the large tank housing the lN$_2$ (Fig. A.27).

(b) Check to make sure the pressure on the lN$_2$ dewar is ≤100 psi (Fig. A.28 (a)). This ensures that when the lN$_2$ is flowing it will not spill too much as some typically does near the dewar end of the hose. If the pressure on the dewar is >100 psi, vent the dewar to 100 psi by opening the vent valve (Fig. A.28 (b)).

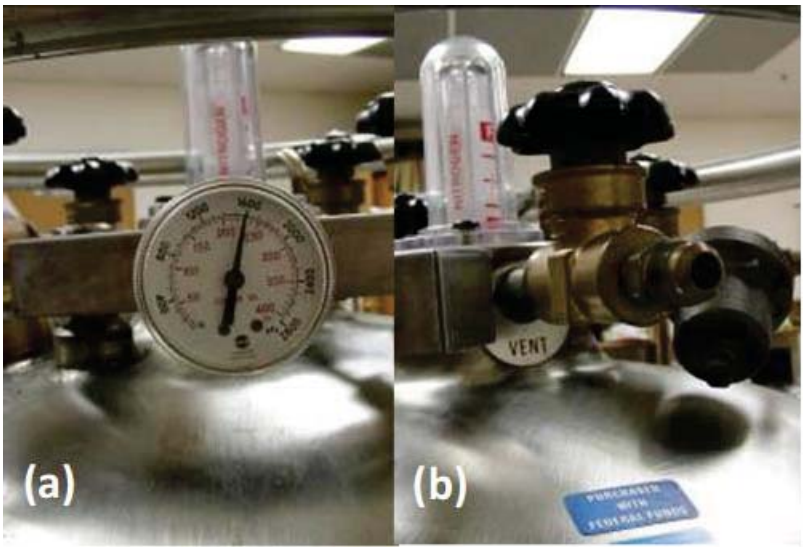

FIG. A.28. (a) lN$_2$ dewar pressure gauge reading ~250 psi. (b) lN$_2$ dewar vent/pressure release valve.

(c) There is a safety valve on the tank (Fig. A.27 (b)) that requires a voltage to keep it open. This valve is controlled by the OMEGA CNL16033-E1 partial integration derivative (PID) controller (Fig. A.29). The temperature of the reservoir is read by the PID box and if the temperature it measures falls below what it is set to, then the PID will shut it off the valve. If the PID measures temperatures that are warmer than the target temperature, it will open the valve and allow the lN$_2$ to flow. If for some reason the PID controller is not working, all that is required to keep the valve open is to plug the valve into a wall outlet. Once the valve is open, lN$_2$ can flow freely from the Dewar, into the hose, through the cold reservoir inside the chamber, and out again.

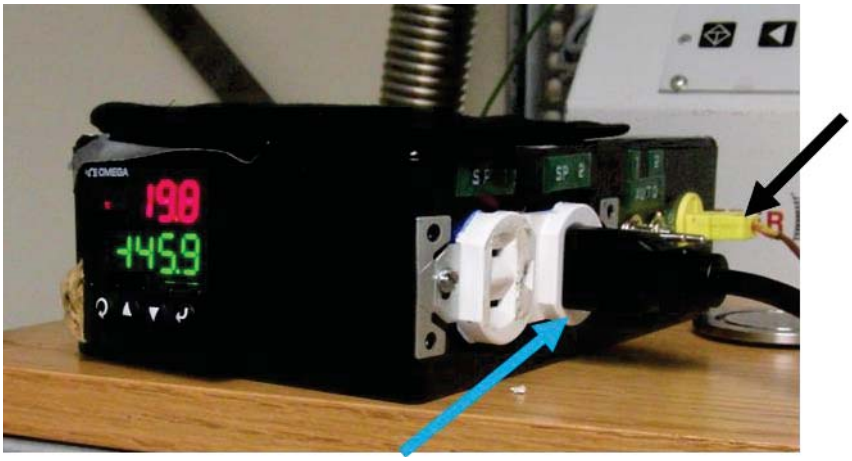

FIG. A.29. PID temperature controller box. The blue arrow indicates the power cord from the LN2 valve controller. The black arrow indicates where the ESD cryogenic reservoir TC cable plugs into the PID control box. The red value on the PID control box is the temperature (°C) read from the TC cable plugged into it. The green value is the target temperature (°C). For more information on the PID box, read its separate documentation.

(d) Begin the flow of lN$_2$ by opening the liquid valve on the tank and monitoring the pressure on the safety valve. It takes some finagling but try to keep the pressure between 10 psi and 20 psi. Either gN$_2$ or lN$_2$ will be seen coming out the other side of where the Dewar connects to the chamber.

(e) Sample temperatures can be monitored through the yellow TC connections on the front panel of the switch box (Fig. A.30).

FIG. A.30. TC connections on switch box. Left to right, cryogenic reservoir, A side, and B side TCs.

(f) Keep a running table of times and temperatures for both the reservoir and the sample. Temperature measurements do not need to be taken more frequently than one every five minutes or so.

(g) Once the temperatures of the samples and the cryogenic reservoir have bottomed out (*i.e.,* have not changed more than ±2 °C in 15 min), then the chamber can be pumped down and cryogenic tests begun. Follow these procedures when pumping down and re-opening the ESD chamber to the pump:

   i. DO NOT OPEN THE CHAMBER VALVE FIRST.
   ii. Turn on the Pfeiffer turbomolecular pumping station.
   iii. Wait until pressure has reached AT LEAST 10^{-1} mbar or less.
   iv. Open the main chamber valve (Fig. A.26) by turning it counterclockwise.
   v. Once the pressure in the chamber has reached $\leq 10^{-5}$ mbar, the tests may proceed.

(h) Indicate the time and temperature on the table of the beginning of the test run. Also make sure that the sample type, plate number (if applicable), and electrode position are noted as well.

(i) Proceed with step (a)-(h) outlined in the room temperature section above.

(j) Continue the table of times and temperatures of both the reservoir and sample during the breakdown run. Temperature measurements do not need to be taken more frequently than one every five minutes or so.

(k) When the sample has broken down, collect ~10-15 points beyond the breakdown point to ensure it has properly broken down. In addition, mark the time and temperature on the table at which it broke down, also a rough estimate of the voltage from the graph in the LabVIEW program.

(l) If multiple cryogenic runs are being done, one right after another, continue the same process as outlined above. However, it is typical to want the chamber to warm up some before the next run is conducted so that a good spread of temperature-dependent data are collected.

A.2.1.3. High Temperature Tests

The setup for a high temperature-dependent test is nearly identical to the room temperature run setup above, with the addition of these extra procedures:

(a) Attach thermocouples to the ESD chambers and multimeters to read both the internal (Fig. A.31) and external temperatures (Fig. A.32) of the chamber.

FIG. A.31. Internal temperature measurements. TC inserted into the cryogenic reservoir (left). TC feedthrough connections (right).

FIG. A.32. External temperature measurements–Aluminum tape is used to attach the TC to the chamber and is read with the multimeter.

(b) Wrap the chamber in heater tape by tying the tape to the handles of the vacuum chamber. Make sure the wire inside the tape is not exposed and that the wires do not cross each other (Fig. A.33).

FIG. A.33. Heater Tape. (left) Tie one end of the heater tape to the handle of the ESD chamber. (center) Wrap the tape around the chamber. Make sure that the internal wire is not exposed and that the wire from the two separate tapes do not cross. (right) Tape the heater tapes to the ESD chamber using aluminum tape so that they do not move. This will stop them from falling across each other when they are hot. Only put aluminum tape over the part that does not heat up.

(c) Plug the heater tapes into a transformer (this allows you to control the voltage that is put into the heater tape). Set the transformer to approximately 150 and adjust as needed (Fig. A.34).

(d) Cover the ESD chamber with a fire blanket to help keep in the heat and raise the temperature.

Follow the same steps outlined in Preparing the ESD VI in Appendix C. It is useful to note in the comments field that this particular breakdown run is a high temperature breakdown run.

FIG. A.34. Transformer. Variac transformer setting corresponding to an outer temperature of approximately 100 °C and an inner temperature of ~82 °C.

Follow the same procedure for starting a run as outlined in the room temperature test section. The only additional thing you need to do is turn on the multimeters, connected to the thermocouples that monitor the internal and external temperatures.

A.2.1.4. SVET Testing

Setup procedures are identical to those found in the room temperature run setup above. See Appendix C how to adjust the LabVIEW control. The process is the similar to the room-temperature instructions apart from the changes outlined for this test type. It is useful to note in the comments field that this particular breakdown run is a SVET run.

A.2.2. Maintenance

- In between tests. If the chamber is not going to be used for more than 1 day, it should be shut and pumped down to $\leq 10^{-1}$ mbar using the Pfeiffer turbomolecular pump. Maintaining vacuum when not in use prevents moisture from finding its way inside and contaminating any of the parts or samples.
- High voltage electrode polishing: Often charred carbon from the polymer is deposited onto the electrode at breakdown (Fig. A.35). This charred carbon, if left unresolved, will potentially increase with additional breakdowns and eventually cause irregular and dubious data. If taken care of quickly it can be removed with methanol and a Kimwipe.

FIG. A.35. Black carbon char marks left on an electrode from a large ESD event through a polymer.

However, most of the time, charring tends to cause scratches in the copper and it is best to remove the electrodes and to polish them. The following describes how to properly polish the electrodes. Read all the instructions before proceeding.

(a) The electrodes need to be polished on an exceedingly flat surface. There are two surfaces one can use to polish the electrodes:

   i. In the SER building machine shop there is a metal block with a flat surface.

   ii. In the sample preparation room, SER 217A, are some glass plates, these may also be used as a flat surface.

(b) All polishing should be done by rubbing the electrodes slowly, evenly, and gently in a circular motion. Do not go to fast or push too hard, this could create an uneven surface on the electrode, which will create places for preferential electric fields.

(c) First, the electrodes should be polished using the 600-grit sandpaper. This stuff is used to remove all the charred carbon from the copper electrode. Only polish the electrode enough to remove any char marks from the electrode. Excessive polishing with this sandpaper could result in shortening the height of the electrode just enough that its surface is not flush with the electrode plate.

(d) The electrodes should be polished using an optical cloth and 6 μm, 3 μm, and 1 μm polishing fluids found in SER 217A.

(e) Starting with the 6 μm fluid first and working down to the one μm fluid, put a small dab of the fluid on the optical cloth, rub the electrode evenly and gently in a circular motion on one of the flat surfaces described in part a. Polish each electrode in each fluid for AT LEAST 15 minutes. A good mirror surface can be obtained by following these procedures:

i. Thoroughly rinse each electrode prior to moving on to the next polishing fluid. These fluids contain microscopic diamond particles suspended in liquid; even the smallest amount left on the surface of the electrode will ruin the next polishing run.

ii. In addition, make sure that NO AMOUNT of polishing fluid from one bottle is mixed into another; the contaminated bottle will become entirely unusable.

(f) Once all electrodes have been polished, place them in a dichloromethane vibration bath for 1 hour. This removes any excess polishing fluids and oils. (Note that dichloromethane is no longer in use in the USU MPG lab due to its personal safety and environmental hazards. Acetone is now used for the primary ultrasonic bath followed by a secondary bath in methanol.)

(g) Take note of which electrode is which when placing the electrodes in a vibration bath. This can be accomplished by placing the A1 electrode in a different beaker than the A2, A3, or B side electrodes or place each in a separate container. This is done so that any potential problems that might arise from inconsistency are avoided.

(h) After all six electrodes have been cleaned using the dichloromethane, place them in an acetone vibration bath for 15 minutes, again making sure the individual electrodes can be differentiated one from another. After completing these two baths and giving the electrodes time to dry, they are ready to be placed back into the ESD chamber.

- Spare Parts: There are spare parts for the ESD chamber in a box on the blue shelves in SER room 217B. This box contains spare wavy spring washers for the electrodes, 100

MΩ resistors, set screws, bits of wire, nylon threaded rod, and other small parts that might be needed for the chamber. Each compartment of the box or any container in the box should be labeled.

- Cleaning: If not having been under vacuum for prolonged periods of time (~2-3 days), all parts should be cleaned in a ultrasonic bath. If the part or piece is non-metal, plastic, or it has plastic parts on it, it should be cleaned in methanol (completely submerged) for one hour in a vibration bath. If the part is completely metal, 15 minutes submerged in acetone and 45 submerged in methanol (both in an ultrasonic bath) should be sufficient. There is a ultrasonic vibration bath with a timer in the sample preparation room, SER room 217A. An additional ultrasonic vibration bath can be found in SER 21 and is used for cleaning larger parts. DO NOT CLEAN PLASTIC PARTS IN ACETONE! ACETONE IS CORROSIVE TO PLASTICS (POLYCARBONATE, NYLON, ETC.) AND IT WILL MELT THEM. ACETONE SHOULD ONLY BE USED TO CLEAN METAL PARTS. Before, during, and after cleaning, the parts should be handled with nitrile gloves. In addition, if the parts are not to be placed immediately back inside the chamber, after cleaning, they should be put inside the glove box with dry nitrogen gas to prevent recontamination.

A.2.3. Troubleshooting

- Getting down to pressure: Because the ESD chamber runs at 10s of kilovolts, there is the possibility of extreme danger if it is not properly grounded. Establishing the proper grounding path and avoiding floating conductors as much as possible will ensure operator safety. Improper grounding can be evidenced by, but is not limited to, the following:
  (a) Is the chamber lid adequately in place?
  (b) Are any wires stuck between the chamber lid and the rim it sits in?
  (c) Does the chamber lid O-ring need any vacuum grease? The viton gasket can be problematic. Regreasing and resting the O-ring usually fixes this problem

(d) Are all quick connects firmly attached and tightened down on the vacuum hoses, pumping station, and ESD chamber?

(e) Is there a leak in any of the vacuum plumbing underneath the chamber? This can be tested by squirting a little bit of acetone near any questionable leaks while monitoring the pressure from the pumping station. If while squirting the pressure jumps significantly and then drops, there is a leak. This test can only be done at pressures of ~10^{-2} mbar and lower.

(f) Have the insides of the chamber been exposed to atmosphere for a prolonged amount of time (>5 days) or handled without nitrile gloves? If so, the inside parts may need to be appropriately cleaned in methanol and acetone. See cleaning instructions above for a description of suitable cleaning procedures.

(g) Has the pressure been staying constant at $3.4 \cdot 10^{-3}$ mbar for a prolonged period of time? Check the Pirani gauge on the Pfieffer TSH 071E turbomolecular pumping station. Prolonged exposure to atmospheric pressures while the gauge and station are turned on can cause buildup of oxidized particles and contamination on the inside of the gauge. If this occurs, carefully follow the cleaning instructions for the Pirani gauge found in the Pfeiffer documentation folder in SER 217.

(h) Has work been done on the Pfeiffer Turbomolecular Pumping Station that has required it being completely disassembled? *E.g.*, has the mechanical pump or Pirani gauge been disassembled? If this is the case, examine first the mechanical pump and make sure there are no particulates in the diaphragms. If so, clean the diaphragms thoroughly using Kim wipes and methanol and ensuring that not particles are left behind. If the Pirani gauge has been removed and handled, make sure no particulates have made their way into there. If the pumping station is not misused, it should not be the problem.

- Common electrical issues:

(a) Arcing heard (and sometimes seen) on the outside of the chamber in the following locations:

i. TC plugs on front of the switch box (Fig. A.30):

ii. Inside of the switch box itself.

Origins of arcs can be located audibly using a plastic stethoscope. Arcs may be located optically in a darkened room.

(b) Erratic behavior in the measured current prior to and at breakdown:

i. Very low currents at breakdown (~1-5 μA) with extremely high resistances (~1000s of MΩ). This can be caused by the sample plate shorting to a TC electrode. This does not invalidate the breakdown voltage but it alters the apparent DCPD and breakdown current magnitudes.

ii. Non-ohmic behavior at breakdown, *e.g.*, the breakdown curve is non-linear. This could be due to an incomplete breakdown or external arcing.

(c) The first step to establishing proper grounding is to thoroughly check conduction paths in the chamber with a multimeter. A handy tool for this job is the system schematic. Check each wire and connection as much as it is possible and mark it off on a printed schematic. In addition, make sure that each wire's insulation has not corroded, deteriorated, or broken in any place. Typical problems include:

i. The white HV plug at the feedthrough is not in the correct position.

ii. The light switch for power is actually off.

iii. Loose electrode to HV wire connection.

iv. HV plate not connected or the wire from the current limiting resistors came loose in the chamber at the feedthrough (try the other plate if the chamber is closed).

v. AB toggle switches not right (in which case you did apply voltage and may have broken down but got no data)

vi. A BNC cable may not be connected.

A.3. Post-Breakdown Measurements

Following breakdown testing samples are not discarded. Thickness is measured after breakdown to avoid damaging the sample. Breakdown site images are taken and samples are labeled and stored for potential future reference.

A.3.1. Sample Thickness

In order to calculate electric field we need to know the sample thickness. The uncertainty in the breakdown field decreases significantly if the individual sample thickness and its uncertainty is used as opposed for the average thickness and corresponding uncertainty for all samples of that type. Thickness of each sample needs to be measured a total of six times. Calibrate the equipment, open the correct program (see below), and measure directly above and below each electrode contact point to do this. Using a digital Mitutoyo IP65 No. 293-330 digital micrometer (±1 μm resolution) with USB connectivity, measurements are to be entered directly into the Excel sheet "Thickness Template V2.xlsx" or the newest version. This sheet is found in Z:\Data & Analysis\Data\Electron Transport\ESD\Analysis Programs and a copy of it should be place in each folder corresponding to thickness measurements in the ESD file structure on the Big Blue file server. This Excel sheet automatically calculates the mean and standard deviation of the mean. These values should be copied as and pasted as numbers (rather than a simple copy and paste which would copy the formulas rather than the values) into the newest version of the ESD Quality Summary Matrix in the corresponding fields. Note that each sample will correspond to three entries (one for each electrode) in the matrix. Save the thickness, Excel worksheet as a new file with the corresponding sample name.

A.3.2. Optical Measurements

Breakdown site images show significant variation and may yield interesting information if the size or shape of the breakdown sites correspond to test parameters such as voltage, temperature, or material (*e.g.*, thermoplastic versus thermoset plastic).

(a) File destination: Prior to the image being taken, the file destination must be selected in the following location on Big Blue: Data + Analysis… Data…Electron Transport… ESD… Material Type… Test Type… Images. Once saved in the correct location, images should be titled using the correct naming convention: material thickness voltage date electrode number and file type: for example, KapE1mil_K20V 5-30-08 B_2.CR2.

(b) Imaging: Tested samples are to be handled carefully to prevent further damage, imaged under the new microscope camera. Images need to be previewed to ensure the full breakdown site is imaged, and image quality is acceptable for taking measurements and recording attributes; focus, lighting, window size, and background color are of particular importance. Attention needs to be given to the image background surface as well as lighting so that breakdowns are clear in the image for analysis. A measurement scale should be present in each image for proper scaling while measuring sites graphically. For future reference, a slide reticle with increments in micrometers (μm) should be used to create an accurate scale.

(c) Analysis: Images can be analyzed using photo editing software, the following should be noted within the ESD Quality Summary Table:

i. Presence of actual breakdown
ii. Major and minor axis diameters
iii. Damage area (see suggestions)
iv. Irregular features notes
v. Presence of secondary breakdown and subsequent measurements
vi. Discolorations

Images' major and minor axis of each breakdown should be measured using the photo software's pixel measurement tool. For our axis measurements, we took 5 measurements of

each scale in 1/100th inch increments using the software pixel measurement tool. The average of these measurements was used to convert our major/minor axis measurements (in pixels) to 1/100th inch measurements; this was later converted into micrometers in our matrix. Scaling of our images was eventually determined to be identical, at which point a single measurement was used to determine the proper scale. If the measurement fell within 10 pixels of our determined data set average scale of 169 pixels to 1/100th inch, then the data set average was used. A standard ratio of 169 (check) pixels per 1/100th inch was used for the remainder of our set. This was determined by averaging the scale measurements of previous samples.

(d) Characterization: Data entered into the matrix can be sorted based on any recorded trait. Table A.1 shows shorthand abbreviations which were used.

(e) Initial results: studies have been reported by Sam Hansen in (Hansen, *et al.*, 2014a; 2014b). Here we report no apparent trend in hole volume with breakdown voltage as shown in Fig. A.36. More work is needed in the characterization of the breakdown site images, but the cataloging system outlined here has laid the groundwork for such studies.

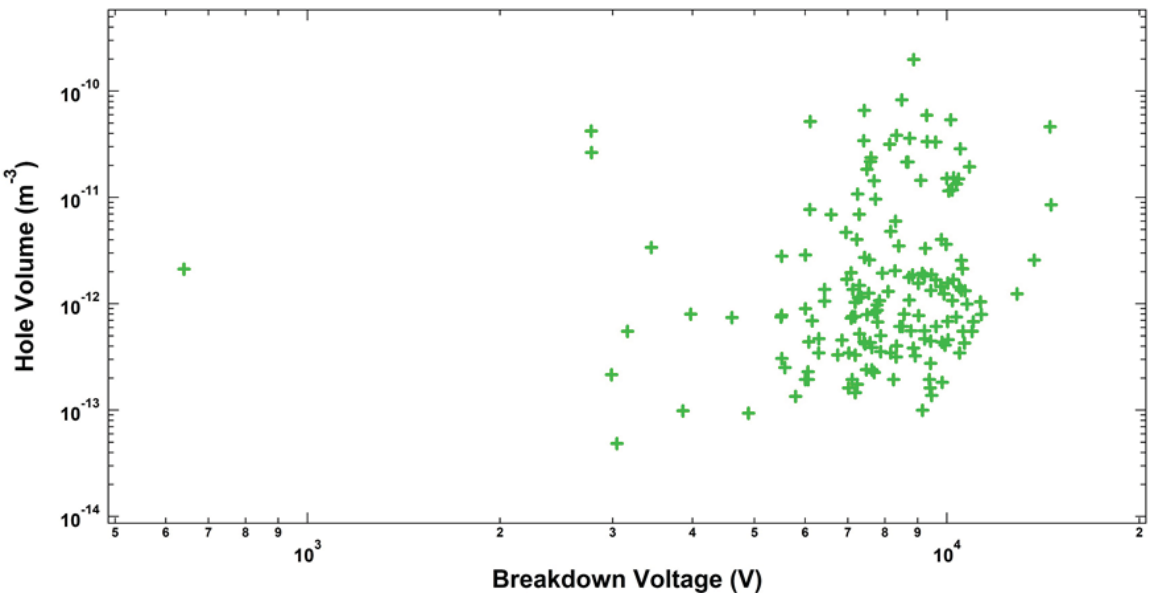

FIG. A.36. Estimated breakdown hole volume verses breakdown voltage.

Table A.1. ESD Image Analysis Categories.

Category	Comments	Example
1. rnd, melt ring:	Round melt ring, no unusual shape or coloration, this is in reference to the shape, not the size. Melt ring refers to the obvious zone around the breakdown hole where material has been melted, but no char is present. This melt zone is the same shape as the actual breakdown hole. This seems to be common in LDPE samples.	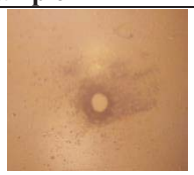
2. part. BD:	Partial breakdown refers to those samples that were obviously effected by melting and or discoloration, however the material was not completely vaporized, meaning no breakdown hole was present.	
3. 2nd partial breakdown	A complete breakdown is present and noted appropriately; this ADDITIONAL notation is in reference to a secondary damage zone, though incomplete as in the partial breakdown described above. To be classified as secondary this damage was not connected to the primary ESD site by melting or missing material and appeared independent of the other site.	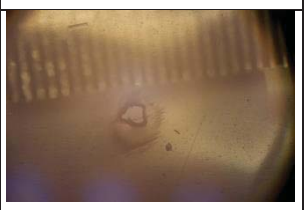
4. no vis BD	Some samples exhibit no signs of breakdown, a sample under microscope showed no melt ring or breakdown. Major and minor axis are entered as "–". Samples having zero signs of melting, that appear unaffected receive this description. Make sure that small breakdowns are not mistakenly passed over, since many pinhole-sized breakdowns are easy to miss.	
5. Irregular	Irregular breakdown do not exhibit uniform roundness as in the case of "rnd, melt ring" and do not have a standard description. For this reason, the term "irregular" should be followed with a short justification, or description of the irregularity. Breakdowns exhibiting a jagged breakdown perimeter are considered irregular. Due to the shape being irregular, a major and minor axis measurement does little to indicate the actual size of the area in question. These measurements (major and minor axis) should still be taken however. Shown at right is an irregular breakdown; the shape is not elliptical, there is no correlation of the melt zone to displaced material, and multiple holes are present.	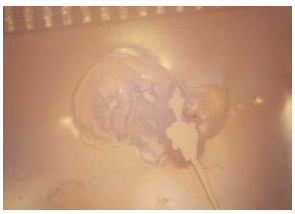
6. rnd melt/char:	Refers to the rnd melt rings that exhibited a dark or black discoloration in the melt ring surrounding a rnd melt ring breakdown. The discoloration may indicate a different process of destruction than other non-colored sites.	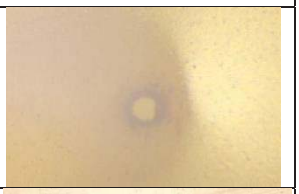
7. rnd, melt ring, mult part bd:	Same as in #1, with the note of additional partial breakdowns as in #2	

A.3.3. Long-term Storage

Used samples are to be placed in a Ziploc plastic bag. Any handling of samples outside the bag should be done with nitrile gloves to prevent contamination with skin oils. The label includes critical identifying information together with check boxes for the status of the sample and the corresponding analysis.

The ESD file naming convention currently is:

Material Thickness Temp Vstep Plate# Electrode# Date-of-bake.txt

For example:

KaptonHN 2mil 300K 20V 5 A1 6-26-13.txt or LDPE 1mil 300K 60V _ B3 3-30-15.txt.

An example of the label follows:

File:_____ _ _____ Test Date:__ /__/20_
Plate/Elec:_____ Thickness: □1 mil □2 mil___µm
Ramp Rate: □20V/4s ____V/____s
Run Type: □Ramp □Endurance □Temp
Temp: □RT □LT □HT ____K Bakeout: __ _/___/20__
Done: □Breakdown □Thickness □Image □Matrix

APPENDIX B

ERROR ANALYSIS

The calculations and figures in this dissertation show that the uncertainty in measurements is small compared to the variations in measurement due to real trends and stochastic variations described. This appendix outlines the representation of uncertainty in USU Materials Physics Group (MPG) dielectric breakdown and other associated measurements.

B.1. Uncertainties in Measurements

For electrostatic discharge tests the values of interest are the electrostatic fields (F) at which breakdown and pre-breakdown arcing occurs and the time (t), current (I), and temperature (T) at which these occur. In order to quantify ESD test results, we must estimate the uncertainty in each of these values for all ESD data. Care was taken to consider any likely source of error to ensure no underestimation of the uncertainty of measurements presented. Estimations of uncertainty will consider both the accuracy and precision of measurement uncertainty.

Let us start with the most important, and perhaps most complicated of these, the electrostatic field, F. The field across an insulating sample in a parallel plate capacitor geometry (assuming $d \ll \sqrt{A}$ in the capacitor) is simply the applied voltage divided by the sample thickness—$F = V/d$. The total uncertainty the field is the result of contributions in the uncertainties in the sample thickness and the applied voltage (Taylor, 1997).

$$\frac{\delta F_{event}}{F_{event}} = \sqrt{\left(\frac{\delta V_{supply}}{V_{event}}\right)^2 + \left(\frac{\delta V_{step}}{V_{event}}\right)^2 + \left(\frac{\delta V_{circuit}}{V_{event}}\right)^2 + \left(\frac{\delta V_{event}}{V_{event}}\right)^2 + \left(\frac{\delta V_{meter}}{V_{event}}\right)^2 + \left(\frac{\delta d_{measured}}{d}\right)^2 + \left(\frac{\delta d_{compression}}{d}\right)^2} \quad \text{B.1}$$

We will see that many of these are so small that especially for large V they quickly become insignificant. Let us address these one by one. This calculation has been automated into the ESD Quality Summary Table.

δV_{supply} is the precision in the voltage given by the power supply, namely a CPS Precision High Voltage Power Supply Model 130N/1314 which is rated to have <200 mV ripple at full load. This is 2% at

only a 10 V and its contribution decreases further as the voltage increases. This is negligible and in any case, the applied voltage is measured regardless independently. In other words, this term is both negligible and redundant.

δV_{step} is the uncertainty in the voltage step given by the circuit's response to the LabView program output. During a detailed analysis of this voltage step, assumed to be 20 V every 4 s, it was discovered that is in fact a cycle of three 16±1 V steps then one 33±1 V step. The net effect comes to 20±7 V steps. This encompasses both the accuracy and precision of the voltage step. As of September 14th, 2015 this has since been corrected and in subsequent tests does not affect δF_{event} since the voltage is read on the multimeter regardless of the step size. For now we can include it since at large voltages, one volt does not matter much. The uncertainty in the voltage step can be measured directly by examining consecutive voltage measurements. The Igor Pro macro "RampRate v1-2.ipf" found in Z:\Data & Analysis\Data\Electron Transport\ESD\Analysis Programs reads in such measurements and outputs the average voltage step and its uncertainty.

$\delta V_{circuit}$ is the accuracy in the voltage divider in the ESD circuit. The variable resister in this circuit can be adjusted so that the voltage read on the multimeter is 1/1000 of the voltage applied across the sample. This is achieved by measuring the HV in line using a high voltage probe simultaneously with voltage measurements in the voltage divider and changing the potentiometer until the two match up to exactly a factor of 1000. This potentiometer has been adjusted on occasion but comparisons were done before and after measurements (see IGOR experiment HV probe vs Multimeter in Z:\Instrumentation\Chambers & Systems\ESD\Characterization Measurements\CPS Power Supply RR Tests) and in the worst observed case, this discrepancy is less than 1.9%. Note that this means that $\frac{\delta V_{circuit}}{V} = 0.019$ regardless of the applied voltage. So far, this is the first significant contribution to our uncertainty at large voltages.

δV_{event} is another significant contribution and varies from event to event. The MPG definition of breakdown (see 4.1 and 4.6.4) is *Breakdown voltage can be defined as the average voltage between the last voltage with current below 10% of the R_{lm} expected ohmic breakdown curve and the first voltage with current increasing (though not necessarily smoothly) between 10% and 110% of the R_{lm} ohmic breakdown*

curve. The uncertainty then is the difference in voltage from the first measurement at breakdown and the last measurement before breakdown divided by two. As an overestimation of the maximum uncertainty, the entire difference between events rather than the half difference was used for the error bars represented in this dissertation. For measuring DCPD, $\delta V_{PD} \lesssim \Delta V_{step}$ but for $\delta V_{breakdown}$ we subtract the voltage with the last baseline current from the first voltage with steady breakdown current.

δV_{meter} is the uncertainty in our Amprobe®, Model 38XR-A multimeter. For dc voltage measurements, is rated to 100 μV ± (0.25 % + 5 dgts). At typical breakdown voltages this is an accuracy of essentially $\delta V_{meter} = 0.0025 * V_{meter}$. Again, we see this is negligible, especially at high voltages.

Now we come to the uncertainty in thicknesses (d). Each identifiable sample was measured in six locations distributed along our polymer samples with a Mitutoyo IP65 No. 293-330 digital micrometer (± 1 μm accuracy). The average (d) and standard deviation of the mean ($\delta d_{measured}$) were calculated for each sample. This is recorded in the ESD Quality Summary table and in individual measurement files in the ESD directory. For older data files that could not be matched to the physical sample, the average thickness and uncertainty of all samples of that type (perhaps bakeout batch) were used.

Both in the ESD sample chamber and in the measuring process, the polymer samples are compressed. $\delta d_{compression}$ was calculated for both the ESD chamber and the micrometer. $\frac{\delta d_{compression}}{d} = \frac{\Delta L}{d_0} = P/E$—the pressure divided by the Young's modulus. In either configuration both LDPE and Kapton have $\frac{\delta d_{compression}}{d} \approx 0.1\%$. This is small compared to most of our other thickness uncertainties.

For uncertainty in time we have

$$\frac{\delta t_{event}}{t_{event}} = \sqrt{\left(\frac{\delta t_{supply}}{t_{event}}\right)^2 + \left(\frac{\delta t_{LabView}}{t_{event}}\right)^2 + \left(\frac{\delta t_{deff}}{t_{event}}\right)^2} \quad \text{B.2}$$

δt_{supply} is the precision in the time stability (drift) of the power supply (CPS Precision H.V. Power Supply Model 130N/1314) This is rated to 0.005% after an hour 0.01% after 8 hours. Since the majority of our experiments take less time than this we will assume 0.01%. We will see that this is small compared to the largest term.

$\delta t_{LabView}$ is the precision in the timing of the LabView Program. Each data point in our LabView data acquisition program is time stamped from the start time of the experiment and stored in an array. The LabView time stamps are the primary time stamps and are recorded as integer ms. Sub-millisecond uncertainty is obviously negligible for test times ranging from tens of minutes to tens of days. We assume that the any inaccuracy in the computer's clock is negligible.

δt_{deff} is the uncertainty in the time of an event given our definition of that event. For pre-breakdown arcs, usually characterized by a single data point, this is at most on the order of a single time step. At breakdown, we use the same methodology as determining the breakdown voltage. The breakdown time is simply the average of the last time with baseline current and the first time with confirmed breakdown current and δt_{deff} is the difference of these divided by two. This can vary from run to run, but is always greater than or at least equal to one half time step.

The ammeter has 100 nA precision so δI_{meter} so for breakdown currents in the tens of μA this is less than 1%. Uncertainties is partial discharge and field-enhanced conductivity values can reach as high as 100% but in most cases are closer to tens of percent.

For temperature measurements, one must consider the precision of the thermocouple and the accuracy of the temperature reading in its location. K-type thermocouples typically have a nominal precision of the greater of 2.2 °C or 0.75% (OMEGA, 2018). The accuracy of the temperature readings depends on the thermal gradient between the thermocouple junction and the sample. The spring-loaded copper thermocouple electrodes in the ESD sample stack are in direct contact with the sample material so this effect should be small. The estimated uncertainty for temperature measurements used was ±2.5 °C. This variation is only ~1% of the temperature range of the tests presented in 6.2.4. These uncertainties are summarized in Table B.1.

From Table B.1 it is clear that the primary sources of uncertainty are the uncertainties in breakdown voltage δV_{event}, sample thickness $\delta d_{measured}$, and measured current δI_{meter}. The uncertainty in the breakdown voltage results from the finite time for complete breakdown to occur. In many tests, this time is much smaller compared to the time step in the voltage ramp rate and therefore the uncertainty is limited only by the voltage step size (typically 20 V). However, it is also common to observe that the

Table B.1. Summary of tests described in this dissertation.

Source of uncertainty	Type of uncertainty	Significance
$\frac{\delta V_{supply}}{V_{event}}$	Precision	0.02% at 1000 V
$\frac{\delta V_{step}}{V_{event}}$	Accuracy and precision	0.7% at 1000 V
$\frac{\delta V_{circuit}}{V_{event}}$	Accuracy	1.9% at 1000 V
$\frac{\delta V_{event}}{V_{event}}$	Physical effect	Varies from ~2-30%
$\frac{\delta V_{meter}}{V_{event}}$	Accuracy and precision	0.25% 0.01%
$\frac{\delta d_{measured}}{d}$	Precision and physical effect	~3% for measured samples ~7% for unmeasured samples
$\frac{\delta d_{compression}}{d}$	Accuracy	0.1%
$\frac{\delta t_{supply}}{t_{event}}$	Precision	~0.01%
$\frac{\delta t_{LabView}}{t_{event}}$	Precision	~0.0002 % at 10 min
$\frac{\delta t_{deff}}{t_{event}}$	Physical effect and precision	~0.3% at 10 min
$\frac{\delta I_{meter}}{I_{event}}$	Precision	<1-100% depending on event type
δT_{TC}	Accuracy and precision	±2.5 °C

transition from negligible leakage current to ohmic current (see 4.6.4) to occur over several voltage steps. The uncertainty is therefore due physical processes in the material rather than instrumentation and therefore cannot be mitigated.

The uncertainty in sample thickness $\delta d_{measured}$ is generally more than twice as large for the many samples have not had their thicknesses measured directly compared to those with direct measurements. The average variability is sample thickness varied by material. Unfortunately, samples from many older tests were not stored in a way where the samples could be uniquely paired to their corresponding tests data. For such samples, the average thickness of all samples of that type had to be assumed with the associated

uncertainty in the mean thickness. In other words, it is critical to measure each sample's thickness to reduce $\delta d_{measured}$. After thickness measurements were identified as a critical way of reducing uncertainty in breakdown field, all identifiable samples were measured as well as all subsequent samples. Over 70 % of samples presented in this dissertation had individual thickness measurements.

Finally, the uncertainty in current measurements is limited by the precision of the ammeter. This precision is excellent for typical breakdown current (<1% uncertainty), but becomes significant when considering events with currents approaching 100 nA. This includes DCPD and field-enhanced conductivity measurements (see 4.6.5). A more sensitive ammeter could mitigate this issue (see 7.4.2).

B.2. Statistical Confidence Intervals

Distribution functions such as a probability density function (PDF) or cumulative distribution function (CDF) such as Weibull distributions are often accompanied by confidence intervals. For now, I will focus on CDFs. There are commercially available programs such as Weibull++ that will automatically produce user-defined confidence intervals (see Fig. B.1) (Rytöluoto*, et al.*, 2014; Boggs, 2017a). From my limited exposure to such programs, it is not apparent how these are calculated. Weibull++ appears to find a region that, for 95% confidence, contains as near to 95% of the data as possible. While such programs are surely very useful for those applications the developers have tailored them for, they are not well suited for this analysis here. For instance, units of voltage or field are not available. As far as Weibull fits are concerned, initial Weibull++ results from a trial download are in good agreement with my Igor Pro analysis, however, Weibull++ lacks an obvious way to put uncertainties on the fitting parameters. It is convenient that several Weibull distributions and mixed Weibulls are built in; however, for the purposes of MPG analysis the custom Igor Pro macro described in Appendix C is more convenient.

The two-parameter Weibull CDF has a closed form way of estimating confidence intervals. However, this is valid only for the two-parameter case (Thoman*, et al.*, 1969; Heo*, et al.*, 2001). For Weibull functions with more than two parameters, there exists a variety of methods for estimating confidence intervals, many of which rely on tables of reference values and/or are computationally difficult (Lawless, 1978; Heo*, et al.*, 2001). In most cases results from different methods are reasonably consistent (Heo*, et al.*, 2001).

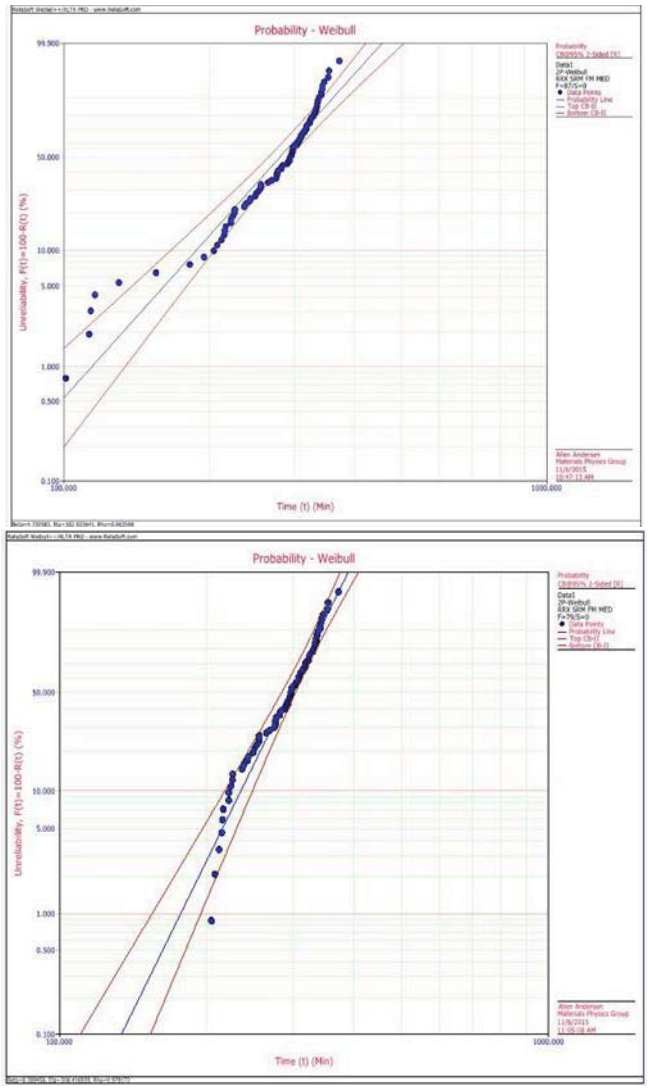

FIG. B.1. LDPE data imported into WEIBULL++ and plotted with 95% confidence bands. Note that spurious data is included in the top plot but not the bottom plot.

Given that I am interested in the ECD of my data as applied not only to Weibull distributions but also to Q-Q plots and physics model fits, some non-parametric measure of confidence would be preferred. If I can use the same standard for all my analysis, I would prefer such a method. Like for Weibull plots, various methods and generalizations of sometimes staggering complexity have been devised for drawing confidence intervals around Q-Q plots (Einmahl and McKeague, 1999; Rosenkrantz, 2000; Valeinis*, et al.*, 2010). Of these I have found the most straightforward to be the Kolmogorov-Smirnov (K-S) statistic (Smirnov, 1948; Rosenkrantz, 2000; Valeinis*, et al.*, 2010). The advantage of this method is that it can be

applied to any data set and a candidate CDF in a way that does not depend on the CDF, $Y(x)$, so long as one is assumed to exist (Smirnov, 1948). For the ECD of the data, $S_n(x)$ the confidence interval can be shown to be simply

$$S_n(x) \pm D_{n,\alpha} \tag{B.3}$$

where $D_{n,\alpha}$ can be found in a table of calculated values based on the desired confidence interval and sample size n (Smirnov, 1948). Rather than confidence bars containing 95% of the data as in Fig. B1, the K-S statistic confidence bars enclose an area with 95% confidence of where the data actually may be. See Fig. B.2 as an example.

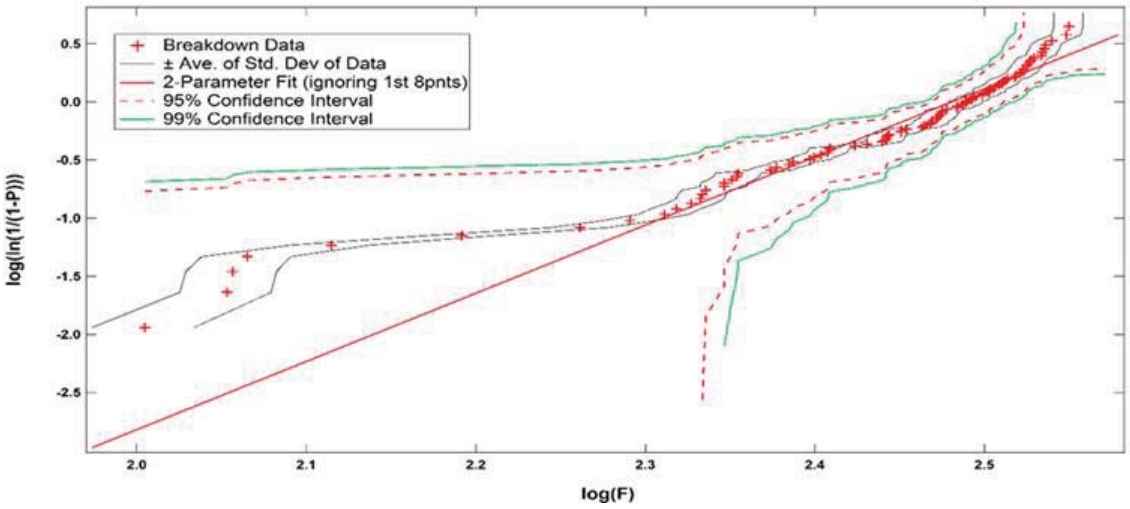

FIG. B.2. LDPE breakdowns with estimated experimental uncertainty and 95% and 99% K-S confidence bars.

Figure B.2 also has the much narrower bands representing the average of the standard deviations in the experimental uncertainty. Although any of these are valid, it seems that the average of the experimental deviations the most useful in that it reflects known uncertainties rather than arising from statistical variations.

The K-S statistic may just as easily be applied to Q-Q plots comparing data and a CDF, but a two-sample K-S statistic or other complicated method is required to place confidence bars on an empirical or

two-sample Q-Q plot (Einmahl and McKeague, 1999; Rosenkrantz, 2000; Valeinis*, et al.*, 2010). However since there are many more DCPD than breakdowns and since $D_{n,\alpha} \propto n^{\frac{-1}{2}}$, it may be justified to use approximate the DCPD field uncertainty as negligible compared to that of the breakdowns. In other words, using the ECD of the DCPD as a CDF may not be a horrible approximation.

APPENDIX C

DETAILS OF DATA ACQUISITION AND PROCESSING SOFTWARE

This appendix outlines the computer control, data acquisition, and data processing used to generate and analyze Materials Physics Group (MPG) electrostatic discharge (ESD) data.

C.1. Logical Flowchart

Figure C.1 is the logical flowchart for MPG ESD data. For the purposes of this appendix, version numbers of programs are not discussed. In general, the newest version should be used if it is functioning correctly.

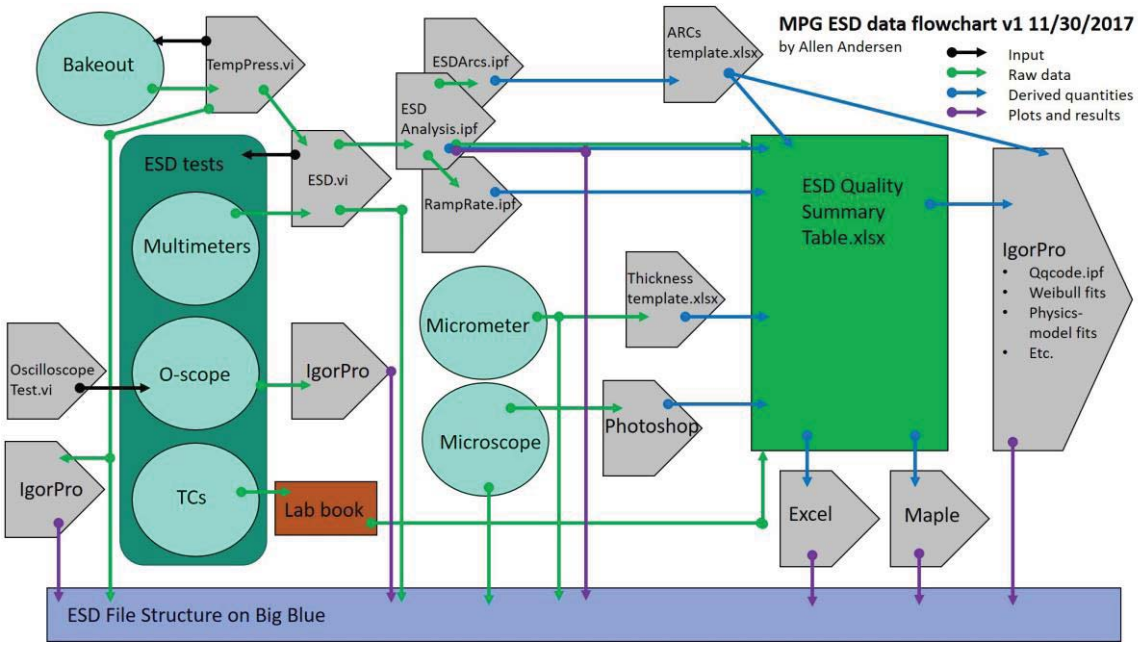

FIG. C.1. MPG ESD Data Flowchart. Black arrows represent computer inputs into test systems, green arrows represent raw data, blue arrows represent derived or manipulated data, and purple arrows represent calculated results including plots. Cyan circles represent instruments that generate data. Grey pentagons represent software functions with the exception of the ESD Quality Summary Table, which has its own symbol to highlight its central role in the data flow. All data and results are stored on the MPG file server, Big Blue, in the ESD archives.

The process shown begins with bakeout as that generates a unique sample name as sample plate and bakeout date combinations should be unique. Bakeout temperature curves may also be of interest. The ESD.vi program controls the ESD test and acquires voltage, current, and time data. Data from each test are analyzed by several Igor Pro routines, the most important of which is ESD Analysis.ipf. Results from these programs—including breakdown voltage, test identifiers, and test parameters—are passed to the ESD Quality Summary Table sortable matrix together with thickness, breakdown site dimensions, and temperature data. With the exception of some DCPD, all relevant data are stored in the ESD Quality Summary Table. From this matrix, individual results can be sorted and grouped together to allow for studies of larger trends. Raw data, processed data, plots, and results are archived in the ESD file structure on Big Blue.

Some work should be done to improve this flow, for example combining some Igor Pro functions, and adding a temperature multiplexer to record temperature electronically data rather than the lab notebook; however, this is representative of the data flow to date.

C.2. LabVIEW

C.2.1. Bakeout

See Appendix A for instructions on operating the bakeout chamber. The bakeout program simply records the temperature measured by a thermocouple placed in the oven during a sample bakeout at user-defined time intervals. Data are plotted in real time in the program for monitoring. The data are output as a .txt file. Note that if the bakeout computer is on the same electrical ground as the ESD chamber, the bakeout computer may shut down or restart when breakdown occurs.

(a) Turn the multimeter on and plugged into the wall. Make sure it is reading the correct temperature.

(b) Check the computer date and time time on the taskbar and correct if needed.

(c) Create a bakeout text file, located in the folder "bakeout current year" on the desktop of the computer by the bakeout oven.

(d) Open the VI (on desktop) labeled TempPress 7.1.

(e) Fill out the required fields (see Fig. C.2):

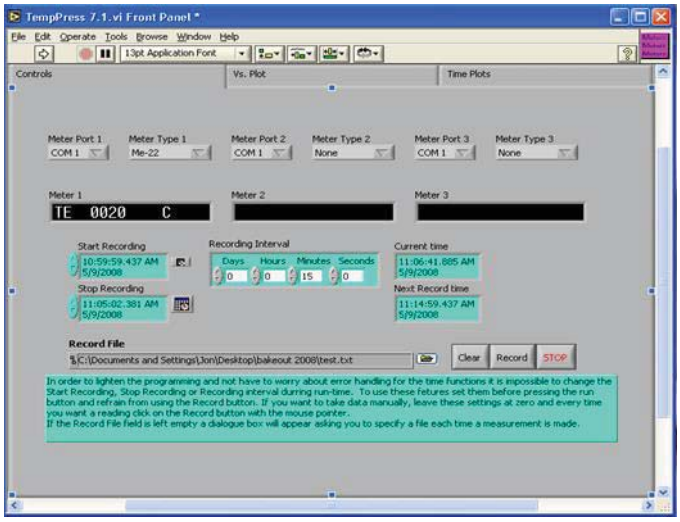

FIG. C.2. TempPress bakeout program main screen.

i. Meter Port 1:COM 2

ii. Meter Type 1: Me-22

iii. Start Recording: set to present time

iv. Stop Recording: set to 4 days in future (or longer for longer bakeouts)

v. Recording Interval: 15 minutes

vi. Record File: browse for the file created in (c)

(f) Start the program by clicking the white arrow in the upper left corner. Assure that the correct temperature appears in the black display area under Meter 1 (around 20 °C).

(g) Turn the oven on and set temperature according to table on the oven front (oven dial is not calibrated). Currently we bake LDPE at 65° C, and all other thin film samples at 105° C.

C.2.2. ESD Tests

See Appendix A for instructions on setting up the ESD system. The ESD VI controls the power supply that provides the high voltage for breakdown and records time and voltage and current data from the ESD system multimeters (see 4.6.2).

- Preparing the ESD VI:

(a) Run LabView and open “ESD V1-01.llb” located n the “ESD VI’s” folder on the desktop (Fig. C.3). Refer to Fig. C.4 for steps b-d.

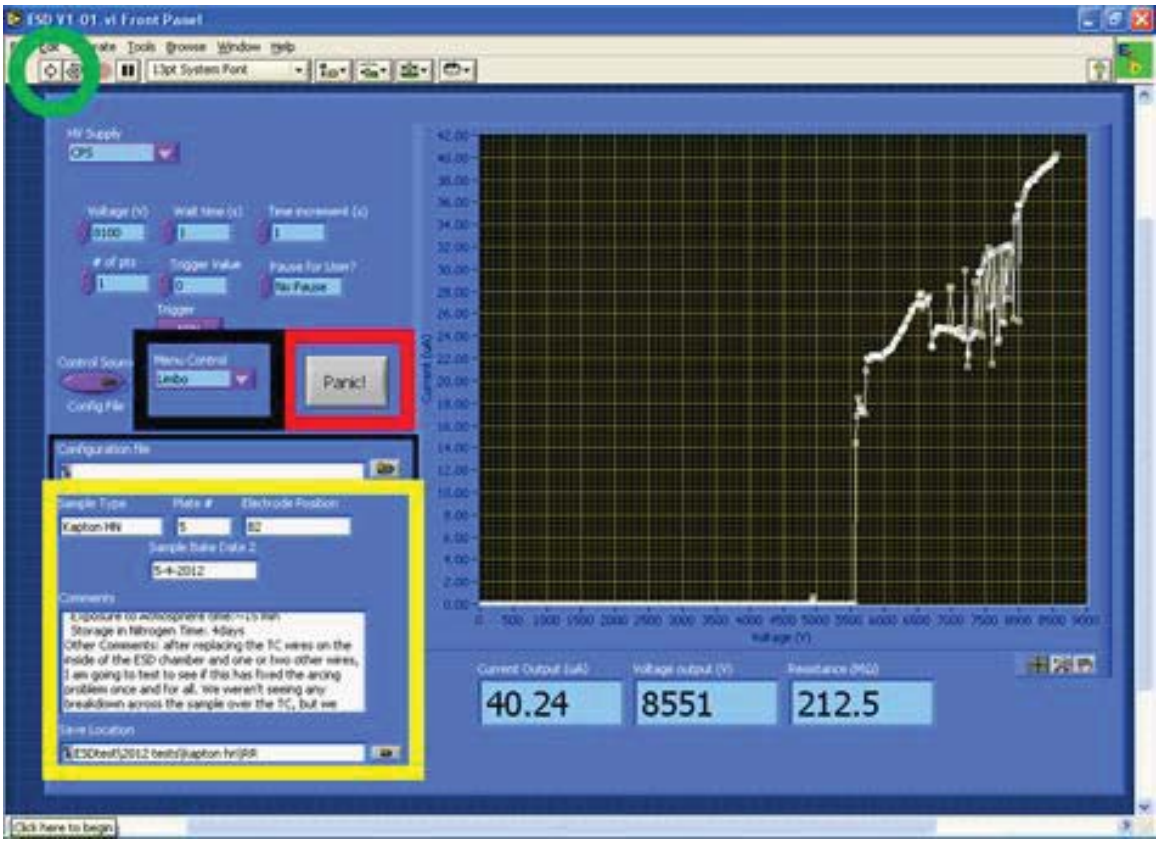

FIG. C.3. ESD LabVIEW VI computer interface. The LabVIEW VI run button (white arrow) is outlined in green. Menu Control is outlined in thick black. Panic Button is outlined in red. Output file information and location is outlined in yellow.

(b) Fill in Sample Type first part of the naming convention, (‘material’ ‘thickness’ ‘temp.’ ‘voltage ramp rate’, *e.g.*, LDPE 1mil 300K 20V4s), Plate # (*e.g.*, P1), electrode location being used (A or A2, etc.), and Sample Bake Date with the date the sample was baked out (1-18-08, not 1/18/08; using / will create new folders). These fields are used to name the output file.

(c) Fill in the comments. Example:

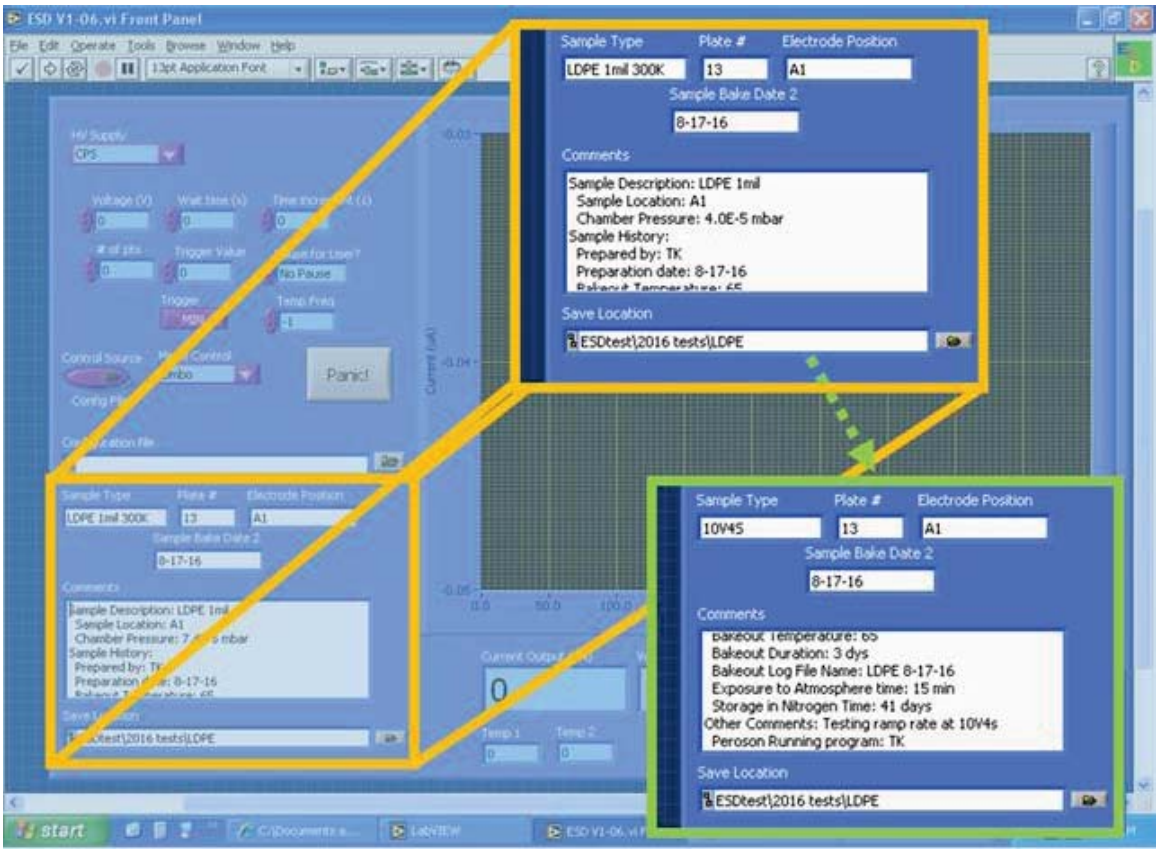

FIG. C.4. ESD LabVIEW output file setup. Fill in the comments section before each test run. The area in the green box shows text not visible without scrolling.

Sample Location: B1

Chamber Pressure: 6.3E-6 mbar

Sample History:

Prepared by: Steve

Preparation date: 1-18-08

Bakeout Temperature: 120C

Bakeout Duration: 3 days

Bakeout Log File Name: ESD 1-18-08.txt

Exposure to Atmosphere time: 15 min

Storage in Nitrogen Time: 2 days

Other Comments:

Person Running program: Dan

(d) Click the file symbol beside the Save Location field. Browse to the folder for the material being run. The folder structure for data files should be: “(year) tests” □ ”material name” □ ”type of test (*e.g.,* RmT, Cryo, Time dep)". Click “Use Current Dir” to select the desired folder as the save location for the data file. *E.g.*, if the current year is 2012, the material being tested is LDPE, and the test run is a time-dependent run, then the file directory location should be named: “\ESDtest\2012\LDPE\Time dependent.”

(e) Change Menu Control to “Limbo” (Fig. C.3). For instrumentation instructions, see Appendix A.

- Starting a test:

(a) Switch the HV monitor Meterman to the second voltage position from the left and the current monitor Meterman to μA. Push the RS232 button on both units. Confirm that batteries are charged and that “sleep off” option is enabled for both of the meters. (This can be done by pressing and holding the MIN MAX AVG button while turning the switch from OFF to the desired function.)

(b) Turn on the left light switch below the switch box (Fig. C.5); this controls the power to the high voltage power supply. If the light is RED, TAKE CAUTION! This means the power supply is currently ON and may be supplying high voltage to the circuit!

(c) In the ESD VI, click the white arrow in the upper left corner to run the program (Fig. C.3).

(d) A dialog box will appear asking for the number of configuration sections (Fig. C.6). Enter 0 if the configuration file is already set correctly (from a previous run) or 1 to define a new configuration. For normal room temperature (and cryogenic) runs, the configuration file should have the following values (Fig. C.7):

i. Starting Voltage: always 0V

FIG. C.5. ESD power supply switch (outlined in red).This switch controls the bank of plugs to the right of it. In this image the current position is "on," turned to the right and the CPS power supply cord is outlined in yellow. The red light (under the switch) indicates that the power supply is on and the user should take caution.

FIG. C.6. Configuration Sections window. 0 is entered if a previous configuration file is going to be used. Enter 1 if a new configuration file is to be created. Select 2 if there needs to be two sections created in the configuration file, *e.g.,* a ramp up to a wait voltage for a time-dependent run.

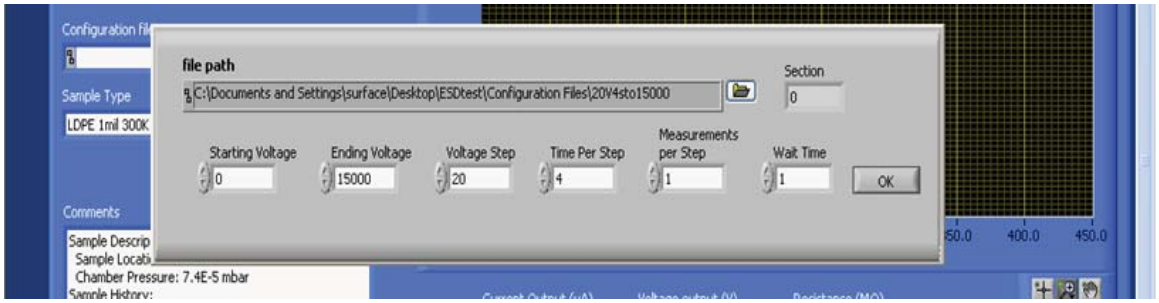

FIG. C.7. Configuration file setup window. Starting Voltage and Ending Voltage tells the ESD VI what voltages to begin and end with. Voltage Step is how many volts one wishes to increment each step (*e.g.*, 20, 50, 100); standard procedure is 20 V increments. Time Per Step is set to 1. Measurements Per Step programs how many points are desired to be measured at a given voltage; a 1 is usually entered here unless an endurance time run is being conducted. Wait Time is set to 1.

ii. Ending Voltage: ~15000V

iii. Voltage Step: 20V

iv. Time Per Step: 4 (An error message will appear during testing if there is a time step error, 4s or longer should not cause this error.)

v. Measurements per Step: 1

vi. Wait Time: 1

(e) Once the above values have been entered, click okay and a save dialog box will come up. Room temperature and cryogenic runs are saved as "ESDConfig.txt" in the "ESDtest" folder on the desktop of the ESD computer.

(f) Change the Menu Control (Fig. C.3) from Limbo to Take Data to start data acquisition. The Menu Control value will automatically change to Stop and the graph will clear before showing new data.

(g) Another dialog box will appear requesting the location of the configuration file (Fig. C.8).

(h) To stop the program before it finishes the configured run (for example, if there is arcing or if the sample breaks down), hit the panic button (Fig. C.3) to bring the power supply to zero and stop the program. Remember to hit the panic button again to clear it before starting a new run. Wait until the voltage on the multimeter reads zero before hitting the panic button a second time.

(i) After the run ends, turn the power supply off, unplug the blue HV wire and return it to the HV dock (Fig. A.19 in Appendix A), and turn off the A or B switch.

- Starting a SVET run: Except for the configuration file, an endurance time run is for the most part identical to standard test as described above.

(a) First, proceed with steps (a)-(c) outlined in the section above.

(b) Note the following changes for part (d):

a. Enter 2 in the dialog box requesting the number of configuration sections and click okay. The first section steps up the voltage in 20V increments to

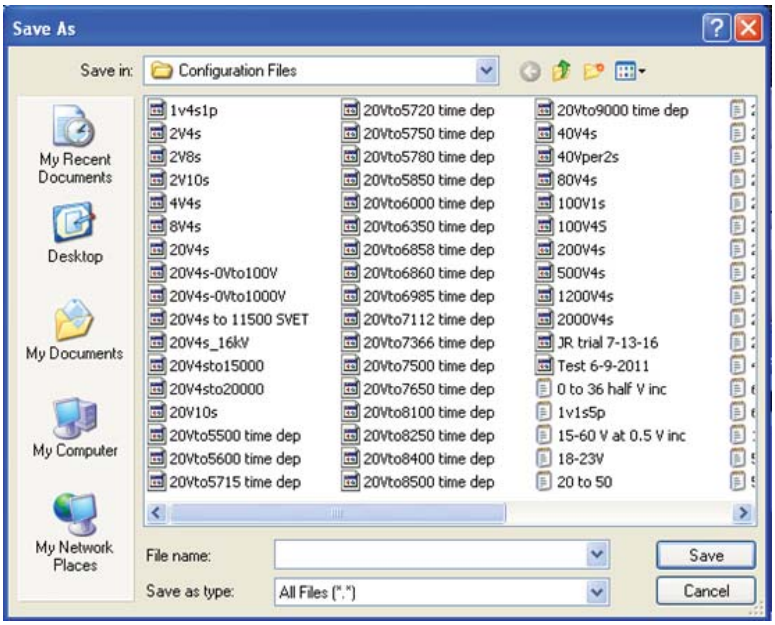

FIG. C.8. Configuration file selection box.

the desired target voltage for breakdown. The second section keeps the voltage static at this target voltage and makes a measurement of current, voltage, and time every four seconds. How long the sample is held at this voltage is determined by the second section.

b. When the configuration window pops up (Fig. C.7), note that it states "section 0", however this means section 1; entering section 1's values"

   i. Starting voltage: always 0

   ii. Ending voltage: enter the desired target voltage for breakdown, *e.g.*, 7200, 6500, etc.

   iii. Voltage Step: always 20

   iv. Time Per Step: always 4

   v. Measurements per Step: 1

   vi. Wait Time: always 0 for section 1

c. Hit okay when finished entering the above values for section 1. The value in the “Section” field will change to 1 which means values entered will be in the SECOND configuration section. These are the following values for the second configuration section:

   i. Starting Voltage: always the desired target voltage for breakdown, *e.g.*, 7200, 6400, etc.

   ii. Ending Voltage: this field does not need to be changed.

   iii. Voltage Step: always 0 for section 2.

   iv. Time Per Step: this field does not need to be changed.

   v. Measurements per Step: this field determines how long the chamber will be running. A value of 1200 will leave the chamber operating at the static voltage for one hour. It is always best to overestimate the time to breakdown. For example, if a given target voltage is believed to take three hours to breakdown, the number of measurements would be 3600 (3 hours * 1200). However, should the material take longer than this, it is safe to enter larger times corresponding to days or weeks depending on the available test time.

d. Click okay and a dialog box will popup prompting for the desired save location and name of the configuration file. The configuration file should always be saved to the “ESDtest\Configuration Files” folder located on the desktop of the ESD computer. The name should reflect that this is an endurance time run.

(c) Continue with the rest of the steps described in the Stating a Test section above.

(d) Depending on the voltage being applied, endurance time runs can last for several days. Because of this, the batteries in the current and voltage multimeters need to be changed when they are drained. However, a battery pack with three 9V batteries

connected in parallel for each multimeter has been created so that the batteries do not need to be changed as often. Have at least three to six fully charged batteries on hand so that when any batteries in the battery pack die they can quickly be replaced. DO NOT PLUG ANY OF THE MULTIMETERS INTO A WALL OUTLET! AT BREAKDOWN THEY CAN POTENTIALLY BE FRIED! Dead batteries or swapping batteries will cause a lapse in the data. This is typically very apparent in the data and only a problem if breakdown occurs during the down time.

(e) Once the material has broken down, the ESD program can be stopped like any other run by hitting the panic button, changing the menu control to "Limbo," turning off the HV power supply, unplugging the blue HV wire and plugging it in the HV dock, turning off the multimeters, and turning the A or B switch off.

C.3. Test Data Analysis

This section describes how to take the raw data generated by the ESD LabVIEW data acquisition software and process it in a useful, standard way. It is important to follow the naming convention for individual runs. The ideal naming convention for files in these folders should relate all the relevant information about the test in question while being as concise as possible. Many older files contain merely sample material and bake out date or even less information. The present naming convention is "material thickness temp Vstep plate# electrode# date-of-bake.ext" *e.g.*, KaptonHN 2mil 300K 20V 5 A1 6-26-13.txt or LDPE 1mil 300K 60V _ B3 3-30-15.pxp. If an unusual time step (not 4s) is used for a ramp rate test the in place of the "Vstep", enter the entire ramp rate *e.g.*, 40V8s.

C.3.1. ESD File Structure

Of critical importance is the ability to store data in an organized structure that allows it to be easily retrieved again. This section outlines the file structure on the MPG Big Blue file server. The following sections assume that the raw data have been placed in its correct location in the ESD file structure on Big Blue: Z:\Data & Analysis\Data\Electron Transport\ESD.

The ESD file structure is as follows:

ESD

- Analysis Programs
- Bakeout Files
    - Processed
    - Raw
- Materials

  Each material has its own set of subfolders as follows. There is a “Materials folder template” that contains the following structure for each material tested. This is standard for each material. There may be empty folders if a given type of test has not yet been done for that sample. (note NBD stands for “No Breakdown”)

    - Temp Dependent
    - RT Ramping
    - Summary
    - Time Endurance (note that EBD stands for “Early Breakdown” in Time Endurance (SVET) tests)

      Each of these folders other than the “Summary” folder contains the following set of folders.

        - Images
        - Multimeter
        - T data
        - Thickness

          Each of these contains the folders

            - Processed
            - Raw
- Papers&Presenations
- Procedures
- Old ESD to sort

This is what remains of the old, less organized, ESD file structure. It contains all the files that have not yet been sorted into the new structure and/or are poorly labeled.

C.3.2. Igor Pro ESD Analysis

Each raw .txt file in the “raw” folders should be processed. If you are processing many data it may be convenient to copy the folder of raw data to your local machine, leaving the files on Big Blue intact, process everything, then copy the processed data to the appropriate place on Big Blue.

Some of the very oldest data, or if there are data with problems or changes with the LabVIEW generated header files, may not be able to be processed normally. In that case, just read the .txt file into Igor Pro under Data-Load Waves-Load General Text and plot the data manually. Normally you should only have to do the following:

(a) Ensure the newest version of the "ESD Analysis" Igor Pro Procedure file is copied to the "processed" folder that will be the destination of your processed data. This ensures that the results can be matched to the version used.

(b) Click on the "ESD Analysis" Igor Pro Procedure file and go to "Macros" in the toolbar. Compile if needed then execute "ESD Analysis…". Browse to the raw data file to be processed. Usually the corresponding "raw" folder will be accessible one folder level up.

(c) The program will run and several plots will appear. For each ESD run in the raw data file (newer tests should normally only contain one) there will be four plots. Voltage vs Time, Current vs ln(Time), Current vs Time, and Current vs Voltage. For most tests only the Current vs Voltage plot will be of interest. The other plots are more useful for static voltage endurance time (SVET) tests.

(d) At this point, save this Igor Pro Experiment! Use the same file name as the raw data file if it is named correctly (if not then correct it). Save the file in the corresponding “processed” folder. The new processed file’s name, type and file location will be sufficient to identify it in the future.

(e) For standard ramp up tests enlarge the Current vs Voltage graph. The markers should already be visible. If not, "Ctrl+I" toggles the info bar with the markers as does "Graph", "Show Info" in the toolbar. The markers should be visible in the bottom left of the info bar (See Fig. C.9).

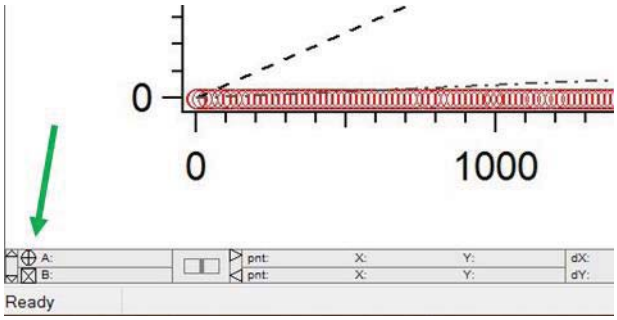

FIG. C.9. A and B markers in Igor Pro plot.

(f) Place the A marker (crossed circle) on the last datum with current below the 10% breakdown current dashed line and the B marker (x-ed box) on the first datum above the 110% breakdown line that is part of a clear breakdown slope (an identifiable slope corresponding to between 10% and 110% of expected circuit's maximum expected limited current). See Fig. C.10 and the ESD breakdown criteria document for further details in Z:\Data & Analysis\Data\Electron Transport\ESD\Analysis Programs.

(g) Ensure the A marker goes on the last pre-breakdown datum; otherwise there could be errors in the "get PDs" macro later on.

(h) The x and y values of the data marked will now appear in the info bar (see Fig. C.11). These data will be entered in the ESD Quality Summary Table as described in the following section. In the case of static voltage endurance time or other data, the markers can be used in a similar way to find the breakdown time rather than the breakdown voltage.

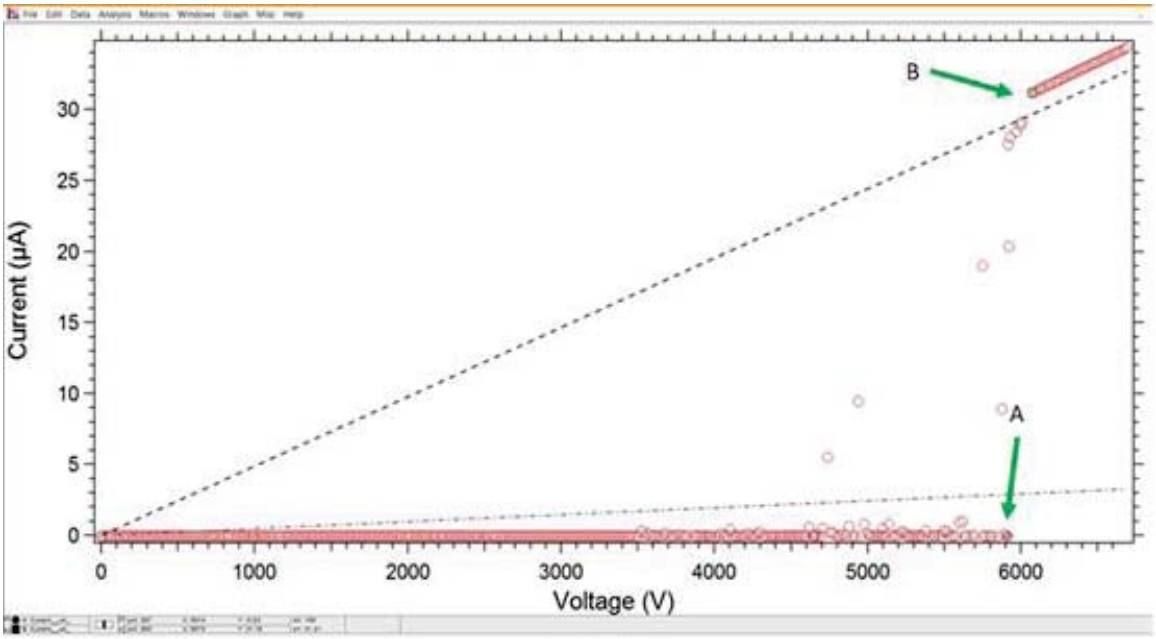

FIG. C.10. A and B markers in place for marking the last datum of pre-breakdown current (A) and the first datum with clear breakdown (B). Note the dashed guidelines marking the expected breakdown current and 10% of the expected breakdown current based on the ESD System circuit.

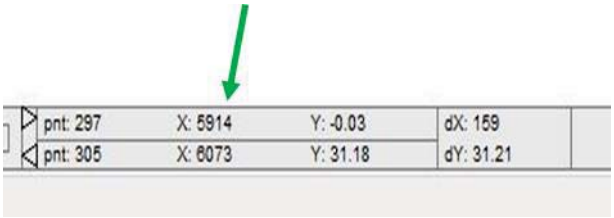

FIG. C.11. The values of markers A and B markers placed in an Igor Pro plot.

C.3.3. ESD Quality Summary Table

In the same directory as the primary instance of the Igor Pro ESD Analysis program is the ESD Quality Summary Table: Z:\Data & Analysis\Data\Electron Transport\ESD\Analysis Programs. This is not moved around to different directories, as it is the final repository of all USU MPG ESD data. It is sortable and selectable columns make it vital for the higher-level analysis described in following sections of this appendix. Any significant updates should be accompanied by an increase in the version number. Starting the entry from a run of tests would warrant this, but not necessarily every time new data from the same

batch is added. Take care not to mess up this matrix! One precaution is the storage of previous versions so that in the event of an error corrections can be made with the least pain possible. The intricacies of the matrix calculations are self-documented in the second tab and outlined in what should be an identical accompanying Word document in the same directory. These should be updated together.

To the right of the last sortable column, the first four rows are suitable for storing values that will be used repeatedly but are not unique to a given experiment and thus do not merit their own sortable column. These include instrument uncertainties and calculations of the average measured thicknesses. There are many cases where current and voltage data exist for a lost and/or unidentifiable sample rendering thickness measurements impossible. In order to estimate the electric field, the average sample thickness and corresponding uncertainty is used.

Each sample has the potential to be used for up to three breakdowns so the number of samples for a given material is calculated by the number of experiments performed on either electrode A2 or B2 (only a very small number of sample—if any—would not include one of these). So the number of samples for a given material (for LDPE, see cell BL3) is calculated using the COUNTIFS function. This function counts the number of times certain criteria are met over a range of cells. In this case the number of samples of a given material, N_{sample}, is given by the number of instances there is sample material with a non-zero thickness entry on electrode A2 added to the number of instances of the same sample material with non-zero thickness entry on electrode B2.

The average thickness for a given material is given using the SUMIFS function, which sums the entries from a range of cells that meet the specified criteria. In our case the average $\bar{d}_{sample}$ is given by the sum of the measured thicknesses of a given sample with non-zero thickness entry on electrode A2 plus the sum of the measured thicknesses of a given sample with non-zero thickness entry on electrode B2 all divided by N_{sample}. The AVERAGEIFS function is not usable in this case because it does not handle OR statements that are needed to include entries on either A2 or B2.

The standard deviation for each measured thickness,

$$\delta_{d_{sample}} = \sqrt{\frac{1}{N_{sample}-1}\sum_{i=1}^{N_{sample}}\left(d_i - \bar{d}_{sample}\right)^2} \qquad \text{C.1}$$

requires a column calculation, column calculation $\left(d_i - \bar{d}_{sample}\right)^2$ (together with a SUMIFS similar to those used before). The column is column G in the matrix. Then the uncertainty as the standard deviation of the mean is

$$\delta_{\bar{d}_{sample}} = \frac{\bar{d}_{sample}}{\sqrt{N_{sample}}}. \quad \text{C.2}$$

We now come to the sortable columns, focusing on those with built-in formulas.

- Column A, "Sample Material."
- Column B, "Sample Thickness for Calculations (mm)." As stated before, there are data that cannot be correlated to a physical sample to measure because many of the earliest samples were not well labeled if they were saved at all. In order to estimate the sample thickness we use $\bar{d}$. So column B contains the statement that IF the measured thickness exists (the cell entry is greater than zero) then use the measured thickness, otherwise, reference the average thickness $\bar{d}_{sample}$.
- Column C, the "Mean Sample Thickness (mm)", refers to the mean of six measurements done on that individual sample, not the mean of all the samples of that material type.
- Column D, "Stdev of Mean Thickness (mm)", is the standard deviation of those six measurements. Each sample measured has its own Excel file containing the individual measurements and standard deviation calculation. These are located in folders in the ESD file structure on Big Blue together with folders containing different data types for test configuration (room temperature step up, SVET, temperature-dependent, etc.).
- Column E, "(delta_d/d)^2". This is symbolically $\left(\frac{\delta_d}{d}\right)^2$ and is used later in the uncertainty calculations. This column is populated using the IF statement, IF the measured thickness exists (>0) then us $\left(\frac{\delta_d}{d}\right)^2$ from the measurements, otherwise use $\left(\frac{\delta_{d_{sample}}}{\bar{d}_{sample}}\right)^2$. Note that the numerator is not $\delta_{\bar{d}_{sample}}$. We are trying to state how well we can guess the thickness based on the average and deviation of the measured thickness, not the uncertainty in the average itself.

- Column F. “(d_i-d_ave)^2” is symbolically $\left(d_i - \bar{d}\right)^2$ and is used in calculating the standard deviation of the measured thicknesses where d_i is the ith entry in column C.
- Column G. “BD temp. (K)” is the temperature at breakdown and should usually be evident from the file name.
- Column H. “Voltage Step (V)” should usually be evident from the file name or, if not, from the data itself.
- Column I. “Sample Plate #” should also be in the file name.
- Column J. “Electrode #” should be in the file name.
- Column K. “Bakeout Date” should also be in the file name. Combinations of plate number and bakeout date, together with the individual electrode numbers, are unique.
- Column L. “Test Date” is retrieved from the data file header and is displayed when data is processed in Igor Pro.
- Column M. “Chamber Pressure (mbar)” is also retrieved from the data file header and is displayed when data is processed in Igor Pro.
- Column N. “Type of Run” is evident from the file name, its location, notes in the data file header, the lab notebook, and often the data itself.
- Column O. “Waiting Voltage (V)” is only applicable to SVET runs and is often in the file name or is evident in the data itself. Note that a mix of these are used (if there is a breakdown before the waiting voltage is reached we have to use the expected value) but the recorded voltage is always preferred.
- Column P. “Waiting E-field (MV/m)” is calculated as (0.001*Waiting Voltage (V))/Sample Thickness for Calculations (mm) to get the units right.
- Column Q. “Time in Nitrogen Storage (days)” estimates the time in the nitrogen storage glove box and is calculated as the test date minus the bakeout date so it does not account for time under vacuum prior to a test (this may be several days if SVET tests are being done) or other discrepancies.

- Column R. “Last Voltage (V) with Base Current” is the voltage at the last recorded data point at base current prior to breakdown or even pre-breakdown current that does not return to the base or zero current. This is obtained during Igor Pro plot analysis.
- Column S. “First Voltage (V) of steady BD current (see 4.6.4).” Also obtained during Igor Pro plot analysis.
- Column T. “delta_V_BD” or ΔV_{BD} is the column entries S – R, the first breakdown current voltage minus the last stead state current voltage. This is the window in which “true” ESD occurs.
- Column U. “Breakdown Voltage (V)” is defined as the average between the first breakdown current voltage minus the last stead state current voltage or (S+R)/2.
- Column V. “Breakdown E-Field (MV/m)” is given by (0.001*Breakdown Voltage (V))/Sample Thickness for Calculations (mm).
- Column W. “BD Field Deff Uncertainty (MV/m)” is the uncertainty in the breakdown field due just to the way it is defined using the average of the first breakdown current voltage minus the last stead state current voltage. It is given by 0.001*(S-R)/2B.
- Column X. “BD Field Uncertainty (MV/m)” is the entire uncertainty in the breakdown field given by the following formula (explained in greater detail in Appendix B)

$$\frac{\delta F_{event}}{F_{event}} = \sqrt{\left(\frac{\delta V_{supply}}{V_{event}}\right)^2 + \left(\frac{\delta V_{step}}{V_{event}}\right)^2 + \left(\frac{\delta V_{circuit}}{V_{event}}\right)^2 + \left(\frac{\delta V_{event}}{V_{event}}\right)^2 + \left(\frac{\delta V_{meter}}{V_{event}}\right)^2 + \left(\frac{\delta d_{measured}}{d}\right)^2 + \left(\frac{\delta d_{compression}}{d}\right)^2} \quad \text{B.1}$$

There are several other columns involving arcing, breakdown image analysis, and other breakdown features. These areas are still under development and are not expounded upon at this time.

When entering new data into the table, do the following:

(a) Check to see if a row exists for your test already. A unique combination of bakeout data, plate number, and electrode number should exist for each test. It is likely that for new data a row may not exist. Simply insert a row among rows of the same materials (this is important for

some of the calculations) or if it is the first of a new material make sure all the entries in the row are devoid of calculations. Refer to the table documentation about how to populate these.

(b) Populate the general information from the naming convention and header information in the row. These are "Sample Material", "Sample Plate #", "Electrode #", "Bakeout Date", "Test Date", "Chamber Pressure (mbar)", and "Type of Run". These are taken directly from the file name for the test and the header information which is printed out in the command line of the ESD Analysis Igor Pro program automatically when it is executed. Simply copy and paste for most of these.

(c) The voltage (x) values from the markers described in C.3.2 should be entered carefully into their corresponding columns "Last Voltage (V) with Base Current" and "First Voltage (V) of steady BD current (defined as the first definable slope about less than or equal to the inverse of about 200 MΩ)". If you did an endurance time test, you will be entering times into the corresponding time columns.

(d) Fill in the other entries as data are available. Especially important is the sample thickness and its uncertainty which will reduce the uncertainty in the breakdown electric field calculations. For some tests, some fields are less important (*e.g.*, breakdown times for standard voltage step-up to breakdown tests or measured ramp rate when the standard ramp rate is used) but it does not hurt to fill them in. Make sure to fill in any fields relevant to the test type (temperature for cryogenic tests or measured ramp rate for ramp rate tests, etc.).

C.3.4. Other Data Analysis

Other ancillary measurements related to ESD tests need to be made, processed, and entered into the ESD Quality Summary Table. These include thickness and imagining or may be secondary results of the ESD data themselves such as voltage ramp rate. Post-breakdown sample imaging has its own procedures which can be found in Z:\Instruction & Procedures\Procedures\Electron Transport\ESD.

- Sample Thickness: Sample thickness is important in that it is key to reducing the uncertainty in breakdown field. Recall that $F_{ESD} = V_{ESD}/d$ so reducing the uncertainty in sample thickness d is key to reducing breakdown field uncertainty. Copy the newest

version of the Thickness Template Excel worksheet to the raw thickness folder for the material in question. For each measurement use the ratcheting micrometer in SER 217 and follow the directions in the worksheet. “Save As” the sample name then repeat for each measurement, entering the results into the corresponding cells in the ESD matrix.

- Voltage Ramp Rate: If any ramp rate other than the standard 20V/4s is used or if the ramp rate is otherwise called into question the Igor Pro Procedure “RampRate v#” (newest version) can be found in Z:\Data & Analysis\Data\Electron Transport\ESD\Analysis Programs. Open it with the Igor Pro Experiment in question (processed data file) already open and it will load into that experiment. Execute in the command line “RampRate(Voltage__V_, Time__ms_)” (or the correctly named voltage and time waves in the function) and the program will calculate the ramp rate, average voltage and time steps, and uncertainties. Beware that if there have been voltmeter errors causing the voltage data to drop unrealistically (often to zero) this can adversely affect the results. This will be obvious the in plots. You may have to manually adjust these points in the waves (usually the average of the points around it is sufficient) to get a reasonable answer for the ramp rate.

C.4. Macro Data Analysis

This section discusses how to go about getting the science out of all these data that has been processed and archived in a big sortable matrix. Before doing this, it is strongly recommended that you make a copy of the ESD Quality Summary Table on your local machine and re-name it relevant to whatever project you are working one. Do not disturb the main instance of the matrix on Big Blue for this level of data analysis!

You may be interested to know if breakdown field—or some other test parameter—changes with temperature, ramp rate, chamber pressure, or phase of the moon. The sortable, selectable columns of the matrix let you do this. See Fig. C.12. By clicking on the sorting arrows, you can see you can sort in ascending or descending alphabetical order, that certain entries can be selected or deselected, and other advanced options. This enables you to sort as desired. You most likely will want to unselect any materials

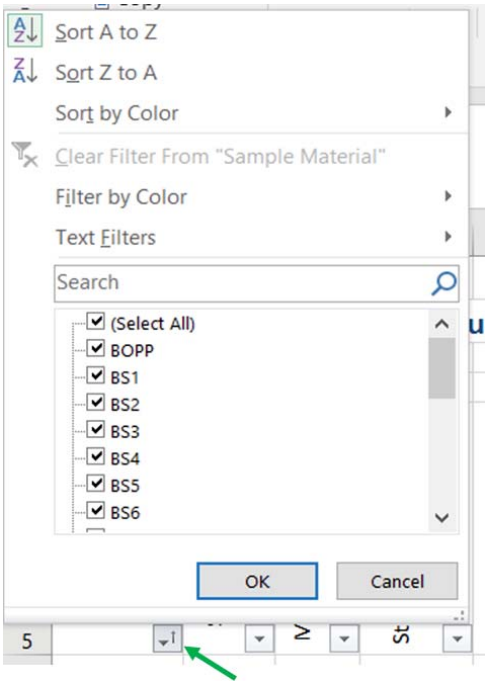

FIG. C.12. Sorting options for columns in the ESD Quality Summary Table.

or test type you are not interested in. Note that, once the file is saved, unselected material may be effectively erased from the spreadsheet. Examples of two typical meta-analysis techniques follow below.

C.4.1. Weibull Analysis and Fitting

(a) First, the breakdown data must be in the ESD Quality Summary table. The column in question is the column of breakdown electric field values. Only runs with the same test configuration including temperature and ramp rate should typically be considered together. Any questionable runs (*e.g.*, setup error, sample not baked, ramp up errors) or runs containing errors should be discarded. This column of breakdown fields should be sorted from smallest to largest.

(b) Open an instance of the Igor Pro routine "EmpiricalCumulativeDist v1-1" or current version in Z:\Data & Analysis\Data\Electron Transport\ESD\Analysis Programs (This code is also included in current version of "QQcode." I recommend loading the QQcode macro because if

you need it later, Igor Pro will not let you compile two instances of the same function in a macro). Before proceeding, save the experiment as a new file name in the desired location.

(c) Create a new table (Windows>New Table, click 'Do It' in pop-up window). Paste the sorted breakdown field values into this table. Rename the wave of breakdowns fields something short but relevant such as "BDF." This can be done by pasting "Rename wave0,BDF;" into the command line. These instructions will assume this wave name from now on.

(d) In the command line, execute the function "ECDF(BDF)" which will give the corresponding quantile (or for large sample size probability) associated with the sorted ascending field values. From here you may create a plot of the Empirical Cumulative Distribution Function (ECD) of the breakdowns for the material in question (Windows>New Graph, under Y Wave(s) select BDF_ECD and under X Wave select BDF, click 'Do It'). In Igor Pro, a "cityscape" mode is a good way to represent the stepwise ECD function. Double click the red plot to change the trace appearance.

(e) ECD plots are not conducive to standard error bars; however, we can give some idea of the uncertainty by bounding the ECD with two copies of the original ECD by shifting it by ± the average of the standard deviations of the breakdown fields. This likely overestimates the variation of the ECD, but gives some idea of error bounds. Other methods exist (see Appendix B for more detail.)

(f) We can now proceed with Weibull analysis. Save a new instance of the experiment for each Weibull fit (2, 3, and 5 parameters) to ensure that each individual fit is preserved. For Weibull analysis we transform the ECD in a way corresponding to the linearization of a 2-parameter Weibull cumulative distribution (Weibull, 1951; Chauvet and Laurent, 1993),

$$P(F) = 1 - \exp\left(-\left[\frac{F}{F_0}\right]^{\beta}\right), \tag{5.2}$$

namely,

$$x = \log(F) \text{ and } y = \log\left[\ln\left(\frac{1}{1-P}\right)\right] \tag{5.3}$$

(g) Make copies of the BDF and BDF_ECD waves and rename them if desired. To make copies you can add the BDF_ECD wave to the table by clicking Table>Append Columns to Table and selecting it. Highlight both columns and use ctrl+c to copy and ctrl+v to paste copies of these waves into the same table. They can be renamed if you highlight them, and while highlighted right click and 'rename waves' will appear as an option.

(h) Transform the new waves. Using the default names of copied waves, executing the following in the command line will perform the transformation.

•'BDF1'=log('BDF1')

•'BDF_ECD1'=log(ln(1/(1-'BDF_ECD1')))

Note that the last entry in the transformed ECD wave will read inf by definition. Error bar waves can be transformed in the same way.

(i) Plot these new waves. The data in these coordinates are traditionally represented by markers.

(j) To fit data to a line select Analysis>Curve fitting. Select "From Target" and under Y Data "BDF_ECD1" or whatever you have named the transformed data and under X Data select "BDF1". The default fit function is the line $y = a + bx$. Under output option you can select "X Range Full Width of Graph" if desired. If you only want to fit to some of the data, before opening the curve fitting window, select the plot and press ctrl+i which toggles the cursor menu. Drag and drop A and B cursors where desired then in the curve fitting menu under "Data Options" select the "Cursors" button. When you are ready to fit click "Do It." Fitting parameter information is printed at the command line and a fit should appear on the plot.

(k) To plot untransformed data—which may be desirable for small data sets—requires the use of a custom fit function. In the curve fitting menu window, click "New Fit Function." You are required to name your function and provide fitting coefficients and variables. For a 2-parameter Weibull fit coefficients could be F0 and B (instead of beta). The independent variable could be x (this would be F above). In the fit expression type after "f(x)=" "1-exp(-(x/F0)^B)" then click "Save Fit Function Now." You will notice in the Curve Fitting Window that the "Do It" box cannot yet be selected. For custom fit functions, Igor Pro needs

reasonable guesses for the fitting coefficients. Under the "Coefficients" tab you can give initial guesses for F0 and B and constrain them to a certain range. F0 must be greater than zero and less than the maximum field value in the data. Beta is typically close to ten but must be positive, confining it from 0 to 50 or 0 to 100 usually works. With initial guesses in place you can now click "Do It" and perform the fit.

(l) Fitting to all points does may not result in a great fit. Record the parameters from the first fits over the full range anyway, then do another fit to the main cluster of points.

(m) Additionally, you can consider a 3-parameter fit by creating a new fitting function for

$$P(F) = 1 - \exp\left(-\left[\frac{F-F_s}{F_{0-F_s}}\right]^{\beta}\right), \tag{5.4}$$

there is not a unique linearization and there is not a linearization for the mixed Weibull fit. In general, we can mix any number S of total subdistributions.

$$P_{mix}(F) = \sum_{i=1}^{S} \frac{n_i}{n} P_i(F) \tag{5.6}$$

where we demand

$$\sum_{i=1}^{S} \frac{n_i}{n} \overset{!}{=} 1 \tag{5.7}$$

in case of S=2, we can say

$$P_{mix}(F) = pP_1(F) + (1-p)P_2(F), \tag{5.8}$$

We see automatically that so long as $1 > \pi > 0$ total probability is conserved. Note that both n_i and p are assumed to be constants but that is not a requirement; they could each be a function of F. Also note that each $P_i(F)$ could be of a different form.

A mix of two two-parameter Weibull distributions is

$$P_{mix}(F) = p\left(1 - \exp\left(-\left[\frac{F}{F_{01}}\right]^{\beta_1}\right)\right) + (1-p)\left(1 - \exp\left(-\left[\frac{F}{F_{02}}\right]^{\beta_2}\right)\right). \tag{5.9}$$

(n) For each of these, Igor Pro can fit the untransformed data then export the fit to a wave. Transforming the exported wave lets us plot it against the "linearized" or rather transformed data where it is visually easier (and traditional) to compare candidate fits. Fitting function can be copied from previous instances of these fits for data in other materials.

C.4.2. Fitting with Physics Models

This section outlines how to fit data using the Crine and dual-defect physics-based models. This is somewhat more difficult than using the Weibull fits.

These models can be related to the ECD of data using

$$P_{step}^{Tot}\left(\Delta t_{step}, N_{step}, \Delta V_{step}, T\right) = 1 - \prod_{j=1}^{N_{step}}\left[1 - P_{def}^{Tot}\left(\Delta t_{step}, \frac{j\Delta V_{step}}{d}, T\right)\right] \quad 3.7$$

where

$$P_{def}^{Tot}(\Delta t, F, T) = \sum_{i=HI,LO} P_{def}^{i} = \left(\frac{2k_bT}{h/\Delta t}\right)\sum_{i=HI,LO} \exp\left[\frac{-\Delta G_{def}^{i}}{k_bT}\right] \sinh\left[\frac{\epsilon_0\epsilon_r F^2}{2N_{def}^{i}k_bT}\right]. \quad 3.1$$

This this is the dual-defect model. However, using only one term in the sum reduces to the Crine mean field theory. Due to issues with representation of numbers in Igor Pro, we have to combine everything we can when fitting, then extract the variables of interest later, ΔG_{def}^{i} and N_{def}^{i}. We can use the following simplification.

$$P_{def}^{Tot}\left(\Delta t_{step}, \frac{j\Delta V_{step}}{d}, T\right) = \sum_{i=HI,LO} \lambda^i \sinh[\xi^i j^2] \quad 5.12$$

Here

$$\lambda^i = \left(\frac{2k_bT}{h/\Delta t_{step}}\right) \exp\left[\frac{-\Delta G_{def}^{i}}{k_bT}\right] \text{ and } \xi^i = \frac{\epsilon_0\epsilon_r\left\{\frac{\Delta V_{step}}{d}\right\}^2}{2N_{def}^{i}k_bT}. \quad 5.13$$

Of course, for the Crine model assumptions, there would only be one of each combined variable λ and ξ.

(a) In Igor, make a copy of the experiment having already done the Weibull analysis described above.

(b) We are not able to enter the Crine or Dual-defect models into due to the product series required to consider the ramp-up process. For each model, we must create a dummy fitting function, and then modify it. To do this, go to Analysis>Curve Fitting then in the new box select “New Fit Function”. Name it Ptot (for the dual defect model) or Crine accordingly. Enter ‘F’ as the independent variable and Ga, Na, Gb, and Nb for the dual defect or for Crine ‘G’ and ‘N’. In the ‘Fit Expression’ window, enter in a dummy function using all the coefficients and the variable just entered. For example “N*F+G” or “F+Ga+Gb+Na*Nb”.

Click “Save Fit Function” then click “Cancel” to exit the fitting routine. We now need to edit the dummy fitting routine in order to have it calculate either of the physics models. To open up the programing dialog enter “ctrl+m”. You will see something like the following in the procedure window:

```
Function Crine(w,F) : FitFunc
	Wave w
	Variable F

	//CurveFitDialog/ These comments were created by the Curve Fitting dialog. Altering them will
	//CurveFitDialog/ make the function less convenient to work with in the Curve Fitting dialog.
	//CurveFitDialog/ Equation:
	//CurveFitDialog/ f(F) = N*F+G
	//CurveFitDialog/ End of Equation
	//CurveFitDialog/ Independent Variables 1
	//CurveFitDialog/ F
	//CurveFitDialog/ Coefficients 2
	//CurveFitDialog/ w[0] = G
	//CurveFitDialog/ w[1] = N

	return w[1]*F+w[0]
End
```

(c) Comment out the return line (see red) and paste the green highlighted text. The Igor Pro procedure window will look like:

```
Function Crine(w,F) : FitFunc
	Wave w
	Variable F

	//CurveFitDialog/ These comments were created by the Curve Fitting dialog. Altering them will
	//CurveFitDialog/ make the function less convenient to work with in the Curve Fitting dialog.
	//CurveFitDialog/ Equation:
	//CurveFitDialog/ f(F) =N*F+G
	//CurveFitDialog/ End of Equation
	//CurveFitDialog/ Independent Variables 1
	//CurveFitDialog/ F
	//CurveFitDialog/ Coefficients 2
	//CurveFitDialog/ w[0] = G
```

```
	//CurveFitDialog/ w[1] = N

	//return w[1]*F+w[0]
	Variable j //counter
	Variable p=1 //This will be the probability of breakdown. It needs to be initialized to one each time this runs
	Variable y=1.2 //This factor is d/V_step, it is unique to each material thickness and is used to determine the number of field step increments

	if ((F*y)<1) //We need to have at least 1. The value 1.2 is unique to Kapton, see Weibull Kapton Ptot v1-1.mw in same directory

		p = 0 //We don't want garbage; this is a bit artificial but it should help later

		else

			for(j=1; j<=(F*y); j+=1) //do this until j reaches F*y

				p=p*(1-w[0]*sinh(w[1]*(j^2))) //see Andersen 2015 IEEE TPS ESD paper
				//all physical constants are absorbed into the fitting parameters to reduce numerical errors

			endfor

			p=1-p // finish the formula as given in Andersen 2015 IEEE TPS ESD paper

			if   (!(p > 0 && p < 1)) //if p is not between zero and one

				p = 1 //if things go outside of reason return 1

			endif

	endif

	return p //return final value of p


End


Function Ptot(w,F) : FitFunc
	Wave w
	Variable F
```

```
	//CurveFitDialog/ These comments were created by the Curve Fitting dialog. Altering them will
	//CurveFitDialog/ make the function less convenient to work with in the Curve Fitting dialog.
	//CurveFitDialog/ Equation:
	//CurveFitDialog/ f(F) = F+Ga+Gb+Na*Nb
	//CurveFitDialog/ End of Equation
	//CurveFitDialog/ Independent Variables 1
	//CurveFitDialog/ F
	//CurveFitDialog/ Coefficients 4
	//CurveFitDialog/ w[0] = Ga
	//CurveFitDialog/ w[1] = Na
	//CurveFitDialog/ w[2] = Gb
	//CurveFitDialog/ w[3] = Nb

	//return F+w[0]+w[2]+w[1]*w[3]
	//This function is built around the simplest form of Ptot from the Andersen 2015 IEEE TPS ESD paper
	// All fitting parameters will need to be deconvoluted to extract physical values.

	Variable j //counter
	Variable p=1 //This will be the probability of breakdown. It needs to be initialized to one each time this runs
	Variable y=1.2 //This factor is d/V_step, it is unique to each material thickness and is used to determine the number of field step increments

	if ((F*y)<1) //we need to have at least 1. The value 1.2 is unique to Kapton, see Weibull Kapton Ptot v1-1.mw in same directory

		p = 0 //We do not want garbage; this is a bit artificial but it should help later

		else

			for(j=1; j<=(F*y); j+=1) //do this until j reaches F*y

				p=p*(1-w[0]*sinh(w[1]*(j^2))-w[2]*sinh(w[3]*(j^2))) //see Andersen 2015 IEEE TPS ESD paper
				//all physical constants are absorbed into the fitting parameters to reduce numerical errors

			endfor

			p=1-p // finish the formula as given in Andersen 2015 IEEE TPS ESD paper

			if   (!(p > 0 && p < 1)) //if p is not between zero and one
```

```
                p = 1 //if things go outside of reason return 1
            endif
        endif
        return p //return final value of p
    End
```

(d) Note that for each fitting routine we need to define the variable y, as it may vary from material to material based on the average sample thickness. This is the electric field step in units of MV/m. This is the voltage step divided by the average thickness for the samples used.
(e) Compile the edited fitting funtions and now these can be used as regular fitting functions in Igor Pro. Note that you will have to provide guesses for the fitting parameters (see 5.4.1). Although these fitting parameters are labeled as Gs and Ns, they correspond to above λ and ξ defined in Eq. 5.13. The results can be sensitive to poor choices in the initial guesses.
(f) After a good fit is found, it can be useful to redo the fit and output the result to a new wave. In the Curve Fitting dialog box, click the 'Output Options' tab and change the Destination from "_auto_" to "_New Wave_". This new wave can be transformed in the same way Weibull fits are transformed so they can be compared to other fits in the Weibull-linear coordinates.

C.4.3. DCPDs and Q-Q plots

This section outlines the process of performing a quantile-quantile q-q analysis, specifically to compare set of breakdowns to a set of DCPD (with same material/test conditions). Igor Pro procedure files can be found in Z:\Data & Analysis\Data\Electron Transport\ESD\Analysis Programs.

Typically, each breakdown test results in many DCPD, so there will be many more DCPD data than breakdown data. If the two distributions are related, the resulting q-q plot will be linear and if the distributions are the same, the plot will show unity slope and zero intercept.

(a) Before we can make a q-q plot we need the empirical cumulative distribution function (ECD) of each data set. If you have already done Weibull analysis creating the ECD of the breakdowns (C.4.1) was an important step and will already exist. Copy the ECD Igor Pro experiment for this data set and save it as something new.
(b) In order to create an ECD of DCPD data must be entered into an Excel worksheet used to combine DCPD data from many runs. Several exist already, generally with the name '"material"Arcs v#' and previous versions can be cleared and populated with relevant data.

(c) These Excel worksheets need the current traces from all the experiments in question (columns may need to be added) only up to the breakdown. Post-breakdown data will contaminate the results. In ESD Analysis v3-3 or later there is a “Get PDs” macro. With the markers set on the I-V curve as outlined in C.4.1, executing this macro will bring a prompt to save a .txt file. This file contains all the current measurements up to the A marker and can be copied into the Excel DCPD sheet. The A marker may need to be adjusted in the case of field-enhanced conductivity.

(d) To perform q-q analysis open the newest version of the “QQcode” Igor Pro macro. Before running the macro, copy from the Excel matrix the breakdown fields of interest in ascending order into a table. Rename that wave “BDF” for breakdown fields. The names here are arbitrary but they are what the macro will be looking for. Now in the Excel sheet for counting DCPD, columns B (electric field) and C (how many small arcs rounded to the nearest integer at this field) need to be copied into a new table in the Igor Pro program. Name “ArcF” and “Arcs” for the field that the DCPD are measured at, and the count of DCPD themselves.

(e) Now under Macros, execute “QQ plots.” This macro results in QQ plots for the DCPD (y) and breakdowns (x). There is a point on the graph for each breakdown. Generally, there are many more DCPD than breakdowns and their ECD is likely to be much denser than the ECD of the breakdowns. In order to construct a QQ plot we need to match the quantiles of each distribution. Since there are many more DCPD data, we will interpolate these to get a reduced ECD of the DCPD that has quantiles that match the quantiles in the ECD of the breakdowns. We propose that a linear interpolation is sufficient since the DCPD data are so dense. The ECD of the DCPD with field plot also appears.

(f) At this point the plots can be re-styled or analyzed further if desired, then exported.

(g) For complicated reasons, you cannot do a simple linear correlation to get the statistical significance of the fit in the usual way (see Appendix B).

APPENDIX D

MATERIALS DATA

This document contains relevant material data for polymeric test materials used by the Materials Physics Group (MPG) for electrostatic discharge (ESD) tests. Data are provided from the manufacturers except for thicknesses and resistivity, which were measured. These materials are low density polyethylene (LDPE) (Goodfellow Cambridge Ltd., 2006; Goodfellow, 2016a), polyimide (PI or Kapton HN) (DuPont Document K-15345-1, 2011; Goodfellow, 2016b), biaxially-oriented polypropylene (BOPP) (Goodfellow, 2016c; Goodfellow Corp., 2017), and polyether ether ketone (PEEK) (Goodfellow, 2016b).

Table D.1. LDPE properties.

Monomer Composition	C_2H_4
Measured Thickness (µm)	29.5±0.2
Density (g/cm^3)	0.92±0.01
Relative Dielectric Constant	2.26±0.05
Nominal Dielectric Strength (MV/m)	200
Volume Resistivity (Ω·cm)	10^{15}-10^{18} from manufacturer 10^{18}-10^{19} MPG equilibrium measurements
Other	Estimated crystallinity of 50% (Wintle, 1983), estimated peak fractional mass distribution of ~$6\cdot10^3$ amu or ~2 10^3 C_2H_4 mers per chain (Peacock, 2000; Brunson, 2010).

Table D.2. PI (Kapton HN) properties.

Monomer Composition	$C_{22}O_5N_2H_{10}$	$C_{22}O_5N_2H_{10}$
Measured Thickness (µm)	24.8±0.8	26.4±0.5
Density (g/cm^3)	1.42±0.01	1.42±0.01
Relative Dielectric Constant	3.4	3.4
Nominal Dielectric Strength (MV/m)	303	300
Volume Resistivity (Ω·cm)	$1.5\cdot10^{17}$ from manufacturer	10^{18} from manufacturer $(5\pm1)\cdot10^{19}$ MPG measurements
Other	DuPont Kapton (2012-2013)	Goodfellow Kapton (2017)

Note: A third batch of Kapton was tested. This batch was received from a contractor in 2008 without manufacturer's data.

Table D.3. BOPP properties.

Monomer Composition	CH_3
Measured Thickness (µm)	27.6±0.4
Density (g/cm^3)	0.90±0.05
Relative Dielectric Constant	2.4±0.2
Nominal Dielectric Strength (MV/m)	200
Volume Resistivity (Ω·cm)	10^{16}-10^{18} from manufacturer
Other	N/A

Table D.4. PEEK properties.

Monomer Composition	$C_{19}H_{12}O_3$
Measured Thickness (µm)	29.6±0.3
Density (g/cm^3)	1.26±0.05
Relative Dielectric Constant	3.25±0.05
Nominal Dielectric Strength (MV/m)	110-150
Volume Resistivity (Ω·cm)	10^{15}-10^{16} from manufacturer ~$2 \cdot 10^{19}$ MPG measurements
Other	N/A

CURRICULIM VITAE

Allen Andersen
(January 2018)

EDUCATION:

PhD in Physics, Utah State University, Logan, Utah. (5/2018). GPA: 3.77. Dissertation: *The Role of Recoverable and Non-Recoverable Defects in DC Electrical Aging of Highly Disordered Insulating Materials*.

BS in Physics, Utah State University, Logan, Utah. (4/2013) GPA: 3.93 (4.0=A), Minor in Spanish, Graduate Magna Cum Laude.

PROFESSIONAL EXPERIENCE:

Solid State Physics Research: Graduate research focused on dielectric breakdown, partial discharge, and dc conductivity phenomena for polymeric, ceramic, glassy, composite, and carbon highly disordered materials with an emphasis on spacecraft charging effects. Familiar with high voltage DC, electron beam, plasma, high vacuum, low current, and cryogenic techniques together with computational data processing, error analysis, and theoretical modeling.

Teaching: Utah State University: Mentor for three undergraduate PHYS 4900 senior research projects (Fall 2013-present); Instructor for Physics for Scientists and Engineers Lab PHYS 2215 (2012-2013). Physics tutor (2012-2013). Brigham Young University-Idaho: Physics and Spanish tutor at all undergraduate levels.

EMPLOYMENT EXPERIENCE:

Graduate Research Fellow: 7/1/2014 to present. NASA Space Technology Research Fellowship (NSTRF). Research in experimental and theoretical solid-state physics. Supervision of undergraduate student senior projects. Utah State University Materials Physics Group, Physics Department, Utah State University; Logan, UT.

Visiting Technologist: Summer 2015 and Summer 2017. Summer internships as part of my NASA Space Technology Research Fellowship. Electron beam induced electrostatic discharge in spacecraft materials. Low-energy electron exposure of spacecraft electronics. Vacuum and electron

beam system upgrades and troubleshooting. Electromagnetic Compatibility Group, Jet Propulsion Laboratory; Pasadena, CA.

Visiting Technologist: Summer 2016. Summer internship as part of my NASA Space Technology Research Fellowship. Differential Ion Flux Probe and other plasma probe measurements for electronic sail (E-Sail) test articles for the Heliopause Electrostatic Rapid Transit System (HERTS). Vacuum and plasma probe system upgrades and troubleshooting. LabVIEW programming. Space Environments Effects Group, Marshall Space Flight Center; Huntsville, AL.

Graduate Research Assistant: Summer 2012 and 5/13/2012 to 7/1/2014. Research in experimental and theoretical solid-state physics. Supervision of undergraduate student senior projects. Utah State University Materials Physics Group, Physics Department, Utah State University; Logan, UT.

Graduate Teaching Assistant: 8/2012 to 5/2013. Physics for Scientists and Engineers Instructor. Tutor for the Physics Learning Center, Physics Department, Utah State University; Logan, UT, Brigham City, UT.

Research Assistant: Summer 2011.Microwave Optics Research. Development and calibration of research equipment. Microwave transmission property studies in wood fiber based materials. Physics Department, Brigham Young University-Idaho; Rexburg, ID.

Physics Tutor Lab Manager: 1/2012 to 4/2012. Supervised the drop-in physics tutoring lab. Tutoring Center, Brigham Young University-Idaho; Rexburg, ID.

Physics and Spanish Tutor: 5/2010 to 4/2012. Held group and individual physics and Spanish tutoring sessions and tutored in the drop-in physics tutoring lab. Tutoring Center, Brigham Young University-Idaho; Rexburg, ID.

HONORS AND AWARDS:

Bill E. Robins Doctoral Student Researcher of the Year Finalist, April 15, 2017

USU College of Science PhD Graduate Researcher of the Year, 2017

David and Terry Peak Outstanding Achievement Award in Physics, April 22, 2015

NASA Space Technology Research Fellowship (NSTRF) Class of 2014.

Gene Adams Endowed Scholarship, April 2014

Howard L. Blood Scholar 2013 and 2014.

Sigma Pi Sigma Member, April 2013

Magna Cum Laude, BYU-Idaho, 2012

SMART Grant, BYU-Idaho, 2010 and 2011

Academic Scholarships, BYU-Idaho, 2010-2012

BYU-Idaho Scholarships, BYU-Idaho, 2010- 2012

Thomas E. Ricks Presidential Scholarship, BYU-Idaho, 2006

Eagle Scout, Sept. 2005

ORGANIZATIONS:

Memberships: American Physical Society, Institute for Electrical and Electronics Engineers, and Sigma Pi Sigma.

Peer Review Activities: IEEE Transactions on Plasma Science (2014-present).

REFEREED PUBLICATIONS:

Allen Andersen and JR Dennison, "An Enhanced Operational Definition of Dielectric Breakdown for DC Voltage Step-up Tests," *Proceedings of the 2017 IEEE Conference on Electrical Insulation and Dielectric Phenomena—(CEIDP 2017)*, 433-436, 2017. DOI: 978-1-5386-1194-4/17

Krysta Moser, Allen Andersen and JR Dennison, "Dependence of Electrostatic Field Strength on Voltage Ramp Rate for Spacecraft Materials," *IEEE Tran. Plasma Science*, 45(8), 2017, 2036-2039. DOI: 10.1109/TPS.2017.2717873

Allen Andersen, Krysta Moser and JR Dennison, "Perspectives on the Distributions of ESD Breakdowns for Spacecraft Charging Applications," *IEEE Tran. Plasma Science*, 45(8), 2017, 2031-2035. DOI: 10.1109/TPS.2017.2655885

Allen Andersen, JR Dennison, Alec M. Sim and Charles Sim, "Electrostatic Discharge and Endurance Time Measurements of Spacecraft Materials: A Defect-Driven Dynamic Model," *IEEE Tran. Plasma Science*, 43(9), 2015, 2941-2953. DOI: 10.1109/TPS.2015.2428258.

Allen Andersen and JR Dennison, "Pre-breakdown Arcing as a Proxy for DC Dielectric Breakdown Testing of Polymeric Insulators," *Proceedings of the 2015 IEEE Conference on Electrical Insulation and Dielectric Phenomena—(CEIDP 2015)*, 574-577, 2015. DOI: 10.1109/CEIDP.2015.7352084

Allen Andersen and JR Dennison, "Mixed Weibull Distribution Model of DC Dielectric Breakdowns with Dual Defect Modes," *Proceedings of the 2015 IEEE Conference on Electrical Insulation and Dielectric Phenomena—(CEIDP 2015)*,570-573, 2015. DOI: 10.1109/CEIDP.2015.7352017

Allen Andersen and JR Dennison, "Pre-breakdown Arcing and Electrostatic Discharge in Dielectrics under High DC Electric Field Stress," *Proceedings of the 2014 IEEE Conference on Electrical Insulation and Dielectric Phenomena—(CEIDP 2014)*, 63-66, 2014. DOI: 10.1109/CEIDP.2014.6995739

CONFERENCE PROCEEDINGS AND OTHER PUBLICATIONS:

Todd Schneider, Jason Vaughn, Kenneth Wright, Allen Andersen, and Nobie Stone, "Flowing Plasma Interaction with an Electric Sail Tether Element," *The Applied Space Environments Conference (ASEC)*, Huntsville, AL, May 15-19, 2017, 5pp.

Allen Andersen, Krysta Moser, and JR Dennison, "Voltage Ramp-rate Dependence of DC Breakdown in Polymeric Insulators: Physical Models versus Data," *Proceedings of the 2016 IEEE Conference on Electrical Insulation and Dielectric Phenomena—(CEIDP 2016)*, 494-496, 2016, DOI: 10.1109/CEIDP.2016.7785465

Allen Andersen, Krysta Moser and JR Dennison, "Perspectives on the Distributions of ESD Breakdowns for Spacecraft Charging Applications," *Proceedings of the 14th Spacecraft Charging Technology Conference*, Space Research and Technology Centre of the European Space Agency (ESA/ESTEC), (Noordwijk, Netherlands, April 4-8, 2016), 2pp.

Krysta Moser, Allen Andersen and JR Dennison, "Dependence of Electrostatic Field Strength on Voltage Ramp Rate for Spacecraft Materials," *Proceedings of the 14th Spacecraft Charging Technology Conference*, Space Research and Technology Centre of the European Space Agency (ESA/ESTEC), (Noordwijk, Netherlands, April 4-8, 2016), 2pp.

JR Dennison, Jodie Corbridge Gillespie, Allen Andersen, Amberly Evans Jensen, Justin Dekany, Gregory Wilson, Alec M. Sim, and Ryan Hoffmann, "Synergistic Models of Electron Emission and Transport Measurements of Disordered SiO2," *Proceedings of the 14th Spacecraft Charging Technology Conference*, Space Research and Technology Centre of the European Space Agency (ESA/ESTEC), (Noordwijk, Netherlands, April 4-8, 2016).

Allen Andersen, JR Dennison, Alec M. Sim and Charles Sim, "Electrostatic Discharge and Endurance Time Measurements of Spacecraft Materials: A Defect-Driven Dynamic Model," Abstract 127, *Proceedings of the 13th Spacecraft Charging Technology Conference*, (Pasadena, CA, June 25-29, 2014), 11 pp.

Allen Andersen (with Todd Lines), "Microwave Optics Research," Senior Thesis, Brigham Young University-Idaho, Rexburg, ID, April 2012.

PRESENTATIONS:

Allen Andersen and JR Dennison, "Using Quantile-Quantile Plots to Compare Experimental Apples and Oranges in Physics Labs," *37th Annual Meeting of the Idaho-Utah Section of the American Association of Physics Teachers*, February 23-24, 2018, Rexburg, ID.

Allen Andersen and JR Dennison, "An Enhanced Operational Definition of Dielectric Breakdown for DC Voltage Step-up Tests," Invited talk, *2017 IEEE Conference on Electrical Insulation and Dielectric Phenomena—(CEIDP 2017)*, October 22-25, 2017, Fort Worth, TX.

Tyler Kippen, Allen Andersen, and JR Dennison, "Temperature Dependence of Electrostatic Discharge in Highly Disordered Insulating Polymers," *American Physical Society Four Corner Section Meeting*, Colorado State University, Fort Collins, CO, October 20-21, 2017.

Tanner Linton, Nelson Green, and Allen Andersen, "ESD Spacecraft Charging Tests of Europa Mission Coatings," *Summer Students' Presentations*, Jet Propulsion Laboratory, Pasadena, CA, August 15, 2017.

Allen Andersen, "Breaking Down Dielectric Breakdown: Improving Methods and Models," *JPL Mission Assurance Division (5100) Invited Talk*, Jet Propulsion Laboratory, Pasadena, CA, August, 9, 2017.

Allen Andersen, Tanner Linton, and Nelson Green, "Electron-Beam Induced ESD in Europa Mission Thermal Control Paints," *Summer Students' Presentations Group 2*, Jet Propulsion Laboratory, Pasadena, CA, August 1, 2017.

Todd Schneider, Jason Vaughn, Kenneth Wright, Allen Andersen, and Nobie Stone, "Flowing Plasma Interaction with an Electric Sail Tether Element," *The Applied Space Environments Conference (ASEC)*, Huntsville, AL, May 15-19, 2017.

Tyler Kippen, Allen Andersen, and JR Dennison, "Temperature Dependence of Electrostatic Discharge in Highly Disordered Insulating Polymers," *National Council on Undergraduate Research*, Memphis, TN, April 6-8, 2017.

Allen Andersen and JR Dennison, "Novel Physical Model for DC Partial Discharge in Polymeric Insulators," *2017 March Meeting of the American Physical Society*, (New Orleans, LA, March 13-17, 2017).

Tyler Kippen, Allen Andersen, and JR Dennison, "Temperature Dependency of Electrostatic Breakdown in LDPE and PEEK," *Utah Conference on Undergraduate Research (UCUR) Meeting*, Brigham Young University, Provo, UT, February 28, 2017.

Tyler Kippen, Allen Andersen, and JR Dennison, "Temperature Dependency of Electrostatic Breakdown in LDPE and PEEK," *American Physical Society Four Corner and Texas Sections*

Meeting, New Mexico State University and University of Texas, El Paso, October 21-22, 2016, Las Cruces, NM.

Allen Andersen, Jason Vaughn, Todd Schneider, and Ken Wright, "Plasma Deflection Test Setup for E-Sail Propulsion Concept," *American Physical Society Four Corner and Texas Sections Meeting*, New Mexico State University and University of Texas, El Paso, October 21-22, 2016, Las Cruces, NM.

Allen Andersen, Krysta Moser, and JR Dennison, "Voltage Ramp-rate Dependence of DC Breakdown in Polymeric Insulators: Physical Models versus Data," *2016 IEEE Conference on Electrical Insulation and Dielectric Phenomena—(CEIDP 2016)*, October 16-19, 2016, Toronto, Canada.

Krysta Moser, Allen Andersen and JR Dennison, "Dependence of Electrostatic Field Strength on Voltage Ramp Rate for Spacecraft Materials," *USU Fall Undergraduate Research Orientation*, Logan, UT, September 9, 2016.

Allen Andersen, Jason Vaughn, Todd Schneider, and Ken Wright, "Test Setup for Measuring Plasma Deflection," *Summer Report to Marshall Space Flight Center EM 50 Group*, August 9, 2016. Marshall Space Flight Center, Huntsville, AL.

Allen Andersen, "Enhanced Predictions of time to Critical Dielectric Breakdown of Materials under Prolonged Exposure to Space Plasma Environments,' *NASA Space Technology Research Fellows Meet and Greet*, July 12, 2016, Marshall Space Flight Center, Huntsville, AL.

Krysta Moser, Allen Andersen and JR Dennison, "Dependence of Electrostatic Field Strength on Voltage Ramp Rate for Spacecraft Materials," *USU Student Research Symposium*, April 12, 2016, Logan, UT.

Allen Andersen, Krysta Moser and JR Dennison, "Perspectives on the Distributions of ESD Breakdowns for Spacecraft Charging Applications," *14th Spacecraft Charging Technology Conference*, Space Research and Technology Centre of the European Space Agency (ESA/ESTEC), (Noordwijk, Netherlands, April 4-8, 2016).

Krysta Moser, Allen Andersen and JR Dennison, "Dependence of Electrostatic Field Strength on Voltage Ramp Rate for Spacecraft Materials," *14th Spacecraft Charging Technology Conference*, Space Research and Technology Centre of the European Space Agency (ESA/ESTEC), (Noordwijk, Netherlands, April 4-8, 2016).

JR Dennison, Jodie Corbridge Gillespie, Allen Andersen, Amberly Evans Jensen, Justin Dekany, Gregory Wilson, Alec M. Sim, and Ryan Hoffmann, "Synergistic Models of Electron Emission and Transport Measurements of Disordered SiO2," *14th Spacecraft Charging Technology Conference*, Space Research and Technology Centre of the European Space Agency (ESA/ESTEC), (Noordwijk, Netherlands, April 4-8, 2016).

Allen Andersen and JR Dennison, "Mixed Weibull Distribution Model of DC Dielectric Breakdowns with Dual Defect Modes," *2015 IEEE Conference on Electrical Insulation and Dielectric Phenomena—(CEIDP 2015)*, (Ann Arbor, MI, October 18-21, 2015).

JR Dennison and Allen Andersen, "Pre-breakdown Arcing as a Proxy for DC Dielectric Breakdown Testing of Polymeric Insulators," *2015 IEEE Conference on Electrical Insulation and Dielectric Phenomena—(CEIDP 2015)*, (Ann Arbor, MI, October 18-21, 2015).

Allen Andersen and JR Dennison, "Comparing Experimental Apples and Oranges with Quantile-Quantile Plots," *American Physical Society Four Corner Section Meeting*, Arizona State University, Tempe, AZ, October 16-17, 2015.

Allen Andersen, Nelson Green, and Andrea Martinez, "RATT Lab ESD System Upgrades and Troubleshooting," *Summer Report to the JPL Electromagnetic Compatibility Group*, Jet Propulsion Laboratory, Pasadena, CA, August, 3, 2015.

Allen Andersen and JR Dennison, "Arcs and Sparks: Enhanced Predictions of Critical Dielectric Breakdown," *JPL Reliability Engineering and Mission Environmental Assurance Section (513) Invited Talk*, Jet Propulsion Laboratory, Pasadena, CA, July, 15, 2015.

Krysta Moser, Allen Andersen, and JR Dennison, "Dependence of Electrostatic Field Strength on Voltage Ramp Rates for Spacecraft Material," *American Physical Society Four Corner Section Meeting*, Arizona State University, Tempe, AZ, October 16-17, 2015.

Krysta Moser, Allen Andersen and JR Dennison,″ Dependence of Electrostatic Field Strength on Voltage Ramp Rates for Spacecraft Materials,″ *USU Physics Colloquium*, Utah State University, Logan, UT, September 22, 2015.

Allen Andersen and JR Dennison, ″Pre-breakdown Arcing and Electrostatic Discharge in Dielectrics under High DC Electric Field Stress,″ *2014 IEEE Conference on Electrical Insulation and Dielectric Phenomena—(CEIDP 2014)*, (Des Moines, IO, October 19-22, 2014).

Allen Andersen and JR Dennison, ″A Dual-defect Model for Predicting Lifetimes for Polymeric Discharges from Accelerated Testing,″ *American Physical Society Four Corner Section Meeting*, Utah Valley University, Orem, UT, October 17-18, 2014.

Sam Hansen, JR Dennison and Allen Andersen, ″Electrostatic Discharge Breakdown Analyses,″ *American Physical Society Four Corner Section Meeting*, Utah Valley University, Orem, UT, October 17-18, 2014. Presentation received award for outstanding Undergraduate Poster.

Allen Andersen and JR Dennison, ″A Dual-defect Model of Electrostatic Discharge in Polymeric Dielectrics,″ *Utah State University Physics Colloquium*, Utah State University, Logan, UT, September 2, 2014.

Allen Andersen, JR Dennison, Alec M. Sim and Charles Sim, ″Measurements of Endurance Time for Electrostatic Discharge of Spacecraft Materials: A Defect-Driven Dynamic Model,″ Invited Talk, *13th Spacecraft Charging Technology Conference*, (Pasadena, CA, June 25-29, 2014).

JR Dennison, Justin Dekany, Jodie Corbridge Gillespie, Phil Lundgreen, Allen Andersen, Amberly Evans Jensen, Gregory Wilson, Alec M. Sim, and Ryan Hoffmann, ″Synergistic Models of Electron Emission and Transport Measurements of Disordered SiO2,″ Invited Seminar, *13th Spacecraft Charging Technology Conference*, (Pasadena, CA, June 25-29, 2014).

Sam Hansen, JR Dennison, and Allen Andersen, ″Electrostatic Discharge Breakdown Analyses,″ *Utah State University Student Showcase*, Logan, UT, April 11, 2014.

Allen Andersen and JR Dennison, "Pre-breakdown Arcing in Dielectrics under Electric Field Stress," *American Physical Society Four Corner Section Meeting*, University of Denver, Denver, CO, October 18-19, 2013.

Allen Andersen and JR Dennison, "Electrostatic Discharge in Solids," *Utah State University Physics Colloquium*, Utah State University, Logan, UT, October 8, 2013.

Allen Andersen and JR Dennison, "Charge Transport and Electrical Degradation Research for Power Grid Applications," *Utah State University Graduate Student Research Symposium*, Utah State University, Logan, UT, April 12, 2013.

Bob Meloy, Charles Bowers, Malcolm Niedner, Jim Heaney, Rudy Ivancic, J.R. Dennison, Justin Dekany, Greg Wilson, Amberly Evans Jensen, Allen Andersen, Charlie Sim, Kelby Peterson, Bobby Johnson, Ryan Hoffman, Joe Minnow, "JWST Architecture Working Group: NIRCam Pickoff Mirror Deep Charging," *James Webb Space Telescope Spacecraft Architectural Working Group Risk Assessment Board*, Goddard Space Flight Center, Greenbelt, MD, November 26, 2012.

Allen Andersen, Charles Sim and JR Dennison, "Electrostatic Discharge Properties of Fused Silica Coatings," *American Physical Society Four Corner Section Meeting*, New Mexico Institute of Mining and Technology, Socorro, NM, October 26-27, 2012. Presentation received award for outstanding Graduate Poster.

Justin Dekany, Allen Andersen, and JR Dennison, "Muon Contribution to Cathodoluminescence Tests?," *American Physical Society Four Corner Section Meeting*, New Mexico Institute of Mining and Technology, Socorro, NM, October 26-27, 2012.

Allen Andersen, Charles Sim and JR Dennison, "Electrostatic Discharge Properties of Fused Silica Coatings," Phillips Air Force Research Laboratory, Albuquerque, NM, October 25, 2012.

Allen Andersen, Todd Lines and Josh Barney, "Microwave Optics Research," *54th Idaho Academy of Science Annual Meeting and Symposium*, University of Idaho, Idaho Falls, ID, March 22-24, 2012.

Allen Andersen, Phil Scott, Todd Lines and Josh Barney, "Microwave Optics Research," *Brigham Young University-Idaho Research and Creative Works Conference*, Brigham Young University-Idaho, Rexburg, ID, December 8, 2011.